# Design and realization of SAW pressure sensor using Aluminum Nitride

Trang Hoang

## ▶ To cite this version:

## HAL Id: tel-00540305
### https://theses.hal.science/tel-00540305

Submitted on 26 Nov 2010

## UNIVERSITE JOSEPH FOURIER- GRENOBLE I
## SCIENCES.TECHNOLOGIE.SANTE

*N° attribué par la bibliothèque*
|__|__|__|__|__|__|__|__|__|

### *T H E S E*

pour obtenir le grade de

### DOCTEUR DE L'UNIVERSITE JOSEPH FOURIER

*Spécialité :*
Radio-Fréquence

préparée au laboratoire CEA/LETI-Minatec  - IMEP-LAHC

dans le cadre de **l'Ecole Doctorale**

*"Electronique, Electrotechnique, Automatique, Télécommunication, Signal"*

présentée et soutenue publiquement

par

## Trang HOANG

Le 19/01/2009

*TITRE*

# Design and realization of SAW pressure sensor using Aluminum Nitride

**DIRECTEUR DE THESE**
*Philippe BENECH*

## JURY

| | |
|---|---|
| M.Daniel Barbier | Président |
| Mme. Hélène Tap-Beteille | Rapporteur |
| M. Gilles Despaux | Rapporteur |
| M.Patrice Rey | Examinateur |
| M.Philippe Robert | Examinateur |
| M.Philippe Benech | Directeur de thèse |

**Dành cho bố mẹ thân yêu của con,**
**bố Nguyễn Sĩ Trí và mẹ Hòang Thị Tuyết**

**Dành cho em yêu dấu,**
**Nguyễn Ngọc Yến**

**Cho tình thương của bố, mẹ dành cho con**
**Cho tình yêu của em dành cho anh**

**To my parents,**
**To my fiancée,**
**for your love**

**À mes parents,**
**À ma fiancée,**

# Acknowledgements

I would like to express my deep gratitude to my advisors, Philippe Benech, Patrice Rey and Philippe Robert for their invaluable support, encouragement, supervision and useful suggestions throughout my thesis work. Their continuous guidance enabled me to complete my thesis work successfully.

I am also highly thankful to Marie-Hélène Vaudaine, for her continuous support throughout this study. She was willing to help me all of thing without hesitation. I really appreciate for that.

My deep gratitude to Hervé Fanet for his warm welcome and his help.

My sincere thanks to Jean-Sébastien Danel, Denis Mercier, Denis Renaud, Guy Parat, Pierre Lemaître-Auger and others that I could not remember their names, for their interests, discussions, supports and suggestions.

I extend my thanks to all the colleagues  in CEA-LETI for their friendship, funs, supports and encouragements, especially Béatrice, Lise, Mari-therese, Henri, Julien, Mouna, Thomas, Sébastien, Stéphane, Karim, Christine, Sophie, ….

Thanks to family REY since without them I probably would have never gotten to know a French culture, a French family. I have no words to describe how thankful I am to them for that.

Many thanks to my friends in Grenoble for their friendship, funs and helps throughout my life during three years in Grenoble.

I would like to express my sincere gratitude to my University of Technology, Viet Nam National University Ho Chi Minh City, especially Vu Dinh Thanh, Ho Trung My, Phan Thanh Binh, Dang Mau Chieu for giving me the opportunity to carry out my PhD study in this beautiful country, FRANCE.

Last, but not least, my profound gratitude to my family, especially my parents and my fiancée for their moral supports and encouragement throughout my life. They have inspired me and given me strength throughout my whole life. They are everything to me. I dedicate this work to them.

Grenoble-France, November 2008

Hoang Trang

# Table of content

# List of Tables

# List of Figures

# Glossary

AFM          Atomic Force Microscope
APM         Acoustic Plate Mode
BAW         Bulk Acoustic Wave
CMP         Chemical Mechanical Polishing
COM         Coupling Of Mode
FE         Finite Element
FEM        Finite Element Method
FPW        Flexural Plate Wave
FWHM     Full-Width at Half Maximum
HF         HydroFluoric acid
ID         IDentification
IDT         InterDigital Transducer
MEMS     Micro Electro Mechnical System
PBC        Periodic Boundary Condition
PCE        Pressure Coefficient of Elastic constant
PCF        Pressure Coefficient of Frequency
PSG        PhosphoSilicate Glass
RF         Radio Frequency
RIE         Reactive Ion Etching
RTV        Room Temperature Vulcanisation
SAW        Surface Acoustic Wave
SCS        Single Crystal Silicon
SEM        Scanning Electron Microscope
SH         Shear Horizontal
SOLT      Short Open Load Through
TCF        Temperature Coefficient of Frequency
TCV       Temperature Coefficient of Velocity
TSM       Thickness Shear Mode
VNA        Vector Network Analyzer

AlCu        Aluminium Copper alloy
AlN         Aluminium Nitride
GaAS       Gallium Arsenide
H3PO4    Phosphoric acid or orthophosphoric acid
LiNbO3    Lithium Niobate
LiTiO3     Lithium Titanate
Mo         Molybdenum
NMP        N-methyl-2-pyrrolidone
Pt-PbTiO3 Platinium - Lead Titanate
PVDF      Polyvinylidene Fluoride
PZT         Lead Zirconate Titanate
Si         Silicon
SiC         Silicon carbide
SiO2        Silicon dioxide
SOI         Silicon On Insulator
ZnO         Zinc Oxyde

# Introduction

In the field of the sensors and actuators, two great principles of detection and excitation coexist:

+ The electrostatic has the easily integrated and advantage of being in high temperature. However, it is very limited in term of density of energy and it requires strong supply voltages, which is not easily compatible with integration on silicon.

+ The piezoelectric offers a strong density of energy and a lower supply voltage. The piezoelectric materials have appeared and pushed by many developments on SAW (Surface Acoustic Wave) and BAW (Bulk Acoustic Wave).

Surface acoustic wave (SAW) and bulk acoustic wave (BAW) devices have been widely used in a variety of applications, both in consumer electronics as well as in industrial, commercial, medical and military applications or equipment. Although the telecommunication industry is the largest user of these devices, SAW based devices have many attractive features to be explored. Due to their small size, high sensitivity to external physical parameters and from the properties of the film deposited on the SAW substrate, they can react very fast to the changes in the environmental conditions. As physical or chemical quantities can be measured from remote locations without the need for a separate power supply, SAW sensors have some advantages as follows:

+ They can be placed on moving or rotating parts, for instance, in tire pressure.

+ They cand be used in hazardous environments such as high voltage plants, contaminated areas, strong radioactive areas, high vacuum process chambers, extreme heat, where the use of conventional sensor with wire connection is impossible, dangerous for human, complicated or expensive.

+ Besides, because SAW sensors can operate at high frequencies (GHz range), they can be well protected from the low frequencies electromagnetic interference that occurs in the vicinity of industrial equipment such as high voltage line.

The more common applications of acoustic wave sensors are Temperature, Pressure, Torque, Mass, Humidity, Vapor Chemical, and Bio sensors. Among these sensors, pressure sensor play a key part of many systems, both commercial and industrial.

SAW pressure sensors have been developed by using many different piezoelectric materials. Conventional piezoelectric materials such as quartz, $LiNbO_3$ and $LiTaO_3$ suffer

from a variety of limitations and in particular low SAW/BAW velocity as well as being incompatible with the CMOS technology. As a low-cost technique, thin-film sputtering of novel SAW materials like ZnO has gained much interest recently. However, their manufacturing methods were not, until the beginning of this thesis, compatible with high temperature process and consequently applications (>500°C). Besides, these piezoelectric materials exhibit medium to low SAW velocity, making them expensive to use in the microwave region due to increased lithography resolution requirements. The resonance frequency of a SAW device is determined by the equation $f = v_{ph} / \lambda$, where f is the resonance frequency, $v_{ph}$ is the phase velocity of SAW and $\lambda$ is the wavelength, which in turn is defined by the electrode pitch in the interdigital transducer (IDT). Hence, high-resolution lithography and/or the use of high acoustic velocity materials are the two main approaches for the fabrication of high-frequency SAW devices. The first one, however, results in an increased fabrication cost due to poorer reliability and durability,; the second one is the limitation to the choice of commercially available piezoelectric materials.

For approximately six years, a new material, the aluminum nitride (AlN), has appeared in the field of micro-electronics, pushed by many developments on BAW RF resonators of the type. AlN is an attractive material for high-frequency SAW and for many SAW applications due to its good properties, such as outstanding ultrasonic velocity, thermal and chemical stability. Beside, its process of deposit compatible with CMOS process offers new prospects for the realization of sensors and piezoelectric actuators, in particular its behavior at high temperature (up to $1000^0$C).

In summary, pressure sensor plays a key role in many applications. Some classical technologies for pressure sensor are use of pressure gauge, piezoresistance … Their detection methods are based on amplitude detection which is sensitive with environment and therefore not correct. Meanwhile, the new approach is based on frequency, phase shift of detection method, and it is also compatible with CMOS process. Among new approaches, SAW technology is a good detection method. When SAW device is used as in wireless sensor, it can be used in hazardous environment and moving objects. In SAW device, AlN is chosen as piezoelectric layer because it doesn't suffer from some disadvantages of conventional materials.

The goal of this thesis is the design and realization of SAW pressure sensor using AlN. Realization of SAW pressure sensor is done by using surface micromachining.

This kind of device can be used in high temperature applications. However, in large range of temperature, properties of materials are affected by temperature variations. Therefore, the center frequency is sensible to temperature changes. For pressure application, this sensitivity must be reduced. Usually, temperature compensation can be done by using one port Inter Digital Transducer (IDT) and at least three reflectors to create several propagation paths of different lengths and then a signal processing step is performed to reduced effect of temperature. This technique was used for quartz pressure sensors. To solve this problem, in SAW pressure sensors, we propose to use a multi-layers structure $AlN/SiO_2/Si$ to obtain an effect of self temperature compensation, by choosing material having opposite temperature coefficients.

## The organization of the manuscript

This thesis is divided into five chapters.

**Chapter 1** presents a general view of acoustic wave devices and SAW sensors. It also gives a comparison between piezoelectric materials and reason why choosing AlN as piezoelectric layer. Another important point presented in this chapter is micro-machining process. To model the SAW devices, some models were proposed and developed by many groups. Among them, the equivalent circuit is chosen to model the SAW device.

From this point of chapter 1, equivalent circuit of SAW device based on Mason model and Coupling-Of-Mode is presented in **chapter 2**. This chapter also analyses the SAW parameters in different structures of SAW devices (AlN/SiO$_2$/Si, AlN/Si, and AlN/Mo/Si).

**Chapter 3** gives the development of the model used for SAW pressure sensor and mechanical analysis of the sensitive membrane under pressure. Besides, the effect of frequency variation due to temperature changes is derived from materials properties. This chapter also gives the results of frequency variations due to temperature changes.

**Chapter 4** presents the details of fabrication process using surface micro-machining as well as the characterization results of AlN films which is an important part in SAW devices.

**The chapter 5** shows the parametric tests and procedure to check the device fabrication. These tests and procedures allow a fast process control of the deposited/etched layers during the fabrication, and also a fast characterization of all dies on the wafer. The major experimental results, the explanations and analyses of obtained results will be given in this chapter.

At the end, a general conclusion and perspectives are given.


This work was done at CEA/LETI/DIHS/LCMS and IMEP-LAHC, Grenoble from 10/2005-09/2008.

# Chapter 1

# BACKGROUND

## 1.1 ACOUSTIC WAVE DEVICES

Acoustic wave devices have been in commercial use for more than 60 years. They offer many applications:

+ In electronics, telecommunications industry, acoustic wave filters used in mobile cell phones and base stations. These are typically surface acoustic wave (SAW) devices which act as band pass filters in both the radio frequency and intermediate frequency sections of the transceiver electronics. They are also used as resonators, delay lines, convolvers or wireless identification systems (ID tags).

+ In sensor devices:

- automotive applications (torque, tire pressure sensors),

- medical applications (chemical sensors),

- Industrial and commercial applications (vapour, humidity, temperature, mass sensors).

Acoustic wave sensors are so called because their detection mechanism uses a mechanical, or acoustic waves. As the acoustic wave propagates through or on the surface of the material, any changes to the characteristics of the propagation path affect the velocity and/or amplitude of the wave. Changes in velocity can be monitored by measuring the frequency or phase characteristics of the sensor and can then be correlated to the corresponding physical or chemical quantity being measured.

All acoustic waves devices and sensors use a piezoelectric material to generate and detect acoustic waves. Devices have been constructed in a number of configurations for sensor applications. Those devices most commonly used in sensor applications include:

- the Thickness Shear Mode (TSM) resonator,

- the Surface Acoustic Wave (SAW) device,

- the Acoustic Plate Mode (APM) device,

- The Flexural Plate Wave (FPW) or Lamb wave device.

Each of these devices shown in Figure 1.1 uses a unique acoustic mode.
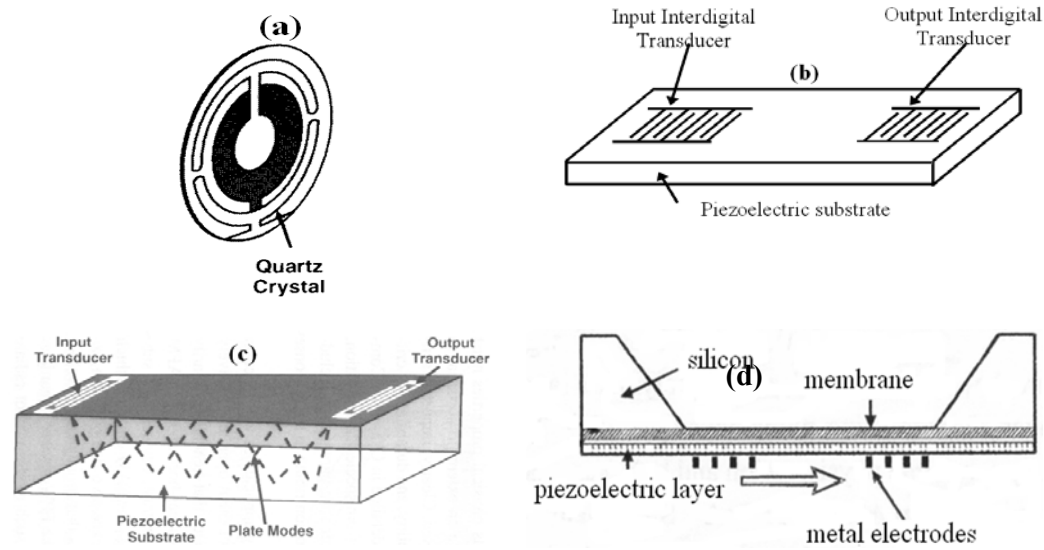


Figure 1.1   Schematic sketches of the four types acoustic sensors (a) the Thickness Shear Mode (TSM) resonator, (b) the Surface Acoustic Wave (SAW) device, (c) the Acoustic Plate Mode (APM) device, (d) the Flexural Plate Wave (FPW) or Lamb wave device

There is a distinction between these devices. They can be divided into two groups: one-port device (TSM resonator) and two-port device (SAW, APM and FPW devices). In one-port acoustic devices, a single port serves as both the input and the output port. The input signal excites an acoustic mode which in turn generates charges on the input electrode. These signals combine to produce an impedance variation that constitutes the TSM resonator response. In two-port devices, one port is used as the input port and the other as an output port, these are typically interchangeable. The input signal generates an acoustic wave that propagates to a receiving transducer, which generates a signal on the output port.

### 1.1.1     Thickness Shear Mode (TSM) resonator

The Thickness Shear Mode (TSM) Resonator widely referred to as a quartz crystal microbalance (QCM), is the best-known, oldest and simplest acoustic wave device. As shown in Figure 1.2, the TSM typically consists of a thin disk of AT-cut quartz with parallel circular electrodes patterned on both sides. The application of a voltage between these electrodes results in a shear deformation of the crystal.
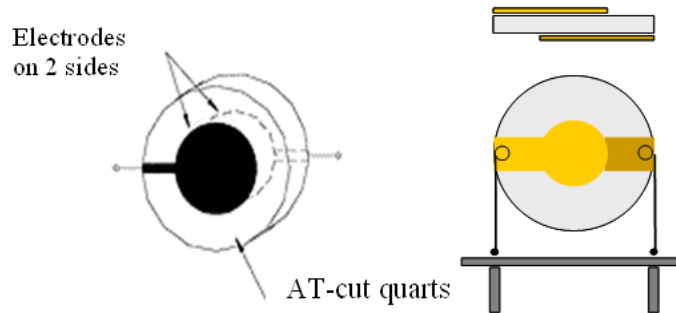
Figure 1.2   The thickness shear mode resonator

This device is known as a resonator because the crystal resonates as electromechanical standing waves are created. The displacement is maximized at the crystal faces, making the device sensitive to surface interactions. The TSM resonator was originally used to measure metal deposition rates in vacuum systems where it was commonly used in an oscillator circuit. The oscillation frequency tracks the crystal resonance and indicates mass accumulation on the device surface. In the late 1960s, the TSM resonator was shown to operate as a vapour sensor.

The TSM features simplicity of manufacture, ability to withstand harsh environments, temperature stability and good sensitivity to additional mass deposited on the crystal surface. Because of its shear wave propagation component, the TSM resonator is also capable of detecting and measuring liquids, making it a good candidate for a biosensor. Unfortunately, these devices have the lowest mass sensitivity of the sensors examined here. Typical TSM resonators operate between 5 and 30 MHz. Making very thin devices that operate at higher frequencies can increase the mass sensitivity, but thinning the sensors beyond the normal range results in fragile devices that are difficult to manufacture and handle. Recent work has been done to form high-frequency TSM resonators using piezoelectric films and bulk silicon micromachining techniques.

### 1.1.2    Surface Acoustic Wave Device

The stress-free boundary imposed by the surface of a crystal gives rise to a unique acoustic mode whose propagation is confined to the surface and therefore is known as a surface acoustic wave (SAW). In 1887, Lord Rayleigh discovered the surface acoustic wave mode of propagation and in his classic paper predicted the properties of these waves [1]. The theoretical aspect of acoustic wave was written by Viktorov [1]. Named for their discoverer, Rayleigh waves have a longitudinal and a vertical shear component that can couple with a

medium in contact with the device's surface (see Figure 1.3). The surface deformation is thus elliptic. Such coupling strongly affects the amplitude and velocity of the wave. This feature enables SAW sensors to directly sense mass and mechanical properties. The surface motion also allows the devices to be used as microactuators. The wave has a velocity that can be ~5 orders of magnitude less than the corresponding electromagnetic wave, making Rayleigh surface waves among the slowest to propagate in solids. The wave amplitudes are typically ~10 Å and the wavelengths range from 1 to 100 microns in sensors applications.
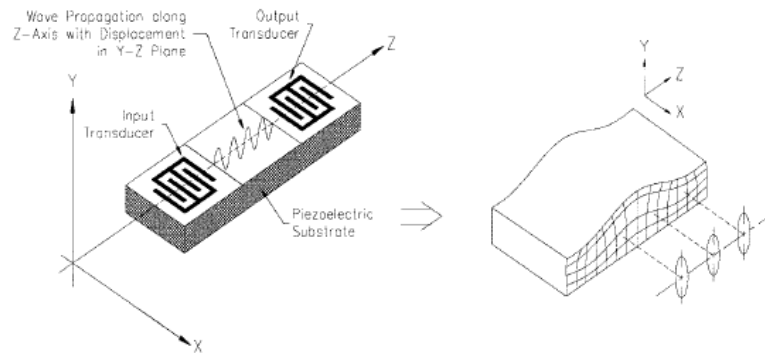


Figure 1.3   Rayleigh waves move vertically in a direction normal to the surface plane of a surface acoustic wave (SAW) sensor. SAW waves are very sensitive to surface changes, but do not work well for most liquid sensing applications

Figure 1.4 details the deformation field caused by a SAW propagating along the Z-axis and the associated distribution of potential energy. Because Rayleigh waves have virtually all their acoustic energy confined within one wavelength under the surface, SAW sensors have the highest sensitivity of the acoustic sensors reviewed.
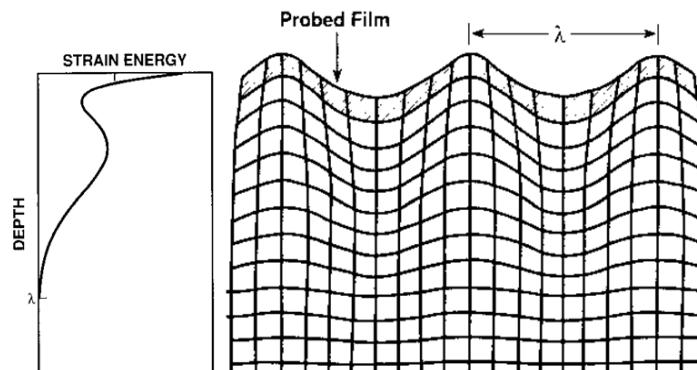


Figure 1.4   The wave energy is confined to within one wavelength from the surface of a SAW sensor. This characteristic yields a sensor that is very sensitive to interactions with the surface

One disadvantage of these devices is that Rayleigh waves are surface-normal waves, making them poorly suited for liquid sensing. When a SAW sensor is contacted by a liquid, the resulting compressional waves cause an excessive attenuation of the surface wave.

### 1.1.2.1  SAW excitation and detection

Viktorov presented some methods for the acoustic wave excitation [1]. And, useful method was discovered by R.M.White of the University of California at Berkeley [3] in which surface acoustic wave could be excited and detected by lithographically pattern interdigital electrodes (or InterDigital Transducer IDT) on the surface of piezoelectric crystals (see Figure 1.5). This discovery has led to widespread use of SAW devices in a number of applications such as frequency filters, delay lines, resonators, convolvers, correlators.
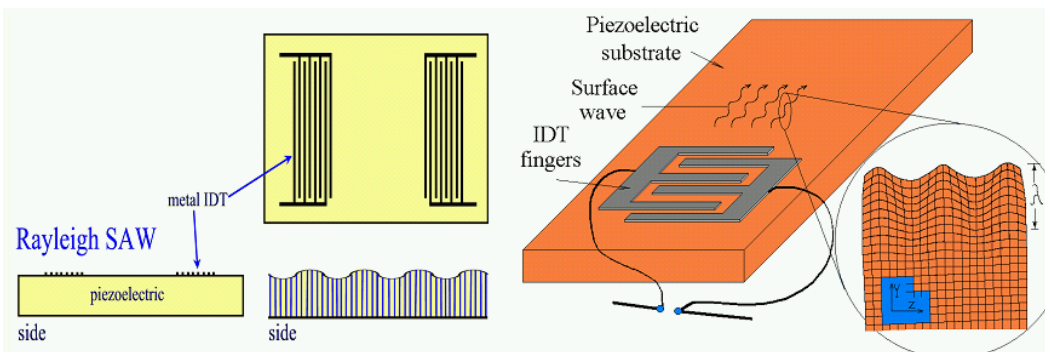


Figure 1.5   SAW with IDT excitation and detection

### 1.1.2.2  SAW perturbation mechanisms

When SAW devices are used for sensors or thin-film characterization, the measured responses arise from perturbation in wave propagation characteristics, specifically wave velocity and attenuation, resulting from interactions between the SAW and a surface layer. Because a SAW propagating in a piezoelectric medium generates both mechanical deformation and an electrical potential, both mechanical and electrical coupling between the SAW and surface film are possible. Therefore, a number of interactions between surface waves and a surface film have been found that give rise to velocity and attenuation responses.

SAW-film interactions that arise from mechanical coupling between the wave and film include *mass loading* caused by the translation of the surface mass by SAW surface displacement, elastic and viscoeleastic effects caused by SAW-induced deformation of a surface film.

SAW-film interactions that arise from electrical coupling between the wave and film include acoustoelectric interactions between electric fields generated by the SAW and charge carriers in a conductive film. Some new interactions are being discovered all the time.

### 1.1.3     Acoustic Plate Mode (APM) devices

These devices utilize a shear-horizontal (SH) acoustic plate mode (APM), which has been developed for sensing in liquids. SH modes have particle displacement predominantly parallel to the device surface and normal to the direction of the propagation. The absence of a surface-normal component of displacement allows each SH plate mode to propagate in contact with a liquid without coupling excessive amounts of acoustic energy into the liquid. By comparison, when surface acoustic waves are propagated at a solid-liquid interface, the surface-normal displacement radiates compressional waves into the liquid and severely attenuates the wave.

These devices use a thin piezoelectric substrate, or plate, functioning as an acoustic waveguide that confines the energy between the upper and lower surfaces of the plate (see Figure 1.6). This is in contrast to the SAW, for which nearly all the acoustic energy is concentrated within one wavelength of the surface. As a result, both surfaces undergo displacement, so detection can occur on either side. This is an important advantage, as one side contains the interdigital transducers that must be isolated from conducting fluids or gases, while the other side can be used as the sensor.
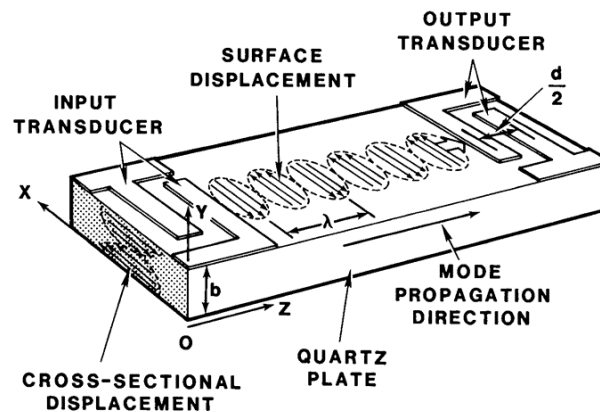


Figure 1.6   In the shear-horizontal acoustic plate mode (SH-APM) sensor, the waves travel between the top and bottom surfaces of the plate, allowing sensing on either side

Although being more sensitive to mass loading than the TSM resonator, SH-APM sensors are less sensitive than surface wave sensors. There are two reasons: the first is that the sensitivity to mass loading and other perturbations depends on the thickness of the substrate, with sensitivity increasing as the device is thinned. The minimum thickness is constrained by

manufacturing processes. Second, the energy of the wave is not maximized at the surface, which reduces sensitivity.

### 1.1.4      Flexural Plate Wave (FPW) or Lamb wave device

A sensor concept similar to SAW sensors but employing Lamb waves was first presented by Stuart W.Wenzel, Richard M.White in 1988 [14]. In a flexural plate wave (FPW) or Lamb wave device (see Figure 1.7), an acoustic wave is excited in a thinned membrane with a thickness small compared to the propagation wavelength. As with the other acoustic sensors mentioned above, the FPW device can sense quantities that cause its phase velocity to change.

A unique feature of FPW is that it can be dimensioned so that its phase velocity is lower than that of most liquids, which lie in the range from 900 to about 1500 m/s. When the FPW device contacts or is immersed in such a liquid, a slow mode of propagation exists in which there is no radiation from the plate. Thus, the FPW device functions well in a liquid environment and is therefore a good candidate for biosensing and chemical sensing in liquid [1].
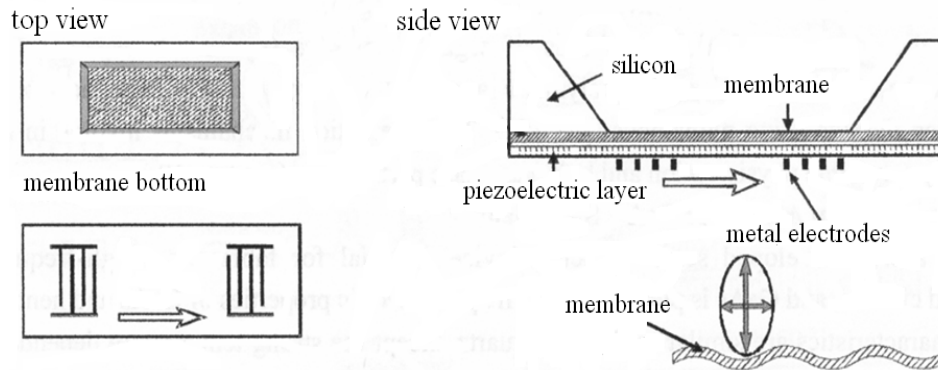


Figure 1.7   Schematic of a flexural plate wave device. The side view shows the different layers and membrane movement. Interdigital electrodes are used for actuation

### 1.1.5      Comparation between four sensors

Figure 1.8 shows the side views and cross sections of four devices, in which lower diagrams in each column illustrate the wave motion; double-headed arrows indicate directions of surface particle displacements and shaded areas illustrate the wave motion or indicate the depth of wave penetration in the plate.

Table 1.1 summarizes qualitatively the characteristics of four sensors discussed above.
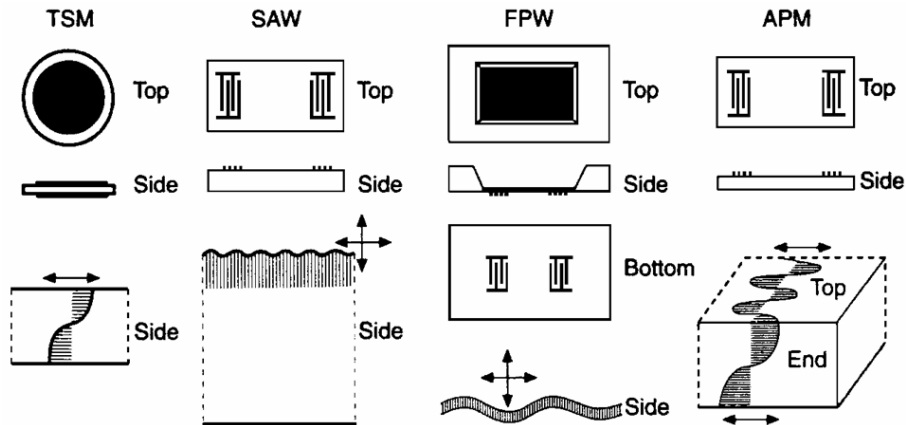
Figure 1.8   Side views and cross sections of four devices

Table 1.1   QUALITATIVE CHARACTERISTICS OF THE FOUR SENSOR FAMILIES DISCUSSED

| Device | Temp. Stability uncoated | Motion at surface of device | Immersible | Frequency of operation | Mechanical strength | Discrete or **Multiple** fabrication | Delay line or **Resonator** |
|---|---|---|---|---|---|---|---|
| **TSM** | High | Transverse | Yes | Low | Med | D | R |
| **SAW** | High/ med | Normal and transverse | No | Med-high | High | D or M | D or R |
| **APM** | High | Transverse | Yes | Med-high | Med | D | D |
| **FPW** | Med | Normal and transverse | Yes | Low | Low-med | M | D or R |

## 1.1.6    SAW sensor and the application pressure sensor in this research

SAW sensors offer many new applications. Because physical, chemical quantities can be measured from remote locations without the need of a separate power supply, SAW sensors have some advantages as follows:

+ They can be placed on moving, or rotating parts, for instance, in tire pressure [4],[5],[6],

+ used in hazardous environments such as high voltage plants, contaminated areas, strong radioactive areas, high vacuum process chambers, extreme heat, where the use of conventional sensors with wire connection is impossible, dangerous for human, complicated or expensive,

+ besides, because SAW sensors can operate at high frequencies (GHz range), the system based on them can be well protected from the electromagnetic interference that occurs in the vicinity of industrial equipment such as high voltage line.

Figure 1.9 shows the influences to SAW sensors and applications. The environmental parameters (such as temperature, pressure, humidity, mass loading . . .) are converted directly to a change in frequency, phase, or delay time of SAW sensor.
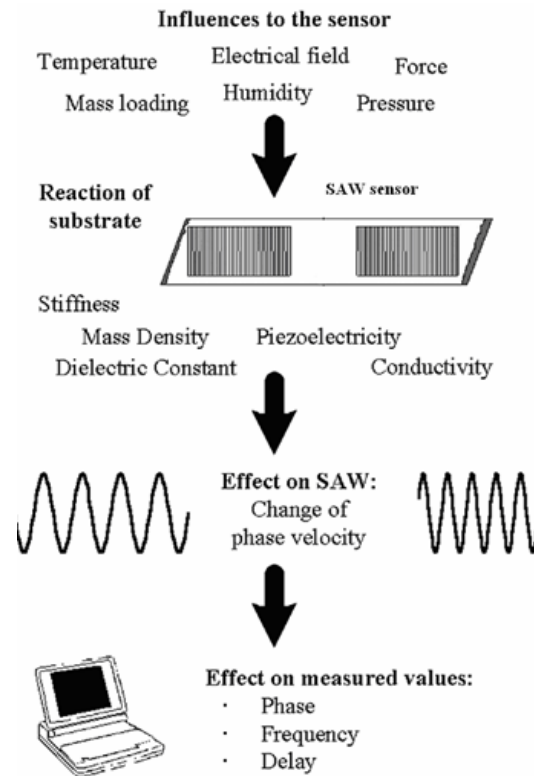


Figure 1.9   Environmental influences to the SAW sensors

Among these applications, the pressure sensor plays a key part of many systems, both commercial and industrial. Our work focuses on this kind of sensor.

SAW pressure sensors could be divided into two types:

+ One port IDT,

+ Two port IDT.

### 1.1.6.1  SAW pressure sensor with one port IDT

The SAW pressure sensor using one port IDT has been studied in literature [4]-[9]. In general, there are two types as follows:

+ Without external sensor circuit (see Figure 1.10)
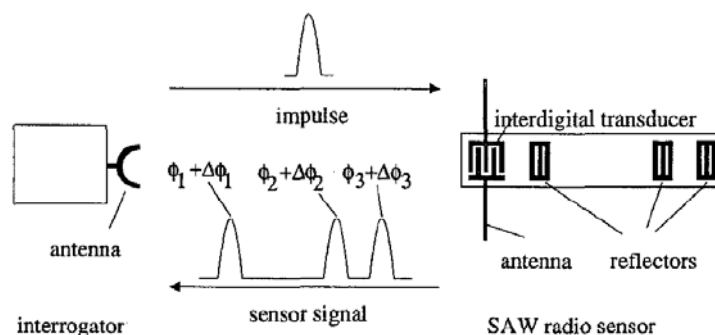
Figure 1.10   SAW wireless pressure sensor with one broadband reflective delay line

The interrogator transmits an RF-impulse which is received by the antenna of the wireless sensor. The interdigital transducer transforms the RF-impulse to a surface acoustic wave. Reflectors are placed in the propagation path of the SAW at which small parts of the SAW is reflected. The impulses are reflected back to the transducer where they excite an RF-impulse train which is detected by the interrogator. The sensor signal is determined by evaluating the phase shifts $\Delta\phi_i$ of the reflected impulses.

The reflective delay line requires at least three reflectors [7]. The first reflector serves as a reference reflector. This makes the sensor response independent on the distance between sensor and interrogator. For optimal reflector configuration, the first and second reflectors divide the delay line into stretched and compressed sections. The third one is placed at the end of the propagation path.

The temperature correction of the pressure signal could be obtained by arranging the electrically loaded reflector equidistantly between two reference reflectors in a second track [6].

+ With external sensor circuit

Figure 1.11 shows the diagram of a SAW pressure sensor with one IDT and external sensor circuit represented by its input impedance Z. Z could be another pressure sensor. When external sensor Z changes due to applied pressure, the reflector parameters will change. Consequently, RF response changes also. By capturing the variation of RF signal, pressure can be measured
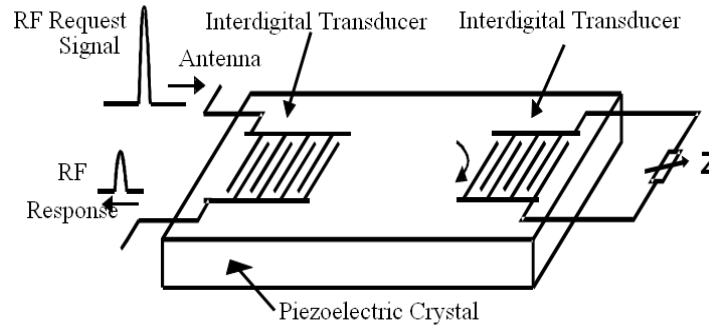
Figure 1.11   SAW pressure sensor, one IDT and with external sensor circuit Z

### 1.1.6.2  SAW pressure sensor with two ports IDT

The general structure of the SAW pressure sensor with two ports IDT is illustrated on Figure 1.12.
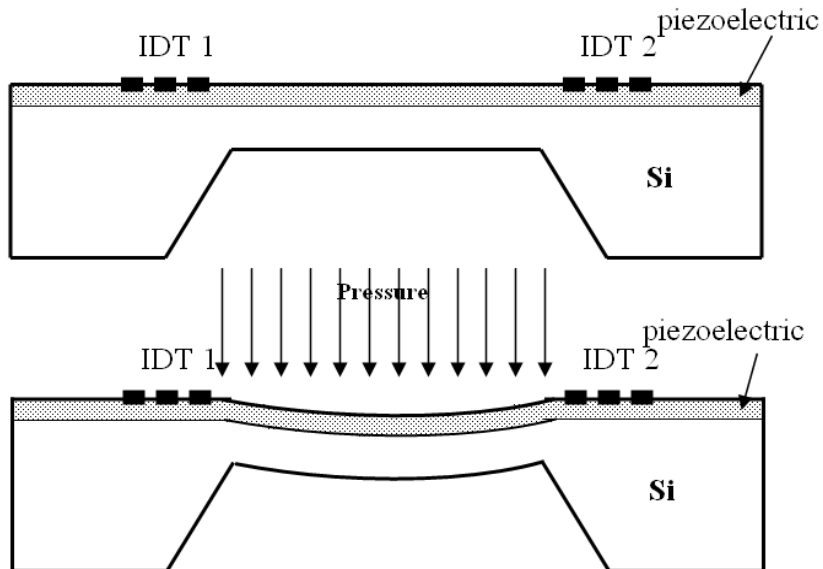


Figure 1.12   General structure of a SAW pressure sensor with two IDTs

The signal frequency: $f = \dfrac{v}{\lambda}$

where $\lambda$ is wavelength,

v is the phase velocity of a SAW and determined in the simple case with only one propagation layer:

$$v = \sqrt{\frac{c^*}{\rho}}$$

where c$^*$ is a linear combination of the elastic constant c$_{ikjm}$, and depends on the cut of the substrate;

$\rho$ is the mass density of the wave guiding layer of the substrate.

For the multi-layers structure, the SAW velocity could be determined by the matrix method developed by Fahmy and Adler [69], [69], [70] and it also depends on the elastic constants of each layer.

The applied pressure will induce static stress and strain and modify the elastic constants, so modify the wave velocity.

$$\frac{\Delta v}{v} = \frac{\Delta c^*}{2c^*} - \frac{\Delta \rho}{2\rho}$$

Consequently, there is variation of frequency.

$$\frac{\Delta f}{f} = \frac{\Delta v}{v} - \frac{\Delta \lambda}{\lambda} = \frac{\Delta c^*}{2c^*} - \frac{\Delta \rho}{2\rho} - \frac{\Delta \lambda}{\lambda}$$

By capturing the frequency variation, the applied pressure could be measured.

The calculation of frequency variation, but also the phase variation, will be stated in Chapter 3. This chapter will show that these variations exist not only by the variations of elastic constants but also by the propagation path changes between two IDTs.

All acoustic wave sensors use a piezoelectric material to generate the acoustic wave. For application of pressure sensor, the ZnO/Si SAW pressure sensor was studied by A.Talbi [10]-[13]. But, in our work AlN is used as piezoelectric material.

## 1.2   PIEZOELECTRIC MATERIALS. ALUMINUM NITRIDE (ALN) AND ITS APPLICATIONS IN SAW DEVICES

### 1.2.1     Piezoelectric materials and the choice of AlN

Piezoelectricity, discovered by brothers Pierre and Paul-Jacques Curie in 1880, received its name in 1881 from Wilhelm Hankel and remained largely a curiosity until 1921, when Walter Cady discovered the quartz resonator for stabilizing electronic oscillators. Piezoelectricity refers to the production of electrical charges by the imposition of mechanical stress. The phenomenon is reciprocal. Applying an appropriate electrical field to a piezoelectric material creates a mechanical stress. Piezoelectric acoustic wave sensors apply an oscillating electric field to create a mechanical wave, which propagates through the substrate and is then converted back to an electric field for measurement.

Common piezoelectric materials:

    Single crystals:

        AlN, ZnO, Quarts, $LiNbO_3$, $LiTiO_3$.

    Piezo-ceramics:

        PZT-$Pb(Zr_xTi_{1-x})O_3$

        PT-$PbTiO_3$

    Piezo-polymers:

        PVDF and its copolymers, nylon…

    Composites:

        PVDF+PZT

        .v.v.

Each has specific advantages and disadvantages, which include cost, temperature dependence, fabrication process, attenuation, propagation velocity, bio-compatible, mechanical adaptability to a variety of applications... An interesting property of quartz is that it is possible to select the temperature dependence of the material by the cut angle and the wave propagation direction. With proper selection, the first order temperature effect can be minimized. An acoustic wave temperature sensor may be designed by maximizing this effect. This is not true for lithium niobate or lithium tantalate, where linear temperature dependence always exists for all material cuts and propagation directions. Other materials with commercial potential include gallium arsenide (GaAs), silicon carbide (SiC), langasite (LGS), zinc oxide (ZnO), aluminium nitride (AlN), lead zirconium titanate (PZT), and polyvinylidene fluoride (PVDF). Another important parameter is that a piezoelectric material can be ferroelectric or not. This has an importance for the fabrication process. Ferroelectric materials required a polarisation step.

The Table 1.2 lists advantages and disadvantages of some piezoelectric materials common used in SAW devices.

Table 1.2   ADVANTAGES AND DISADVANTAGES OF SOME PIEZOELECTRIC
MATERIALS COMMON USED IN SAW DEVICES

| Material | Advantages | Disadvantages |
|---|---|---|
| Quartz | Low acoustic loss<br>Good temperature stability | Weak piezoelectricity |
| AlN | Retain the properties beyond $1000^0$C<br>High longitudinal acoustic velocity (two time larger than ZnO [87]<br>High E-M coupling<br>Low K and low loss<br>Relative good thermal conductivity<br>Compatible with microelectronic CMOS processes | High electrical resistance<br>Until 5 μm available fabrication in CEA/LETI. |
| ZnO | High E-M coupling<br>For small bandwidth application | High dielectric loss<br>High electrical resistance |
| LiNbO$_3$ | High E-M coupling<br>Chemical stable<br>Low K<br>Excellent sensitivity with good bandwidth | |
| PZT | High E-M coupling<br>Low electric loss<br>High Curie temperature and spontaneous polarization<br>Can be doped with La (0~5%)<br>Prepared by sol-gel processing | High K<br>High density and less mechanically stable |
| PT | High E-M coupling<br>High Curie temperature and wide operating T range<br>Good thermal stability | High K |
| PVDF | Low acoustic impedance<br>Low K<br>Low density and Flexible and mechanically compliant<br>High g coefficient | Low E-M coupling<br>Poor sensitivity<br>Low d coefficient<br>High electrical loss<br>9~110 microns available |

In SAW applications, conventional piezoelectric materials (such as quartz, LiNbO$_3$, and LiTaO$_3$) exhibit medium-to-low SAW velocity, making them expensive to use in the microwave region due to increased lithography resolution requirements. The resonance frequency of a SAW device is determined by the equation $f = v_{ph} / \lambda$, where f is the resonance frequency, $v_{ph}$ is the phase velocity of SAW and $\lambda$ is the wavelength, which in turn is defined by the electrode pitch in the interdigital transducer (IDT). Hence, high-resolution lithography and/or the use of high acoustic velocity materials are the two main approaches for the fabrication of high-frequency SAW devices. The first one, however, results in an increased fabrication cost due to poorer reliability, power durability, and fabrication margins in the manufacturing process; the second one is limited to the choice of commercially available piezoelectric materials.

In literature, SAW devices are typically fabricated on quartz, $LiNbO_3$ and $LiTaO_3$. However, there is an increasing interest to identify new piezoelectric materials where SAW devices can operate at frequencies above 1GHz, a common requirement of most modern telecommunication applications. As a low-cost technique, thin-film sputtering of novel SAW materials like ZnO and AlN has gained much interest recently [13], [24]-[37]. It has been demonstrated, however, that the control of the perfection of the polycrystalline grains and other essential parameters such as orientation, stress and surface roughness is of importance [33], [35] because these parameters determine the nature and properties of the elastic waves.

In Table 1.2, AlN was shown that it has better properties than ZnO in fabrication of SAW; especially that AlN has larger velocity than ZnO. AlN could also maintain good properties at high temperature and its deposition is compatible with microelectronics process. Besides, AlN also was proposed and has gained much interest in new prospects such as BAW, FBAR technology [15], [16], [17] or mechanical resonators and actuators [18], [19].

With all results stated above, in this research, AlN is chosen for SAW sensors.

### 1.2.2    General Information of AlN

While AlN's discovery occurred over 100 years ago, it has been developed into a commercially viable product with controlled and reproducible properties within the last 10 years.

AlN is a III-V semiconducting compound. When pure, AlN crystals are hard, colourless and transparent [26]. AlN has a hexagonal crystal structure and is a covalent bonded material. The material is stable to very high temperatures in inert atmospheres. In air, surface oxidation occurs above 700°C. A layer of aluminum oxide forms which protects the material up to 1370°C. Above this temperature bulk oxidation occurs. AlN is stable in hydrogen and carbon dioxide atmospheres up to 980°C.

To ensure the operation of all devices using AlN, the AlN films should fulfil simultaneously two conditions: be highly (002)-oriented and exhibit high electromechanical coupling. Many works have been done to improve the crystal quality of AlN sputtered films. They have taken for granted that low values of Full-Width at Half-Maximum (FWHM) of x-ray rocking curves around the (002) reflection ensure a good piezoelectric response. However, in some cases, AlN films with a very good crystal quality exhibit a poor or even in existent piezoelectric response [19], which could be attributed to the existence of grains with opposite polarities [20], [21]. Therefore, a narrow rocking curve around the (002) does not guarantee a good piezoelectric response. In this research, after depositing AlN films, FWHM of AlN is

measured and at the end of fabrication process, the SAW devices are characterised to ensure the existence of piezoelectric response of AlN.

The sputter deposition conditions of AlN films should be considered carefully. The supply of energy to the substrate during the sputter deposition of AlN films is essential to grow (002)-oriented films [33]. This energy must be high enough to obtain the desired orientation, but not so high as to damage the crystal structure. On the other hand, an energy supply slightly below that needed to obtain pure (002) orientation leads to films with good crystal quality but very low piezoelectric response, which suggests that the growth of micro-crystal with opposite piezoelectric polarities has taken place. Therefore, it is necessary to adjust carefully the amount of energy supplied to the substrate. This can be achieved by controlling the total pressure and the substrate bias voltage [22], [23]. The studies of the influences of the sputtering parameters on the preferred orientation of AlN films were done [23].

In CEA/LETI, the deposition of AlN film have been studied and developed. In this research, we follow the condition of AlN deposition done in previous work [19].

In conclusion, AlN is an attractive material for high-frequency SAW and for many SAW applications due to its good properties, such as outstanding ultrasonic velocity, good thermal and chemical stability [32], [33]. Some key properties and typical uses of AlN are given as follows:

**Key Properties**

Good dielectric properties ($\varepsilon$=8.5, see Appendix A)

High thermal conductivity [19]

Low thermal expansion coefficient, close to that of Silicon

Non-reactive with normal semiconductor process chemicals and gases

**Typical Uses**

SAW sensors

Substrates for electronic and IC packages

Heat sinks

Power transistor bases

Microwave device packages

Semiconductor processing chamber fixtures and insulators

## 1.3    MODELLING SAW DEVICES

The design of SAW devices should require precise and efficient models and simulation tools. Several methods have been proposed for modelling and analyzing the SAW devices. These include the impulse model, the equivalent circuit models, the coupling-of-mode (COM) model, P-matrix model, angular spectrum of waves models [38] and the Scattering Matrix approach that was presented by Coldren and Rosenberg [39]. While the impulse model is only a first order model, the other models include second order effects, e.g. reflections, dispersion, and charge distribution effects. Purely numerical methods have also been and are being developed by many authors [40]-[72].

### 1.3.1    Why Equivalent Circuit model is chosen?

Actual devices exist in a three-dimensional physical continuum. Their behaviour is governed by the laws of physics, chemistry, biology, and electronics. From a general point of view, the analysis of devices can be carried out by using some equations of laws of physics, chemistry … For example; the analysis of piezoelectric resonators or transducers and their application to ultrasonic system can be solved by using the wave equation [73],[74]. But through analysis, equivalent electrical circuit representations of devices can be extracted. So, they can be readily expressible with Equivalent Electric Circuit. Below is the presentation of advantages and disadvantages of equivalent circuit.

**Advantages:**

+    There are an immensely powerful set of intellectual tools to understand electric circuits.

+    The equivalent circuit approach has distinct advantages over the direct physical, chemical equations approach (such as direct wave equations approach).

+    Many theories, problems of electric circuits have already been solved such as microwave network theory, integrated circuit etc.

+    Electric circuit approach is intrinsically correct from an energy point of view [75].

+    A further advantage of electric circuit model is that it permits efficient modelling of the interaction between the electric and non-electric components of a

microsystem. Both the electrical and mechanical portions of a system are represented by the same means. With software like Simulink, the block diagram is easily constructed, easily to build a more complex system but when we would like to connect a mechanical element to electrical circuits, Simulink can not do that. The analogies between electrical and mechanical elements are presented clearly by Warren P.Mason [73], [74].

**Disadvantages:**

+ Care must be taken to make sure whether the boundary conditions are compatible with those used in the original derivation of the equivalent circuit [74].

In many systems, both commercial and industrial, pressure measurement plays a key role. Since pressure is a normal stress (force per unit area), pressure measurement can be done by using piezoelectric material which can convert stress into voltage. Equivalent circuits such as Mason's model [73] provide a powerful tool for the analysis and simulation of piezoelectric transducer elements. Most of the analogous circuits which have appeared in the literature implement transducers as the circuit elements. This model simulates both the coupling between the mechanical and electrical systems and the coupling between the mechanical and acoustical systems [76]. The mechanical, electrical and acoustic parts of piezoelectric transducer can be varied and analysed about behaviour by implementing equivalent circuits on computer tools such as Ansoft®, Spice, ADS, etc. For IDT composing of N periodic sections, Smith et al [78] developed the equivalent circuit model based on Berlincourt et al [77] work about equivalent circuit for Length Expander Bar with parallel electric field and with perpendicular electric field and based on the equivalent circuit for electromechanical transducer presented by Mason [73]. We will use "Smith model" henceforth to indicate this model. From this model, some models for SAW device in literature have been implemented. However, these models would include only IDTs [79], [80]. In SAW pressure sensor, one of sensitive parts is propagation path. It should be included in the model. We have constructed the hybrid model based on Smith model for SAW pressure sensor which includes the IDTs and propagation path.

Another equivalent model is based on the Coupling-Of-Modes (COM) theory. The COM theory is a branch of the highly developed theory of wave propagation in periodic structures, which has an history of more than 100 years. This theory covers a variety of wave phenomena, including the diffraction of EM waves on periodic gratings, their propagation in periodic waveguides and antennas, optical and ultrasonic waves in multilayered structures,

quantum theory of electron states in metal, semiconductors, and dielectrics…. An excellent recent review of COM theory used in SAW devices was written by K.Hashimoto [47]. Based on the COM equations, as the force and voltage analogy can be used, the relationships between the terminal quantities at the one electrical port and two acoustic ports for an IDT have been done. A simple equivalent circuit for IDT based on COM approach was proposed by K.Nakamura [81]. This model would be useful to analyse and design SAW devices. The model based on COM theory take into account the reflection between fingers.

In conclusion, the equivalent-circuit model is chosen because it can allow fast design. This allows the designer to determine the major dimensions and parameters in number of fingers, fingers width, aperture, delay line distance, frequency response, impedance parameters and transfer characteristics of SAW device.

### 1.3.2     The Finite Element Model (FEM)

In the design procedure of SAW devices, simple models like Equivalent Circuit Model coming from Smith Model and COM Model as presented above are used to achieve short calculation time and to get a general view of response of SAW devices. They are a good approach for designing SAW devices, for getting the frequency response, impedance parameters and transfer characteristics of SAW device. They could allow the designer to determine the major dimensions and parameters in number of fingers, finger width, and aperture. However, they are subjected to some simplifications and restrictions.

Field theory is the most appropriate theory for the design SAW devices as it involves the resolution of all the partial differential equations for a given excitation. The Finite Element Model (FEM) is the most appropriate numerical representation of field theory where the piezoelectric behaviour of the SAW devices can be discretized [82], [83]. Besides, nowadays, FEM tools also provide 3D view for SAW device, such as COMSOL® [84], Coventor® [85], ANSYS® [86].

The typical SAW devices can include a lot of electrodes (hundreds or even thousands of electrodes). In fact, we would like to include as many IDT finger pairs as possible in our FEM simulations. This would however significantly increase the scale of the device. Typically finite element models of SAW devices require a minimum of 20 mesh elements per wavelength to ensure proper convergence. A conventional two-port SAW devices consisting of interdigital transducers (IDT) may have – especially on substrate materials with low piezoelectric coupling constants - a length of thousands of wavelengths and an aperture of hundred wavelengths. Depending on the working frequency, the substrate which carries the

electrode also has a depth of up to one hundred wavelengths. Taking into account that FEM requires a spatial discretization with at least twenty first order finite elements per wavelength and that an arbitrary piezoelectric material has at least four degrees of freedom, this leads to 8 x $10^8$ unknowns in the three dimensional (3-D) case. Hence, the 3-D FEM representation of SAW device with hundreds of IDT fingers would require several million elements and nodes. The computational cost to simulate such a device is extremely high, or the amount of elements could not be handled by nowadays computer resources.

Fortunately, SAW devices consist of periodic section. M.Hofer et al proposed the Periodic Boundary Condition (PBC) in the FEM that allows the reduction of size of FE model tremendously [82], [83].

A good agreement between FEM and analytic method is obtained; this agreement was also presented in literature [80]. However, it takes a long time and it would require a trial and error to find the results. Consequently, to reduce time, in our work, the analytical method and equivalent circuit are used to extract the parameters of SAW devices; FEM is used to get a 3D view and explain some results that can not be explained by equivalent circuit.

## 1.4 MICROMACHINING PROCESS, THE CHOICE OF SURFACE MICROMACHINING

The emergence of silicon micromachining has enabled the rapid progress in the field of microelectromechanical systems (MEMS). Silicon micromachining is the process of fashioning microscopic mechanical parts out of a silicon substrate or indeed, on top of a silicon substrate. It is used to fabricate a variety of mechanical structures which have been used successfully to realise a wide range of microsensors and microactuators. Silicon micromachining comprises two technologies: bulk micromachining and surface micromachining. The term bulk micromachining expresses the fact that this is used to realize the micromechanical structures within the bulk of a single-crystal silicon (SCS) wafer by selective removing the wafer material. In bulk micromachining, etching is the key technological step. The etching process in bulk micromachining comprises several of the following techniques:

+ Wet isotropic etching.

+ Wet anisotropic etching.

+ Plasma isotropic etching.

+ Reactive ion etching (RIE)

+ Etch-stop.

Since the beginning of the 1980s, much interest has been directed toward micromechanical structures fabricated by a technique called surface micromachining, a new age for silicon sensors and actuators [88]. There are several approaches to the making of MEMS devices using surface micromachining. The first is sacrificial layer technology to realise mechanical microstructures. The second approach incorporates IC (Integrated Circuit) technology and wet anisotropic etching. And the third is using plasma etching to fabricate microstructures at the silicon wafer surface. Sacrificial layer technology is used in our process to create exactly the membrane. In sacrificial layer technology, the key processing steps are as follows:

+ Deposition and patterning of a sacrificial layer ($SiO_2$ is a popular and preferred material choice).

+ Deposition and definition of a poly-Si film.

+ Removal of the sacrificial layer $SiO_2$ by lateral etching in hydrofluoric acid (HF).

It was shown in literature that there are the relative advantages and disadvantages of these two technologies. Table 1.3 summarizes the relative advantages and disadvantages of bulk and surface micromachining. Perhaps, the most attractive feature of surface micromachining is wider range of structural geometry than bulk micromachining.

Table 1.3   COMPARISON BETWEEN BULK AND SURFACE MICROMACHINING TECHNOLOGIES

| Bulk micromachining | | Surface micromachining | |
|---|---|---|---|
| Advantages | Disadvantages | Advantages | Disadvantages |
| | | Uses several materials and allows for new applications. | |
| Allows rugged structures that withstand vibration and shock. | Large die areas that give it high cost. | Small die area that makes it cheaper. | Less-rugged structures with respect to vibration and shock. |
| Large mass/area. | Not well fully integrated with IC processes. | Fits well with IC processes. | Small mass/area, which would typically reduce sensitivity. |
| Well characterised material (i.e. Si). | Limited structural possible geometries. | Wider range of structural geometries. | Fabrication process is not well known for some materials. |

Our novel fabrication process presented in this thesis by using surface micromachining technique is proposed to create exactly the dimensions of membrane used in pressure sensor and this process also allows having a well defined membrane with any geometry due to the

silicon etch stop walls. In our fabrication process, the property of creating any geometry is promising in many applications.

In literature, SAW devices used both individually as well as in arrays find applications in telecommunications, chemical, physical and biological sensing as well as in materials characterization [3], [4], [7], [9], [89]-[101]. Conventional SAW devices typically comprise of one delay-line or dual delay-line configurations with one delay-line used as a reference to compensate for environmental variations [102], [103], [104]. These conventional SAW devices can be fabricated by bulk micromachining, for instance, pressure sensor [10].

Recent efforts have focused on the design and fabrication of acoustic wave devices which can allow for better sensor characteristics as well as material characterisation possibilities [104], [105].

One such device with a complicated transducer design is the hexagonal SAW sensor proposed as in [106], [107], [108]. The hexagonal SAW device is shown in Figure 1.13. It is made of three different delay paths aligned to allow for generation of acoustic waves which are different in character in the different directions. It is possible to exploit the generated multiple wave modes to develop SAW devices that can be used as better chemical sensor and bio-sensor elements. There are several advantages to the hexagonal SAW device. The three different delay paths could be used for simultaneous detection and the data collected across the three delay paths allow for better characterisation of the sensing (thin film) material. This design allows for the simultaneous extraction of multiple properties (material density or thickness, sheet conductivity) of a thin film material to achieve a more complete characterisation than when a single SAW delay-line is used. Thus, this device can serve as a better in-situ characterisation tool in thin film physical and chemical deposition equipment and is expected to perform better than the typically utilised quartz crystal microbalance [109]. Preliminary experimental results have shown increased sensitivity for these devices in chemical sensor applications [106].
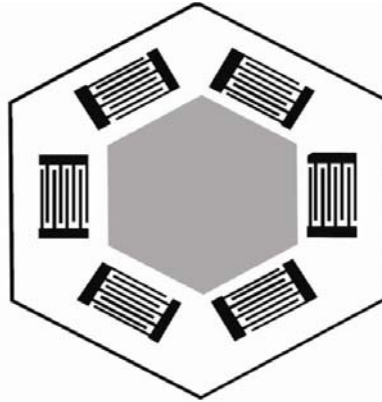
Figure 1.13   Hexagonal SAW device

In conclusion, there are several advantages to the hexagonal SAW device. In case of using it with membrane, it is too difficult to fabricate the device by bulk micromachining. Besides, to create exactly membrane with dimensions much smaller than the thickness of silicon bulk, for instance, 200µm x 200µm membrane and 760 µm thickness of silicon bulk, in bulk micromachining, this is not easy. With our fabrication process, the hexagonal SAW device with membrane or SAW device with membrane of any geometry could be easily realized.

## 1.5   CONCLUSION

This chapter gives a general view of acoustic wave devices used for sensor applications; the reason why choosing equivalent circuit model. Equivalent circuit of SAW device is presented in Chapter 2. It also gives the SAW parameter analysis in different structures of SAW device. Based on this chapter, Chapter 3 presents the development of model used for SAW pressure sensor, mechanical analysis of membrane under pressure, the pressure sensitivity calculation as well as the frequency variation due to temperature change.

AlN is chosen as attractive material for many SAW applications due to its good properties that are compatibility with microelectronics process, high acoustic velocity, and high coupling factor. The AlN characterisation will be presented in Chapter 4.

Surface micromachining technique is proposed to fabricate the SAW pressure sensor due to its interesting characters. It could create exactly the dimensions of membrane used in pressure sensor and allows having a well defined membrane with any geometry due to the silicon etch stop walls. The property of creating any geometry is promising in many applications. The fabrication process using surface micromachining will be given in Chapter 4.

# Chapter 2

# SAW PARAMETERS ANALYSIS AND EQUIVALENT CIRCUIT OF SAW DELAY LINE

## 2.1 INTRODUCTION

Surface Acoustic Wave (SAW) devices, using interdigital electrodes, play a key role in today's telecommunication systems and are widely used as electronic filters, resonators, delay lines, convolvers or wireless identification systems (ID tags).

During the last three decades, demands set by the expansion of the telecommunication industry and many applications in sensor have resulted in the introduction of a new generation of the SAW devices. Consequently, the design of high performance SAW devices requires precise and efficient models, simulation tools. Several methods have been proposed for modeling, analyzing SAW devices. These include the impulse model, the equivalent circuit models, the coupling-of-mode (COM) model, P-matrix model, angular spectrum of waves models [38] and the Scattering Matrix approach that was presented by Coldren and Rosenberg [39]. While the impulse model is only a first order model, the other models include second order effects, e.g. reflections, dispersion, and charge distribution effects. Purely numerical methods have also been and are being developed by many authors [72]-[78].

In this chapter, the method for calculating the SAW parameters, including modeling and simulation, is given.

The most important parameter for SAW device design is the center frequency, which is determined by the period of the IDT fingers and the acoustic velocity. The governing equation that determines the operation frequency is:

$$f_0 = v_{SAW}/\lambda \qquad\qquad \text{eq.(2. 1)}$$

where

$\lambda$ is the wavelength, determined by the periodicity of the IDT and $v_{SAW}$ is the acoustic wave velocity . For the technology being used in this research:

$$\lambda = p = \text{finger width} \times 4 \qquad\qquad \text{eq.(2. 2)}$$

with the finger width (as shown in Figure 2.1) is determined by the design rule of the technology which sets the minimum metal to metal distance.

$v_{SAW}$ is surface acoustic wave velocity.
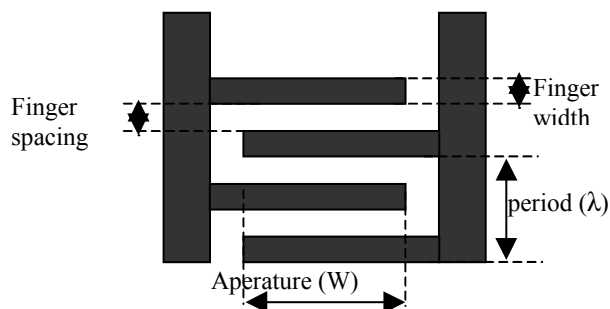


Figure 2.1   IDT parameters

Section 2.2 gives the analyses of different SAW device structures.

Section 2.3 presents the equivalent circuit of SAW delay line based on Mason model.

The equivalent circuit of SAW delay line based on Couple-Of-Mode theory is presented in section 2.4.

Based on section 2.3 and 2.4, section 2.5 shows comparison between using the equivalent circuit of SAW delay line device based on Mason model and COM theory. This model is useful and fast model for designing the SAW device.

Section 0 gives the conclusion of this chapter from analyses in each section.

## 2.2   CALCULATION OF SAW PROPERTIES

The SAW propagation properties on one layer or multilayer structure are obtained by using matrix approach, proposed by J.J.Campbell and W.R.Jones [112], K.A.Ingebrigtsen [116], and then developed by Fahmy and Adler [68], [69], [70] and other authors  [113], [114], [115]. The numerical solution method is based on characterizing each layer by means of a transfer matrix relating the mechanical and electrical field variables at the boundary planes. The boundary conditions for multilayer are based on the mechanical and electrical field variables those quantities that must be continuous at material interfaces. This matrix method is used to calculate the wave velocity and therefore, the electromechanical coupling factor. A general view and detail of this approach are given in [112]-[115].

By using matrix method, the velocity v of acoustic wave is derived in two cases:

  + Wave velocity $V_0$ is velocity in case of free surface.

  + Wave velocity Vs is velocity in case of short-circuit surface.

Therefore, the electromechanical coupling coefficient K is calculated approximately by Ingebrigtsen [116] as:

$$K^2 = 2\frac{V_o - V_s}{V_o}$$

<div align="right">eq.(2. 3)</div>

By using the matrix method and approximation of coupling factor as in eq.(2. 3), we have calculated and analysed the SAW parameters in different structures AlN/Si, AlN/SiO$_2$/Si and AlN/Mo/Si. These calculations and analyses will be given in three next sections.

## 2.2.1 Wave velocity, coupling factor in AlN/Si structure

Figure 2.2 shows the dependence of Rayleigh wave velocity $V_0$ and Vs on the normalized thickness as respect to the wavelength, khAlN of AlN layer in SAW device AlN/Si substrate, where normalized thickness is define by:

$$kh = \frac{2\pi h}{\lambda}$$

<div align="right">eq.(2. 4)</div>

In this graph, when the normalized thickness of AlN, khAlN is larger than 3, the wave velocity reaches the velocity of the Rayleigh wave in AlN substrate v(AlN substrate)=6169 (m/s). This could be explained that the wave travels principally in AlN layer when khAlN is larger than 3, because for low frequency the wave penetrates inside the other layer and this work is in the case where the wave are dispersive. It is better to be in the frequency range where the Rayleigh wave is obtained to have a constant velocity.

The coupling factor K for this kind of device is shown in Figure 2.3. When normalized thickness of AlN layer is larger than 3, the coupling factor K still remain at 4.74% by that the wave travels principally in AlN layer.

In this configuration, K is at its maximum value of 5.34% when khAlN=0.5495.
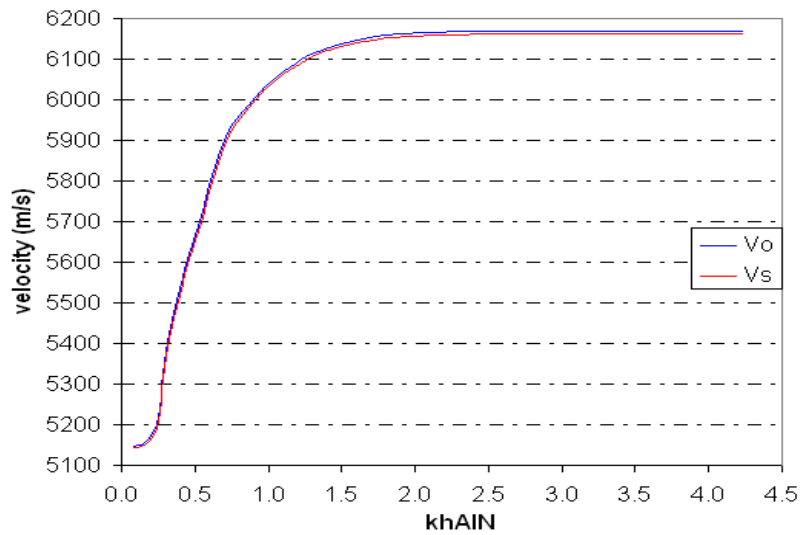
Figure 2.2   Calculated values of wave velocity $V_0$ and Vs in SAW device AlN/Si substrate depend on the normalized thickness khAlN of AlN layer
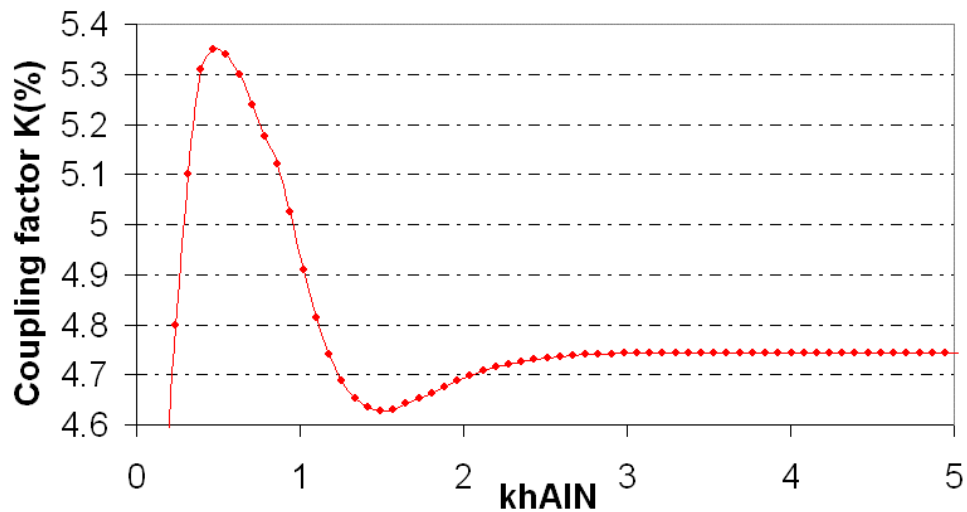


Figure 2.3   Calculated values of coupling factor K(%) in SAW device AlN/Si substrate depends on the normalized thickness khAlN of AlN layer

## 2.2.2      Wave velocity, coupling factor in AlN/SiO$_2$/Si structure

Wave velocity and coupling factor in structure AlN/SiO$_2$/Si are also presented in Figure 2.4 and Figure 2.5, respectively.
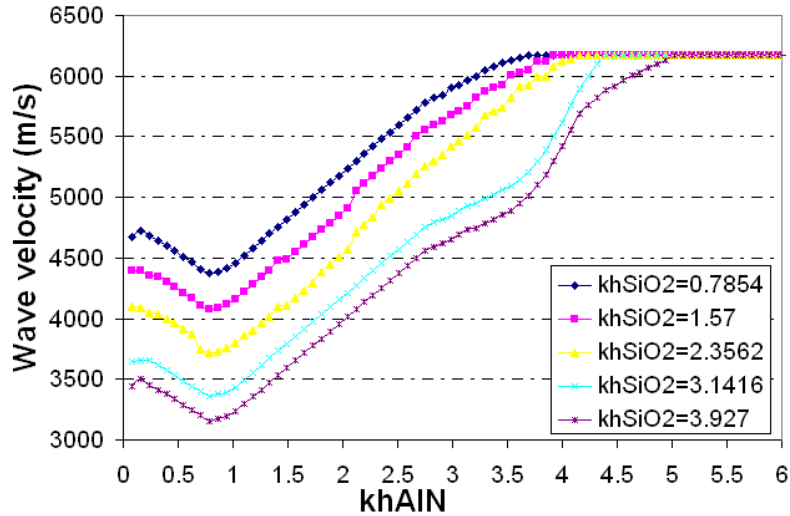
Figure 2.4   Dependence of wave velocity in SAW device AlN/SiO$_2$/Si substrate on
the normalized thickness khAlN of AlN layer and khSiO$_2$
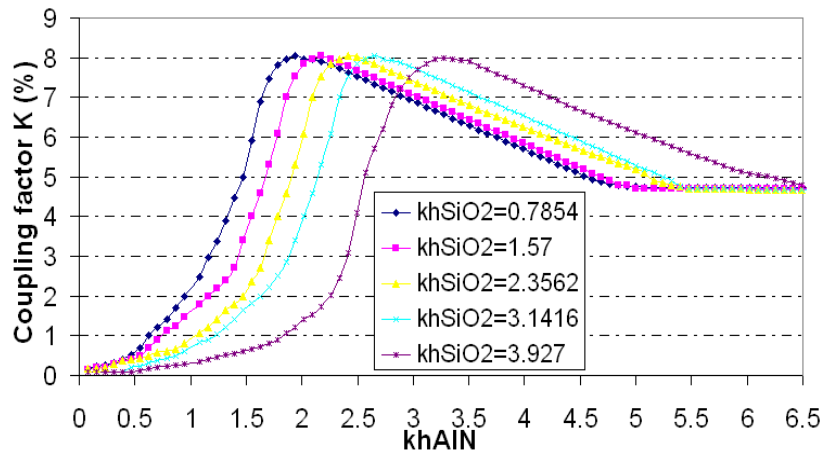


Figure 2.5   Dependence of coupling factor K(%) in SAW device AlN/ SiO$_2$/Si
substrate on the normalized thickness khAlN of AlN layer and khSiO$_2$

In this configuration, as results in Figure 2.4, when $khAlN < 6$, with the same thickness of AlN layer, an increase in thickness of SiO$_2$ would decrease the wave velocity. When $khAlN > 6$, the wave velocity reaches the velocity of the Rayleigh wave in AlN substrate v(AlN substrate)=6169 (m/s). A same conclusion is formulated also for coupling factor for this kind of structure, AlN/SiO$_2$/Si, in Figure 2.5; when $khAlN > 6$, K remains at the value of 4.7%.

To understand the above behavior, we use FEM method to display displacement profile along the depth of multilayer $AlN/SiO_2/Si$. These results obtained from FEM method in case of $khSiO_2$=0.7854, khAlN=5 and khAlN=0.2 are compared as in Figure 2.6.
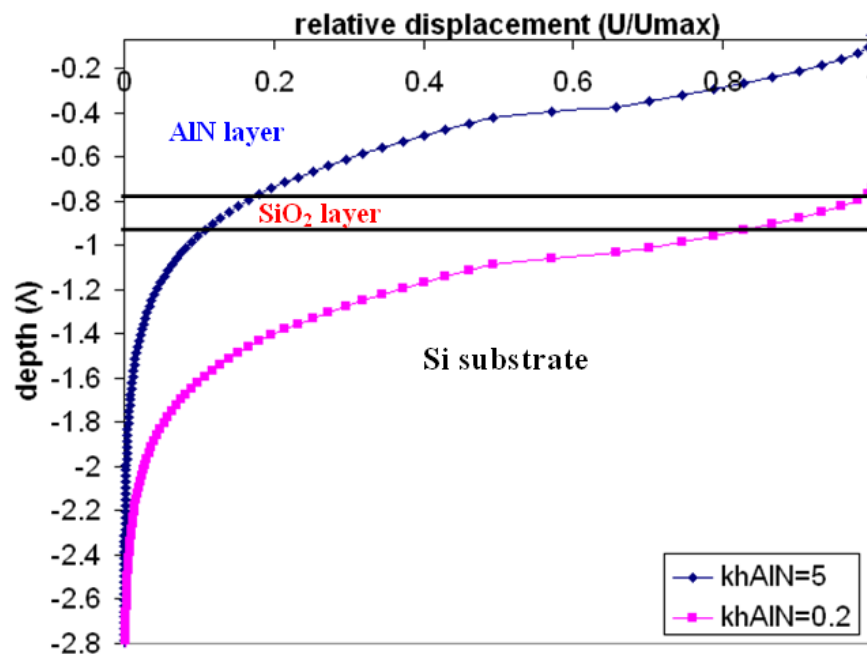


Figure 2.6   Displacement profile along the depth of the multilayer $AlN/SiO_2/Si$, $khSiO_2$=0.7854

From Figure 2.6, we note that wave travels principally in AlN layer for a khAlN value of 5. By this reason, from a khAlN value of larger than 5, the coupling factor K remains at 4.7% and wave velocity remains at 6169m/s. For khAlN=0.2, wave travels principally in $SiO_2$ layer and Si substrate that are not piezoelectric layer. Consequently, the coupling factor K reaches the value of 0%.

In conclusion, the values of wave velocity and coupling factor depend on wave propagation medium, in which constant values of wave velocity and coupling factor indicate a large contribution of AlN layer, and coupling factor value of near 0% indicates a large contribution of $SiO_2$ layer and Si substrate.

### 2.2.3    Wave velocity, coupling factor in AlN/Mo/Si structure

For our devices, a thin Mo layer will be also deposited below the AlN layer to impose the crystal orientation of AlN. The results of dependence of AlN layer crystalline orientation on a Mo layer are given in Chapter 5, section 5.3.4 . Besides this dependence, the Mo layer also

has influences on wave velocity and coupling factor K. These influences are shown in Figure 2.7 and Figure 2.8, respectively.
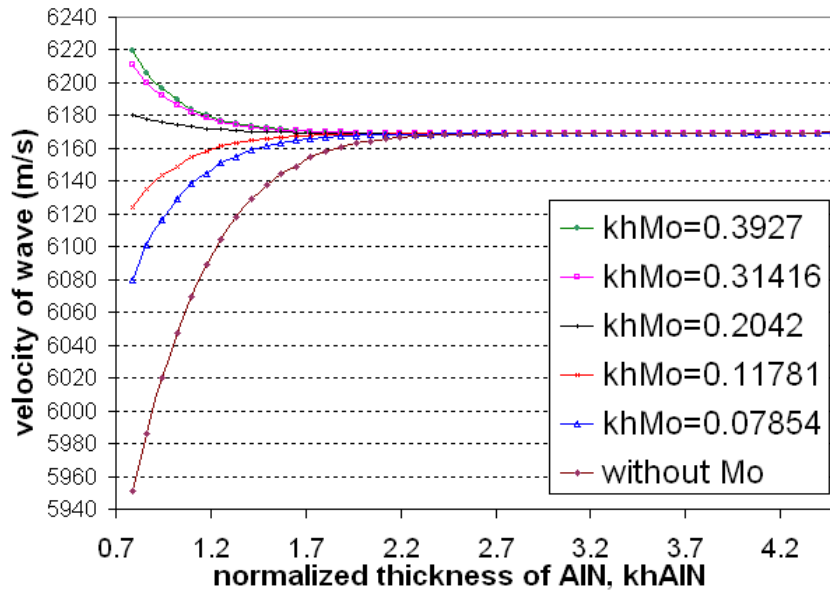


Figure 2.7   Wave velocity AlN/Mo/Si substrate depends on the normalized
thickness khAlN and khMo
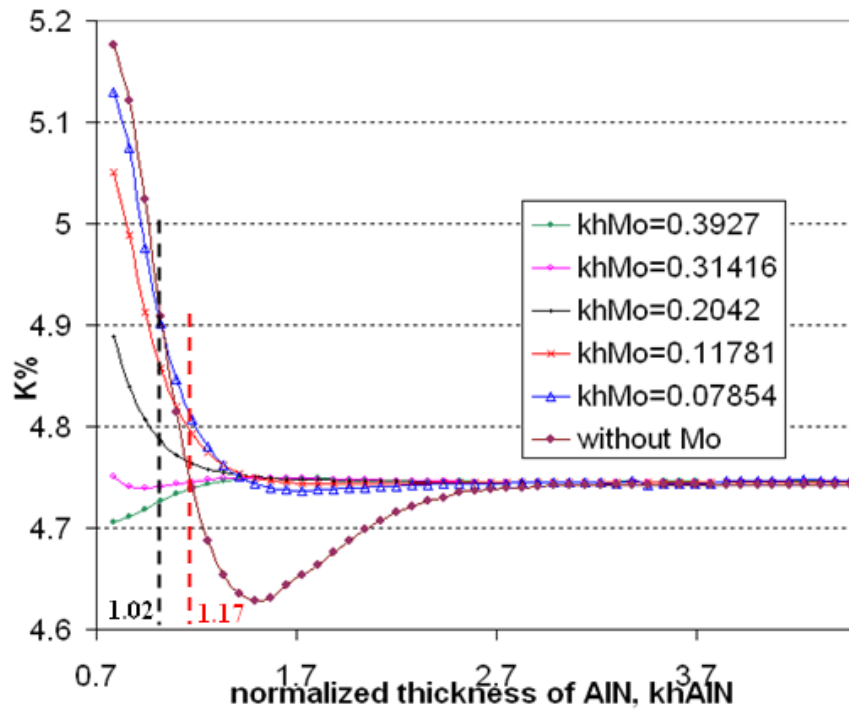


Figure 2.8   Coupling factor K(%) in SAW device AlN/Mo/Si substrate depends
on the normalized thickness khAlN and khMo

From Figure 2.7, the use of Mo layer would increase the wave velocity with any thickness of AlN layer and Mo layer. In case of coupling factor K as in Figure 2.8, the Mo layer, however, could decrease K when the khAlN is less than 1.02. When the normalized thickness of AlN layer khAlN is in the range from 1.17 to 2.7, the Mo layer would increase the coupling factor K. And when the khAlN is larger than 2.7, the Mo has no influence on wave velocity and coupling factor. The reason of this effect could be explained by the displacement profile in AlN/Mo/Si structure, as shown in Figure 2.9 for thickness AlN value of khAlN=2.7. We could note that when $khAlN \geq 2.7$, the first interesting point is that the wave travels principally in AlN layer and Si substrate, the second one is that the relative displacement U/Umax in Mo layer will be smaller than 0.5. These point would explain the reason why when $khAlN \geq 2.7$ the use of Mo has no influence on wave velocity and coupling factor.
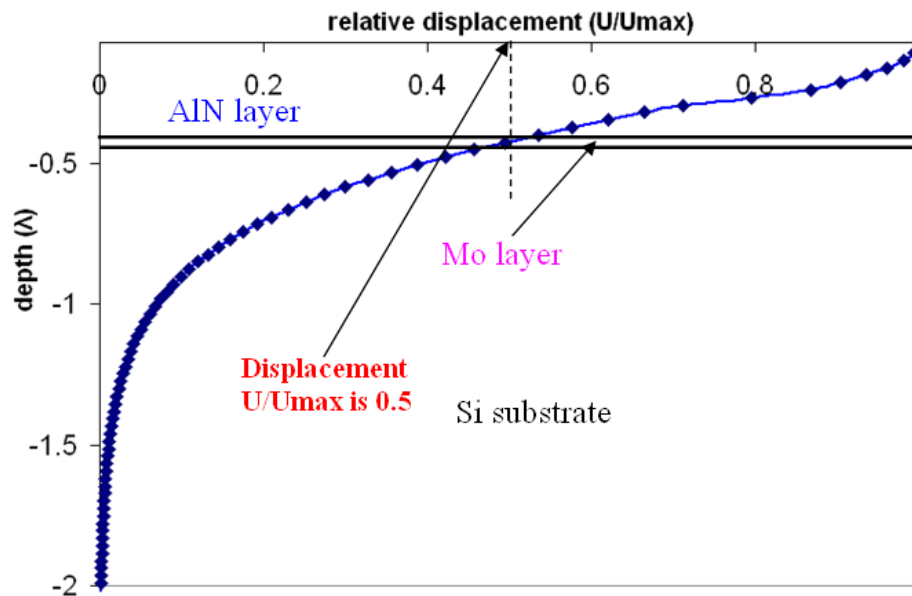


Figure 2.9   Displacement profile along the depth of the multilayer AlN/Mo/Si, khAlN=2.7

## 2.3    EQUIVALENT CIRCUIT FOR SAW DELAY LINE BASED ON MASON MODEL

### 2.3.1    Equivalent circuit for IDT including N periodic sections

Based on Berlincourt et al [76] about equivalent circuit for Length Expander Bar with parallel electric field and with perpendicular electric field and based on the equivalent circuit for electromechanical transducer presented by Mason [73], Smith and al [78] have developed

the equivalent circuit for IDT composed of N periodic sections of the form shown in Figure 2.10.
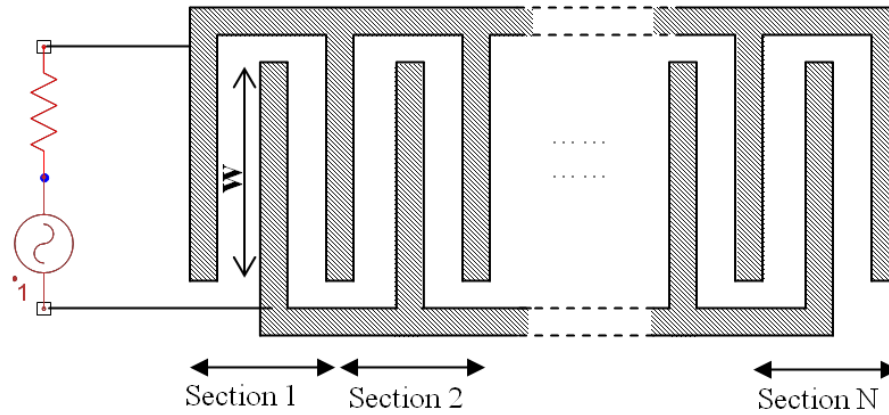


Figure 2.10   Interdigital transducer diagram

One periodic section as shown in Figure 2.11(a) can be presented by analogous one-dimensional configurations: "crossed-field" model as in Figure 2.11(b) , and "in-line" model as in Figure 2.11(c). In "crossed-field" model, the applied electric field is normal to the acoustic propagation vector; while in "in-line field" model, the electric field is parallel to the propagation vector.
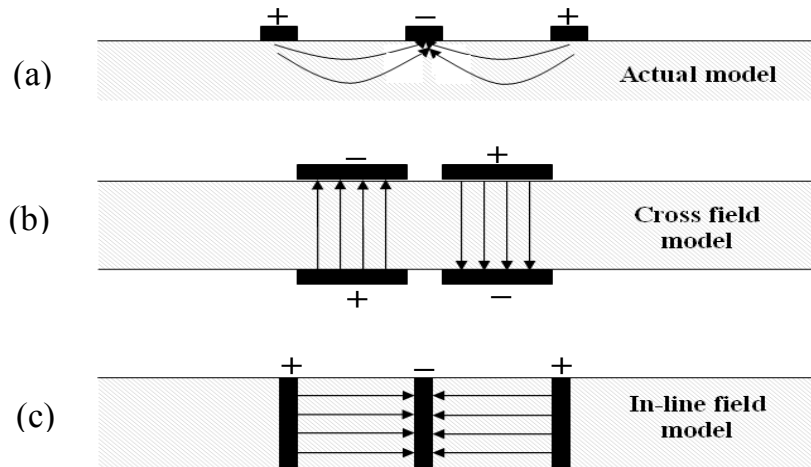


Figure 2.11   Side view of the interdigital transducer and 2 analogous one-dimensional configurations (a) Actual model, (b) "crossed-field" model, (c) "in-line field" model

The important advantage of two one-dimensional models is that each periodic section can be represented by equivalent circuit of Mason, as shown in Figure 2.12 for "crossed-field" model and Figure 2.13 for "in-line field" model. The difference between these two equivalent circuits is that in "crossed-field" model, the negative capacitors are short-circuited.
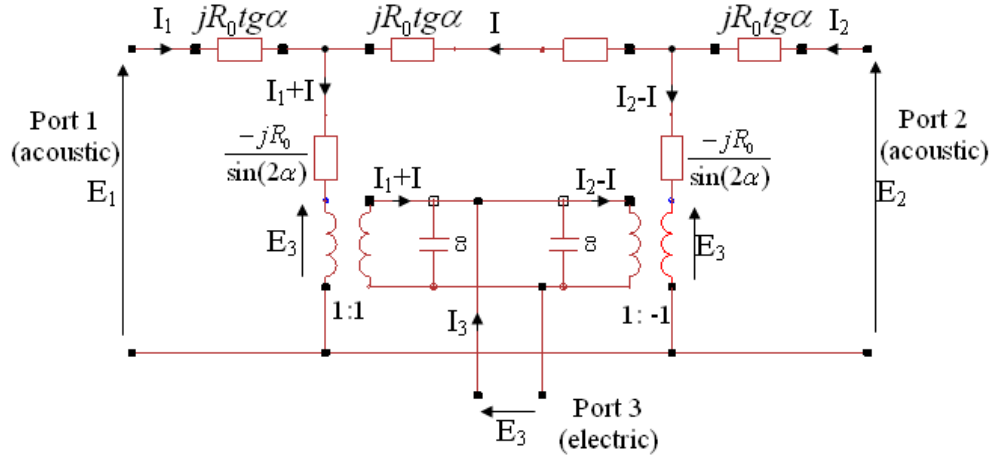
Figure 2.12   Mason equivalent circuit for one periodic section in "crossed-field" model
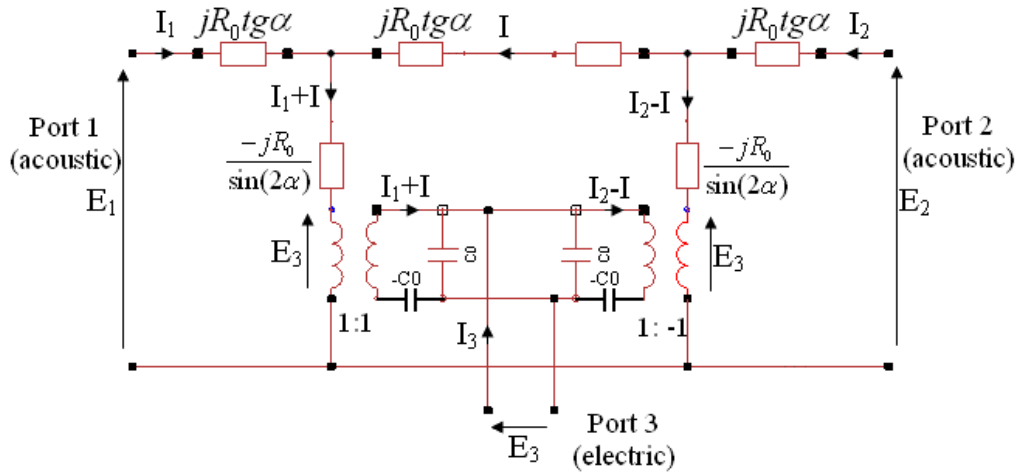


Figure 2.13   Mason equivalent circuit for one periodic section in "in-line field" model

Where:

$$\alpha = \frac{\theta}{4} = \frac{\pi}{2}\frac{\omega}{\omega_0}$$

eq.(2. 5)

With periodic section transit angle

$$\theta = 2\pi\frac{\omega}{\omega_0}$$

$$R_0 = \frac{2\pi}{\omega_0 C_s k^2}$$

eq.(2. 6)

$R_0$ is electrical equivalent of mechanical impedance $Z_0$ [78]

k: electromechanical coupling coefficient

$C_0 = Cs/2$ with Cs : electrode capacitance per section

$\omega_0$ is center angular frequency

One periodic section can be represented by the 3-port network [y] matrix. The [y] matrix of one periodic section for 2 models as follows (see Appendix B, section B. 1), with $G_0 = R_0^{-1}$, $R_0$ is expressd by eq.(2. 6):

+ for the "crossed-field" model:

$$
\begin{aligned}
y_{11} &= -jG_0 \cot g\,(4\alpha) \\
y_{12} &= \frac{jG_0}{\sin(4\alpha)} \\
y_{13} &= -jG_0 tg\,\alpha \\
y_{33} &= j(2\omega C_0 + 4G_0 tg\,\alpha)
\end{aligned}
\qquad \text{eq.(2. 7)}
$$

+ for the "in-line field" model:

$$
y_{11} = -jG_0 \cot g\,\alpha \left( \frac{G_0}{\omega C_0} - \cot g\,(2\alpha) \right) \left[ 2 - \frac{\left( \dfrac{G_0}{\omega C_0} - \dfrac{1}{\sin(2\alpha)} \right)^2}{\left( \dfrac{G_0}{\omega C_0} - \cot g\,(2\alpha) \right)^2} \right]
$$

$$
y_{12} = jG_0 \frac{\cot g\,\alpha \left( \dfrac{G_0}{\omega C_0} - \dfrac{1}{\sin(2\alpha)} \right)^2}{2 \left( \dfrac{2G_0}{\omega C_0} - \cot g\,\alpha \right) \left( \dfrac{G_0}{\omega C_0} - \cot g\,(2\alpha) \right)}
$$

$$
y_{13} = -jG_0 \frac{tg\,\alpha}{1 - \dfrac{2G_0}{\omega C_0} tg\,\alpha}
$$

$$
y_{33} = \frac{j2\omega C_0}{1 - \dfrac{2G_0}{\omega C_0} tg\,\alpha}
$$

$$\text{eq.(2. 8)}$$

In IDT including N periodic sections, the N periodic sections are connected acoustically in cascade and electrically in parallel as represented in Figure 2.14.
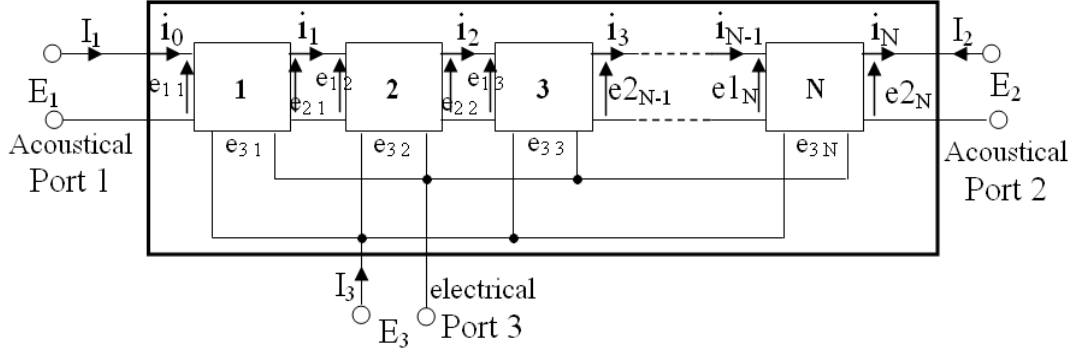
Figure 2.14   IDT including the N periodic sections connected acoustically in cascade
and electrically in parallel

Matrix [Y] representation of N-section IDT for two models, "crossed-field" model and "in-line" model are in eq.(2. 9) and eq.(2. 10), respectively (the calculation development is presented in Appendix B, section B. **1**):

+ In "crossed-field" model:

$$Y_{11} = -jG_0 \cot g(4N\alpha)$$

$$Y_{12} = \frac{jG_0}{\sin(4N\alpha)}$$

$$Y_{13} = -jG_0 tg\alpha$$

$$Y_{33} = jN(2\omega C_0 + 4G_0 tg\alpha)$$

eq.(2. 9)

+ In "in-line field" model:

$$Y_{11} = -\frac{Q_{11}}{Q_{12}}$$

$$Y_{12} = \frac{1}{Q_{12}}$$

$$Y_{13} = -jG_0 \frac{tg\alpha}{1 - \frac{2G_0}{\omega C_0} tg\alpha}$$

$$Y_{33} = \frac{j2\omega N C_0}{1 - \frac{2G_0}{\omega C_0} tg\alpha}$$

eq.(2. 10)

It was shown in the literature that the crossed field model yielded better agreement than the experiment when compared to the in-line model when K is small. In section 2.2, K is always smaller than 7.2%. Besides, in section stated above, the "crossed-field" model is simpler than

"in-line field" model in term of equations of all element of [Y] matrix. Consequently, the "crossed-field" model is selected henceforth for the calculating, modeling the devices.

### 2.3.2    Equivalent circuit for propagation path

In our work, delay line SAW device is used for pressure sensor application. The sensitive part of this kind of device will be the propagation path. To model the pressure sensor using SAW, it is necessary to construct the model for propagation path. Based on the equivalent circuit for electromechanical transducer presented by Mason [73], equivalent circuit of propagation path is presented as in Figure 2.15.
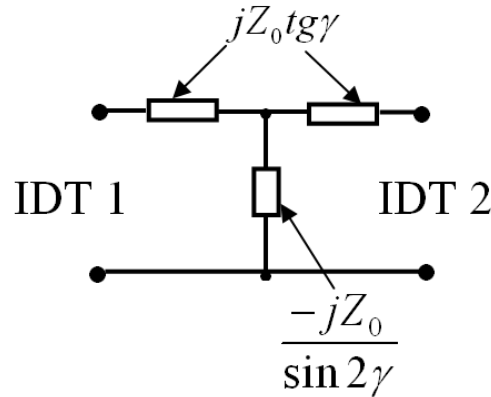


Figure 2.15   Equivalent circuit of propagation path, based on Mason model

Where

$$\gamma = \frac{\omega l}{2v}$$

<div align="right">eq.(2. 11)</div>

With v is SAW velocity, l is propagation length.

### 2.3.3    Equivalent circuit for SAW delay line

Due to the piezoelectric effect, an RF signal applied at input IDT stimulates a micro-acoustic wave propagating on its surface. These waves propagate in two directions, one to receiving IDT and another to the medium. The approximations as follows are assumed to construct the equivalent circuit for SAW delay line:

+ Assume that the IDT radiates the wave into a medium of infinite extent. Experimentally, an infinite medium is approximated either by using absorber, such as wax, polyimide (see Chapter 4, section 4.11) to provide acoustic termination, or by using a short RF pulse measurement. The condition of infinite medium means that no wave reflects back to

input IDT. This is created for SAW device model by connecting the acoustic characteristic admittance $Y_0$ to one terminal of IDT.

+ Assume that the wave propagating to receiving IDT has no attenuation during propagation way between two IDTs. So, the propagation path between two IDTs can be expressed as the no-loss transmission line.

Based on these two approximations, the [Y] matrix representation of IDT in section 2.3.1, and propagation path representation in section 2.3.2, the SAW delay line can be expressed as equivalent circuit as in Figure 2.16.
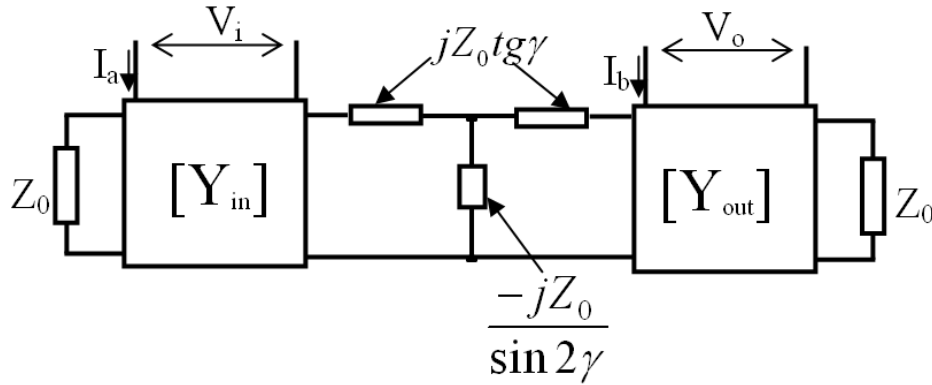


Figure 2.16   Equivalent circuit of SAW delay line, based on Mason model

Section 2.3 gives the equivalent circuit of SAW delay line, including IDT input, IDT output and propagation path. All of calculation developments are presented in appendix B, section B.2. In this appendix, a new equivalent circuit of IDT including N periodic section plus one finger, which we call it "N+1/2", also are developed and presented. Another representation of SAW delay line is [ABCD] matrix representation which also proposed in Appendix  B, section B. 4. [ABCD] matrix representation has one interesting property that in cascaded network, the [ABCD] matrix of total network can be obtained easily by multiplying the matrices of elemental networks.

## 2.4    EQUIVALENT CIRCUIT FOR IDT BASED ON THE COUPLING-OF-MODE THEORY

The Coupling-Of-Modes formalism is a branch of the highly developed theory of wave propagation in periodic structure, which has an history of more than 100 years. This theory covers a variety of wave phenomena, including the diffraction of EM waves on periodic gratings, their propagation in periodic waveguides and antennas, optical and ultrasonic waves in multi-layered structures, quantum theory of electron states in metal, semiconductors, and

dielectrics…. Theoretical aspects of the wave in periodic media and applications were reviewed by C.Elachi [41], in which it included theories of waves in unbounded and bounded periodic medium, boundary periodicity, source radiation in periodic media, transients in periodic structures, active and passive periodic structures, waves and particles in crystals. An excellent recent review of COM theory used in SAW devices was written by K.Hashimoto [47].

A simple equivalent circuit for IDT based on COM approach was proposed by K.Nakamura [66]. This model would be useful to analyze and design SAW devices. Based on the COM equations, the relationships between the terminal quantities at the one electrical port and two acoustic ports for an IDT have been done.

### 2.4.1     COM equation for particle velocities

Consider an IDT including N periodic sections with periodic length of L as shown in Figure 2.17.
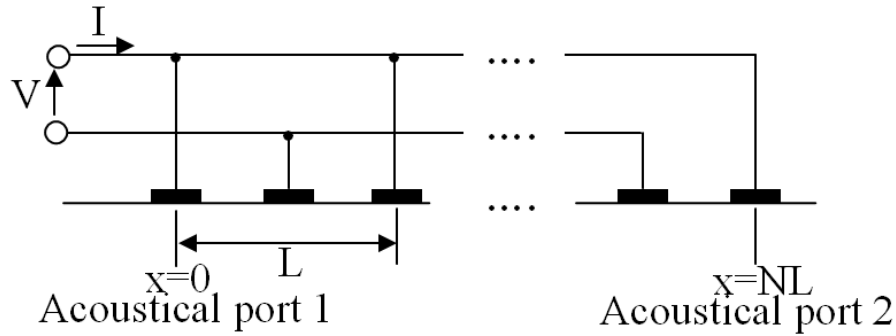


Figure 2.17   IDT including N periodic sections

The particle velocities $v^+(x)$ and $v^-(x)$ of the wave propagating in the +x and –x directions in the periodic structure can be expressed as follows with the time dependence $\exp(j\omega t)$ term:

$$v^+(x) = A^+(x)e^{-jkx}$$

<div align="right">eq.(2. 12)</div>

$$v^-(x) = A^-(x)e^{jkx}$$

<div align="right">eq.(2. 13)</div>

Where k is the wave number

$$k = \omega / V_{SAW}$$

<div align="right">eq.(2. 14)</div>

The amplitude $A^+(x)$ and $A^-(x)$ obey the following coupled-mode equations [117]:

$$\frac{dA^+(x)}{dx} = -jK_{11}A^+(x) - jK_{12}e^{j2\delta x}A^-(x) + j\zeta e^{j\delta x}V \qquad \text{eq.(2. 15)}$$

$$\frac{dA^-(x)}{dx} = jK_{12}e^{-j2\delta x}A^+(x) + jK_{11}A^-(x) - j\zeta e^{-j\delta x}V \qquad \text{eq.(2. 16)}$$

Where V is the voltage applied to the IDT,

$\zeta$ is the constant associated with the convention from electrical to SAW quantities,

$K_{11}$ and $K_{12}$ are coupling coefficients, sum of the coupling coefficient coming from the piezoelectric perturbation and that coming from the mechanical perturbation.

$$\delta = k - k_0 \text{ , with } k_0 = \frac{2\pi}{L} \qquad \text{eq.(2. 17)}$$

The solution to eq.(2. 15)and eq.(2. 16) can be expressed as

$$v^+(x) = \left( h_1 e^{-j\beta_1 x} + p h_2 e^{-j\beta_2 x} + q\zeta V \right) e^{-jk_0 x} \qquad \text{eq.(2. 18)}$$

$$v^-(x) = \left( p h_1 e^{-j\beta_1 x} + h_2 e^{-j\beta_2 x} + q\zeta V \right) e^{jk_0 x} \qquad \text{eq.(2. 19)}$$

Where the subscripts 1 and 2 indicate the elementary waves with wavenumbers $k_0 + \beta_1$ and $k_0 + \beta_2$ in the +x direction, and the magnitudes $h_1$ and $h_2$, respectively.

$$\beta_1, \beta_2 = \pm\sqrt{(\delta + K_{11})^2 - K_{12}^2} \qquad \text{eq.(2. 20)}$$

$$p = \frac{\beta_1 - \delta - K_{11}}{K_{12}} \qquad \text{eq.(2. 21)}$$

$$q = \frac{1}{\delta + K_{11} + K_{12}} \qquad \text{eq.(2. 22)}$$

### 2.4.2    Equivalent circuit for IDT based on COM theory

From the equations eq.(2. 18) and eq.(2. 19), the particle velocities at the both ends of the IDT can be expressed as:

$$v^+(0) = h_1 + p h_2 + q\zeta V \qquad \text{eq.(2. 23)}$$

$$v^-(0) = p h_1 + h_2 + q\zeta V \qquad \text{eq.(2. 24)}$$

$$v^+(NL) = \pm\left(e^{-j\beta_1 NL}h_1 + e^{j\beta_1 NL}ph_2 + q\zeta V\right) \qquad \text{eq.(2. 25)}$$

$$v^-(NL) = \pm\left(e^{-j\beta_1 NL}ph_1 + e^{j\beta_1 NL}h_2 + q\zeta V\right) \qquad \text{eq.(2.26)}$$

The upper and lower signs in eq.(2. 25) and eq.(2.26) correspond to the cases N=i and N=i+0.5, respectively, where i is an integer. Consequently, the total particle velocities at the two acoustical ports can be expressed as:

+ Particle velocity at port 1 (x=0):

$$v_1 = v^+(0) + v^-(0) = (1+p)(h_1 + h_2) + 2q\zeta V \qquad \text{eq.(2. 27)}$$

+ Particle velocity at port 2 (x=NL):

$$v_2 = -\left[v^+(NL) + v^-(NL)\right] = \mp\left[(1+p)(e^{-j\beta_1 NL}h_1 + e^{j\beta_1 NL}h_2) + 2q\zeta V\right] \qquad \text{eq.(2. 28)}$$

The two forces at two acoustic ports are considered to be proportional to the difference of $v^+$ and $v^-$. For the simplicity, these forces can be expressed as follows:

$$F_1 = v^+(0) - v^-(0) = (1-p)(h_1 - h_2) \qquad \text{eq.(2. 29)}$$

$$F_2 = v^+(NL) - v^-(NL) = \pm\left[(1-p)(e^{-j\beta_1 NL}h_1 - e^{j\beta_1 NL}h_2)\right] \qquad \text{eq.(2. 30)}$$

From these equations, $h_1$ and $h_2$ are the terms of $F_1$ and $F_2$ as follows:

$$h_1 = \frac{e^{j2\beta_1 NL}}{(1-p)(e^{j2\beta_1 NL}-1)}F_1 \mp \frac{e^{j\beta_1 NL}}{(1-p)(e^{j2\beta_1 NL}-1)}F_2 \qquad \text{eq.(2. 31)}$$

$$h_2 = \frac{1}{(1-p)(e^{j2\beta_1 NL}-1)}F_1 \mp \frac{e^{j\beta_1 NL}}{(1-p)(e^{j2\beta_1 NL}-1)}F_2 \qquad \text{eq.(2. 32)}$$

The current I at the electrical ports can be expressed as:

$$I = \eta \int_0^{NL}\left[(1+p)(h_1 e^{-j\beta_1 x} + h_2 e^{-j\beta_2 x}) + 2q\zeta V\right]dx + j\omega NC_s V$$

$$= j\eta\left\{(1+p)\left[\frac{h_1}{\beta_1}(e^{-j\beta_1 NL}-1) + \frac{h_2}{\beta_2}(e^{j\beta_1 NL}-1)\right]\right\} + 2q\zeta\eta NLV + j\omega NC_s V \qquad \text{eq.(2. 33)}$$

where $\eta$ is the constant associated with the convention from SAW to electrical quantities, therefore associated with the coupling factor K.

$C_s$ is the capacitance for one electrode pair.

By substituting equations eq.(2. 31) and eq.(2. 32) in eq.(2. 27), eq.(2. 28) and eq.(2. 33), the following equations can be obtained:

$$I = (j\omega NC_s + 2q\zeta\eta NL)V + \frac{\eta(1+p)}{j\beta(1-p)}F_1 \mp \frac{\eta(1+p)}{j\beta(1-p)}F_2 \qquad \text{eq.(2. 34)}$$

$$v_1 = 2q\zeta V + \frac{1+p}{1-p}\frac{1}{j\tan 2\theta}F_1 \mp \frac{1+p}{1-p}\frac{1}{j\sin 2\theta}F_2 \qquad \text{eq.(2. 35)}$$

$$v_2 = \mp 2q\zeta V \mp \frac{1+p}{1-p}\frac{1}{j\sin 2\theta}F_1 + \frac{1+p}{1-p}\frac{1}{j\tan 2\theta}F_2 \qquad \text{eq.(2. 36)}$$

Where

$$\theta = \beta NL/2 \qquad \text{eq.(2. 37)}$$

$$\beta \equiv \beta_1 = -\beta_2 \qquad \text{eq.(2. 38)}$$

From these equations, the matrix as follows can be obtained:

$$\begin{bmatrix} I \\ v_1 \\ v_2 \end{bmatrix} = \begin{bmatrix} (j\omega NC_s + 2q\zeta\eta NL) & \dfrac{\eta(1+p)}{j\beta(1-p)} & \mp\dfrac{\eta(1+p)}{j\beta(1-p)} \\ 2q\zeta & \dfrac{1+p}{1-p}\dfrac{1}{j\tan 2\theta} & \mp\dfrac{1+p}{1-p}\dfrac{1}{j\sin 2\theta} \\ \mp 2q\zeta & \mp\dfrac{1+p}{1-p}\dfrac{1}{j\sin 2\theta} & \dfrac{1+p}{1-p}\dfrac{1}{j\tan 2\theta} \end{bmatrix}\begin{bmatrix} V \\ F_1 \\ F_2 \end{bmatrix} \qquad \text{eq.(2. 39)}$$

In the acoustic wave transducer using piezoelectric effect, the force and voltage analogy can be used. Therefore, the COM-based circuit of IDT as matrix in eq.(2. 39) can be considered as the reciprocal circuit. The reciprocity theorem states that if a voltage source E acting in one branch of a network causes a current I to flow in another branch of the network, then the same voltage source E acting in the second branch would cause an identical current I to flow in the first branch. By using this theorem in this case, replacing V and $F_1$ together, the same value I requirement leads the following equations:

$$2q\zeta = \frac{\eta(1+p)}{j\beta(1-p)} \qquad \text{eq.(2. 40)}$$

$$\eta = 2j\zeta \qquad \text{eq.(2. 41)}$$

From eq.(2. 39), eq.(2. 40), and eq.(2. 41), the matrix as in eq.(2. 39) becomes:

$$\begin{bmatrix} I \\ v_1 \\ v_2 \end{bmatrix} = \begin{bmatrix} j\omega C_T + \dfrac{\phi^2}{j2\theta Z_0} & \dfrac{\phi}{j2\theta Z_0} & \mp\dfrac{\phi}{j2\theta Z_0} \\[2mm] \dfrac{\phi}{j2\theta Z_0} & \dfrac{1}{jZ_0 \tan 2\theta} & \mp\dfrac{1}{jZ_0 \sin 2\theta} \\[2mm] \mp\dfrac{\phi}{j2\theta Z_0} & \mp\dfrac{1}{jZ_0 \sin 2\theta} & \dfrac{1}{jZ_0 \tan 2\theta} \end{bmatrix} \begin{bmatrix} V \\ F_1 \\ F_2 \end{bmatrix} \qquad \text{eq.(2. 42)}$$

Where

$$Z_0 = \frac{1-p}{1+p} = \frac{1}{q\beta} \qquad \text{eq.(2. 43)}$$

$$\phi = \eta N L = 2 j\zeta N L \qquad \text{eq.(2. 44)}$$

$$C_T = N C_s \qquad \text{eq.(2. 45)}$$

Consequently, the simple equivalent circuit obtained for IDT with N electrode pairs is shown in Figure 2.18:
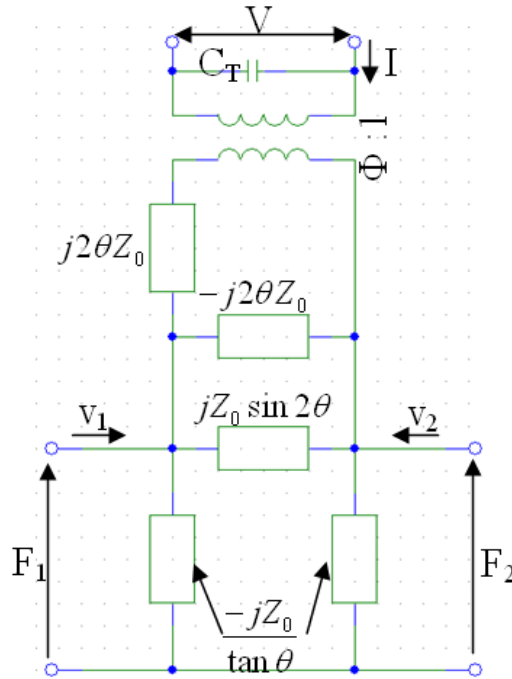


Figure 2.18   Equivalent circuit IDT based on COM theory

### 2.4.3 Equivalent circuit for propagation path based on COM theory

In SAW devices, the propagation path should be taken into account. It is necessary to determine the equivalent circuit for a propagation path of distance l between 2 IDTs. This propagation path is a uniform section of length l, with a free surface or a uniformly metallized surface. In this case, $K_{11}=K_{12}=0$, and $\beta=\delta$.

Consequently, from equations eq.(2. 31) and eq.(2. 32), $h_1$ and $h_2$ can be expressed as:

$$h_1 = \frac{e^{j2\beta l}}{e^{j2\beta l}-1}F_1 - \frac{e^{j\beta l}}{e^{j2\beta l}-1}F_2 \qquad \text{eq.(2. 46)}$$

$$h_2 = \frac{1}{e^{j2\beta l}-1}F_1 - \frac{e^{j\beta l}}{e^{j2\beta l}-1}F_2 \qquad \text{eq.(2. 47)}$$

And, the particle velocities are expressed as:

$$v^+(x) = h_1 e^{-j(k_0+\beta_1)x} = h_1 e^{-jkx} \qquad \text{eq.(2. 48)}$$

$$v^-(x) = h_2 e^{j(k_0+\beta_1)x} = h_2 e^{jkx} \qquad \text{eq.(2. 49)}$$

If the $v_1$, $v_2$, $F_1$, and $F_2$ are defined as:

$$v_1 = v^+(0) + v^-(0) \qquad \text{eq.(2. 50)}$$

$$v_2 = -[v^+(NL) + v^-(NL)] \qquad \text{eq.(2. 51)}$$

$$F_1 = v^+(0) - v^-(0) \qquad \text{eq.(2. 52)}$$

$$F_2 = v^+(NL) - v^-(NL) \qquad \text{eq.(2. 53)}$$

Then, by expressing $h_1$ and $h_2$ in terms of $F_1$ and $F_2$ based on equations eq.(2. 46) and eq.(2. 47), the $v_1$ and $v_2$ become as follows:

$$v_1 = h_1 + h_2 = \frac{e^{j2\beta l}+1}{e^{j2\beta l}-1}F_1 - \frac{2e^{j\beta l}}{e^{j2\beta l}-1}F_2 \qquad \text{eq.(2. 54)}$$

$$v_2 = h_1 e^{-jkl} + h_2 e^{jkl} = \frac{2e^{j\beta l}}{e^{j2\beta l}-1}F_1 - \frac{e^{j2\beta l}+1}{e^{j2\beta l}-1}F_2 \qquad \text{eq.(2. 55)}$$

Using the relation between complex number and trigonometry, the $v_1$ and $v_2$ can be expressed as follows:

$$v_1 = \frac{1}{jZ_0' \tan 2\theta'} F_1 - \frac{1}{jZ_0' \sin 2\theta'} F_2 \qquad \text{eq.(2. 56)}$$

$$v_2 = -\frac{1}{jZ_0' \sin 2\theta'} F_1 + \frac{1}{jZ_0' \tan 2\theta'} F_2 \qquad \text{eq.(2. 57)}$$

Consequently, the equivalent circuit for propagation path can be represented by the $\pi$-circuit of Figure 2.19:
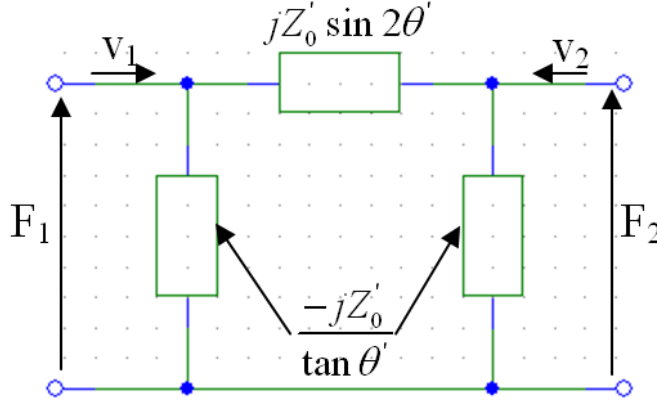


Figure 2.19   Equivalent circuit of propagation path based on COM theory

Based on Mason model, the equivalent circuit of propagation path was presented in Figure 2.15, which has star form. In Figure 2.19, the circuit has triangle form. By using triangles and stars transformation theory published by A.E. Kennelly, equivalent circuit of propagation in these two figures is the same. Consequently, the approachs that are based on Mason model and COM theory can get the same equivalent circuit of propagation path.

## 2.4.4    Equivalent circuit for SAW delay line based on COM theory

Based on section 2.4.2 and 2.4.3, equivalent circuit of SAW delay line based on COM theory is presented in Figure 2.20.
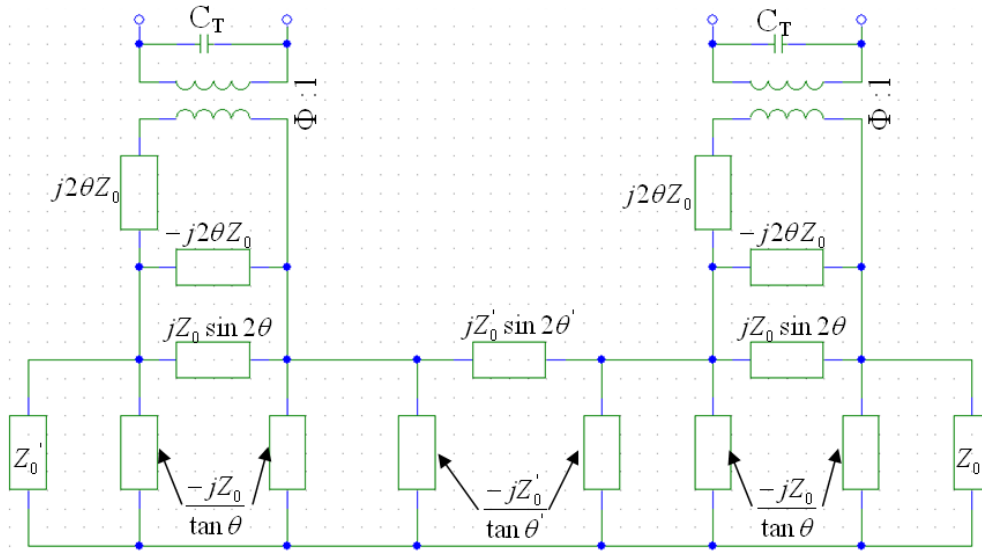
Figure 2.20   Equivalent circuit of SAW delay line based on COM theory

In this model, some parameters must to be calculated or extracted. SAW velocity v, piezoelectric coupling factor K could be calculated from section 2.2. The periodic length L (or wavelength λ) is determined by design and fabrication.

The parameters $K_{11}$ and $K_{12}$ are coupling coefficients. They are sum of the coupling coefficient coming from the piezoelectric perturbation and that coming from the mechanical perturbation, and their equations for calculation are complicated [117]. Exact equations for $K_{11}$ and $K_{12}$ were given by Y.Suzuki et al [117], but it seems so complex that their usefulnesses could be limited. However, from this work of Y.Suzuki et al [117], we propose the $K_{11}$ and $K_{12}$ could be expressed as follows:

$$K_{11} = O_{11}K^2k_0$$

eq.(2. 58)

$$K_{12} = O_{12}K^2k_0$$

eq.(2. 59)

Where $k_0$ is stated by eq.(2. 17) $k_0 = \dfrac{2\pi}{L}$ and K is piezoelectric coupling factor.

$O_{11}$ is so-called self-coupling constant of finger, and $O_{12}$ is so-called coupling constant between fingers. $O_{12}$ could also presents the reflective wave between two fingers.

Figure 2.21 shows the effects of $O_{12}$ on S21(dB) of SAW device N=50, $v_{SAW}$=5120m/s, λ=8μm, K=0.066453 when $O_{11}$=0. $S_{21}$ is the transmission coefficient in the scattering matrix representation [65].
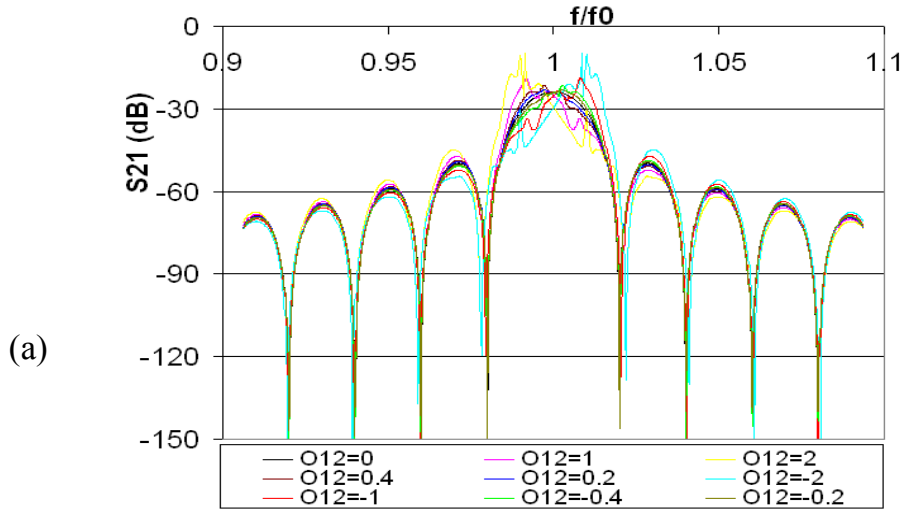
Figure 2.21  Effect of $O_{12}$ on S21(dB), N=50, $v_{SAW}$=5120m/s, λ=8μm, K=0.066453, $O_{11}$=0

Figure 2.22 shows the effects of $O_{11}$ on S21(dB) of SAW device N=50, $v_{SAW}$=5120m/s, λ=8μm, K=0.066453 when $O_{12}$=0. So, $O_{11}$ coefficient shifts the center frequency of SAW device, the positive value of $O_{11}$ reduces the center frequency $f_0$ of device, the negative on will increase the $f_0$.
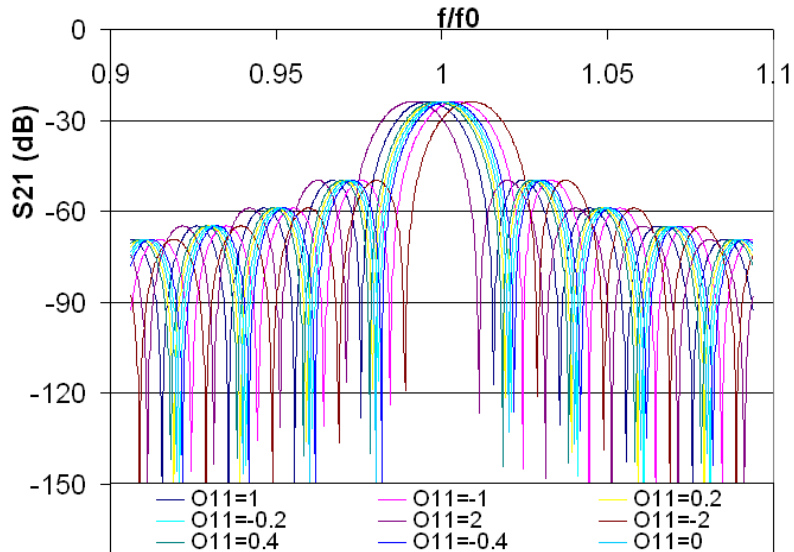


Figure 2.22   Effect of $O_{11}$ on S21(dB), N=50, $v_{SAW}$=5120m/s, λ=8μm, K=0.066453, $O_{12}$=0

The effect of $K_{11}$ and $K_{12}$ could be explained by their measurement method [66]. $K_{11}$ could be derived from the measurement of frequency response, therefore the usefulness of its

calculation could be limited. Meanwhile, $K_{12}$ can be extracted from FEM. It is shown in literature that $K_{12}$ depends on the thickness of finger with respect to the wavelength. In our work, the ratio thickness/wavelength (its maximum value is 300nm/8μm) is too small that its effect can be ignored. In conclusion, in our work, value of $K_{11}$ and $K_{12}$ are 0.

## 2.5 COMPARISON OF EQUIVALENT CIRCUIT OF SAW DEVICE BASED ON MASON MODEL AND COM THOERY

Figure 2.23 presents the comparison between hybrid model and COM model in that $O_{11}$= $O_{12}$=0, distance between 2 IDTs is 50λ. These models could be the same, except that a small difference in the peak value of $S_{21}$ (dB) occurs. This difference could be explained by using "crossed-filed" model instead of actual model as in Figure 2.11.
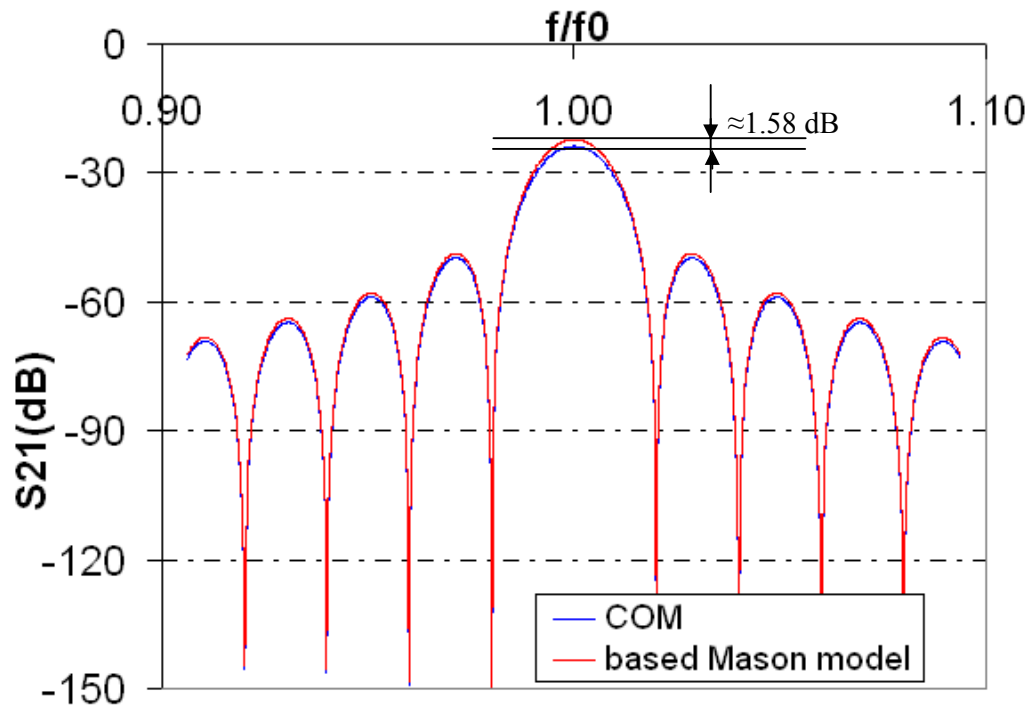


Figure 2.23   Comparison between Hydrid model and COM model ($O_{11}$=$O_{12}$=0)

## 2.6 CONCLUSION

The model used for SAW pressure sensor based on delay line are presented. For usefulness and reduction of time in design process, the equivalent circuit based on COM model, in which $K_{11}$, $K_{12}=0$ is proposed to be used.

Acoustic wave properties in different structures of $AlN/SiO_2/Si$, $AlN/Si$, and $AlN/Mo/Si$ are analyzed. The wave velocity, coupling factor could depend on the wave propagation medium.

From analyses of these structures, the range in which there is a weak dependence of the wave velocity, coupling factor on the AlN layer thickness could be known. The SAW devices should be fabricated in this range to facilitate manufacturing.

For AlN/Si structure, this range is $khAlN \geq 3$.

For $AlN/Mo/Si$, if this kind of SAW device is fabricated in the range from $khAlN \geq 2.7$ to facilitate manufacturing, the use of Mo layer is useless. Consequently, to take full advantage of using Mo layer in term of wave velocity and coupling factor, it should be required to control the fabrication process carefully to obtain the required AlN thickness from khAlN=1.02 to khAlN=2.7. The further advantage of using Mo will be presented in Chapter 4, section 4.9.3 and also characterized in Chapter 5, section 5.3.4.

For $AlN/SiO_2/Si$, this range is $khAlN \geq 5$ for khSiO2=0.7854, for thicker $SiO_2$ layer, this range changes based on Figure 2.4 and Figure 2.5. Besides, using $SiO_2$ layer would reduce temperature dependence of frequency. To choose the thickness of $SiO_2$ layer, it would consider the effect of temperature dependence and analyses of wave velocity, coupling factor.

This effect will be presented in next chapter, Chapter 3, section 3.2.

Chapter 3 will also presents the pressure dependence of frequency, phase and mechanical analysis of membrane under pressure.

# Chapter 3

# DESIGN OF SAW PRESSURE SENSOR DEVICES

## 3.1 INTRODUCTION

In SAW pressure sensor, the pressure induced stress and strain. Consequently the acoustic wave will be modified and therefore the frequency response of the device. The pressure can be obtained by measuring frequency response change. Besides, the effect of frequency variation by temperature change [82], [118] is derived from that properties of materials affected by temperature variation. For pressure application, this sensitivity must be reduced. Usually, temperature compensation can be done by using one port Inter Digital Transducer (IDT) and at least three reflectors to create several propagation paths of different lengths [6], [7] and then a signal processing step is performed to reduced effect of temperature. Another solution is to use a multi-layers structure like AlN/SiO2/Si to obtain an effect of self temperature compensation, by choosing material having opposite temperature coefficients.

Section 3.2 presents the temperature dependence of frequency of our structure and the structure for self temperature compensation.

Section 3.3 gives the mechanical analysis of membrane under pressure and pressure dependencies of frequency and phase of SAW device.

All calculations of velocity and center frequency are done by matrix method (as stated in Chapter 2, section 2.2) and also by FEM method.

## 3.2 TEMPERATURE COMPENSATED STRUCTURE FOR SAW DEVICE

### 3.2.1 Temperature dependence of Si, $SiO_2$, AlN properties

Temperature dependence of Si, $SiO_2$, and AlN were evaluated and measured by some authors [119]- [123]. Table 3.1 and Table 3.2 present these dependencies that will be used for designing the temperature compensation structure in section 3.2.2.

Table 3.1 TEMPERATURE DEPENDENCE OF $S_I$, $S_{I}O_2$ AND ALN PROPERTIES

| Materials | | Si | SiO₂ | AlN |
|---|---|---|---|---|
| Temperature coefficients of elastic constants ($10^{-4}$ K$^{-1}$) | $\dfrac{1}{c_{11}}\dfrac{dc_{11}}{dT}$ | -0.53 | 2.39 | -0.37 |
| | $\dfrac{1}{c_{12}}\dfrac{dc_{12}}{dT}$ | -0.98 | | Table 3.2 |
| | $\dfrac{1}{c_{13}}\dfrac{dc_{13}}{dT}$ | -0.75 | 5.84 | Table 3.2 |
| | $\dfrac{1}{c_{33}}\dfrac{dc_{33}}{dT}$ | -0.53 | 2.39 | -0.37 |
| | $\dfrac{1}{c_{44}}\dfrac{dc_{44}}{dT}$ | -0.42 | 1.51 | -0.57 |
| Temperature coefficients of mass density p ($10^{-6}$ K$^{-1}$) | $\dfrac{1}{p}\dfrac{dp}{dT}$ | -2.6 | -1.65 | -13.7 |

Table 3.2 TEMPERATURE DEPENDENCE OF $C_{12}$ AND $C_{13}$ OF ALN

| T ($^0$K) | c₁₂ (GPa) | c₁₃ (GPa) | T ($^0$K) | c₁₂ (GPa) | c₁₃ (GPa) |
|---|---|---|---|---|---|
| 0 | 148.9 | 99.4 | 600 | 147.1 | 97.7 |
| 50 | 148.9 | 99.4 | 700 | 146.6 | 97.2 |
| 100 | 148.9 | 99.3 | 800 | 145.9 | 96.7 |
| 150 | 148.8 | 99.3 | 900 | 145.2 | 96.2 |
| 200 | 148.7 | 99.2 | 1000 | 144.5 | 95.7 |
| 250 | 148.6 | 99.0 | 1100 | 143.8 | 95.3 |
| 300 | 148.4 | 98.9 | 1200 | 143.1 | 94.8 |
| 400 | 148.1 | 98.5 | 1300 | 142.4 | 94.3 |
| 500 | 147.6 | 98.1 | 1350 | 141.9 | 94.0 |

## 3.2.2 Temperature Coefficient of Frequency (TCF) and temperature compensated structure for SAW sensor

Temperature stability is a critical issue for SAW sensor. As given in section 3.2.1, both AlN and Si have negative temperature dependence of elastic coefficients and mass density. On the contrary, SiO₂ has positive temperature dependence coefficient of elastic constants and negative temperature dependence coefficient of mass density. So, temperature compensated structures of SAW sensor are constructed based on these properties and temperature compensated structure should include multilayer Si, AlN and SiO₂.

The operating frequency of SAW device is determined from the surface wave velocity v and the spatial period of IDT ($\lambda$)

$$f = \frac{v}{\lambda} = \frac{v}{D}$$

eq.(3.1)

Where λ, the wavelength, is equal to D, center to center distance between 2 fingers of an IDT.

So, temperature coefficient of frequency (TCF) can be expressed as:

$$TCF = \frac{1}{f_0}\frac{df}{dT} = \frac{dv}{vdT} - \frac{dD}{DdT} \qquad \text{eq.(3. 2)}$$

Where the theoretical temperature coefficient of velocity (TCV) is obtained by substituting velocity calculated at temperature t, (t+5) and (t-5) [124]:

$$TCV = \frac{dv}{vdT} \approx \frac{v(t+5^0 C) - v(t-5^0 C)}{v(t)10} \qquad \text{eq.(3. 3)}$$

$$\frac{dD}{DdT} = \alpha_a \qquad \text{eq.(3. 4)}$$

Where $\alpha_a$ is the thermal expansion coefficient of AlN, in structure where IDTs are on the AlN surface [122]: $\alpha_a = 4.2.10^{-6}$ ($^0C^{-1}$)

So, the temperature coefficient of frequency (TCF) of SAW device is obtained:

$$TCF \approx \frac{v(t+5^0 C) - v(t-5^0 C)}{v(t)10} - \alpha_a \qquad \text{eq.(3. 5)}$$

In literature, TCF were calculated at t($^0$C)=25 [124], [125]. For stable results, we have performed TCF calculation for SAW device with different structures at different temperature t($^0$C)=25, 65, 105, 145, 185, 225, 265 and 305. The results are shown in Table 3.3 where the normalized thickness kh=2π/λ.

It seems that the TCF values from Table 3.3 in each structure of SAW device are constant. Consequently, for an approximation, the frequency shift could depend linearly on the temperature as:

$$\frac{\Delta f}{f_0} \approx TCFxT \qquad \text{eq.(3. 6)}$$

Where TCF is the average value of TCF values calculated at different temperatures.

Table 3.3   VALUES OF TCFs IN SAW DEVICES AT DIFFERENT TEMPERATURE ($^0$C)

| TCF($\times 10^{-5}$) | | | | | | | | |
|---|---|---|---|---|---|---|---|---|
| Temperature ($^0$C) | 25 | 65 | 105 | 145 | 185 | 225 | 265 | 305 |
| AlN(khAlN=0.157)/SiO$_2$(kh SiO$_2$=0.3927)/Si substrate | 6.42 | 6.62 | 6.83 | 6.38 | 6.4 | 6.53 | 6.61 | 6.34 |
| AlN(khAlN=0.2355)/SiO$_2$(kh SiO$_2$=0.3927)/Si substrate | 6.18 | 6.19 | 6.2 | 6.04 | 6.19 | 6.08 | 6.11 | 6.16 |
| AlN(khAlN=3.69)/SiO$_2$(kh SiO$_2$=0.3927)/Si substrate | -4.74 | -4.73 | -4.8 | -4.71 | -4.68 | -4.73 | -4.69 | -4.74 |
| AlN(khAlN=0.157)/SiO$_2$(kh SiO$_2$=0.0785)/Si substrate | 4.87 | 4.95 | 4.77 | 4.82 | 4.8 | 4.83 | 4.82 | 4.69 |
| AlN(khAlN=0.7065)/SiO$_2$(kh SiO$_2$=0.0785)/Si substrate | 2.31 | 2.18 | 2.21 | 2.09 | 2.28 | 2.13 | 2.1 | 2.14 |
| AlN(khAlN=5.181)/SiO$_2$(kh SiO$_2$=0.0785)/Si substrate | -675 | -667 | -680 | -677 | -691 | -683 | -692 | -669 |

Figure 3.1 and Figure 3.2 give the obtained results of the frequency shift $\Delta f/f0$(ppm) for SAW devices with AlN/SiO$_2$(khSiO$_2$=0.0785)/Si substrate, with different thickness of AlN layer. For the clarity of reading, Figure 3.2 which is the inset of Figure 3.1 is presented in different scale of smaller range of khAlN from 0.157 to 0.8635.
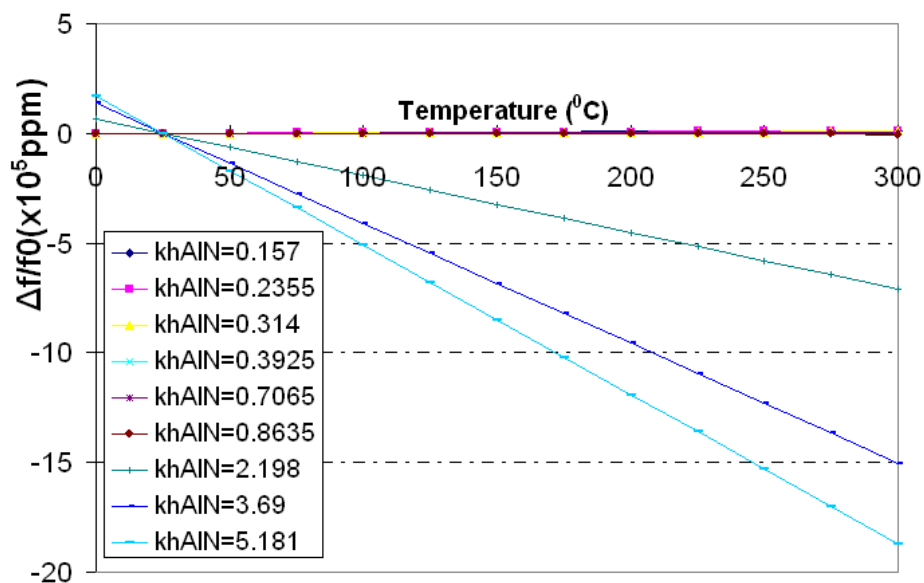


Figure 3.1   $\Delta f/f0$(ppm) depending on temperature in SAW device:
AlN/SiO$_2$(khSiO$_2$=0.0785)/Si substrate
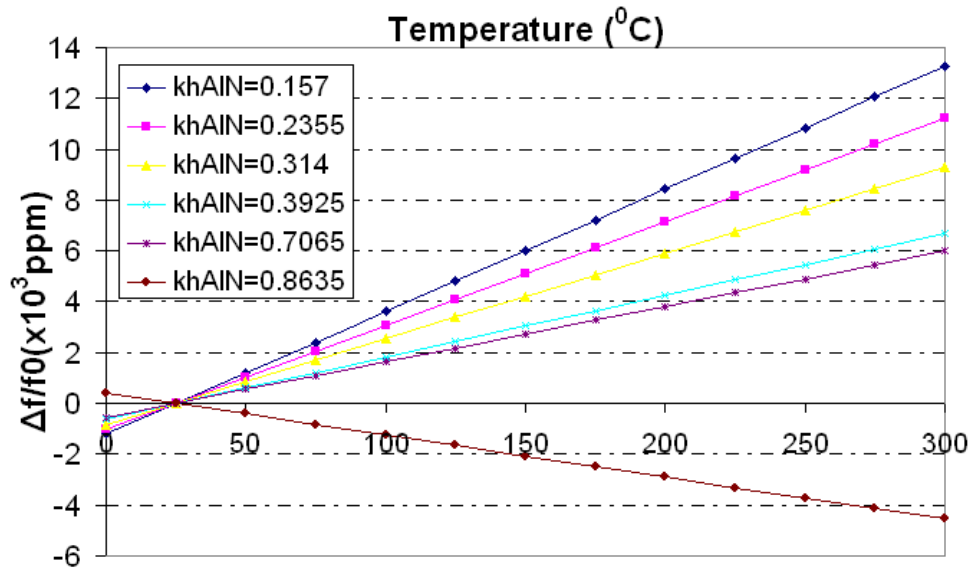
Figure 3.2   $\Delta f/f0$(ppm) depending on temperature in SAW device:
AlN/SiO$_2$(khSiO$_2$=0.0785)/Si substrate

Figure 3.3 and Figure 3.4 give the obtained results of frequency shift $\Delta f/f0$(ppm) for SAW devices with AlN/SiO$_2$(khSiO$_2$=0.3927)/Si substrate. For the clarity of reading, Figure 3.4 which is the inset of Figure 3.3 is presented in different scale of smaller range of khAlN from 0.157 to 3.847.
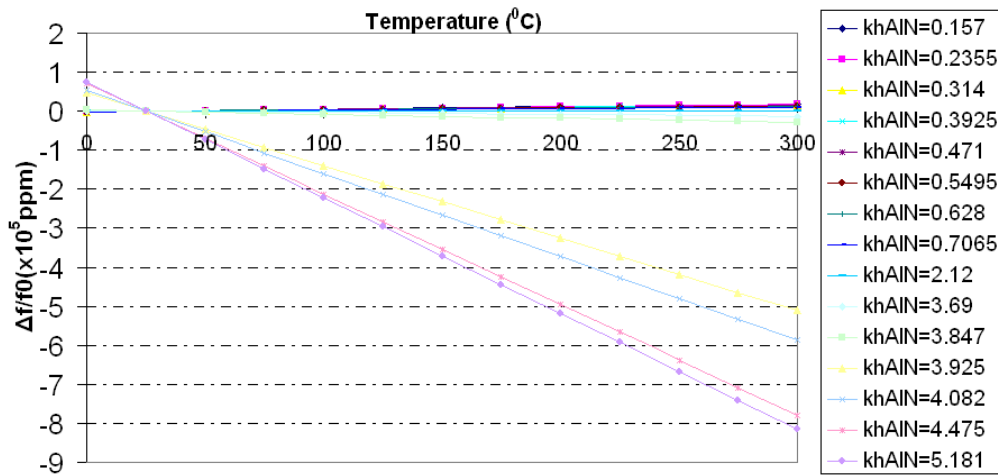


Figure 3.3   $\Delta f/f0$(ppm) depending on temperature in SAW device:
AlN/SiO$_2$(khSiO$_2$=0.3927)/Si substrate
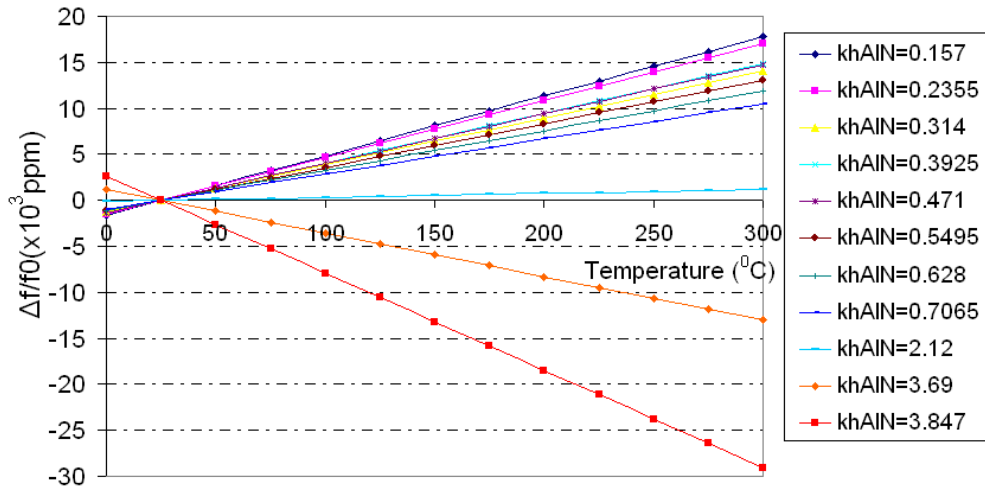
Figure 3.4   $\Delta f/f0$(ppm) depending on temperature in SAW device:
AlN/SiO$_2$(khSiO$_2$=0.3927)/ Si substrate

So, from these results in Figure 3.1 to Figure 3.4, in SAW device AlN/SiO$_2$/Si substrate, it seems that when the thickness of AlN layer increases, the TCF would become negative. TCF is negative if:

khSiO$_2$=0.0785, khAlN > 0.8 (see Figure 3.1 and Figure 3.2);

or   khSiO$_2$=0.3927, khAlN > 3.6 (see Figure 3.3 and Figure 3.4).

And vice versa, the positive sign of TCF could be obtained when the thickness of SiO$_2$ increases. From Figure 3.1, TCF (khAlN=2.198, khSiO$_2$=0.0785) is negative, but in Figure 3.4, when the thickness of SiO$_2$ is five times larger (khSiO$_2$=0.0785 x 5=0.3927, the same thickness of AlN: khAlN=2.198), the TCF becomes positive.

Therefore, we can conclude that a positive sign of the temperature dependence of frequency indicates a large contribution from the SiO$_2$ layer, and a negative sign indicates a large contribution from AlN layer.

And, we could also conclude approximately that:

when the ratio (thickness of AlN/thickness of SiO$_2$)>10, the TCF is negative;

when the ratio (thickness of AlN/thickness of SiO$_2$)<10, the TCF is positive.

This boundary value "10" could be explained by that the temperature dependencies of elastic constants of SiO$_2$ is larger 5-8 times than those of AlN (see Table 3.1).

And, from Figure 3.4, the self temperature compensated structure can be obtained with AlN(khAlN=2.12)/SiO$_2$(khSiO$_2$=0.3927)/Si substrate.

## 3.3   PRESSURE DEPENDENCE OF FREQUENCY AND PHASE IN SAW DELAY LINE

### 3.3.1   Mechanical analysis of membrane under pressure

Thin film or membrane has been used in a vast range of technological applications, such as integrated circuit comprises of multiple thin layers of semiconducting, dielectric, conductive materials; MEMS used for sensor, optical, solar cell … applications. Consequently, many authors have researched properties of membrane. Among them, the mechanical properties of membrane under pressure have been calculated by many authors [126]-[131] with different approaches for different geometries of membrane. The comparison between different approaches was reviewed in [130].

In this research, the rectangle membrane with four boundaries fixed is used, as in Figure 3.5.
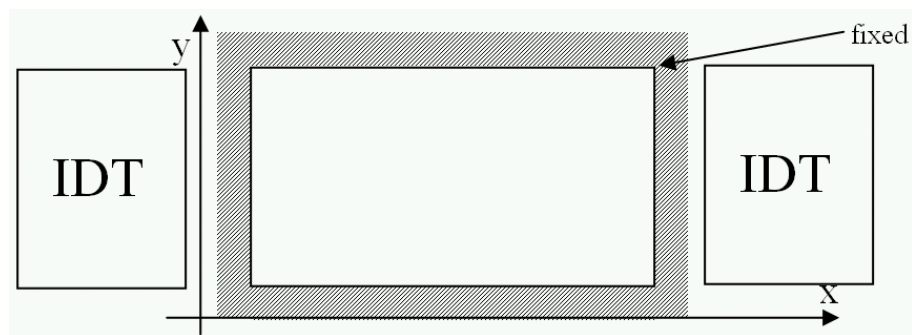


Figure 3.5   The rectangle membrane with four fixed-boundaries

When this kind of membrane is under pressure, the distance d between two IDTs is not uniform over y-axis. In pressure sensor based on SAW delay line, the variation of the distance d between two IDTs is an important parameter as it is used in simulation of device as well as it is used to calculate the sensitivity. To simplify the calculation and the simulation, the infinitely long rectangular membrane is assumed to be used, as shown in Figure 3.6.
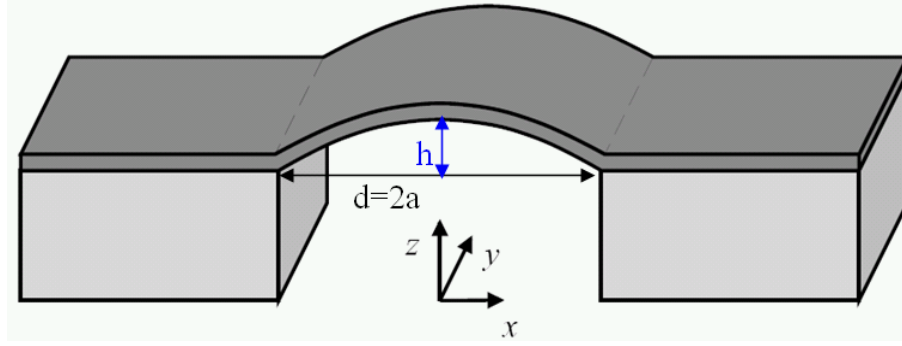
Figure 3.6   The infinitely long rectangular membrane with two fixed-boundaries

For infinite long rectangular membrane, the exact solution of relation between p (pressure applied on membrane) and h (vertical displacement at the centre of membrane, or height of deflection) can be expressed as follows [130]:

$$p = \frac{4.2}{(1-\upsilon^2)} \frac{Et^3}{a^4} h + \frac{1.58}{(1-\upsilon)} \frac{Et}{a^4} h^3 \qquad \text{eq.(3. 7)}$$

Where E is Young's Modulus, t is membrane thickness, a is the half length of the membrane, $\upsilon$ is Poisson's ratio and p is pressure.

The deflection range is divided into two regions: a small deflection (deflection less than 25% of membrane thickness) described by the linear term in eq.(3.7) and a large deflection region described by the non-linear term in eq.(3.7).

In multilayer membrane, made up of n layers of thickness $t_i$ to $t_n$ respectively, the pressure p applied on this multilayer could be seen as the sum of n elemental pressures $p_1$, $p_2$, …, and $p_n$ in which each element pressure $p_i$ depends on each individual layer i properties:

$$p=p_1+p_2+p_3+…+ p_n \qquad \text{eq.(3. 8)}$$

Each element $p_i$ is used to apply on each layer i and each layer deflects the same height of deflection h

$$h=h_1=h_2=h_3=…= h_n \qquad \text{eq.(3. 9)}$$

Substitution of $h_i$ into eq.(3. 7) to get the $p_i$, and substitution of $p_i$ into eq.(3. 8) will yield the exact relation of pressure p and deflection h for multilayer membrane:

$$p = \frac{4.2}{a^4} \left\{ \sum_{i=1}^{n} \frac{E_i t_i^3}{(1-\upsilon_i^2)} \right\} h + \frac{1.58}{a^4} \left\{ \sum_{i=1}^{n} \frac{E_i t_i}{(1-\upsilon_i)} \right\} h^3 \qquad \text{eq.(3. 10)}$$

The strain in infinitely long rectangular membrane is expressed by the deflection h [130]:

$$S_{xx} = \frac{2h^2}{3a^2}$$ <span style="float:right">eq.(3. 11)</span>

Where h is extracted from equation eq.(3. 10), and substitution h into eq.(3. 11) yields the strain $S_{xx}$.

In case of a large deflection (deflection larger than 25% of membrane thickness), h is extracted by the non-linear term in eq.(3.10), and $S_{xx}$ could be expressed as:

$$S_{xx} = \frac{2}{3}\left(\frac{1}{1.58}\right)^{2/3}\left(\frac{a}{B}\right)^{2/3}p^{2/3}$$ <span style="float:right">eq.(3. 12)</span>

Where B is expressed as

$$B = \sum_{i=1}^{n}\frac{E_i t_i}{(1-\upsilon_i)}$$ <span style="float:right">eq.(3. 13)</span>

The pressure applied on the membrane will increase the distance between two IDTs. The distance variation Δd could be expressed by:

$$\Delta d = S_{xx}d = S_{xx}(2a)$$ <span style="float:right">eq.(3. 14)</span>

In case of a large deflection, Δd is extracted from substitution eq.(3. 12) into eq.(3. 14) and is given by eq.(3.15) in the case of multilayer structure. Figure 3.7 and Figure 3.8 represent the obtained calculations of the strain as function of pressure for two different structures.

$$\Delta d = \frac{4}{3}\left(\frac{1}{1.58}\right)^{2/3}\left(\frac{1}{B}\right)^{2/3}a^{5/3}p^{2/3}$$
$$\approx 0.98\left(\frac{1}{B}\right)^{2/3}a^{5/3}p^{2/3}$$ <span style="float:right">eq.(3. 15)</span>
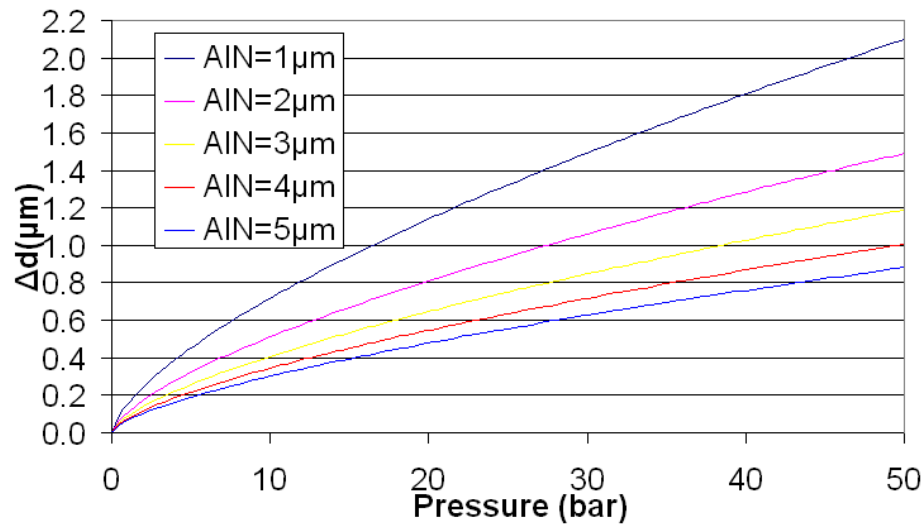
Figure 3.7   $\Delta$d in multilayer: Si (1 μm), SiO$_2$ (200nm), AlN (1-5 μm)
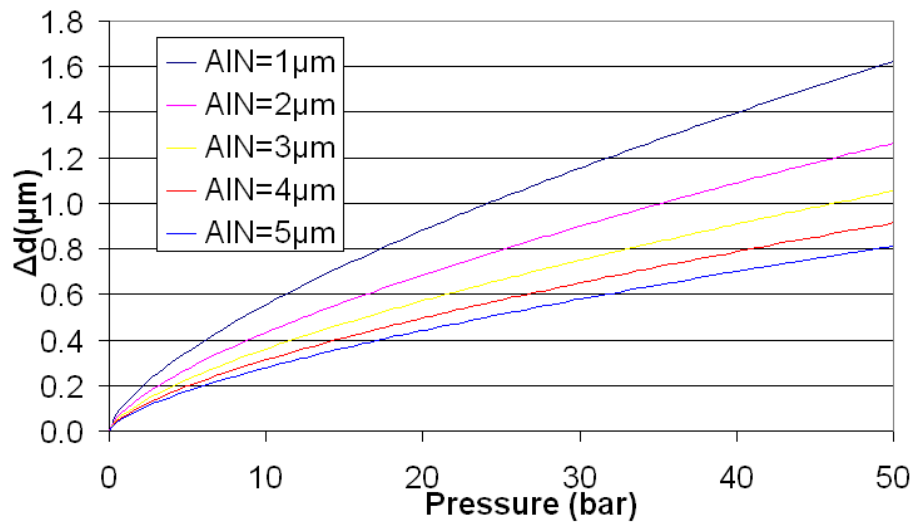


Figure 3.8   $\Delta$d in multilayer: Si (2.42 μm), SiO$_2$ (200nm), AlN (1-5 μm)

## 3.3.2    Pressure-dependence of frequency by pressure dependence of AlN elastic properties

An excellent recent review for all of calculations and experiments of pressure dependence of elastic constants was written by M.B.Kanoun et al [132]. M.B.Kanoun et al have found a linear dependence of AlN elastic constants with applied pressure. Figure 3.9 and

Table 3.4 present the variation of elastic constants of AlN with respect to the variation of pressure [132].
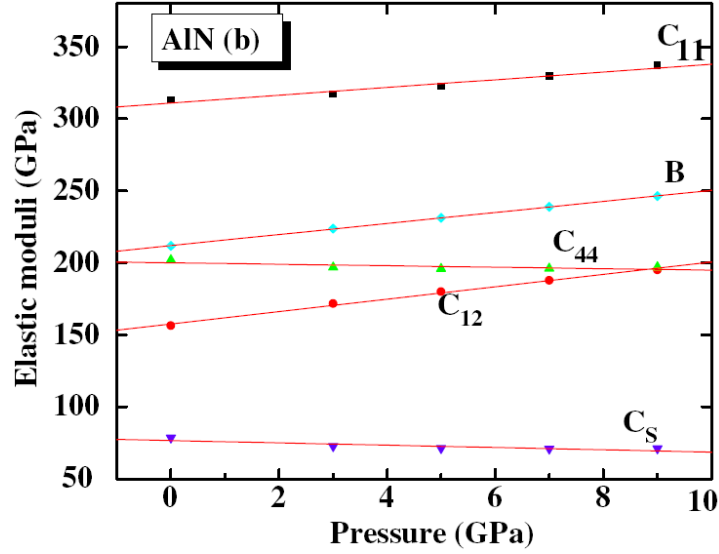
Figure 3.9   Pressure dependence of AlN elastic constants [132]

Table 3.4   THE PRESSURE DEPENDENCE OF ALN ELASTIC CONSTANTS

| $\dfrac{dc_{11}}{dP}$ | $\dfrac{dc_{12}}{dP}$ | $\dfrac{dc_{44}}{dP}$ |
|---|---|---|
| 2.701 | 4.287 | -0.511 |

From equation eq.(3.1), pressure coefficient of frequency (PCF) can be expressed as:

$$PCF = \frac{1}{f_0}\frac{df}{dP} = \frac{dv}{vdP} - \frac{dD}{DdP} \qquad \text{eq.(3. 16)}$$

Where pressure coefficient of velocity (PCV) is obtained by substituting velocity calculated at pressure P, (P+0.1bar) and (P-0.1bar) as in eq(3.17):

$$PCV = \frac{dv}{vdP} \approx \frac{v(P+0.1bar) - v(P-0.1bar)}{v(P)0.2} \qquad \text{eq.(3. 17)}$$

$$\frac{dD}{DdP} = 0 \qquad \text{eq.(3. 18)}$$

So, the pressure coefficient of frequency (PCF) of SAW device is obtained by pressure-dependence of AlN elastic properties

$$PCF \approx \frac{v(P+0.1bar) - v(P-0.1bar)}{v(P)0.2} \qquad \text{eq.(3. 19)}$$

We have performed the calculations of PCF for SAW device with different structures at P(bar)=2, 3, 4, 5, 6 and 7. The results are shown in Table 3.5 where the normalized thickness kh=$2\pi/\lambda$.

Table 3.5   VALUES OF PCFS IN ALN/SIO$_2$(KHSIO$_2$= 0.1571)/SI SAW DEVICES AT DIFFERENT PRESSURE (BAR)

| PCF(x $10^{-6}$) | | | | | | | | |
|---|---|---|---|---|---|---|---|---|
| | Pressure (bar) | | | | | | | |
| khAlN | 2 | 3 | 4 | 5 | 6 | 7 | 8 | 9 |
| 0.785 | -14.19 | -14.47 | -14.35 | -14.33 | -14.45 | -14.35 | -14.22 | -14.44 |
| 1.57 | -12.34 | -13.1 | -12.78 | -12.23 | -12.23 | -12.45 | -11.21 | -12.02 |
| 2.67 | -2.19 | -2.07 | -2.15 | -2.17 | -2.11 | -2.29 | -2.02 | -2.1 |
| 3.29 | 13.62 | 13.86 | 13.21 | 12.92 | 12.54 | 13.23 | 13.87 | 13.41 |
| 3.69 | 17.23 | 17.87 | 17.1 | 18.43 | 18.1 | 17.76 | 16.78 | 17.12 |

It seems that the PCF value from Table 3.5 in each structure of SAW device is constant. Approximately, the frequency shift could depend linearly on the applied pressure as:

$$\frac{\Delta f}{f_0} \approx PCFxP$$

eq.(3. 20)

For stable result, PCF is the average value of PCF values calculated at different pressures.

Consequently, SAW device using AlN would have a linear dependence of frequency shift on applied pressure. It was shown in literature [35], [82] that this linear property could be obtained with SAW device using ZnO.

The pressure-dependence of frequency shift by the pressure-dependence of elastic constants in SAW device: AlN/SiO$_2$ (khSiO$_2$=0.1571)/Si substrate is shown in Figure 3.10.
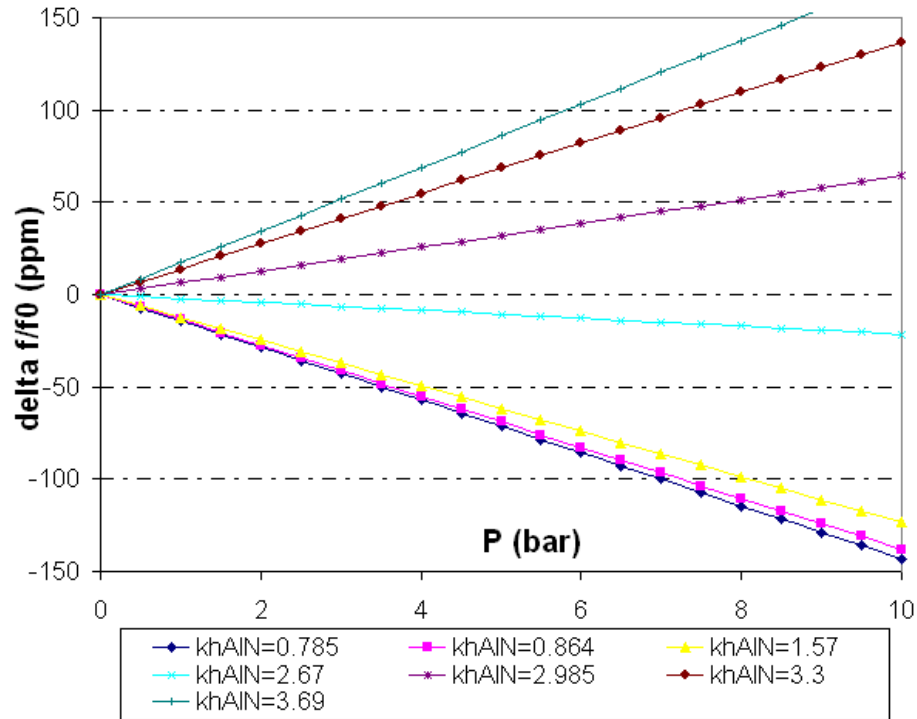
Figure 3.10   $\Delta f/f_0$ (ppm) by pressure-dependence of elastic in AlN/SiO$_2$
(khSiO$_2$=0.1571)/Si substrate

The equation eq.(3. 20) could be expressed as:

$$\Delta f_{pe} = A_{pe} f_0 P$$                                   eq.(3. 21)

Where PCF=$A_{pe}$ is coefficient depending on the pressure dependence of elastic constants of materials and the thickness of each layer in SAW device. We would like to use the subscript "pe" that means the dependence of frequency to applied Pressure by the pressure dependence of Elastic constants.

For Figure 3.10, coefficient $A_{pe}$ depends on the normalized thickness of AlN as in Table 3.6.

Table 3.6   A$_{PE}$ COEFFICIENT IN SAW DEVICE A$_L$N/S$_I$O$_2$ (KHSIO$_2$=0.1571)/S$_I$
SUBSTRATE

| Normalized thickness of AlN (khAlN) | $A_{pe}$ (x10$^{-6}$/bar) |
|---|---|
| 0.785 | -14.35 |
| 0.864 | -13.81 |
| 1.57 | -12.34 |
| 2.67 | -2.138 |
| 2.985 | 6.41 |
| 3.3 | 13.7 |
| 3.69 | 17.2 |

These our calculations were done based on the values obtained by experiments. However, in literature, pressure dependence of the second order of elastic constants have been measured. We think that if the pressure dependence of third and fourth orders of elastic constants can be known, PCF-by-PCE could be more accurate.

### 3.3.3 Pressure-dependence of frequency by delay line

By applying the pressure on the membrane, the propagation path will increase.

Using the SAW delay line model in Chapter 2, section 2.3.3 or section 2.4.4; simulations were done for SAW devices with N=50 (number of finger pairs in one IDT), velocity v=5120 m/s, distance between two IDTs is $l_0$=300μm (with no pressured applied) and $l_1$=301μm (with pressure applied).

The simulated center frequency shift is -34.2 kHz. This value corresponds to Δd=1 μm. From the section 3.3.1, the pressure could be extracted from the value of Δd. For instance, from Figure 3.7, the pressure corresponding to Δd=1μm in a multilayer membrane of d=300μm, with Si of 1μm, $SiO_2$ of 200nm, AlN of 1μm thick, is 16.5 bar. In SAW device with this membrane, the pressure dependence of frequency by delay line approach is $\Delta f/f_0$ (ppm/bar)= -3.24 (ppm/bar).

The dependence of center frequency on the delay line was also measured by experiments, where Δd is large enough to see the center frequency shift. The SAW devices were fabricated with different delay line length: d=500μm, 400μm, 350μm, 300μm, 250μm, 200μm and 150μm. These measurements were done without applied pressure to make sure that the center frequency shift is obtained by only the delay line, not including the pressure effect on elastic constants.

Measurements were done on different wafers, in two different batches: N309P and P528P (the name of batches are given during the fabrication process).

Figure 3.11 shows the measurements in wafer 4 of lot N309P, for three SAW devices with N=50 and distances between IDTs of d1=350μm, d2=400μm, and d3=500μm. The center frequency of SAW device for this test is $f_0$ = 543 MHz. The center frequency difference between devices with d1=350μm and d2=400μm is -125 kHz and between devices with d2=400μm and d3=500μm is -212.5 kHz. The accuracy of this measurement is ±12.5 kHz. In simulation, the frequency shift between devices with d1=350μm and d2=400μm is -100.56 kHz; between devices d2=400μm, d3=500μm is -168 kHz.
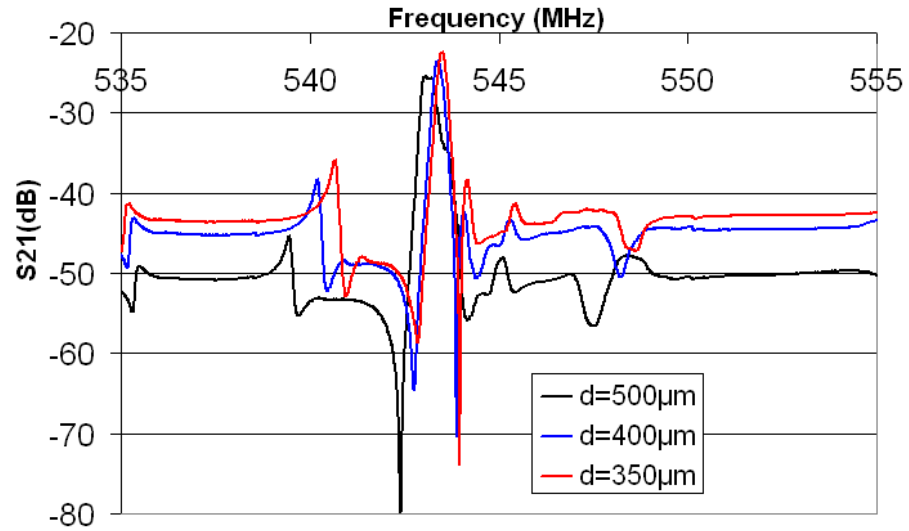
Figure 3.11   The measurement of frequency shift only by different delay line

Figure 3.12 and Figure 3.13 show the measurements on wafer 7, lot P528P of SAW devices with different delay line 500μm, 350μm, 300μm, 250μm, and 200μm.
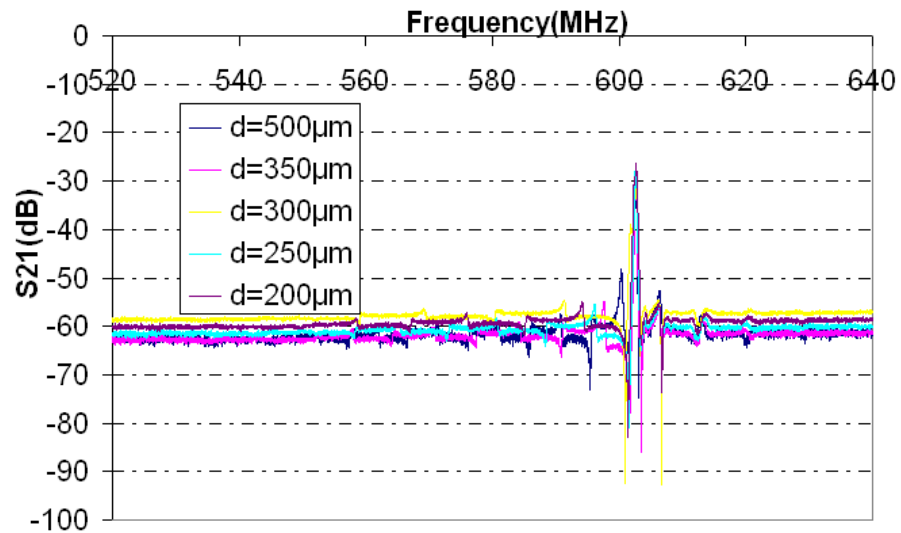


Figure 3.12   The measurement of frequency shift only by different delay line
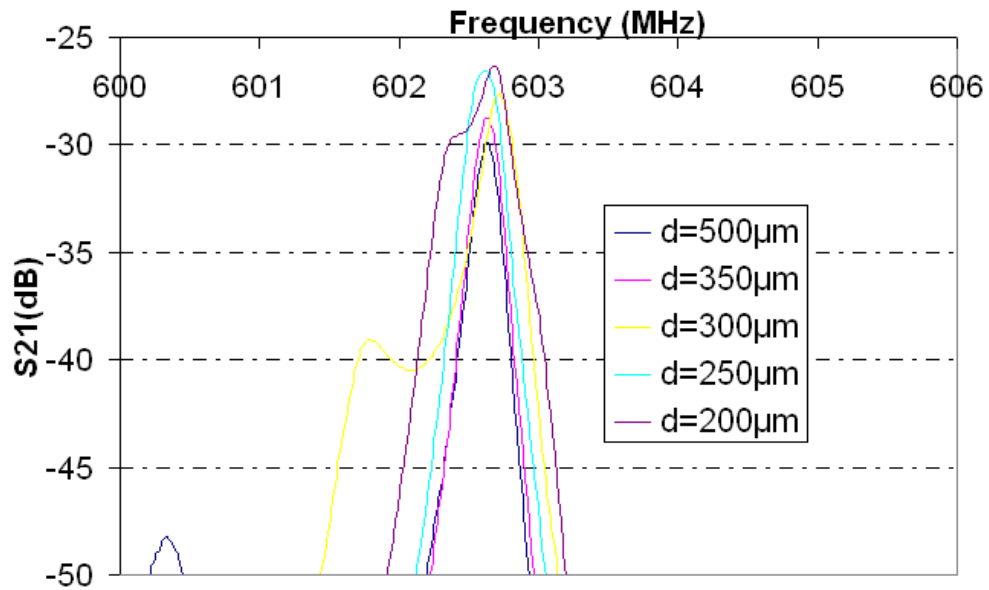
Figure 3.13   The measurement of frequency shift only by different delay line (zoom in from Figure 3.12)

Figure 3.14 and Figure 3.15 present the measurement of frequency shift only by delay line, the experiments were done on four wafers from N309P and P528P, respectively.
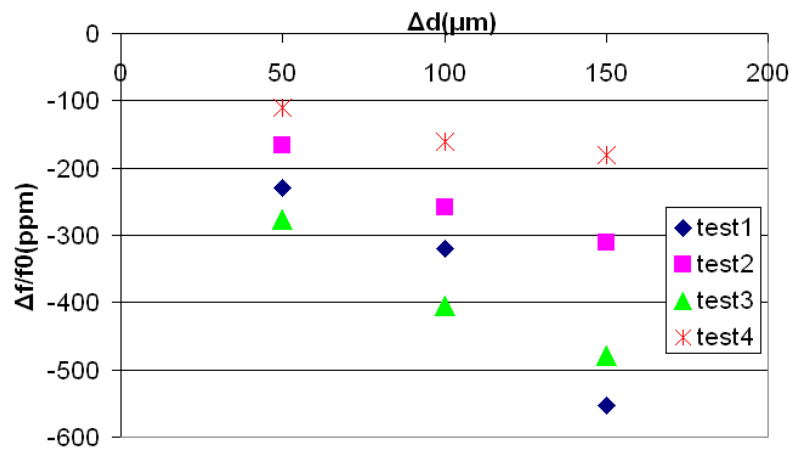


Figure 3.14   The measurements of frequency shift only by different delay line, on four wafers of N309P
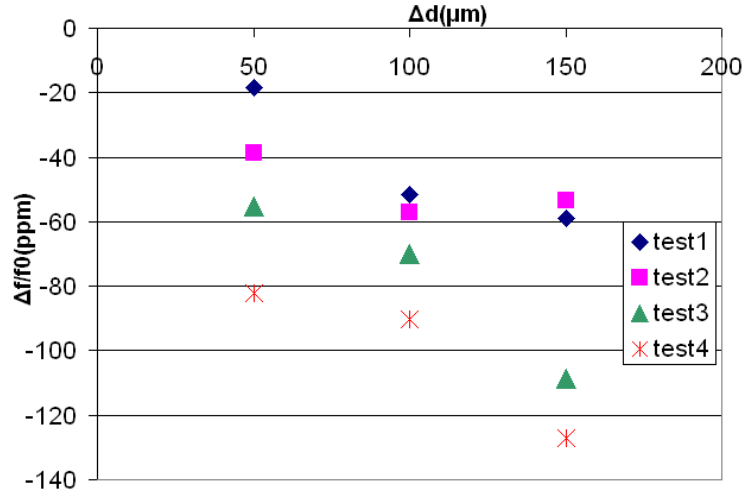
Figure 3.15   The measurement of frequency shift only by different delay line, on four wafers of  P538P

From the measurements reported in Figure 3.14 and Figure 3.15, approximately, the $\Delta f/f_0$ could depend linearly on $\Delta d$ as:

$$\frac{\Delta f_{pl}}{f_0} = R\Delta d$$

eq.(3. 22)

Where the average of R is:

R$_1$= -3.1(ppm/μm) for N309P, in Figure 3.14

eq.(3. 23)

R$_2$= -0.74(ppm/μm) for N309P, in Figure 3.15

eq.(3. 24)

And as equation eq.(3. 15), the frequency shift could be written as:

$$\Delta f_{pl} = A_{pl}f_0 P^{2/3}$$

eq.(3. 25)

Where A$_{pl}$ is a coefficient depending on the pressure dependence of delay line Length. The subscript "pl" means the dependence of frequency on applied Pressure by the pressure dependence of delay line Length.

From eq.(3. 15), eq.(3. 22), and eq.(3. 25), the coefficient A$_{pl}$ can be expressed as

$$A_{pl} \approx 0.346667\left(\frac{1}{B}\right)^{2/3} d^{5/3}R$$

eq.(3. 26)

Two average values of R are values from experiments, they could be used to calculate the value of A$_{pl}$ in SAW device with the other thicknesses of membrane. For membrane with

thickness of 2.42μm for Si, 200nm for SiO$_2$ and 1μm to 5μm for AlN ; the values of A$_{pl}$ are expressed as in Table 3.7.

Table 3.7   THE VALUE OF COEFFICIENT A$_{PL}$

| Thickness of AlN (μm) | A$_{pl}$ (x10$^{-11}$) | R |
|---|---|---|
| 1 | 5.5R | |
| 2 | 4.33R | |
| 3 | 3.65R | R can get the value of R$_1$= -3.1(ppm/μm) or R$_2$= -0.74(ppm/μm) |
| 4 | 3.14R | |
| 5 | 2.79R | |

To compare the pressure dependence of frequency to pressure dependence of elastic constant and to effect of pressure on delay line, the same SAW devices with the same thicknesses of multilayer are used. Calculations of Δd are then used in model of SAW delay line. The pressure used for all cases is 20 bars. The comparison is shown in Table 3.8. From this table, it seems that in each case of AlN thickness, the pressure sensitivity of frequency shift could be mainly affected by pressure dependence of elastic constants.

Table 3.8   COMPARISON BETWEEN THE PRESSURE DEPENDENCE OF FREQUENCY SHIFT, PRESSURE DEPENDENCE OF ELASTIC CONSTANT AND EFFECT OF PRESSURE ON DELAY LINE IN SAW DEVICE (WAVELENGTH:  8μm)

| Pressure applied = 20 bar | | |
|---|---|---|
| normalized thickness of AlN (khAlN) | Δf/f$_0$ (ppm) by pressure dependence of elastic constant | Δf/f$_0$ (ppm) by delay line prolonged |
| 0.785 | -286 | -3.6 |
| 0.864 | -276 | -3.1 |
| 1.57 | -246.8 | -2.4 |
| 2.67 | -42.76 | -0.9 |
| 2.985 | 128.3 | -0.78 |
| 3.3 | 274 | -0.52 |
| 3.69 | 344 | -0.38 |

### 3.3.4    Pressure-dependence of phase shift

In the studied SAW devices, the propagation path variation due to applied pressure, will give propagation time variation. This point of view must be analyzed as respect to harmonic excitation of the input IDT. In fact this will give a phase variation of the signal as compare to the situation where no pressure is applied. In this section, we will evaluate the phase shift of the signal.

The electrical signal at the transmitting IDT could be expressed as:

$$S_{in}(t) = A\cos(\omega_0 t)$$

eq.(3. 27)

The electrical signal at the receiving IDT $S_0(t)$ and $S_p(t)$ in case no pressure applied and pressure P applied, respectively, could be expressed as follows:

$$S_o(t) = A_0 \cos \omega_0 (t - t_0) \qquad \text{eq.(3. 28)}$$

$$S_p(t) = A_p \cos \omega_p (t - t_p) \qquad \text{eq.(3. 29)}$$

With

$$t_0 = \frac{d_0}{v_0} + T \qquad \text{eq.(3. 30)}$$

$$t_p = \frac{d_p}{v_p} + T \qquad \text{eq.(3. 31)}$$

Where:

$\omega_0$, $\omega_p$ is the angular frequencies with no pressure and pressure applied, respectively;

$d_0$, $d_p$ is the length of delay line with no pressure and pressure applied, respectively;

$$d_p = d_0 + \Delta d = d_0 (1 + S) \qquad \text{eq.(3. 32)}$$

S is strain

$v_0$, $v_p$ is the SAW velocity with no pressure and pressure applied, respectively;

T is the total time of other delays (such as the delay in the electronic circuit, in device, and the traveling time of the electromagnetic wave). This time could be negligible for short distances.

The SAW velocity with pressure applied $v_p$ can be expressed as:

$$v_p = v_0 + \Delta v \qquad \text{eq.(3. 33)}$$

Where velocity change is caused by the pressure dependence of elastic constant of material. From eq.(3. 19) and eq.(3. 21), the relation between $\Delta v$ and $v_0$ could be written as:

$$\frac{\Delta v}{v_0} = \frac{\Delta f}{f_0} = A_{pe} P \qquad \text{eq.(3. 34)}$$

The difference of the two phases could be written as:

$$\Delta\varphi = \varphi_0 - \varphi_p \approx \omega_p t_p - \omega_0 t_0 \qquad \text{eq.(3. 35)}$$

Where

$$\omega_p = 2\pi(f_0 + \Delta f) \qquad \text{eq.(3. 36)}$$

$\Delta f$ is caused by pressure dependence of elastic constants as $\Delta f_{pe}$ in eq.(3. 21) and by delay line dependence of frequency as $\Delta f_{pl}$ in eq.(3. 25)

$$\Delta f = \Delta f_{pe} + \Delta f_{pl} = f_0(A_{pe}p + A_{pl}p^{2/3}) \qquad \text{eq.(3. 37)}$$

By substituting eq.(3. 30), eq.(3. 31), eq.(3. 32), eq.(3. 33), eq.(3. 34), eq.(3. 36) and eq.(3. 37) in eq.(3. 35), the phase shift by pressure applied could be given as follows:

$$\Delta\varphi = 2\pi f_0 \frac{d_0}{v_0}\left[ S + A_{pl}\frac{1+\varepsilon}{1+A_{pe}p}p^{2/3} \right] \qquad \text{eq.(3. 38)}$$

Substituting S by eq.(3. 12) in eq.(3. 38), $\Delta\varphi$ can be expressed by:

$$\Delta\varphi = 2\pi f_0 \frac{d_0}{v_0}\left[ 0.346667\left(\frac{1}{B}\right)^{2/3}d_0^{2/3} + A_{pl}\frac{1+0.346667\left(\frac{1}{B}\right)^{2/3}d_0^{2/3}p^{2/3}}{1+A_{pe}p} \right]p^{2/3}$$

eq.(3. 39)

Figure 3.16 shows the pressure dependence of phase shift in SAW device: AlN(1-5μm)/SiO$_2$ (200nm)/Si (2.4μm).
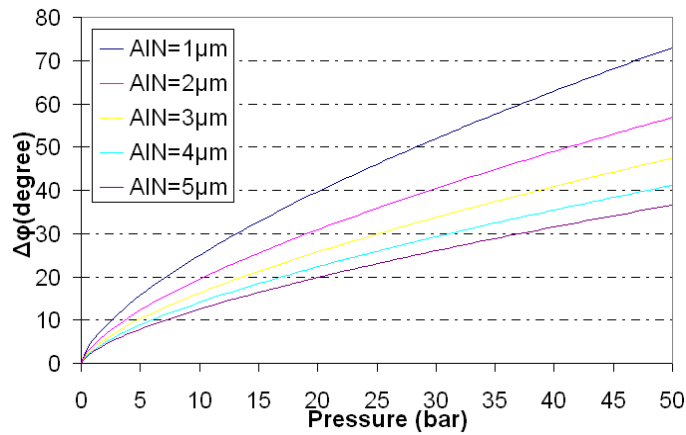


Figure 3.16   Pressure dependence of phase shift in SAW device: AlN(1-5μm)/SiO$_2$ (200nm)/Si (2.4μm)

From the analyses in sections 3.3.2, 3.3.3 and 3.3.4 as stated above, the pressure dependence of phase shift is more sensitive than that of frequency shift.

## 3.4 CONCLUSION

+ Temperature dependence of frequency shift in SAW device is presented. The frequency shift could depend linearly on the temperature.

+ The structure for self temperature compensation of SAW device could be obtained with three layers AlN, $SiO_2$ and Si.

+ A positive sign of the temperature dependence of frequency indicates a large contribution from the $SiO_2$ layer and a negative sign indicates a large contribution from AlN layer.

+ Approximate condition is obtained that:

when the ratio (thickness of AlN/thickness of $SiO_2$)>10, the TCF is negative;

when the ratio (thickness of AlN/thickness of $SiO_2$)<10, the TCF is positive.

+ The mechanical analysis of membrane under pressure is given.

+ Pressure dependencies of frequency are the sum of the pressure dependence of frequency by the pressure dependence of elastic constants and that by the pressure dependence of delay line. However, the pressure sensitivity of frequency shift could be mainly affected by pressure dependence of elastic constants.

+ The pressure dependence of phase of SAW device is also analyzed.

+ If it is desired to operate the sensor over a wide temperature range, the multilayer AlN/$SiO_2$/Si should be used to reduce the temperature dependence. In such a multilayer structure, from the electromechanical coupling factor as in Figure 2.5, khAlN=1.942, kh$SiO_2$=0.785 could be used to obtain a maximum coupling factor K=8.02%, but it sacrifices the wave velocity which does not reach the maximum value of velocity (maximum value of velocity is 6169m/s, while wave velocity in this case is 5140m/s) (see Figure 2.4). Besides, this structure sacrifices the maximum reduction of temperature dependence (the condition AlN thickness/$SiO_2$ thickness ≈10 is not obtained). The structure AlN(khAlN=1.942)/$SiO_2$(kh$SiO_2$=0.785)/Si has the calculated frequency variation: deltaf/f0 (ppm/bar) = -4.503 (ppm/bar).

If structure AlN/Si should be used, the reduction of temperature dependence could not be obtained. However, it has some advantages. From the calculation of coupling factor and wave velocity in Chapter 2, section 2.2, the AlN (khAlN=3)/Si structure has K%=4.74%,

velocity=6169m/s. The coupling factor is smaller and wave velocity is larger than those of AlN/SiO$_2$/Si structure stated above. Besides, the calculated frequency variation in this structure is: deltaf/f0 (ppm/bar) = 7.8 (ppm/bar), it is larger than that in AlN/SiO$_2$/Si structure stated above.

Consequently, it is too difficult to choose the best configuration for SAW pressure sensor. There are tradeoffs between temperature reduction, coupling factor, wave velocity and pressure sensitivity and facility in manufacturing as stated in section 0.

For pressure sensitivity based-on phase-shift, the choice of configuration could be simpler. The thinner the membrane is, the better the pressure sensitivity is. However, it should be consider the wave velocity, coupling factor as analyzed in Chapter 2, section 2.2.

# Chapter 4

# FABRICATION PROCESS

A novel fabrication process presented in this chapter by using surface micromachining technique is proposed to create exactly the dimensions of membrane used in pressure sensor, and this process also allows having a well defined membrane with any geometry due to the silicon etch stop walls.

This chapter presents the fabrication process used to realize the devices.

Section 4.1 gives the general description of fabrication process.

Section 4.2 presents briefly the designed mask applied to the realization.

Section 4.3 to section 4.11 describe the different stages of manufacture; also give some results during manufacture.

Many batches of wafer were done to dertemine process flow, process conditions. At the final process, three batches for electric purposes were processed. These are correspondent to 50 wafers and at least 110.000 devices.
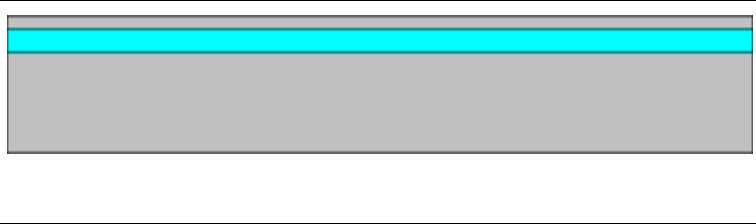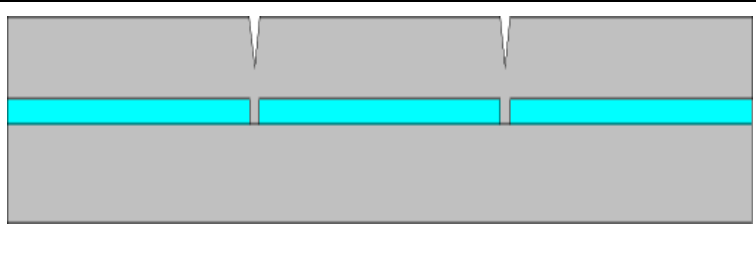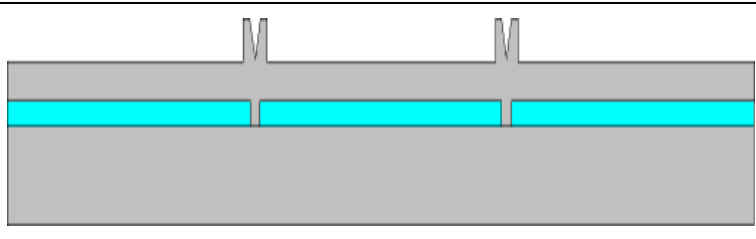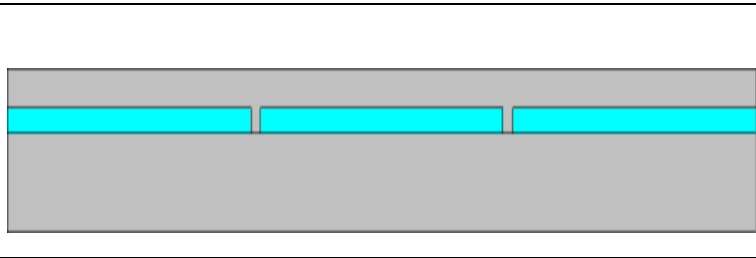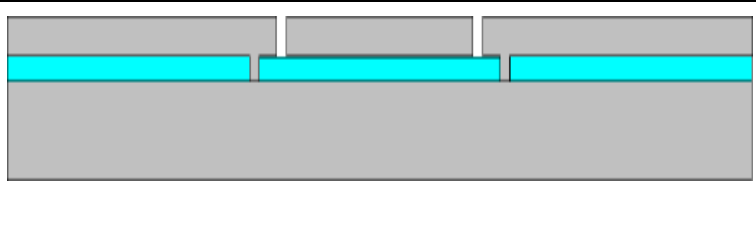
## 4.1 GENERAL DESCRIPTION
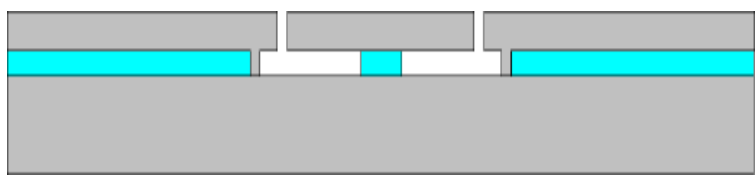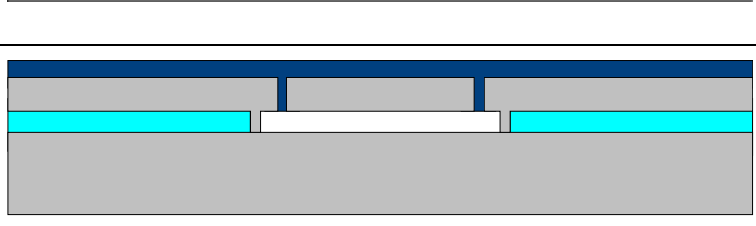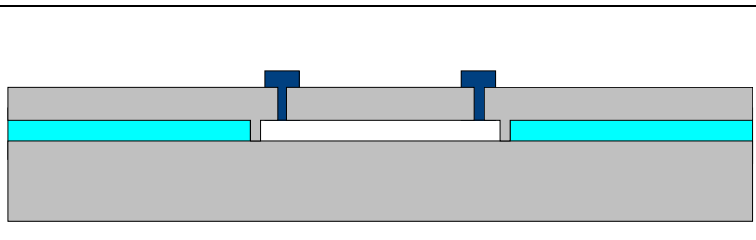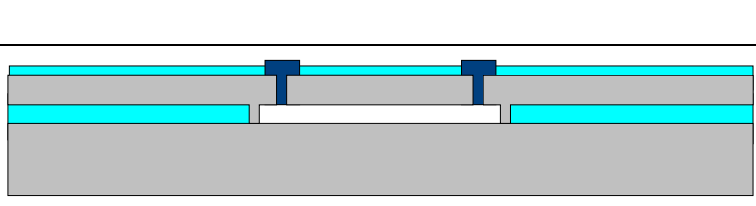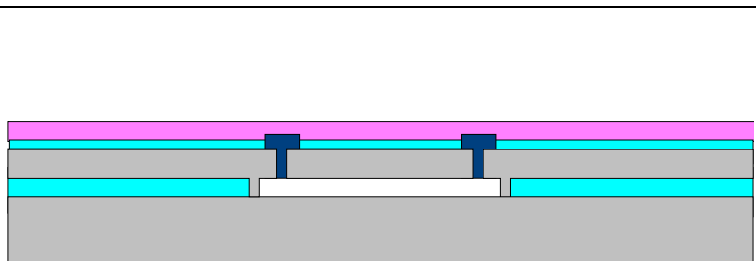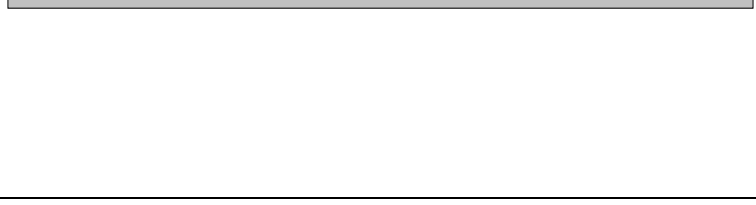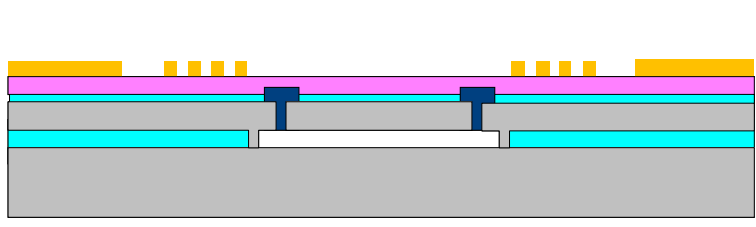
The process is performed on a SOI substrate with superficial silicon 340nm thick and a buried $SiO_2$ layer of 2µm thick. Trenches 1µm wide are etched through the superficial layers. Then a non selective epitaxy step takes place to fill the trenches and to increase the superficial silicon layer. After that CMP is realized to remove the grooves and to adjust the thickness on the silicon layer to the required membrane thickness. Holes are etched through the Si layer and the sacrificial layer is partially etched with wet HF. The complete release is performed using vapor HF to avoid sticking problems of the membrane. Etching is stopped on the Si walls. Then, cavities are hermetically plugged under vacuum with a reflowed PSG deposition about 3µm thick. Thermal oxide 200nm is grown. After that, AlN as the piezoelectric active material between 1 and 4µm thick is deposited and etched using a $H_3PO_4$ solution. Interdigital combs and probing pads are dry etched in an AlCu layer of about 0.5µm thick. Finally, absorbers of 1µm thick are defined by patterning a polyimide layer.

Contrary to time controlled etching process, this process allows having a well defined membrane with any geometry due to the silicon etch stop walls. Moreover, plugs are located at the edge of the membrane outside its sensitive part.

Some different fabrication processes are done and checked, and in this chapter, the better fabrication process is presented and described in Table 4.1.

Table 4.1   FABRICATION PROCESS

| | |
|---|---|
| | SOI substrate with superficial silicon 340nm thick and a buried $SiO_2$ layer of 2μm thick. |
| | 1- 2μm-wide trenches are etched through the superficial layers and $SiO_2$.<br>2- Remove resist. |
| | 3- Non selective epitaxy step takes place to fill the trenches and to increase the superficial silicon layer. |
| | 4- Counter mask lithography.<br> 5- Si etching 2 to 4μm thick<br>6- Remove resist. |
| | 7- CMP is realized to remove the grooves and to adjust the thickness on the silicon layer to the required membrane thickness. |
| | 8- Hole lithography.<br>9- Etch Si 2-4μm (through superficial Si layer to create holes of diameter 1.6 μm).<br>10- Remove resist |

| | |
|---|---|
|  | 11- The sacrificial layer SiO$_2$ is partially etched with wet HF. |
|  | 12- The sacrificial layer SiO$_2$ is completely etched by using vapor HF to avoid sticking problems of the membrane. |
|  | 13- Cavities are hermetically plugged under vacuum with a reflowed PSG deposition about 3µm thick. |
|  | 14- PSG lithography.<br>15- PSG is etched (firstly dry etched, and at the end, wet etched to have a smooth Si surface and better piezoelectric properties of the AlN<br>16- Remove resist. |
|  | 17- 200nm-thick thermal oxide is grown. |
|  | 18- AlN as the piezoelectric active material with the thickness between 1 and 3µm is deposited. Another configuration fabricated is using Mo layer below AlN. In this configuration, 260nm-thick Mo is deposited before AlN deposition.<br>19- Mask PIEZO lithography.<br>20- AlN layer is etched (H$_3$PO$_4$ - 130°C). |
|  | 21- AlCu metal layer (for IDT and probes) is deposited.<br>22- IDT lithography.<br>23- AlCu layer is dry etched.<br>24- Remove resist. |

| | 25- Polyimide absorber is deposited. |
| | 26- Absorber lithography. |
| | 27- Polyimide is etched. |
| | 28- Remove resist. |
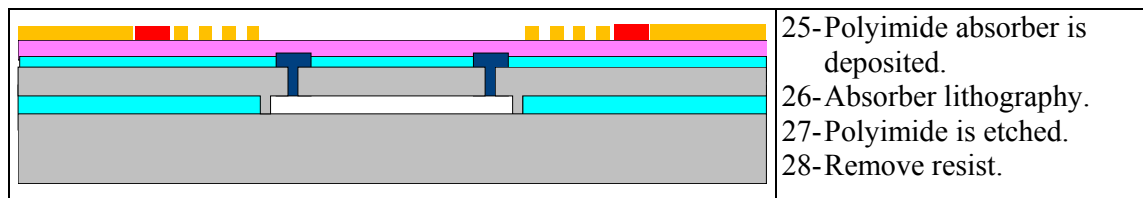
The final SAW devices are shown in Figure 4.1 and Figure 4.2, in which the thicknesses of AlN, AlCu, SiO$_2$ and polyimide have different values.
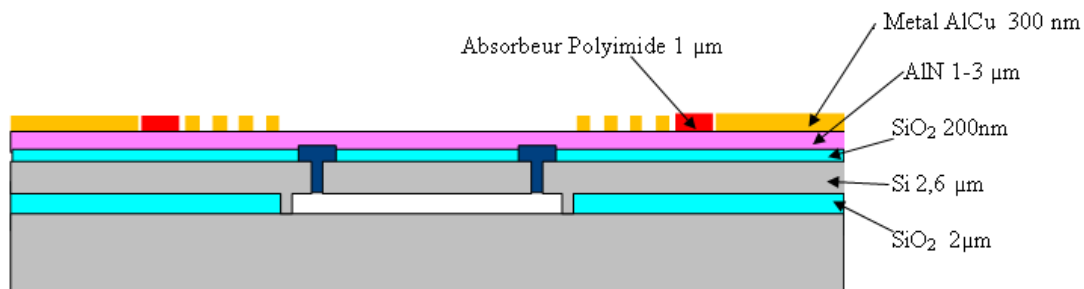


Figure 4.1   A configuration of SAW device
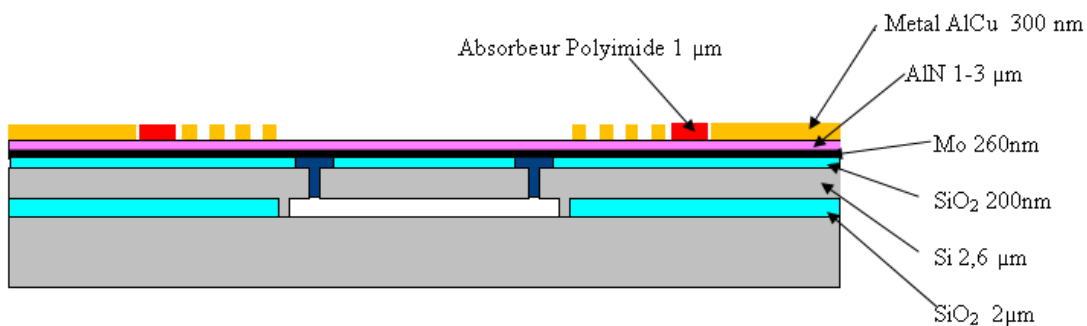


Figure 4.2   A configuration of SAW device with Mo layer

After each step, the devices are characterised to verify some requirements and consider whether the process can be continued or not. The devices were characterized morphologically by using optical, infrared microscopes, scanning electron microscope (SEM), optical interferometer and atomic force micrograph (AFM) equipments. These equipments and measurement conditions are presented in Appendix C.

## 4.2   MASKS DESIGNED

This section describes the general view of mask designed for every layer as stated above.

### 4.2.1   Trench, counter masque, hole, and PSG layers

Figure 4.3 presents the mask for 2μm wide Trench, 6μm wide counter mask (or contre masque), 1.6 μm in diameter Hole and 5.6 μm in diameter PSG layers.
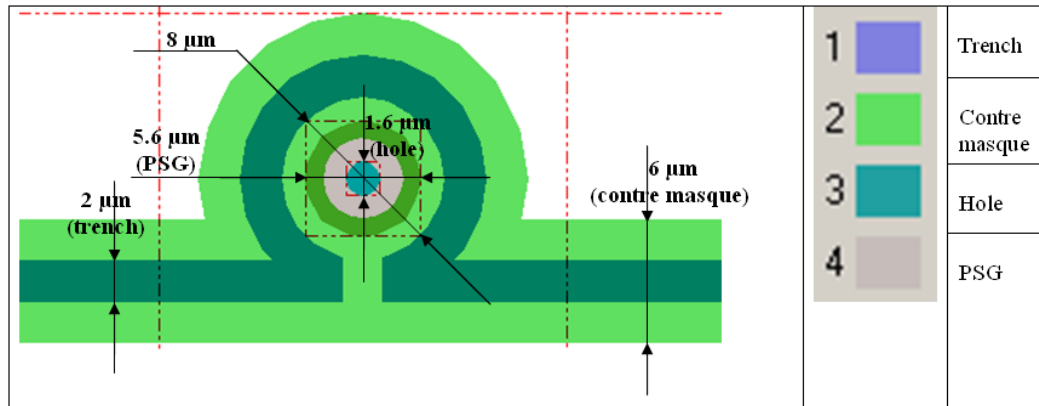
Figure 4.3   Masks for Trench, counter mask, hole, and PSG layers

### 4.2.2      Metal AlCu and polyimide layers

The general view for all of devices designed in one die and also their positions is shown as Figure 4.4. In this figure, devices are different in size of IDT, size of absorber, distances between IDTs, and different in number of section in IDT (see Table 4.2).
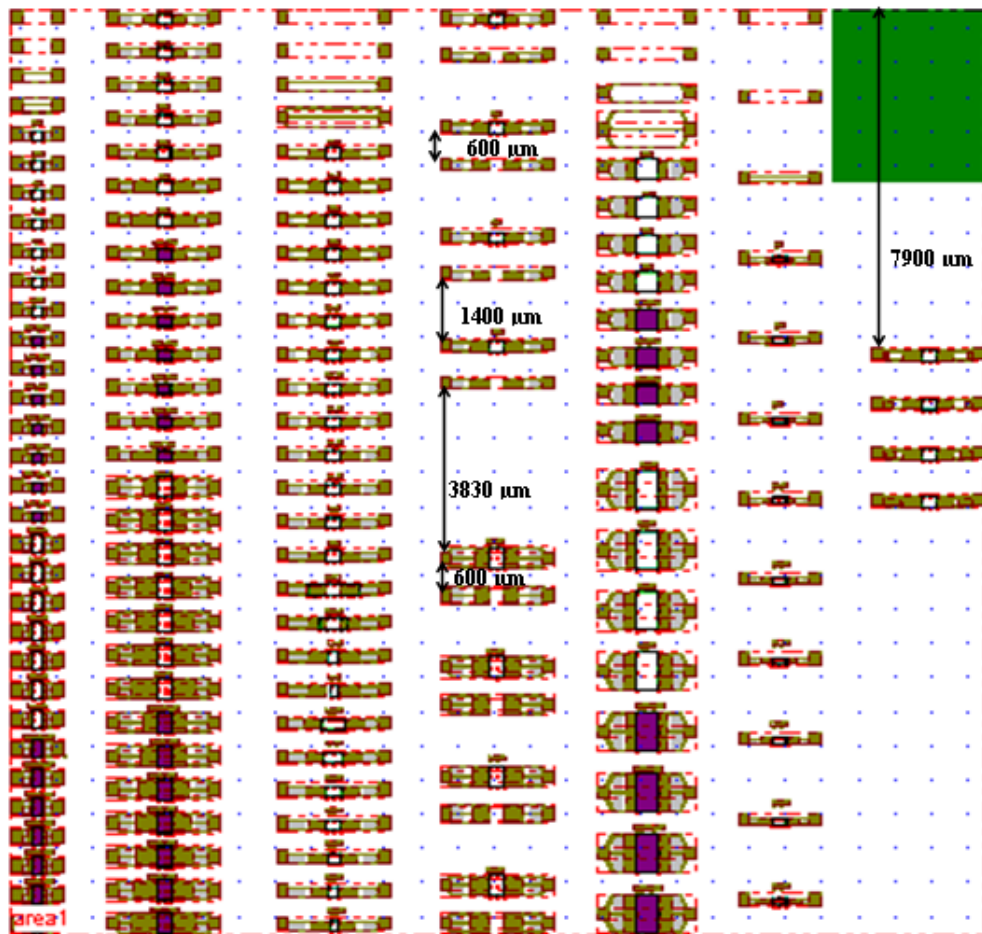


Figure 4.4   General view for all of devices in one die

The closer view for the devices is shown in Figure 4.5 with the dimensions summarized in Table 4.2.
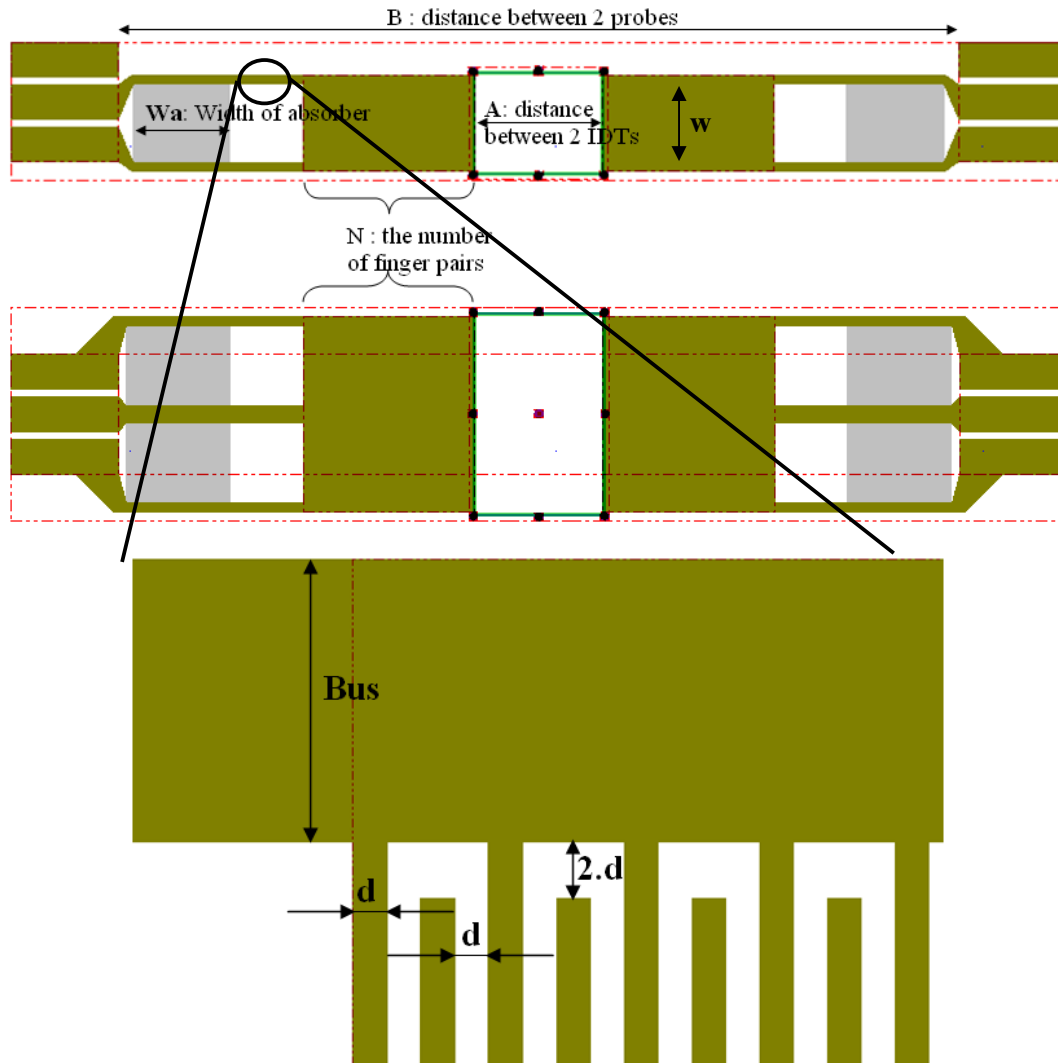


Figure 4.5   Description of devices

Table 4.2   THE DIMENSION OF DEVICES

| Device | | N | d (µm) | w (µm) | Bus (µm) | Wa (µm) | A (µm) |
|---|---|---|---|---|---|---|---|
| Device 4 | | 10, 14, 16, 18, 20, 22 | 1.4 | 154 | 5.6 | 80 | 200 |
| Device 5 | 5_colume 1 | 40, 45, 50, 55, 60, 65, 70 | 2 | 180 | 20 | 228 | 300 |
| | 5_colume 2 | | | | | | |
| | 5_colume 3 | | | | | | |
| Device 6 | | 18, 20, 22, 24 | 3 | 400 | 12 | 209 | 480 |
| Device 7 | | 14, 16, 18 | 2.4 | 100 | 9.6 | 70 | 300 |

## 4.3    CREATING THE STOP WALL OF ETCHING SiO₂- TRENCH

The top view of one trench design is shown in Figure 4.6.
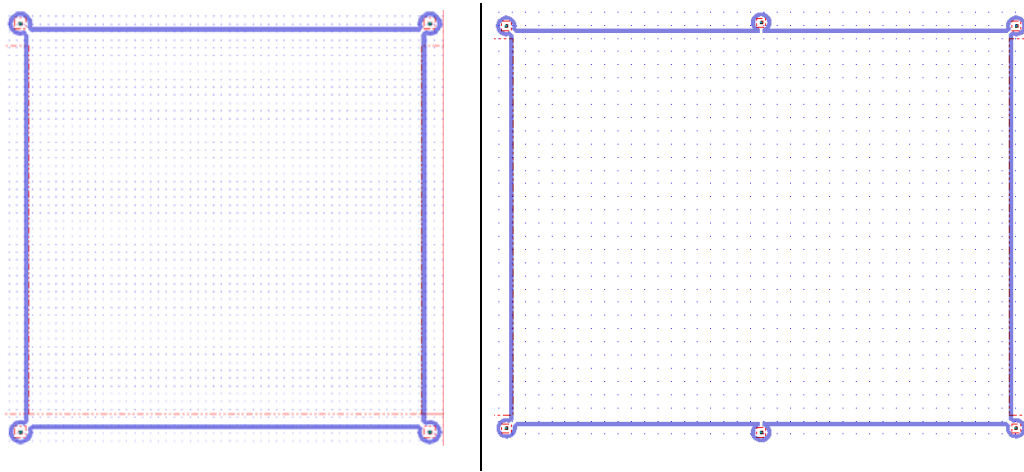


Figure 4.6   Top view of one trench designed

The expected 1.2 µm and 3 µm wide trenches are etched and characterized. Instead of obtaining a trench with purely vertical flanks, the trapezoid groove is created as in Figure 4.7. The measured values of a and b are presented in Table 4.3

Table 4.3   MEASURED VALUES OF TRAPEZOID GROOVE, A AND B

| Expected value of trench width | Position of the die under test | Measured values | |
|---|---|---|---|
| | | a (µm) | b (µm) |
| 3 µm | Near boundary of wafer | 2.375 | 3.167 |
| | Center of wafer | 2.312 | 3.156 |
| 1.2 µm | Near boundary of wafer | 0.771 | 1.354 |
| | Center of wafer | 0.719 | 1.375 |

Some SEM image of expected 1.2 µm and 3 µm trenches are shown in Figure 4.8 and Figure 4.9, respectively.
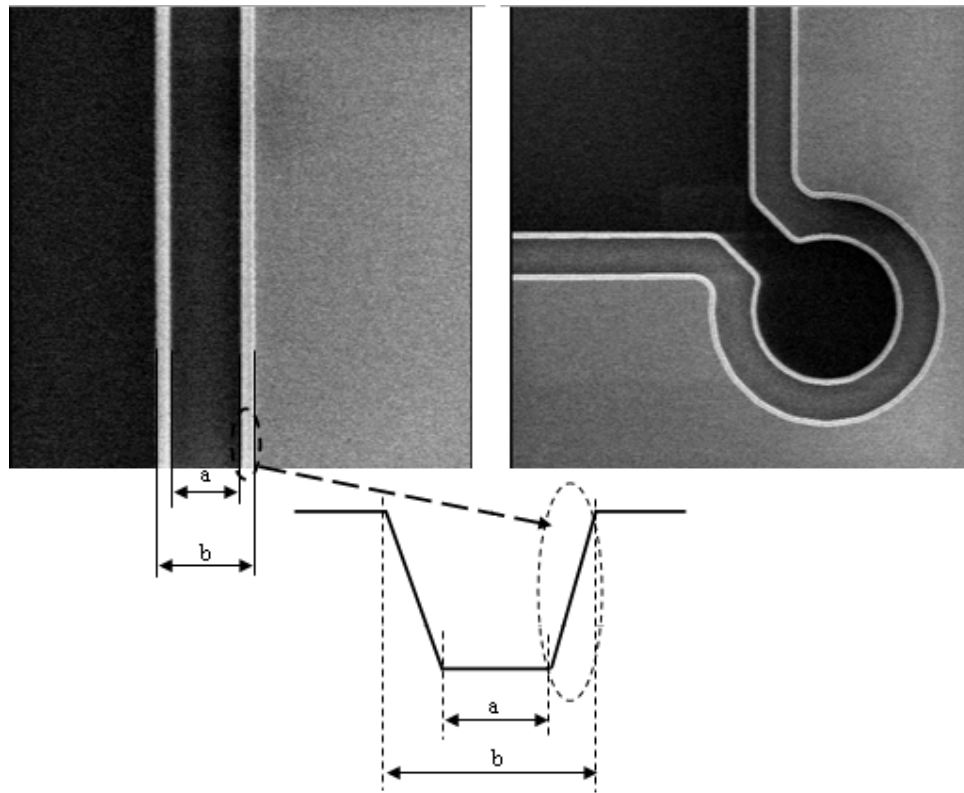
Figure 4.7   Trapezoid groove after etching trench
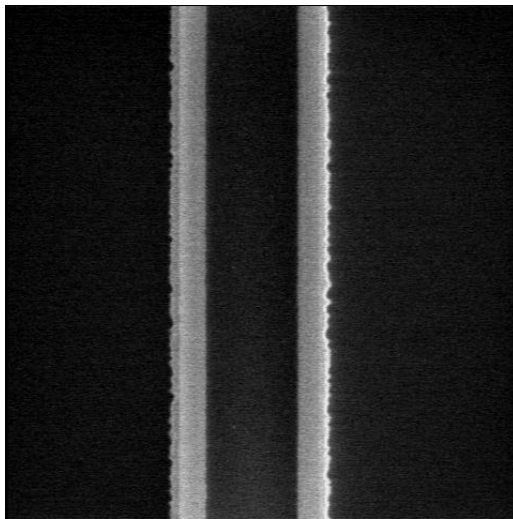


| Figure 4.8   Trench of expected 1.2µm width | Figure 4.9   Trench of expected 3µm width |
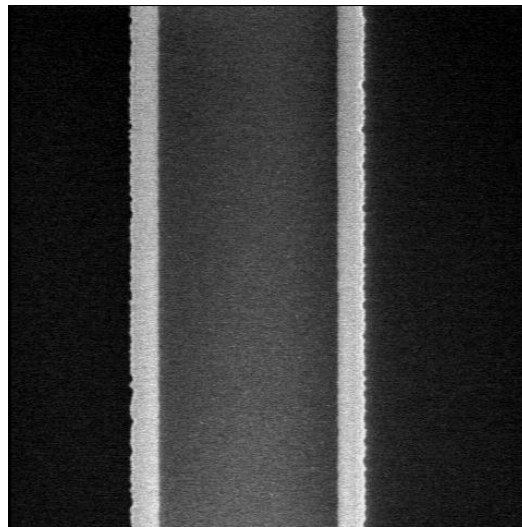
The perspective view of etching trench is shown in Figure 4.10
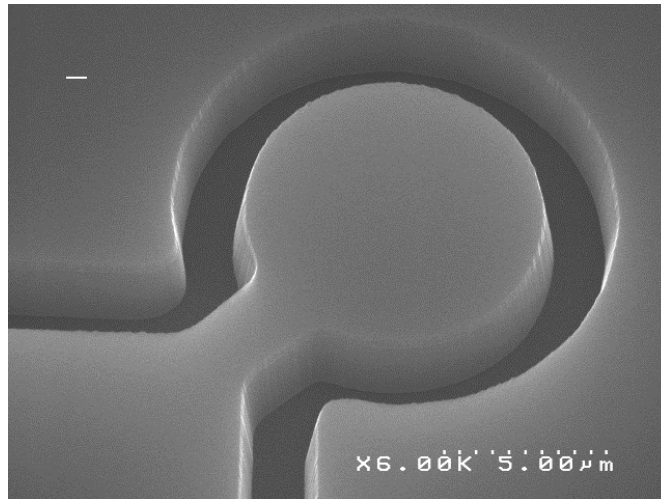
Figure 4.10   Perspective view of 2 µm wide trench

## 4.4   NON-SELECTIVE EPITAXY

After etching the trench, the non-selective epitaxy is used to fill the trench and to increase the thickness of superficial Si layer as shown in Figure 4.11.
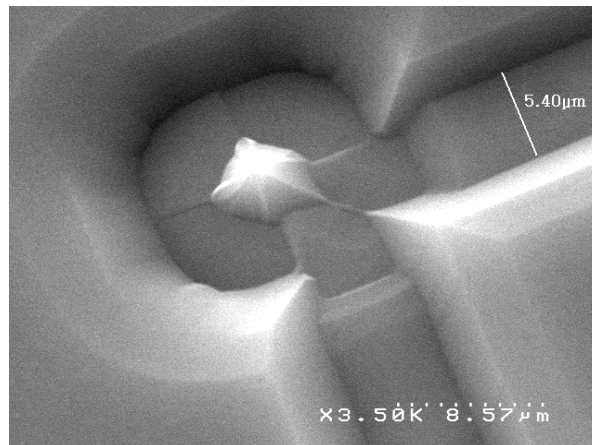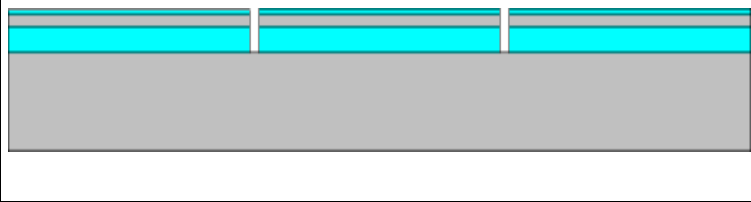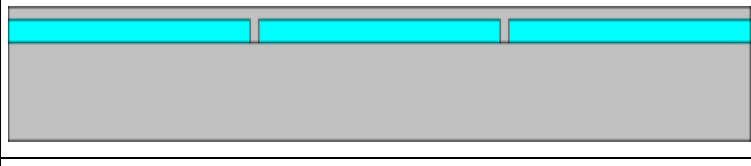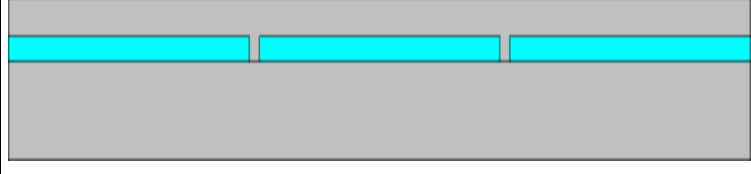


Figure 4.11   Perspective view after non-selective epitaxy

A question could be formulated: why the non-selective epitaxy is used to fill the trench? To answer to this probem, the non-selective and selective epitaxy was done, characterized and compared. To use the selective epitaxy, the fabrication process steps 1 to 7 are shown in Table 4.1, section 4.1, are replaced by the steps in Table 4.4.

Table 4.4   FABRICATION STEPS TO TEST SELECTIVE EPITAXY

| | |
|---|---|
| | 1b. 50nm-thick thermal oxide is grown. |
| | 2b. 2μm-wide trenches are etched through the superficial layers and SiO$_2$. <br> 3b. Remove resist. |
| | 4b. Selective epitaxy step takes place to fill the trenches. |
| | 5b. Remove the thermal oxide. |
| | 6b. Si epitaxy is done to increase the thickness of Si layer to the required membrane thickness. |

The difference between non-selective and selective epitaxy is performance of filling up the trench. This difference is viewed in different widths of trench, which are shown in Figure 4.12 to Figure 4.19. These figures present the slide view of trenches 1.2 μm, 2 μm, 3 μm and 4 μm wide after the non selective, selective epitaxy and CMP (Chemical and Mechanical Polishing) step for flattening the surface.
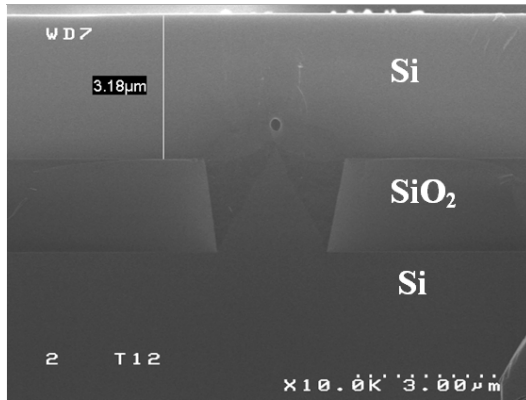
Figure 4.12　Slide view of 1.2μm wide trench, non selective epitaxy
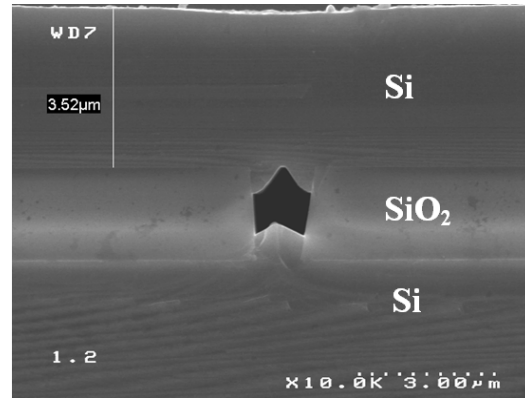


Figure 4.13　Slide view of 1.2μm wide trench, selective epitaxy
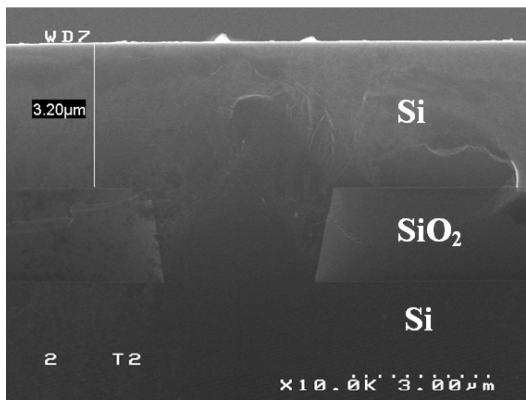


Figure 4.14　Slide view of 2μm wide trench, non selective epitaxy
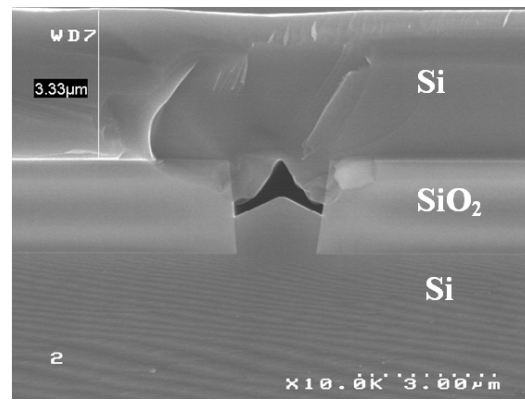


Figure 4.15　Slide view of 2μm wide trench, selective epitaxy
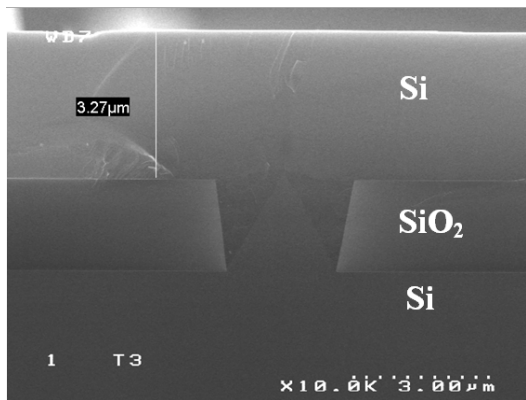


Figure 4.16　Slide view of 3μm wide trench, non selective epitaxy
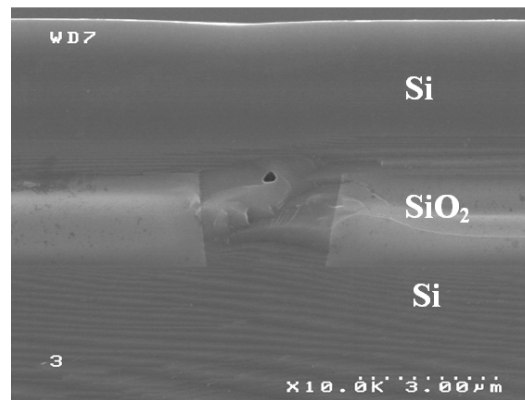


Figure 4.17　Slide view of 3μm wide trench, selective epitaxy
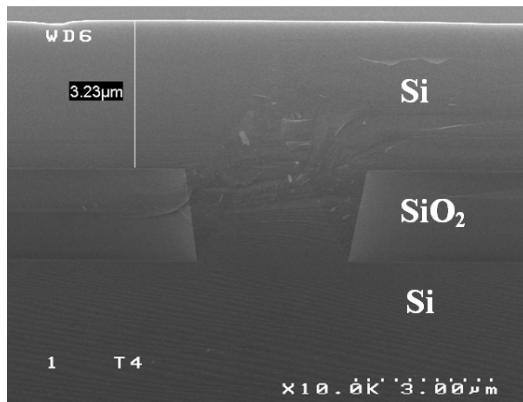
Figure 4.18    Slide view of 4µm wide trench, non selective epitaxy
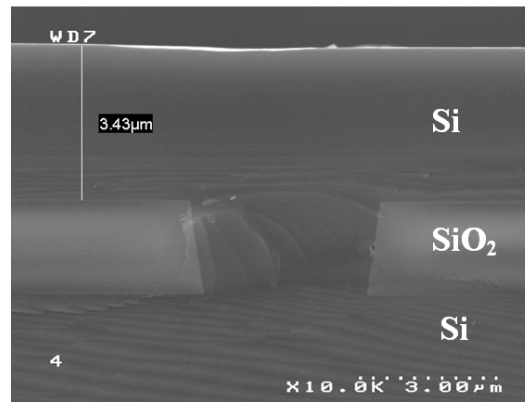


Figure 4.19    Slide view of 4µm wide trench, selective epitaxy

From these figures, the selective epitaxy cannot fill up completely the trench, especially in 1.2µm wide and 2µm wide trenches. Consequently, the purpose of Si wall to stop the HF etching sacrificial layer $SiO_2$, can not be obtained. In conclusion, the non-selective epitaxy is used and fabrication process is described in Table 4.1, section 4.1. The steps using selective epitaxy as in Table 4.4 are not used.

## 4.5    COUNTER MASK LITHOGRAPHY, ETCHING Si AND CMP PROCESS

After that, the etching process is done. Result is shown in Figure 4.20. Then, CMP is realized to remove the grooves and to adjust the thickness of the silicon layer to the required membrane thickness. Result is shown in Figure 4.21.
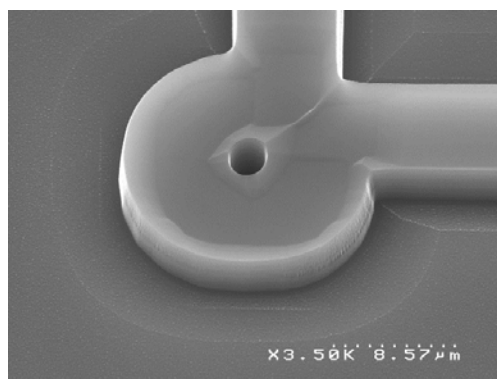


Figure 4.20   Etching is used to partially etch superficial Si layer
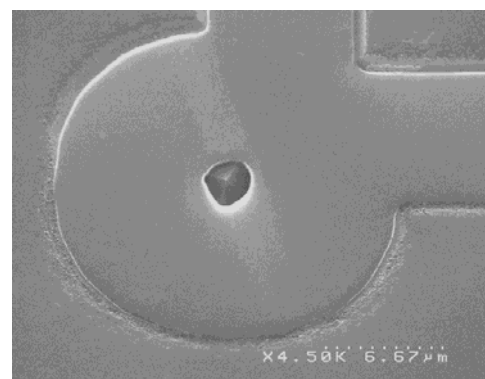


Figure 4.21   CMP is use to remove the groove and to adjust the required thickness of superficial Si layer

## 4.6   ETCHING HOLES

Holes are etched through the Si layer to access to the SiO$_2$ layer for the next step in which wet HF 49% and vapor HF are used to etch the SiO$_2$ sacrificial layer. The SEM image of one hole with expected 1.6µm in diameter is shown in Figure 4.22.
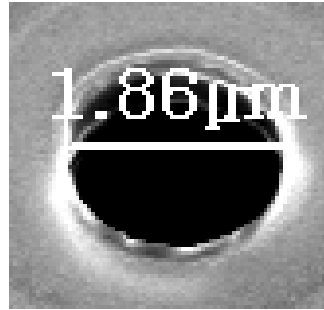


Figure 4.22   SEM image of a hole with expected 1.6µm in diameter

The holes and plugs are located outside the membrane (see Figure 4.23), so they do not affect the sensitive part of device. The number and the position of holes are dependent on the shape and dimension of membrane and also the etching speed of HF (see next section 4.7).
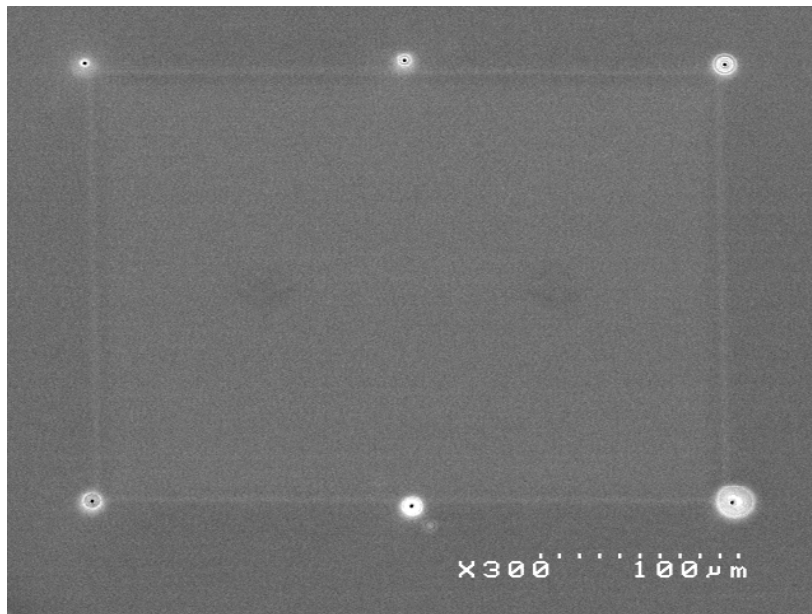


Figure 4.23   SEM image of trench and holes being outside the expected membrane

## 4.7 HF ETCHING OF THE SACRIFICIAL LAYER

The sacrificial layer is partially etched with wet HF and the complete release is performed using vapor HF to avoid sticking problems of the membrane.

To save time for the sacrificial layer etching step, firstly the etching speeds of wet HF and vapor HF are measured on wafers without trenches and with different hole diameters .(1.2µm, 2µm, 3µm, and 4µm). The wet etching is performed with HF 49% during 110 minutes and followed by etching with vapor HF during 20 hours. The results are shown in some SEM images as Figure 4.24 to Figure 4.31.
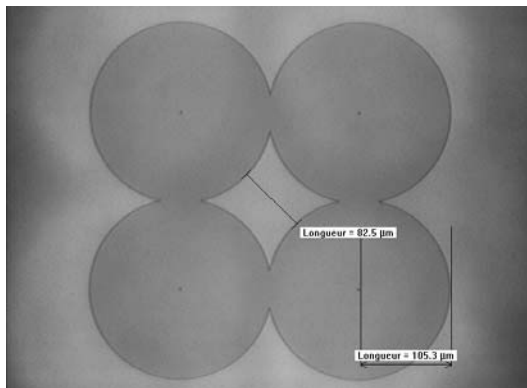


Figure 4.24   Wet HF 49% etching $SiO_2$ layer during 110 minutes throughout hole of 1.2µm in diameter
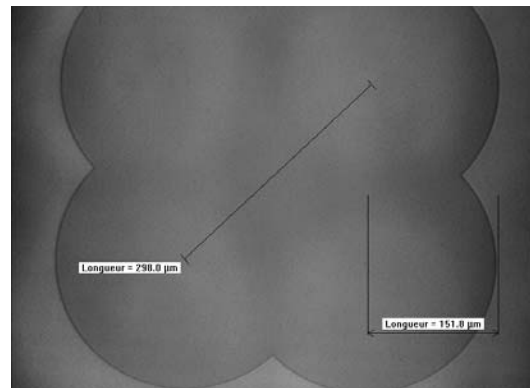


Figure 4.25   Vapor HF etching $SiO_2$ layer during 20 hours throughout hole of 1.2µm in diameter after wet HF etching
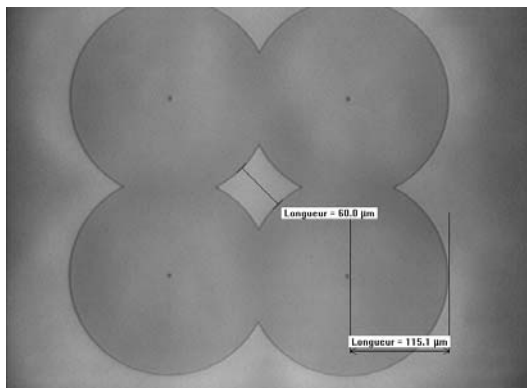


Figure 4.26   Wet HF 49% etching $SiO_2$ layer during 110 minutes throughout hole of 2µm in diameter
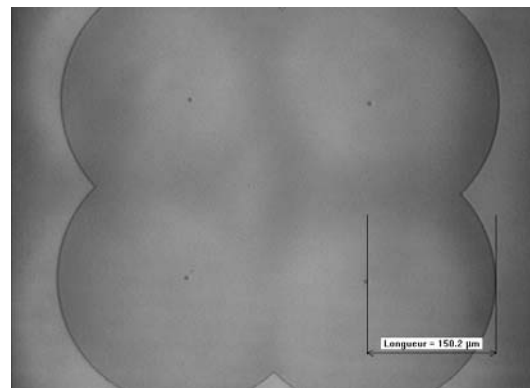


Figure 4.27   Vapor HF etching $SiO_2$ layer during 20 hours throughout hole of 2µm in diameter after wet HF etching

—
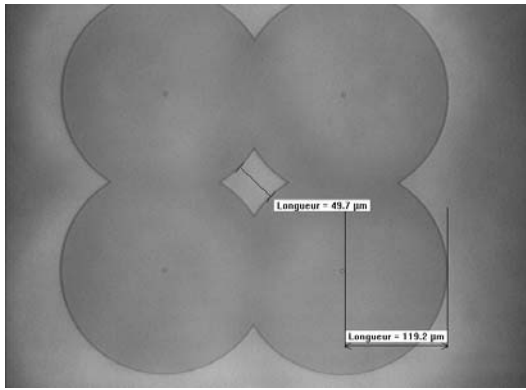
Figure 4.28   Wet HF 49% etching $SiO_2$ layer during 110 minutes throughout hole of 3µm in diameter
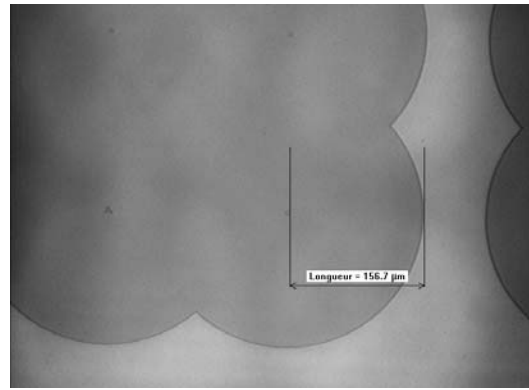


Figure 4.29   Vapor HF etching $SiO_2$ layer during 20 hours throughout hole of 3µm in diameter after wet HF etching
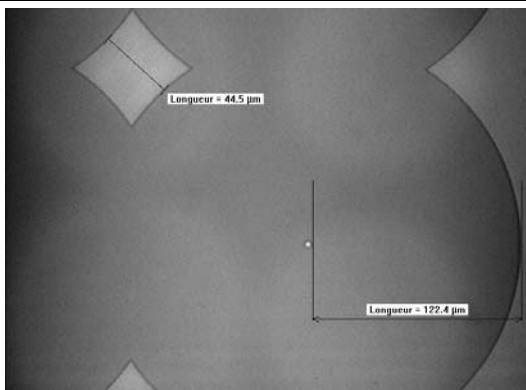


Figure 4.30   Wet HF 49% etching $SiO_2$ layer during 110 minutes throughout hole of 4µm in diameter
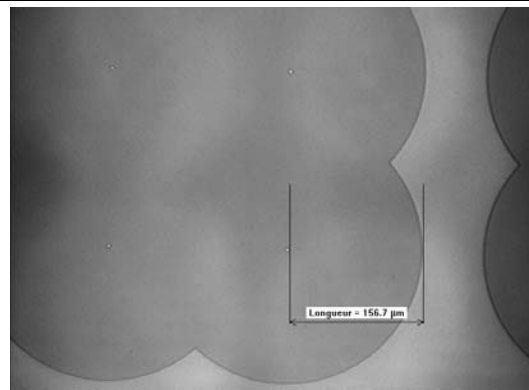


Figure 4.31   Vapor HF etching $SiO_2$ layer during 20 hours throughout hole of 4µm in diameter after wet HF etching

The etching speed of wet HF 49% and vapor HF are resumed in Table 4.5 which shows dependence of etching speed on the diameter of holes.

Table 4.5   SPEED OF ETCHING SACRIFICIAL LAYER $SiO_2$ BY WET HF 49% AND VAPOR HF ON THE WAFER WITHOUT TRENCHES ETCHED

| Diameter of the hole (µm) | 1,2 | 2 | 3 | 4 |
|---|---|---|---|---|
| Length etched by wet HF (µm) | 105 | 108-115 | 112 -120 | 122 -127 |
| Wet HF 49% speed (µm/minute) | 0.955 | 0.982-1.0455 | 1.0182-1.091 | 1.11-1.155 |
| Length etched by vapor HF (µm) | 43 | 42 | 45 | 44 |
| Vapor HF speed (µm/h) | 2.15 | 2.1 | 2.25 | 2.2 |

The wet etching speed is also obtained by testing the same procedure on wafers with etched trenches. Figure 4.32 to Figure 4.35 show the results after $SiO_2$ sacrificial layer etching with HF 49% during 110 minutes. The etching speeds are summarized in Table 4.6. We can see that the etching speed with the trenches etched is larger than one without etched trenches.

This may be derived from that in the case with etched trench, the wet HF concentrates on etching only in a quarter of space.
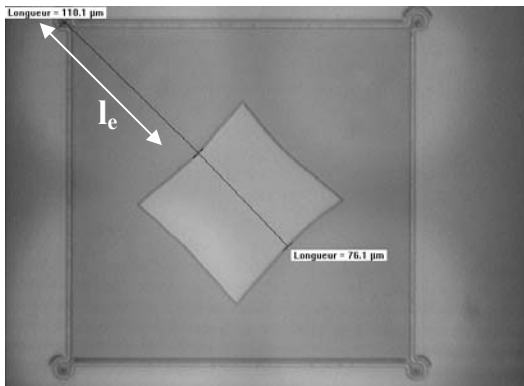


Figure 4.32   HF etching with 1.2µm-diameter hole during 110 minutes
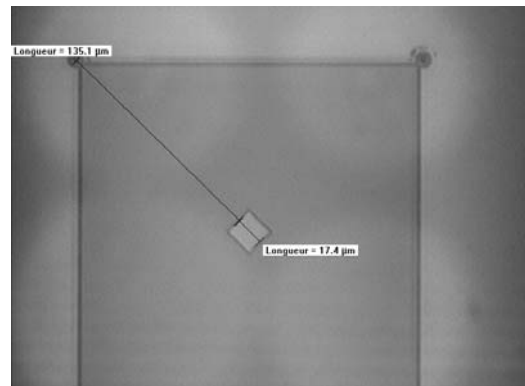


Figure 4.33   HF etching with 2µm-diameter hole during 110 minutes
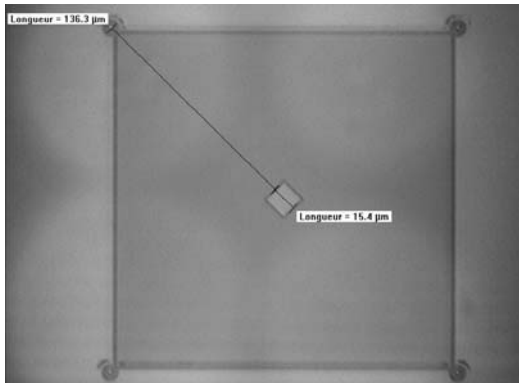


Figure 4.34   HF etching with 3µm-diameter hole during 110 minutes
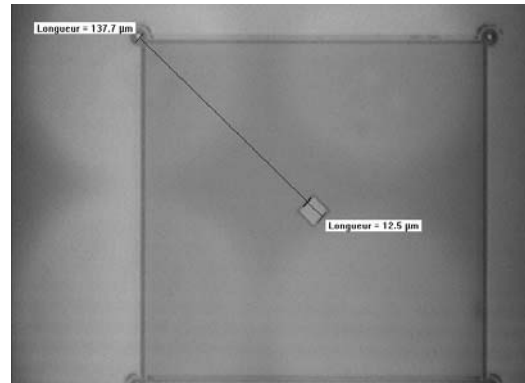


Figure 4.35   HF etching with 4µm-diameter hole during 110 minutes

After that, vapor HF is used to remove the rest of $SiO_2$ sacrificial layer in 20 hours. The membrane is now created completely as shown in Figure 4.36 to Figure 4.37.

Table 4.6   SPEED OF ETCHING SACRIFICIAL LAYER $SiO_2$ BY WET HF 49% ON THE WAFER WITH TRENCHES ETCHED

| Diameter of holes (µm) | 1,2 | 2 | 3 | 4 |
|---|---|---|---|---|
| Etching length $l_e$ (µm) | 110-124 | 134-137 | 136,5-138 | 137-139 |
| Etching speed of wet HF (µm/minute) | 1-1.127 | 1.218-1.245 | 1.241-1.255 | 1.246-1.264 |
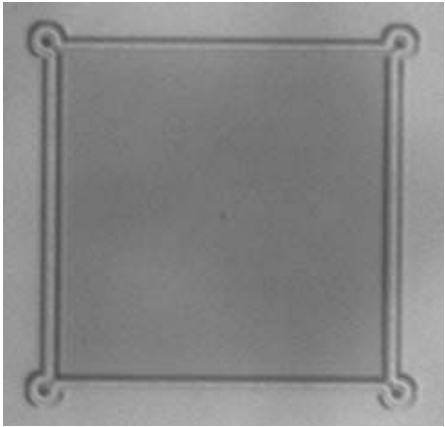
Figure 4.36   Top view of the membrane completed
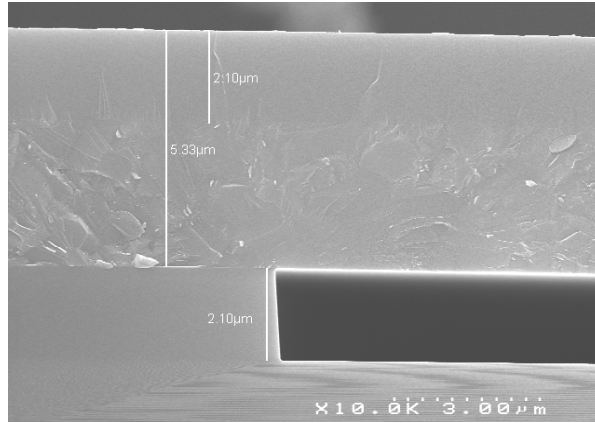


Figure 4.37   SEM image of the membrane

## 4.8     PSG (PHOSPHO SILICATE GLASS)

Cavities are hermetically plugged under vacuum with PSG deposition of about 3µm thick. PSG is deposited (Figure 4.38), etched (Figure 4.39) and annealed at $950^0$C during 1 hour and at $1030^0$C during 5 hours to create the plug as shown in Figure 4.40- Figure 4.41.
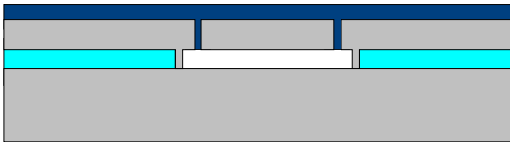


Figure 4.38   Depositing PSG
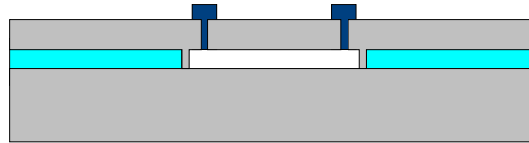


Figure 4.39   Etching PSG
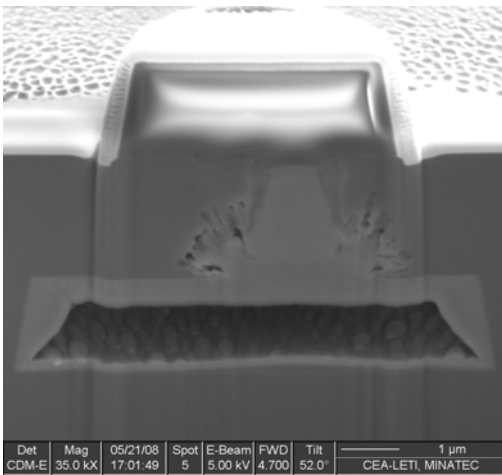


Figure 4.40   SEM slide view 1 of PSG plug
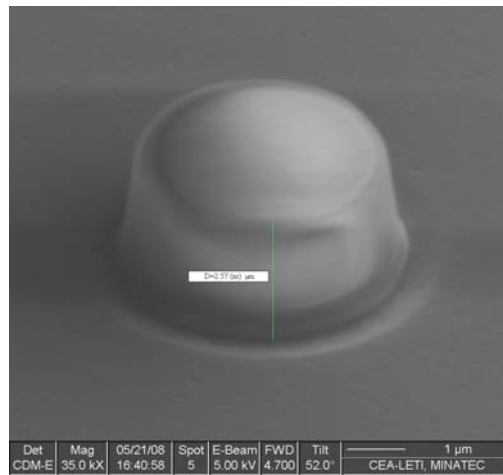


Figure 4.41   SEM image of a PSG plug

## 4.9 DEPOSITING AlN AS THE PIEZOELECTRIC LAYER AND ITS PROPERTIES

AlN films were deposited by reactive DC pulsed sputtering, equipment ∑Sigma fxP. The sputtered films for this research are typically between 0.5µm and 4µm. The deposition of AlN film was done according to the parameters shown in Table 4.7.

Table 4.7   PARAMETERS USED FOR DEPOSITION OF AlN

| Sputtering gas | Argon, N2 |
|---|---|
| DC power | 2 kW – 8 kW |
| Bias power | 80 W |
| Deposition temperature | 350 $^0$C |
| Stress | <100MPa, tensile |

The AlN is used as piezoelectric layer in SAW devices. It is important to characterize its piezoelectric. As stated in section 1.2.2, it is necessary to measure FWHM, although a narrow rocking curve around the (0002) AlN does not guarantee a good piezoelectric response. The crystalline orientation of AlN film is obtained by XRD.

### 4.9.1 Influence of substrate roughness on crytal quality of AlN

It is shown in literature that the texture of AlN films is strongly influenced by the roughness of the substrate material [137], [138]. To characterize this property, we prepared three different Si substrates whose measured roughnesses (rms) are 0.102nm, 1.920nm, and 7.103nm. The FWHM of AlN are measured and shown in Figure 4.42.
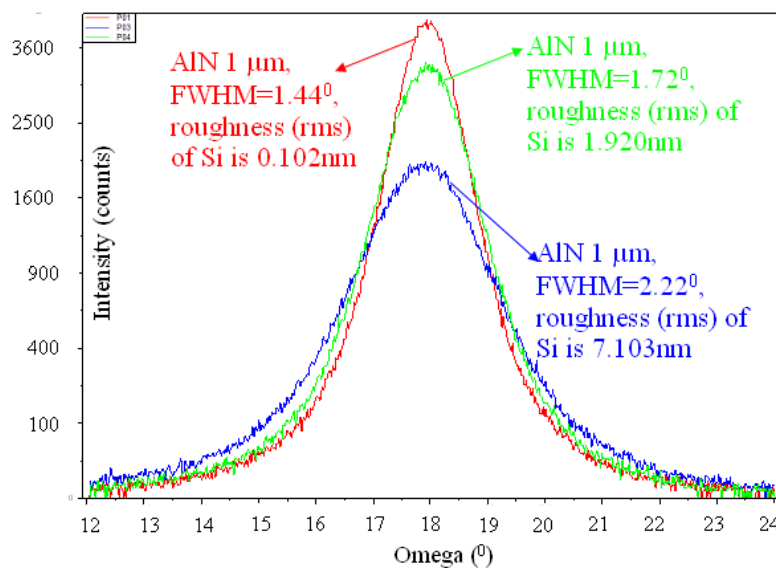


Figure 4.42   Influence of substrate roughness on crystal quality of AlN

As evident from Figure 4.42, the FWHM decreases with decreasing the roughness of substrate, it means the crystal quality of AlN is better. A good crystal quality could mean the narrow rocking curve. Consequently, to increase the crystal quality, therefore the piezoelectric property of AlN, the roughness of substrate must be decreased to be smaller than an acceptable value of roughness (rms). This value that used in our group is 0.2nm in roughness (rms). The requirement that substrate roughness is smaller than 0.2nm can be obtained by using CMP.

As the texture of AlN films is strongly influenced by the roughness of the substrate, in the three next sections (4.9.2, 4.9.3, and 4.9.4), to validate the results the samples are prepared to get the same roughness of substrate.

### 4.9.2        Dependence of FWHM of AlN on AlN thickness

The crystalline orientations of 1µm and 3µm AlN films that are deposited on a Si substrate and on a Mo layer are measured and shown in Figure 4.43.
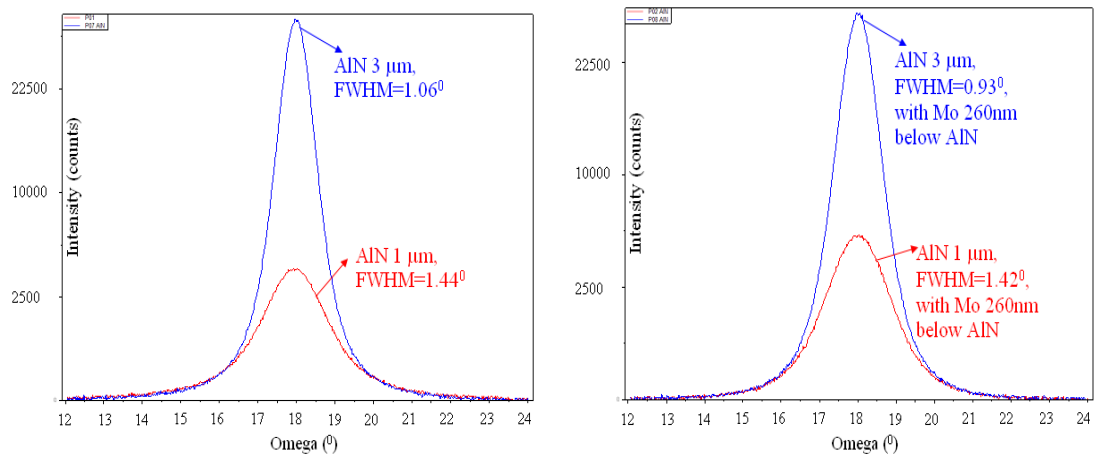


Figure 4.43   The FWHM of 1µm and 3µm AlN films, (a) without Mo layer below AlN, (b) with Mo layer below AlN

As apparent from Figure 4.43, the larger thickness of AlN is, the better crystal orientation is. These measurements were done in two cases, AlN/Si substrate and AlN/Mo/Si substrate.

### 4.9.3        Dependence of FWHM of AlN on using bottom Mo layer

The texture of AlN films is strongly influenced by the bottom metal electrodes [35]. In this research, using bottom Mo layer is proposed. The effect of using Mo on SAW device is characterized and presented in Chapter 5, section 5.3.4 . In this section, the effect of Mo on crystal quality of AlN is characterized.

As stated in section 4.9.1, to validate the influence of using Mo on crystal quality of AlN, CMP is required to get the same roughness of Si substrates in two cases, using Mo and not using Mo. In this section, roughness (rms) of Si substrate in the two cases is 0.102 nm. Case 1 is that the 1µm and 3µm AlN are deposited on Si substrate. Case 2 is that Mo deposited on Si substrate is followed by depositing 1µm and 3µm AlN. The FWHMs of AlN films are measured and shown in Figure 4.44.
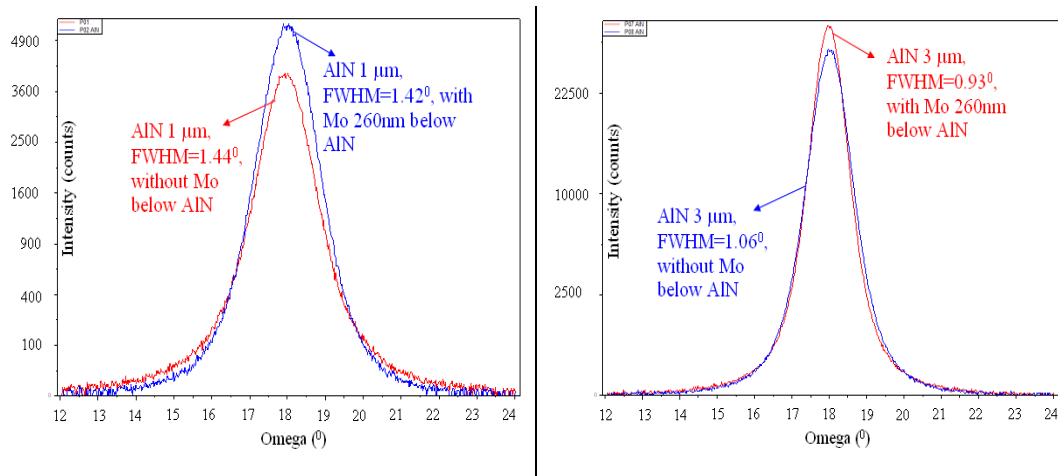


Figure 4.44   Effect of using bottom Mo on crystal quality of AlN, 1µm and 3µm

One conclusion that should be extracted from Figure 4.44 is that using bottom Mo layer could increase the crystal quality of AlN. From this point, the effect of using Mo layer on SAW device could be explained in section 5.3.4.

### 4.9.4      AlN at high temperature

As stated in 1.2, AlN could retain its properties at high temperature, up to $1000^0$C. To confirm this, FWHM measurements of AlN films are done before and after annealing AlN in high temperature. Four samples are prepared as (Table 4.8).

Table 4.8   STEPS TO CHARACTERISE ALN IN HIGH TEMPERATURE, FOUR SAPMPLES

| Sample | P01 | P02 | P03 | P04 |
|---|---|---|---|---|
| 1. Deposit Mo 260 nm | x | x | | |
| 2. Deposit AlN 1µm (1008 nm) | x | x | x | x |
| Measure FWHM of AlN **(measures 1)** | x | x | x | x |
| 3. Deposit PSG 2.9 µm (2919.2 nm) | x | x | x | x |
| Measure FWHM of AlN **(measures 2)** | x | x | x | x |
| 4. Anneal PSG in $N_2O_2$ at 950°C during 1h and at 1020°C during 5h. | x | x | x | x |
| Measure FWHM of AlN **(measures 3)** | x | x | x | x |

The FWHM measurements (measure 1, 2 and 3) of AlN for four samples are shown in Figure 4.45.
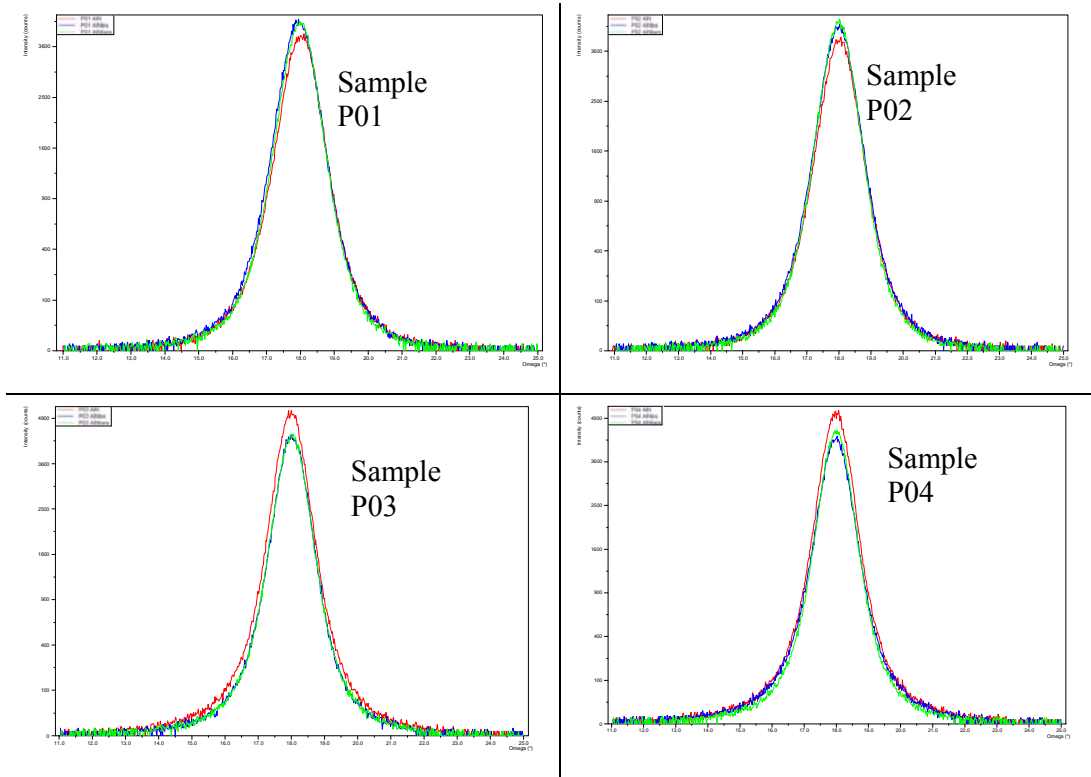


Figure 4.45   FWHM of AlN 1μm films for four samples. The red line is measure 1, the green line is measure 2, and the blue line is measure 3

For clarity, these measurements are summarized and compared in Figure 4.46.
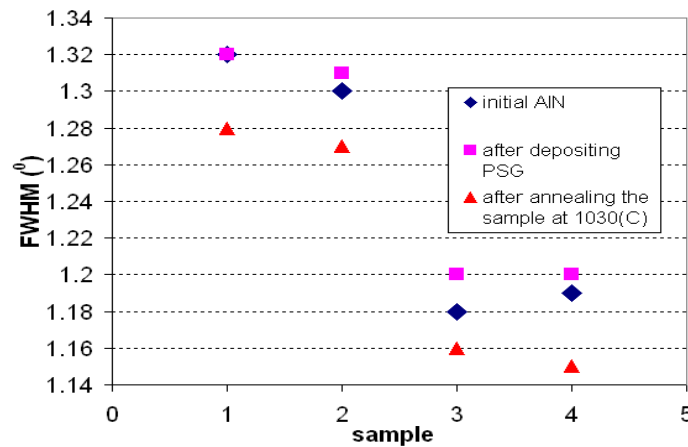


Figure 4.46   The FWHM comparison of 1μm AlN films in four samples

From these measurements in Figure 4.45 and Figure 4.46, an important property of AlN is that it could retain its properties after a high temperature process, up to $1000^0$C.

## 4.10   METAL LAYER AlCu FOR IDT AND PROBES

The AlCu metal layer (for IDT and probes) is deposited and dry etched to create IDT. The results are shown in Figure 4.47.
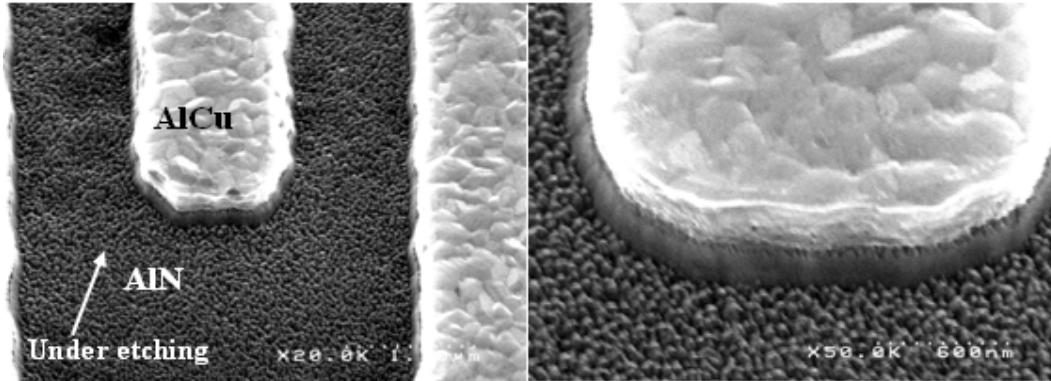


Figure 4.47   AlCu metal layer is created on the AlN layer

## 4.11   POLYIMIDE AS ABSORBER

In these SAW devices, the transmitting transducer launches the surface acoustic waves in opposite directions simultaneously while the receiving transducer receives the waves traveling in either direction. This is a critical issue in most SAW devices because in addition to responding to surface acoustic waves traveling directly from the transmitting to receiving transducer, the transducers respond to surface acoustic wave reflected from the ends of the substrate. These waves produce unwanted signals, for example, as spurious signal in the time domain, ripples of the frequency response domain that distort the main desired signal, so adversely affecting the performance of the SAW device [142]. Therefore, the edges of substrates are often provided with materials which absorb the surface acoustic wave.

There are two absorption mechanisms, resistive damping and viscous damping that are used for attenuation of surface acoustic waves [141].

In the resistive absorption mechanism, currents induced in the layer by the propagating wave are damped by the resistive loss, thereby producing attenuation of the wave. So, this technique is only strongly effective in substrates with a high piezoelectric coupling factor, not suitable for low coupling substrate. A highly resistive thin film of amorphous silicon deposited on the surface of $LiNbO_3$, has been used to attenuate surface acoustic wave [142], [143].

Viscous absorption is, however, more common due to the wide variety of materials and their ease of use. Viscous absorption is due to the viscosity of the absorption material. Absorption layers have to provide superior elongation properties and superior adhesion to the substrate material. Energy dissipation occurs when a particle of the substrate is resisted by a force that has a magnitude proportional to the velocity of the particle and a direction opposite to that of the particle velocity. It suppresses the wave energy by acting as a compliant layer to absorb mechanical stress during the surface wave propagation. Wax, Room Temperature Vulcanization (RTV) rubber, epoxy resin are viscous organic materials used extensively to absorb the acoustic wave. Disadvantages of these materials, however, include incompatibility with high temperature sealing and difficulty in accurately patterning them. A very useful material is polyimide that does not suffer from these limitations.

Polyimide is a viscous organic material which maintains its absorptive acoustic properties after curing [139], [140]. Polyimide films are patternable on wafers with high accuracy, they do not degrade in the high temperature sealing of packages and have good adhesion on substrate. With SAW device using $LiNbO_3$, the attenuation of 3.0 to 3.5 μm thick polyimide films was measured to be in the range of 10-20dB/100μm at frequencies in the range of 300 MHz-500 MHz [139]. Generally, the attenuation rate of absorber is proportional to the length and the thickness of the absorber film. So, because of the limitation of the device size, to increase the attenuation rate of the reflected wave, the thickness of the absorber film must be increased. Ref [140] showed the attenuation rate of 14 μm, 20 μm thick polyimide films, while ref [139] presented the rate of 3.0-3.5 μm thick polyimide films.

The polyimide used in this work is PI-2610 in PI-2600 series-Low Stress Polyimides [144]. PI-2600 Series products are supplied as polyamic acid precursors dissolved in an N-methyl-2-pyrrolidone (NMP) based solvent carrier suitable for spin coating applications (solution properties of PI-2610 are shown in Table 4.9). These polyimides can be coated and patterned over a variety of substrates and metal surfaces such as silicon, silicon nitride, polyimide, aluminum or chrome/copper. After application, the polyacid precursor is thermally cured into a fully aromatic polyimide film.

PI-series polyimide solutions are highly viscous due to their high molecular weight. To dispense the polyimide, it is important to assure that the polyimide is dispensed in the exact center of the wafer. Acceleration to final spin speed should be as slow as possible to allow the polyimide to flow across the substrate. Often one or more intermediate spin speeds can be used to allow the polyimide to gradually cover more than 80% of the substrate before

continuing on to the final spin speed. The final spin speed and spin time is determined by the film thickness required as Figure 4.48.

Table 4.9   SOLUTION PROPERTIES OF PI-2610

| Test | Units | PI-2610 |
|---|---|---|
| Solids | % | 10.5 ± 1 |
| Viscosity | Poise | 25-30 |
| Chloride Content | Maximum ppm | 5 |
| Sodium or Iron Content | Maximum ppm | 1.0 |
| Potassium or Copper Content | Maximum ppm | 0.5 |
| Total Metals | Maximum ppm | 10 |
| Ash | Maximum % | 0.10 |
| Density | g/cm$^3$ | 1.064 ± 0.013 |
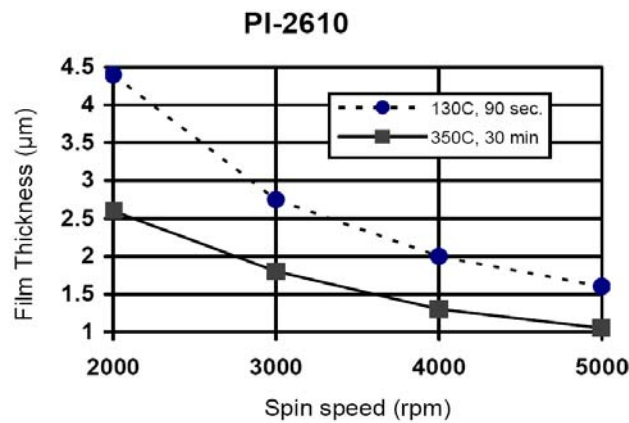
Figure 4.48   Spin speed curve (coated for 30 seconds at indicated speed)

At the end of the fabrication process, the devices with different dimensions are obtained as in Figure 4.49.
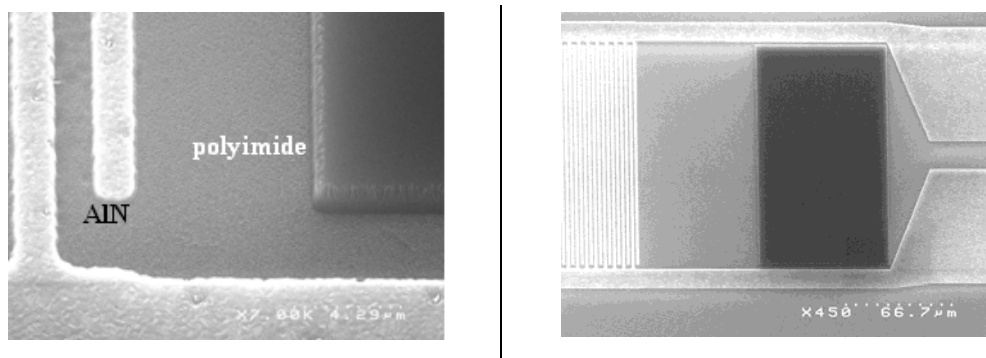
Figure 4.49   SEM images of polyimide on AlN

## 4.12 CONCLUSION

+ Fabrication process using surface micromachining is proposed and done successfully. This kind of fabrication process could create exactly the dimensions of membrane used in pressure sensor and it also allows having a well defined membrane with any geometry due to the silicon etch stop wall.

+ As the stress problem in layer at the end of fabrication, the fabricated membrane could be bended and stick the Si substrate. The stress control should be concerned to avoid this problem.

In our work, SOI substrate with buried $SiO_2$ layer of 2µm thick is used. There were some wafers that have the sticking problem of membrane due to stress and due to small thickness of $SiO_2$. To avoid this problem, the SOI substrate with large thick buried $SiO_2$ is proposed. Also, using this kind of SOI substrate could increase the pressure operation range of SAW pressure sensor.

+ AlN could retain its properties after high temperature process, up to $1000^0C$.

+ To increase the piezoelectric response of AlN, there are three ways that can be done:

    a. Using the bottom Mo layer.

    b. Decrease the roughness of the layer below AlN layer until be smaller than 0.2nm. This requirement can be obtained by using CMP.

    c. Increase the thickness of AlN. However, it is not possible to deposit any thickness of AlN due to stress in AlN. The maximum thickness of AlN could be fabricated is 5µm.

# Chapter 5

# CHARACTERIZATION OF SAW DEVICE

This chapter is divided into three sections.

Section 5.1 presents the parametric tests and procedure to check the device fabrication and the layer properties such as square resistance, under etching, isolation, continuity. These tests and procedures allow a fast process control of the deposited/etched layers during the fabrication, and also a fast characterization of all dies on the wafer.

The experimental setup is given in section 5.2.

Last but not least, section 5.3 presents experimental results and also the explanations and analyses of obtained results.

During fabrication, three batches for electric purposes were processed. These are correspondent to 50 wafers and at least 110.000 devices. During characterization, about 2.000 devices were tested on 18 wafers.

## 5.1 PARAMETRIC TESTS

The parametric tests are used in research and industry to make a fast process control of the deposited/etched layers during the fabrication. These are electrical tests and come as an added value to the well known optical tests. They allow controlling process stability over time. In general the needed patterns for the parametric tests are implemented in the fabrication mask and they are photo-repeated all over the wafer in order to get information on the layers on the whole wafer area.

This section presents the patterns designed in the mask used to measure the square resistance, under etching, isolation and continuity of the metal layer.

### 5.1.1     The Square Resistance: Van Der Pauw
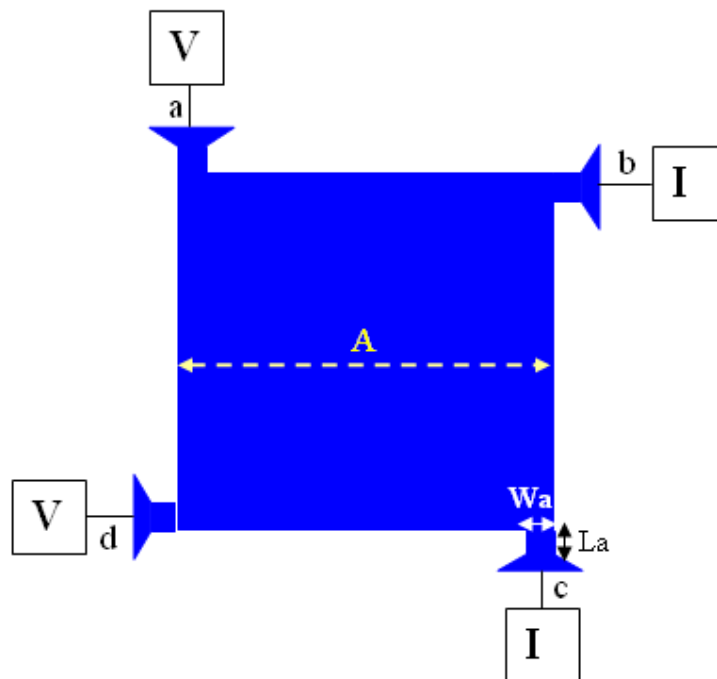


Figure 5.1   The pattern to measure the square resistance, Van Der Pauw method

The pattern to measure the square resistance based on Van Der Pauw method is presented in Figure 5.1, in which V is direct voltage and I the direct current applied for measurement. The goal of this pattern consists in measuring the square resistance (Rs) of one conductive layer based on Van Der Pauw method. This method was first propounded by L.J.Van Der Pauw in 1958 [150], [151]. It is a commonly used technique to measure the square resistance of a material. The Van der Pauw method is often used to measure the Hall effect, which characterises a sample of  semiconductor material and can be successfully completed with a current source, a voltmeter and a magnet. From measurements, some properties of the material can be calculated such as the square resistance, the doping type material, the density of the semiconductor (the doping level), the mobility of the majority carrier.

The square resistance can be express by the formula of Van Der Pauw as follows:

$$R_S = \frac{\pi}{\ln 2} R \text{ where } R = \frac{V}{I} \qquad\qquad \text{eq.(5. 1)}$$

Where V is voltage on two ports a and b, I is measured between two ports c and d.

The pattern design is: an area A= 100μm², for access lines Wa=La=10μm.

To refine the results and in particular away from the disturbances caused by the method of etching, the resistances can be measured by making a circular permutation as follows:

$$R_S = \frac{\pi}{\ln 2} \left( \frac{R + R'}{2} \right) \text{ where } R_{ab,cd} = \frac{V_{cd}}{I_{ab}}; R'_{bc,da} = \frac{V'_{da}}{I'_{bc}}$$

eq.(5. 2)

### 5.1.2      Isolation and continuity

The SAW devices include IDT with a lot of electrodes (hundreds or even thousands of electrodes), in which electrodes width can be small up to 1.2μm in this study. It is difficult to know the continuity of the metal layer AlCu creating IDT by visual inspection, but it is very easy to check it electrically.

The pattern "two in one" as in Figure 5.2 allows measuring the isolation and continuity of the metal layer.
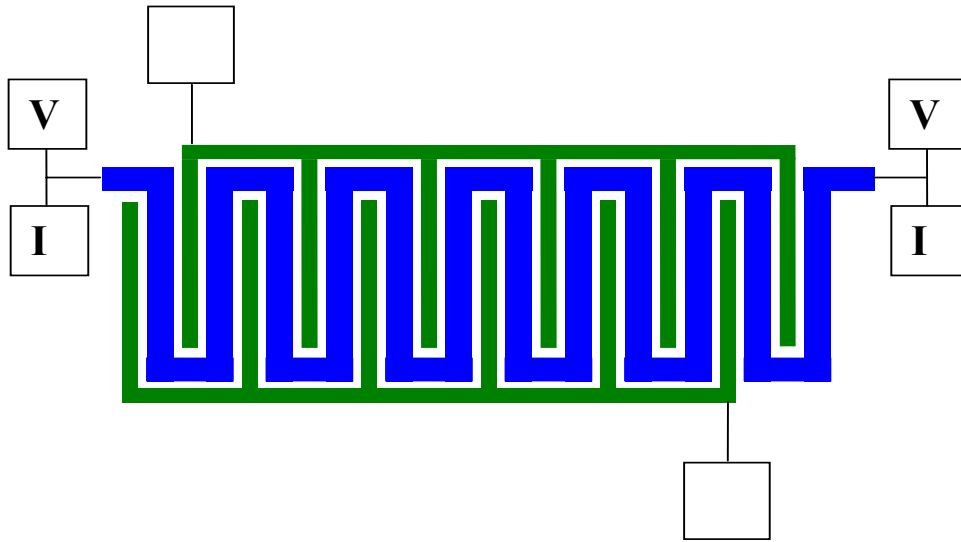


Figure 5.2   The pattern for checking the isolation and continuity

The coil pattern (the blue line in Figure 5.2) is used to measure the continuity of the metal layer. The theoretical resistance of the coil can be measured from the value of the square resistance Van Der Pauw in section 5.1.1.

$$R_{C(th)} = R_{S(VdP)} \frac{L}{W}$$

eq.(5. 3)

Where L is the length of blue line, and W is the width of the blue line.

The measurement is valid when the requirement as follows is respected:

$$0.1 \; R_{C(th)} < R_{measured} < 10 \; R_{C(th)} \qquad \text{eq.(5. 4)}$$

Measuring resistance between the blue and green lines (as in Figure 5.2) allows verifying the isolation of metal layer.

### 5.1.3 Measuring under etching
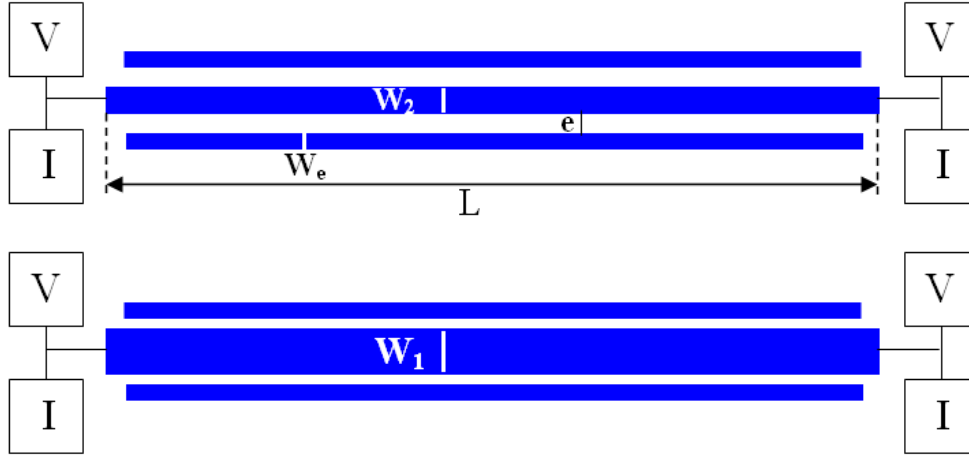


Figure 5.3   The pattern to measure under etching

The pattern as in Figure 5.3 allows us to measure under etching $\Delta W$ that is the difference value between values of expected width and fabricated width for center conductor.

The measuring principle is simple, it consists in measuring the resistance of two lines that have the same length and different width $W_1$ and $W_2$.

Line 1: the initial width (design width) is $W_1$, after etching, the final width is $(W_1 - \Delta W)$ and the resistance is $R_1$.

Line 2: the initial width (design width) is $W_2$, after etching, the final width is $(W_2 - \Delta W)$ and the resistance is $R_2$.

It is assumed that the width variation is the same for the two lines and is independent of the line width. $R_1$ and $R_2$ can be expressed as follows:

$$\begin{aligned} R_1 &= \frac{\rho L}{e(W_1 - \Delta W)} \\ R_2 &= \frac{\rho L}{e(W_2 - \Delta W)} \end{aligned} \qquad \text{eq.(5. 5)}$$

Consequently, the relation is obtained:

$$R_1(W_1 - \Delta W) = R_2(W_2 - \Delta W)$$
$$\Delta W = \frac{W_2 R_2 - W_1 R_1}{R_2 - R_1}$$

eq.(5. 6)

Design rules should be taken into account as follows:

$+ \dfrac{W_1}{W_2} \geq 1.5$

+ The line width can be changed dependently on the thickness of the metal layer or the etching type-chemical or plasma ($W_{min} > 10$ μm).

$+ \dfrac{L}{W} \geq 40$ condition should be obtained to validate the measurement.

+ The line resistance must be larger than 1Ω to insure the precision of this measurement.

+ Minimum 6 contacts are required for this pattern.

Proposed values are designed as follows:

L=600 μm, $W_1$=20μm , $W_2$= 10μm, $W_e$=e=5μm.

### 5.1.4     Mask for parametric test

From the patterns as described above, the patterns as in Figure 5.4 and Figure 5.5 are designed to check the continuity, the isolation, the resistance and under etching of the metal layer.
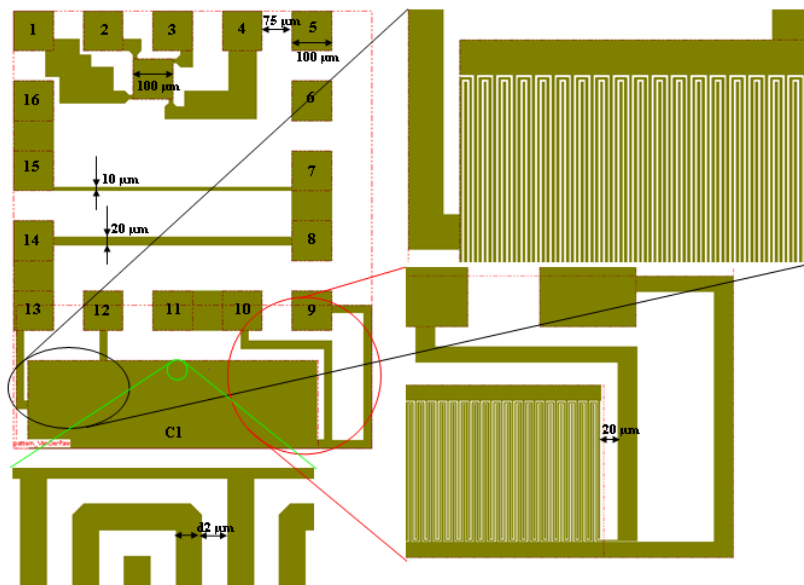


Figure 5.4   The mask 1 designed for parametric test: square resistance, isolation, continuity, under etching
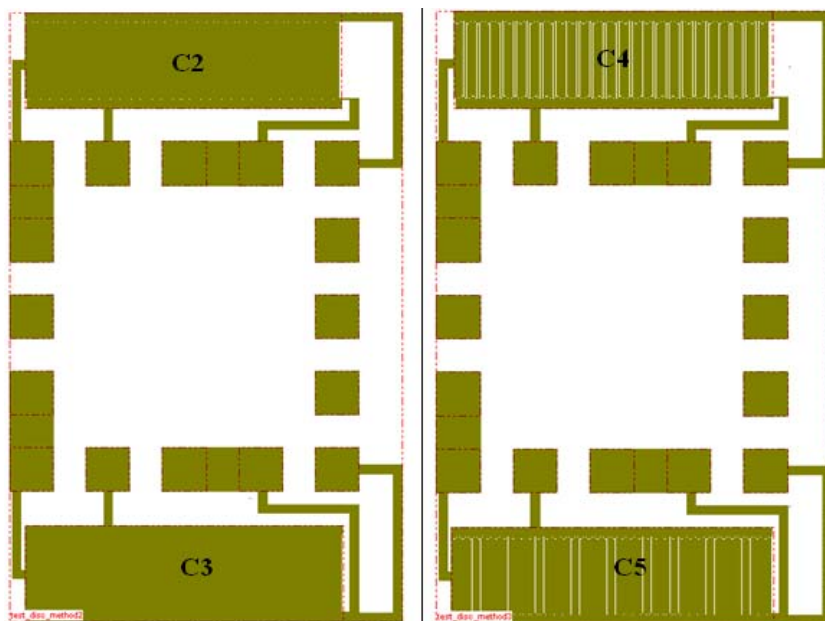
Figure 5.5   The mask 2 designed for parametric test: isolation, continuity

Table 5.1 describes the pin and the values of designed mask used for parametric tests including square resistance, isolation, continuity, and under etching.

Table 5.1   DESCRIPTION OF MASK 1 FOR PARAMETRIC TESTS: SQUARE RESISTANCE, ISOLATION, CONTINUITY, UNDER ETCHING

| Purpose of measuring | Pin | Value |
|---|---|---|
| Square resistance Van Der Pauw | 1,2,3,4 | A=100μm, Wa=La=10μm |
| Under etching | 7,8,13,14,15,16 | $W_1$=20μm, $W_2$=10μm |
| Continuity of the coil | 10,11,13,14 | Width $d_2$ (see Table 5.2) |
| Comb for isolation | 9,12 | Width $d_2$ (see Table 5.2) |

The values A, $W_a$, $L_a$, $W_1$, $W_2$ used in Table 5.1 are proposed to measure the square resistance, under etching.

The value d2 (μm) in Table 5.2 is also the value of IDT width of SAW device fabricated. With the fabrication technology used in this research, the minimum width of IDT is 1.2 μm. For the devices under test, the IDT width is 2 μm. Other values are used in these mask just for checking the isolation and continuity of deposition technology of metal layer.

Table 5.2   THE VALUE OF THE FINGER WIDTH IN MASK 1, MASK 2 (Figure 5.4- Figure 5.5)

| Field | C1 | C2 | C3 | C4 | C5 |
|---|---|---|---|---|---|
| d2 (μm) | 1.4 | 2 | 1.4 | 3 | 2.4 |
| Pins for verifying continuity | 10 and 13 | 1 and 4 | 10 and 13 | 1 and 4 | 10 and 13 |

### 5.1.5      Parametric characterization

The parametric tests are automatically performed using a prober computer controlled which allows a fast characterization of all dies on the wafer. The position of the parametric tests on a 200mm-wafer are shown in Figure 5.6.
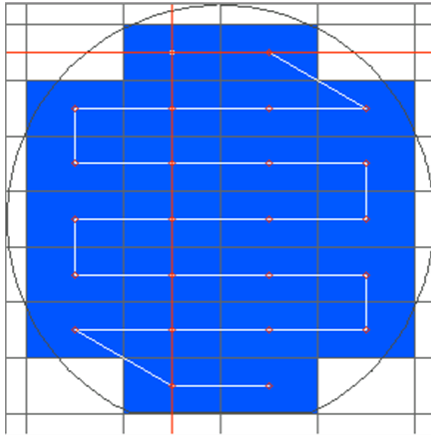


Figure 5.6   Dies position on 200mm-wafer

The continuity, the isolation, the resistance and the under etching of the metal layer are characterized and shown as the color map to get a visual map of the wafer under test. The color of each die is dependent on the value of resistance. The color map of resistance could be defined. For instance, to check the isolation between two metal lines, well-isolated metal lines is defined as the resistance is larger than 100 MΩ. For example, Figure 5.7 and Figure 5.8 show the results of isolation and resistance continuity characterization of a well-fabricated wafer in which all of dies are almost the same values. Figure 5.9 and Figure 5.10 show these results of other wafers. In Figure 5.9, in one die, the resistance between two metal lines was measured as smaller than 10 MΩ. This die could be considered as not isolated. Figure 5.10 shows the color map of resistance measured between two ends of one metal line in every dies on a wafer. With the color map in this figure, it would be easily considered that all of dies on this wafer are not the same in term of continuity. Consequently, color map of parametric characterization would be useful to locate and choose the good dies and the good devices.
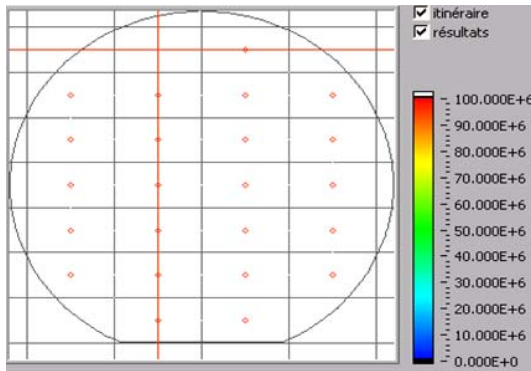
Figure 5.7   Color map of isolation between pin 9 and pin 10
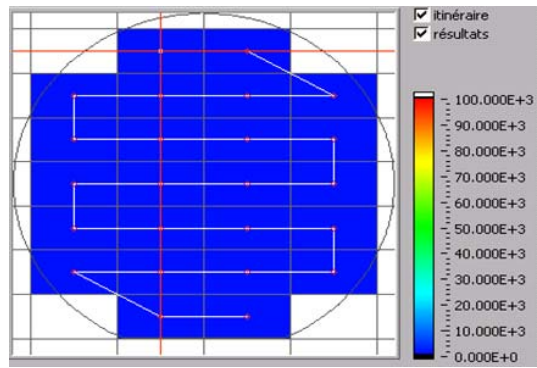


Figure 5.8   Color map of resistance continuity
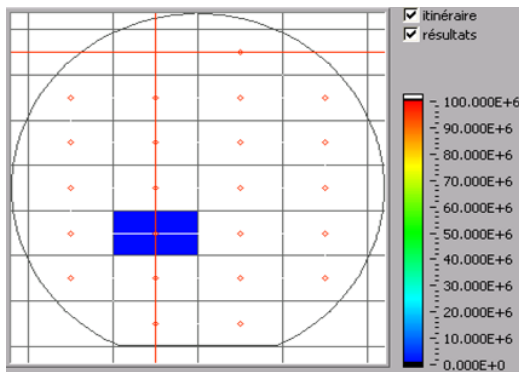


Figure 5.9   Color map of isolation between pin 1 and pin 2, one die is not isolated
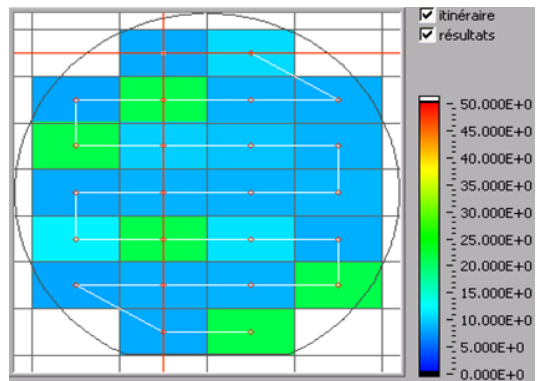


Figure 5.10   Color map of continuity pin 16, 1, 3 and 4 of one wafer

Based on method to measure the square resistance in section 5.1.1, Figure 5.11 shows the measurement results of square resistance for all dies on one wafer.
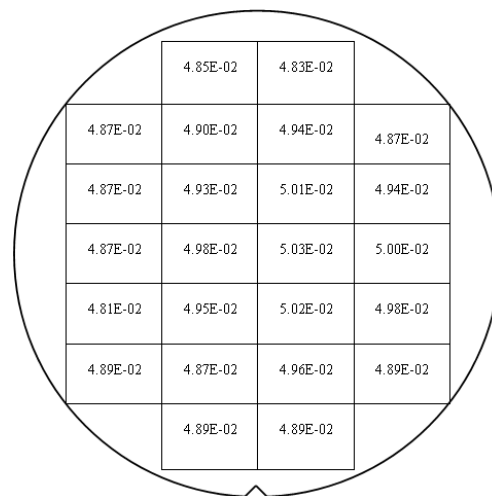


Figure 5.11   Results of square resistance characterization of all dies on one wafer

## 5.2 EXPERIMENTAL SETUP

After the parametric tests described in section 5.1.5, the non working device are removed from the map test in order to decrease the testing time that can be long for a large number of devices. The devices are characterized using a Vector Network Analyzer (VNA) HP 8753E. A Short Open Load Through (SOLT) Calibration is performed using calibration substrate associated with RF probes (Rosenberger Z-probes GSG-Ground Signal Ground with a 100µm pitch) to measure the S parameters of the SAW devices.

The devices in one die on the wafer were characterized manually to get basic information like center frequency. The first frequency range used for the all different devices on the wafer is 50MHz-1GHz. It will only give a rough estimation of the SAW devices center frequency but the advantage of doing so is that only one calibration is needed to get the center frequency of all devices on the wafer. Figure 5.12 shows the typical $S_{21}$ parameter (transmission coefficient) obtained for a device with a center frequency of 600 MHz.
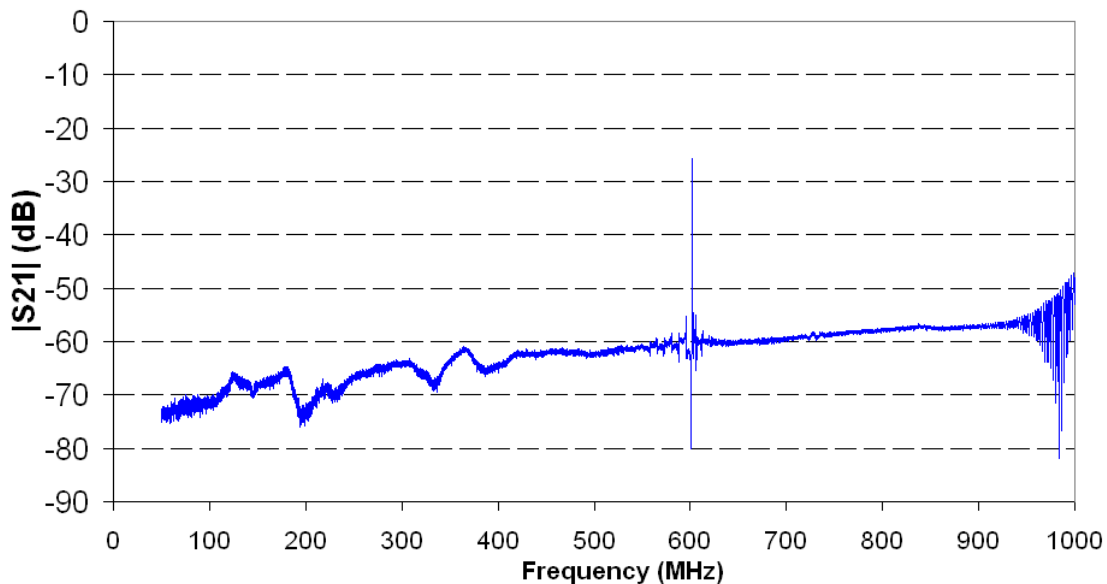


Figure 5.12   General view of device under test, frequency range of 50MHz-1GHz

Once the center frequency $f_0$ of all devices of one die has been extracted, the measurement frequency range is set to a smaller value around $f_0$ in order to get a better accuracy. The automatic (and accurate) measurements of all devices on the wafer are then performed and the S parameters are saved in .txt files to allow later data processing. The automatic test is done thank to an automatic prober computer controlled with a home made software called GAMME. The interface of the software is shown in Figure 5.13 and the automatic prober with a wafer under the RF probes can be seen in Figure 5.14.
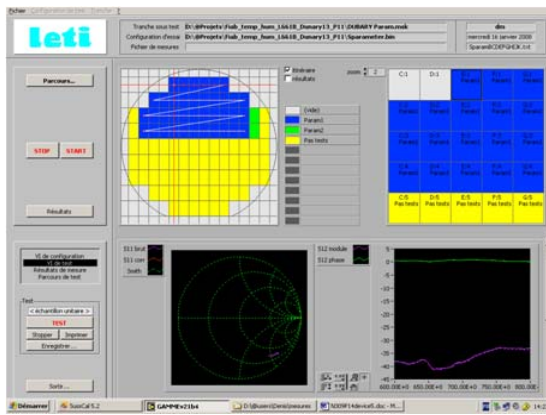
Figure 5.13   The software interfacing between PC and machine
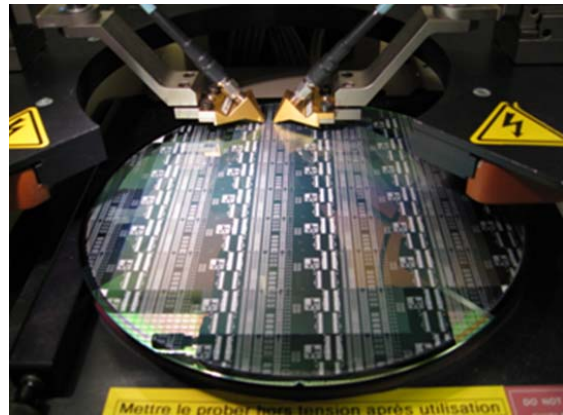


Figure 5.14   Snapshot of measurement with 2 probes GSG

After a post-treatment of the measured data, the best working devices are selected to realize frequency measurements as a function of ambient pressure. The measurements as a function of the pressure are done in a pressured chamber that only allows the characterization of a single device at a time. So, before performing the measurements, the wafer needs to be cut and the device should be wire-bonded to a PCB as shown in Figure 5.15.
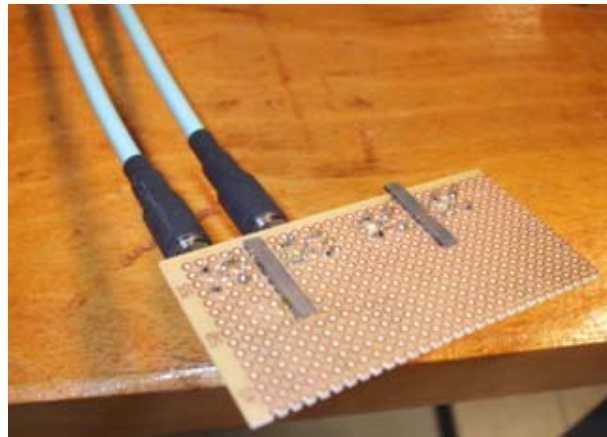


Figure 5.15   Devices are cut and wire bonded

Once the device is wire-bonded, it is placed in the pressurized chamber and connected to the VNA thank to sealed feed through as seen in Figure 5.16.
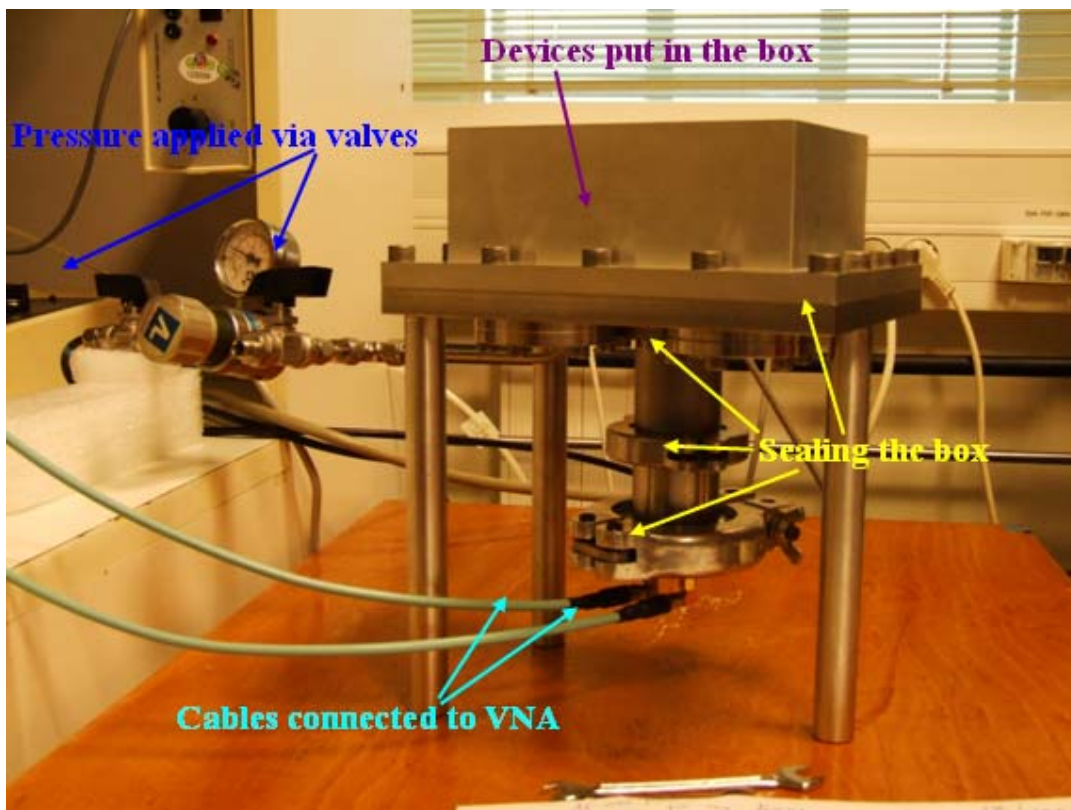
Figure 5.16   Box sealed to apply the pressure with the devices in it

The pressure in the chamber can be changed by using two valves, one for increasing the pressure in the chamber and the other for letting the air out of the chamber (Figure 5.17). To obtain the variation of the resonant frequency as a function of the pressure, the S parameters of the device for different pressures are computed to extract the center frequency variation.



Figure 5.17   Pressure meter with two valves

## 5.3    EXPERIMETAL RESULTS

### 5.3.1       Propagation losses measurement

The acoustic propagation losses were determined by measuring the insertion losses of SAW devices showing identical geometry except the delay line length.

Figure 5.18 shows a typical frequency response obtained.
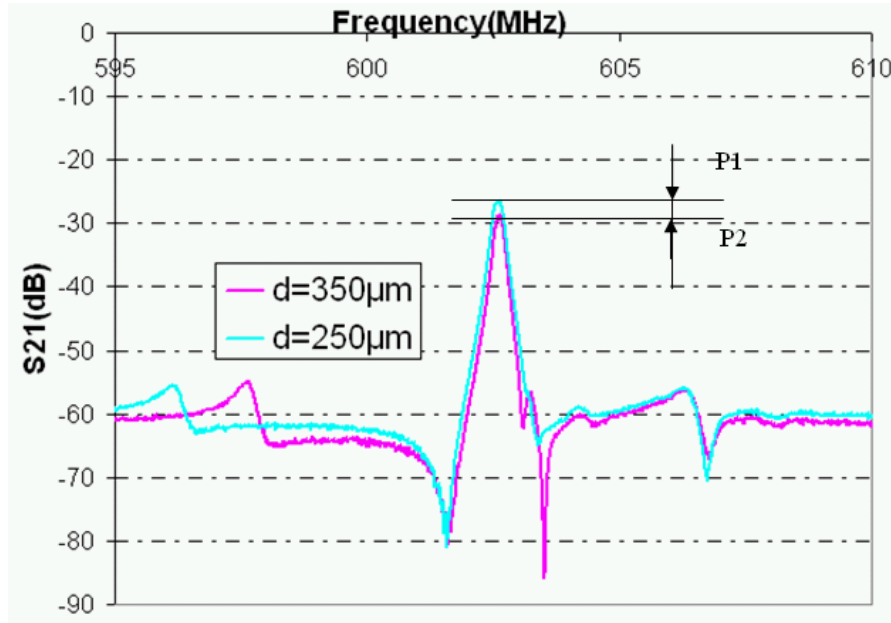


Figure 5.18   A typical insertion loss vs. frequency for two propagation paths of length 350 µm and 250 µm

The propagation loss could be expressed by:

$$Ploss = \frac{P1-P2}{l2-l1}(dB/mm) = \lambda \frac{P1-P2}{l2-l1}(dB/\lambda) \qquad \text{eq.(5. 7)}$$

Where P1 and P2 are the insertion loss at center frequency $f_0$ corresponding with delay line length l1 and l2, respectively.

In our work, the lengths of the different delay lines realized in SAW devices are 200µm, 250 µm, 300 µm, 350 µm, 400 µm and 500 µm. The measured propagation loss value is the average of values measured for l=500 µm and l=400 µm, l=400 µm and l=350 µm and other combinations.

Figure 5.19 shows the dependence of the propagation loss on the SAW center frequency in three different wafers. In these measurements, the propagation losses increase with the center frequency. This is a good agreement with the literature [30],[156] in which the propagation

losses increase approximately as the frequency squared for AlN on sapphire and AlN on Si. The difference in value in our work and [30] in case of AlN on Si can be due to the different qualities of the grown AlN, the surface roughness and defects in the AlN films, as well as the measured values done at different frequency.
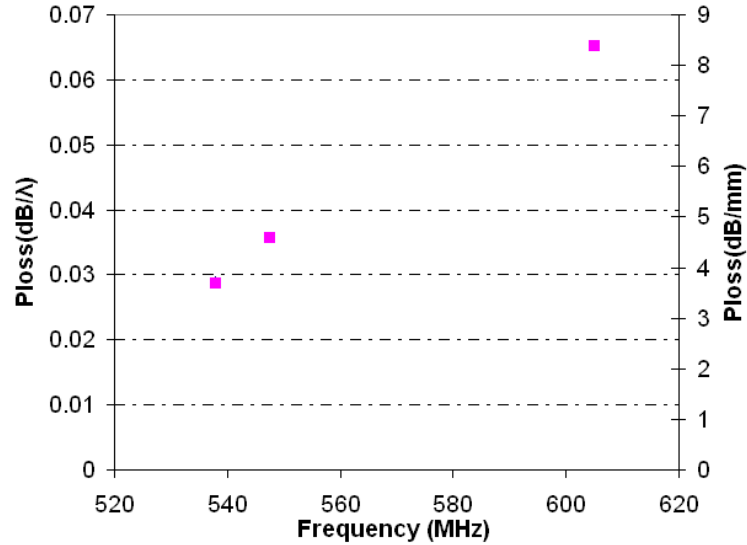


Figure 5.19   Measured propagation losses at three center frequencies

### 5.3.2      Piezoelectric coupling factor extraction

The experimental piezoelectric coupling factor K was determined by using measured data of $S_{11}$ parameter.

Port input impedance $Z_j$ (j=1,2) can be expressed as:

$$Z_j = Z_0 \frac{1+S_{jj}}{1-S_{jj}}$$   eq.(5. 8)

The transmission line characteristic impedance $Z_0$ used in our work is 50Ω. The $Z_j$ is expressed as [157]:

$$Z_j = R_p + Z_a$$   eq.(5. 9)

Where $Z_a$ is acoustic impedance, $R_p$ is parasitic resistance.

The real and imaginary portions of the input impedance $Z_1$ can be found from eq.(5. 8).

Figure 5.20 illustrates the real part of input impedance for AlN(2μm)/SiO$_2$(0.5μm)/Si substrate, number of finger pair N=50, w=180μm.
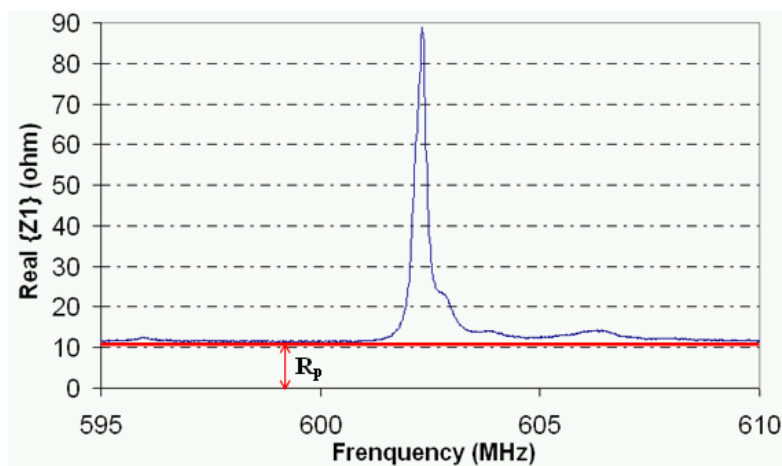
Figure 5.20   Real part of input impedance

The parasitic resistance $R_p$ can be easily found as the constant offset in the real part of port input $Z_j$. In Figure 5.20, $R_p$ is 11.5(ohm).

$R_p$, then, is subtracted from the input impedance $Z_j$, this step will yield acoustic impedance $Z_a$. $Z_a$ can then be inverted to yield the acoustic input admittance $Y_a(f)$:

$$Y_a(f) = G_a(f) + jB_a(f)$$
<div align="right">eq.(5. 10)</div>

Where $G_a(f)$ and $B_a(f)$ are, respectively, the radiation conductance and susceptance.

The acoustic input admittance $Y_a(f)$ extracted from Figure 5.20 is shown in Figure 5.21:
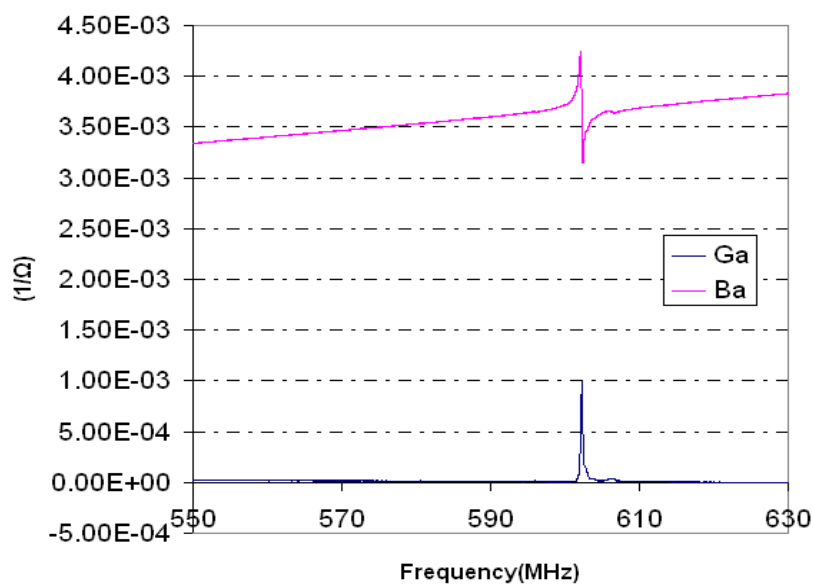


Figure 5.21   Acoustic input admittance $Y_a(f)$ extracted from $Z_a(f)$

The coupling factor K could be extracted from the relation as follows:

$$K^2 = \frac{\pi}{4N} \frac{G_a(f_0)}{B_a(f_0)}$$

eq.(5. 11)

The comparisons between calculation and measurement of coupling factor in AlN/Si, AlN/SiO$_2$/Si structure versus thickness of AlN are shown, respectively, in Figure 5.22 and Figure 5.23.

Two points should be concerned from these comparisons.

Firstly, the change of measured values versus AlN thickness is similar with that of calculated values. The second point is that the measured coupling factor is higher than the theoretical one. This difference could be explained firstly by using Ingebrigtsen approximation to calculate the coupling factor by equation (2.11) in chapter 2 [116]. The difference between theoretical and measured values also could be explained by the fact that in the theoretical calculation, the mass loading effects of metal layer are not taken into account. This coupling factor depends also on the oxygen contained in AlN film [158], in which the author showed that the cause is a change in crystallographic structure based on how the oxygen substitutes in the lattice. This could be the reason explaining the difference between theoretical and measured values.
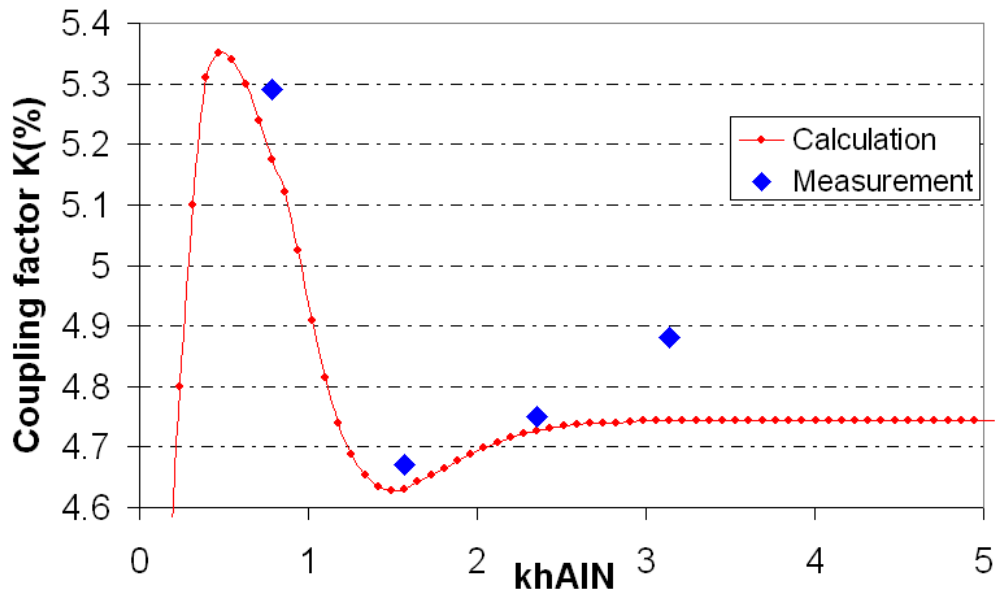


Figure 5.22   Coupling factor K(%) in AlN/Si, comparison between calculation and measurement
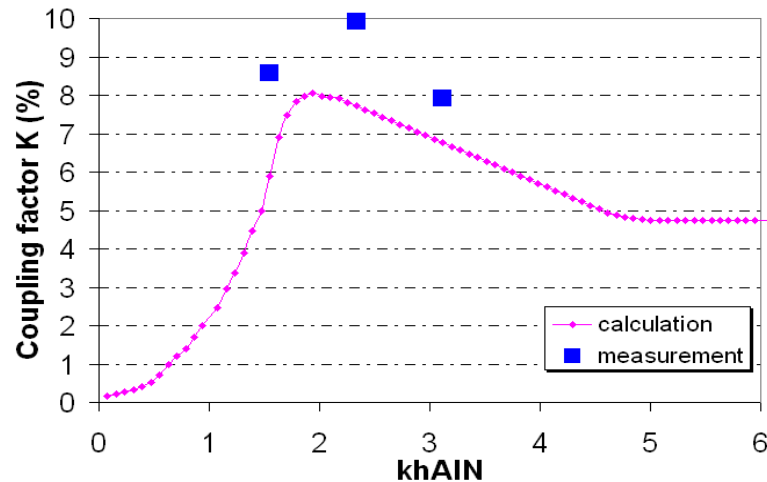
Figure 5.23   Coupling factor K(%) in AlN/SiO$_2$/Si, comparison between calculation
and measurement

These measurements of coupling factor K will be used in simulation in next sections.

### 5.3.3       Comparison between experiment and simulation

The simulation and experiments of SAW devices with all of the same parameters (number of finger pairs N=50, finger width is 2μm, aperture W=180μm, distance between two IDTs d=200μm) on high substrate and normal substrate are shown in Figure 5.24. There is a good agreement of center frequency between experiment and simulation. The center frequency $f_0$ from experiment is 602.24 MHz, while that from simulation is 600.4 MHz.
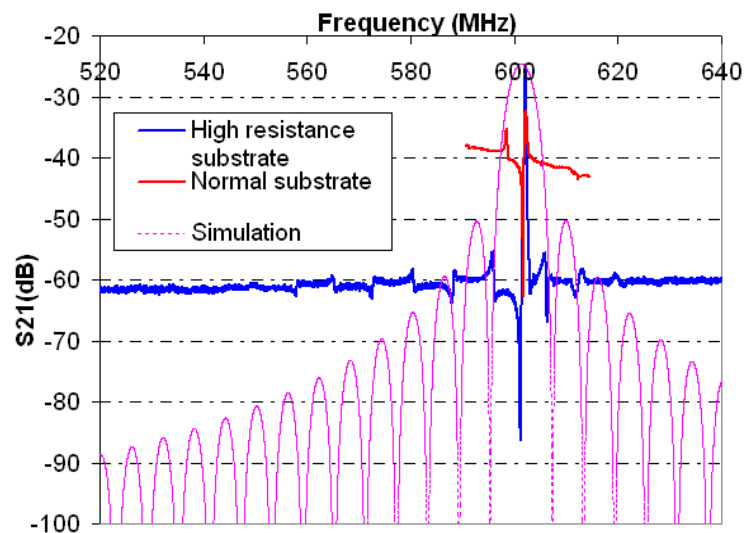


Figure 5.24   Frequency response and Comparison between experiment (high
resistance and normal substrate) and simulation.

In Figure 5.24, the observed frequency responses of simulation and experiment are considered. The pass-band width in simulation is broader than that in experiment. There could be several reasons which would be too difficult to explain for the reduced pass-band width in case of the experiment when compared to the equivalent circuit model. For example, the modifications of the SAW delay path to promote energy trapping can lead to reduced bandwidth and insertion losses [159]. Another reason could come from the parasitic effects that can cause an unacceptable reduction of the out-of-band rejection and an effective increase of the in-band losses [160].

The difference in experimental frequency responses of SAW devices on high resistance substrate and normal substrate can be observed clearly in Figure 5.24. The difference could be explained by the energy loss between high substrate and normal substrate. This difference could also explained by the different values of parasitic in high resistance substrate and normal substrate [160].

### 5.3.4    Effect of Mo layer on performance of AlN/Si SAW device

To see the effects of Mo layer, SAW devices with different configurations AlN/Mo/Si and AlN/Si were measured. These measurements are shown in Figure 5.25. The parameters of devices are: 45, 50 and 55 finger pairs, finger width is 2μm, aperture is 180μm, distance between 2 IDTs is 300μm.
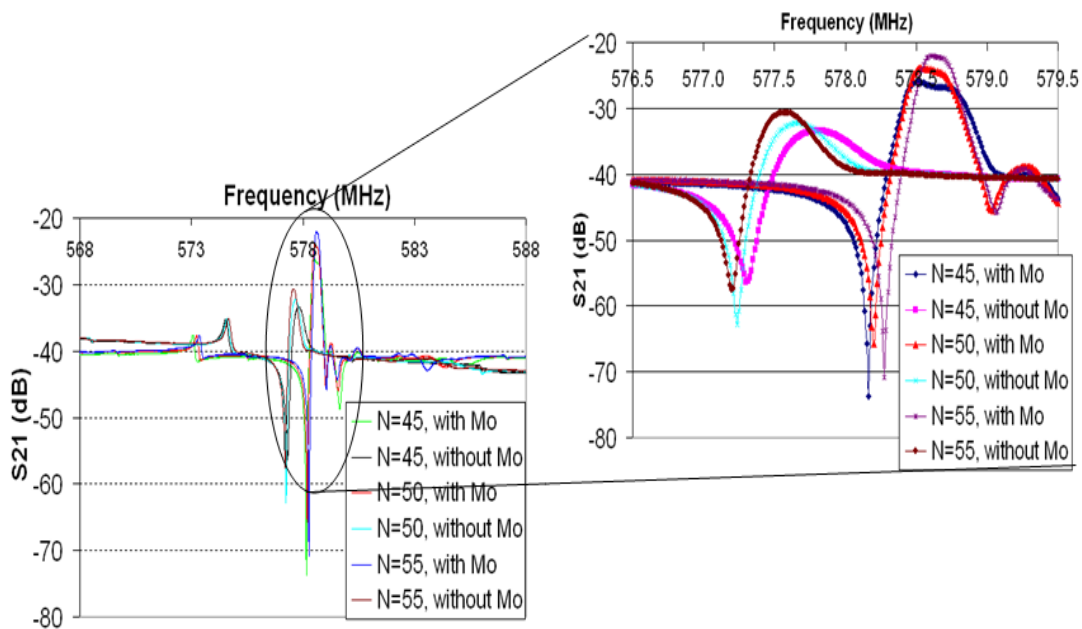


Figure 5.25   Comparison between AlN/Mo/Si and AlN/Si SAW devices

Comparison between different SAW devices is also shown in Table 5.3 to state clearly the differences in the center frequencies and the peak of $S_{21}$.

Table 5.3    COMPARISON OF MEASUREMENTS OF SAW FILTERS WITH AND WITHOUT Mo

| Number of finger pair | $f_0$ (MHz) | | Peak of $S_{21}$ (dB) | |
|---|---|---|---|---|
| | With Mo | Without Mo | With Mo | Without Mo |
| N=45 | 578.51 | 577.8 | -25.99 | -33.42 |
| N=50 | 578.54 | 577.65 | -23.90 | -32.27 |
| N=55 | 578.61 | 577.58 | -22.08 | -30.63 |

The SAW devices using Mo layers below AlN have the center frequency larger than devices not using Mo. The gap between these center frequencies is about 1 MHz. Another different point, but very important, is the difference in peaks of $S_{21}$ (dB). This difference is 8 to 9 dB, and this is extremely high.

The difference in center frequency can be explained by the difference in velocity of the wave that was presented in Chapter 2, section 2.2.3. For clarity of reading, Figure 5.26 shows again the dependence of the velocity on the normalized thickness of AlN and Mo layers.
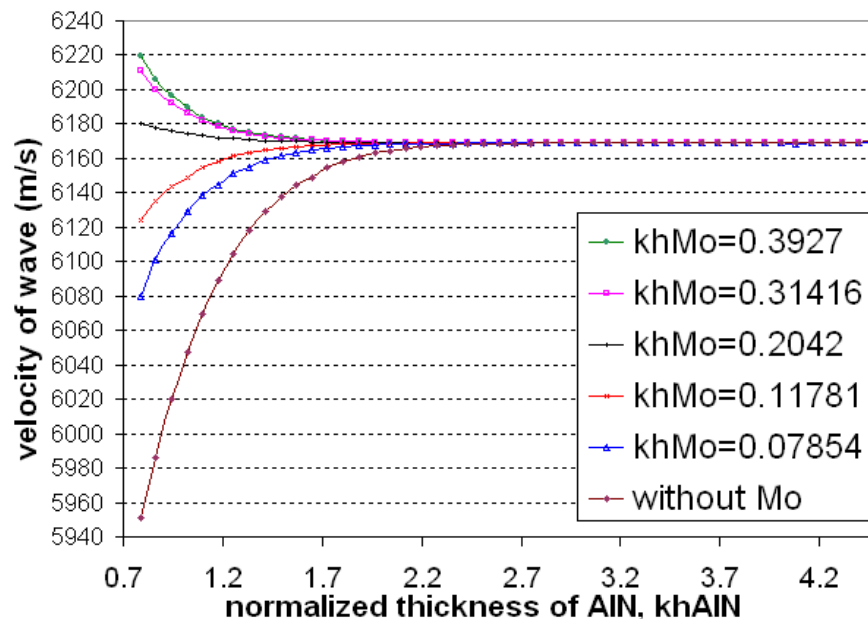


Figure 5.26   Wave velocity AlN/Mo/Si substrate depends on the normalized thickness khAlN and khMo

The SAW device under test has khMo=0.2042, khAlN=1.5708. From Figure 5.26, the velocity in configuration with Mo layer (khMo=0.2042) is larger than in configuration without Mo, the correspondent center frequency with Mo also is larger than that without Mo.

The second interesting difference between the two configurations is the maximum of the transmissions coefficient of SAW filter. This difference can be explained with several reasons.

In SAW devices, the propagation loss of SAW would be the primary point of interest. The SAW propagation loss increases approximately as the frequency squared, as stated in section 5.3.1. In these measurements, the center frequency difference in two configurations is very small, about 1 MHz; therefore, the SAW propagation loss would not be the good reason to explain the big difference of the $S_{21}$ peak.

The second explanation is difference in coupling factor K% between two configurations. For the clearness of reading this section, it is necessary to show again the dependence of coupling factor on the thickness of Mo and AlN layers in Figure 5.27. This dependence of coupling factor can be explained qualitatively.
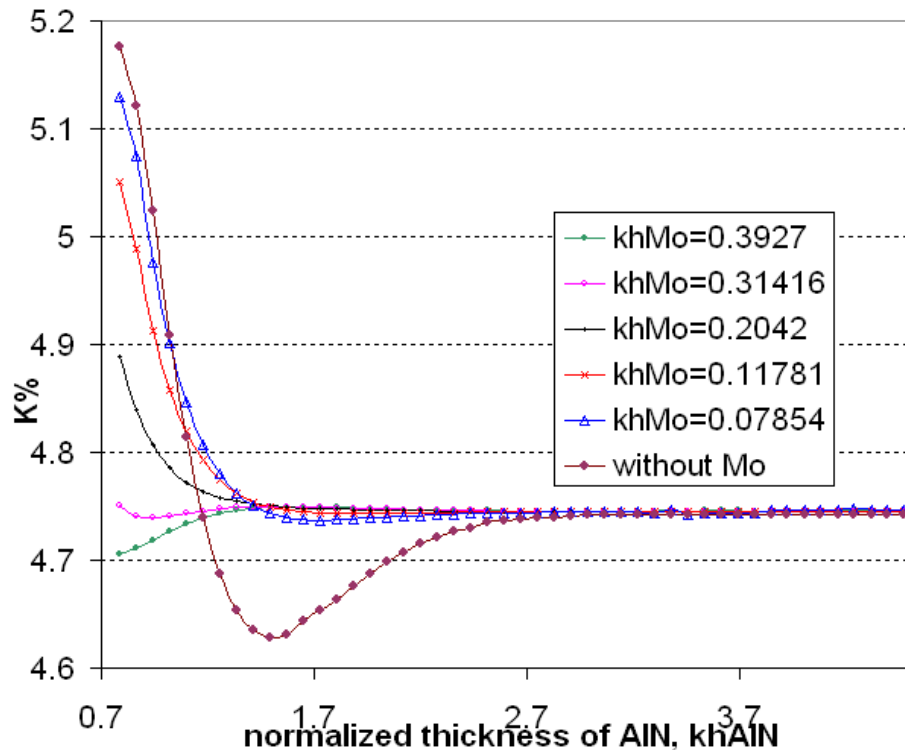


Figure 5.27   Coupling factor K(%) in SAW device AlN/Mo/Si substrate depends on the normalized thickness khAlN and khMo

When applying the coupling factor value from Figure 5.27 (4.75% for case with Mo and 4.62% for case without Mo) into the model in chapter 2, the difference between the peaks of $S_{21}$ is 0.05 dB. So, the difference in coupling factors would not be a good explanation for the difference of 8 to 9 dB.

The frequency-dependence of SAW propagation loss, the difference in coupling factors would not be good reasons for large difference of gains in the two configurations with and without Mo layer. This difference can be explained with several irregularities. The primary point of the problem would be the crystal orientation and crystal imperfection of AlN layer. As analyzed in Chapter 4, section 4.9.3, the use of bottom Mo could increase the crystal quality of AlN. This would be a good reason to explain the effect of Mo in the large difference of gains in the two configurations with and without Mo layer.

Another irregular reason could be the difference in surface of AlN films with Mo below and without Mo layer. These surfaces are viewed as in Figure 5.28 and Figure 5.29.
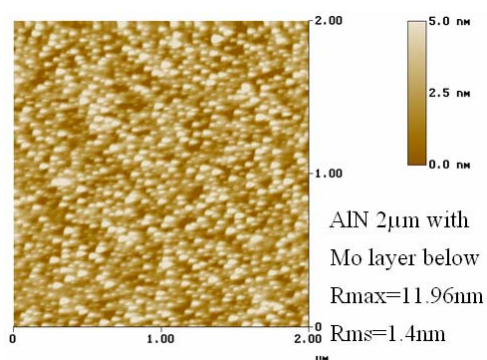


Figure 5.28 Atomic force micrographs of AlN 2μm with Mo layer below
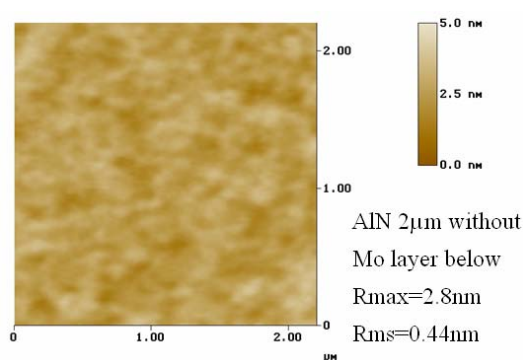


Figure 5.29 Atomic force micrographs of AlN 2μm without Mo layer below

From these observations of AlN surface, using bottom Mo increases the roughness of AlN film, from roughness (rms) of 0.44nm to that of 1.4nm. We believe that the difference in roughness could change the propagation loss.

In conclusion, the use of bottom Mo could increase the crystal quality of AlN. This would be the good reason to explain the effect of Mo in large difference of gains in the two configurations with and without Mo layer. The Mo layer can increase the peak of $S_{21}$ up to 8-9 dB and is very interesting. From Table 5.3, to increase more (2-3 dB), the SAW filter would be fabricated with the number of finger pairs N=45 up to N=55. Without using Mo layer, to increase the $S_{21}$ peak in SAW filter (configuration N=55, without Mo layer, $S_{21}$ peak of -30.63dB) up to the same in SAW filter with Mo layer ($S_{21}$ peak of -20.08dB), by the simulation of model in chapter 2, the number of finger pairs has to be increased from N=55 up to N=85. Therefore, in $S_{21}$ peak point of view, using Mo layer can save the die area on the wafer.

### 5.3.5      Effect of thin Polyimide film

The need of using polyimide as absorber is presented in Chapter 4, section 4.11. In this section, the effect of polyimide is characterised. The SAW devices with different lengths of absorber are realized, where length of absorber is $a\lambda$, with a=0, 2, 4, 6, 8, 10, 15, 20, 25, 30, 35, 40, 45 (see Figure 5.30)



| a=0, no polyimide | a= 10 | a=20 | a=40 |
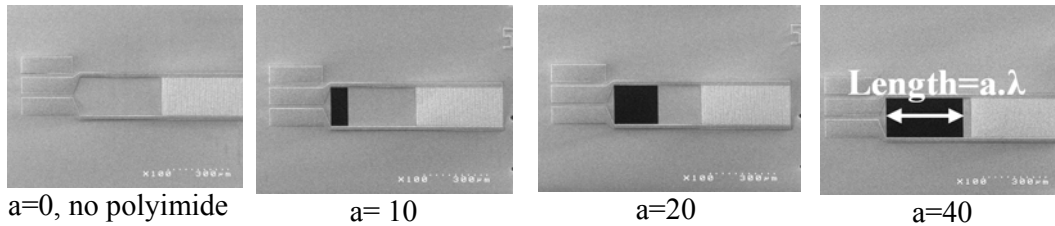
Figure 5.30   SAW devices with different length of absorber are realized

For clarity of reading, Figure 5.31 just shows the effect of different lengths of polyimide on the center frequency in cases: a=0, 10, 20, and 40.
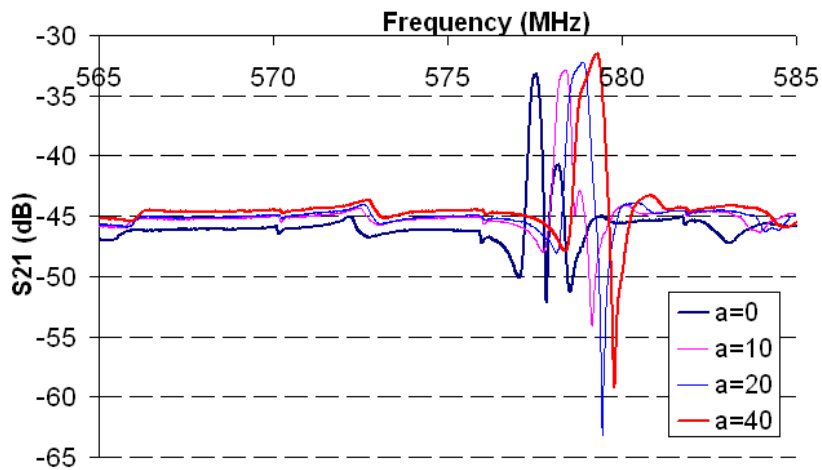


Figure 5.31   S21(dB) with different lengths of polyimide

The center frequency is simulated: $f_0$= 584 MHz.

While, the center frequency in experiments is 577.5 MHz-579.3 MHz. The comparison between center frequencies of devices with different lengths of polyimide is shown in Table 5.4.

Table 5.4   COMPARISON BETWEEN CENTER FREQUENCIES OF DEVICES WITH DIFFERENT LENGTHS OF POLYIMIDE

|  | a=0 | a=10 | a=20 | a=30 | a=40 |
|---|---|---|---|---|---|
| $f_0$ (MHz) | 577.5375 | 578.2625 | 578.8625 | 579.1875 | 579.3 |

The different polyimide films seem to affect the center frequency, in which the center frequency could be proportional to the length of thin polyimide film. This effect can be shown in Figure 5.32.
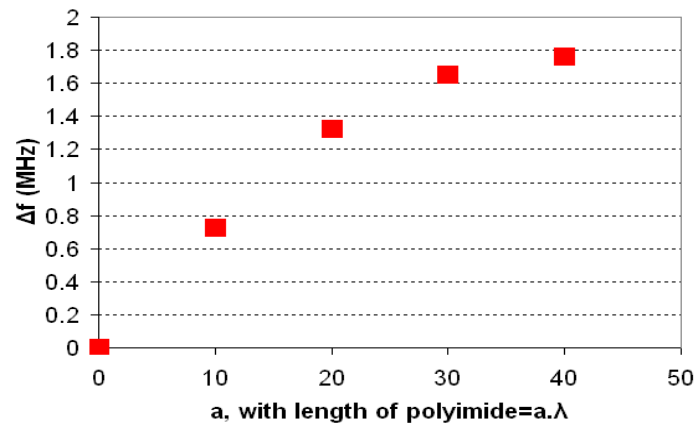


Figure 5.32   The effect of different lengths of polyimide on the center frequency

The polyimide are also deposited at different thickness, and their effects on the center frequency are shown in Figure 5.33 and summarized as in Table 5.5 as well as in Figure 5.34. Figure 5.33 (a) and (b) show the frequency shift Δf measured at absorber thicknesses of 95nm and 2850nm, in which the polyimide have the same length. It seems that the polyimide of large thickness affects on the center frequency less than that of small thickness.

Table 5.5   EFFECT OF DIFFERENT THICKNESSES OF POLYIMIDE ON CENTER FREQUENCY

| $f_0$ (MHz) | a=0 | a=20 | a=40 | Measured frequency shift (MHz) between a=0 and a=40 | Measured thickness of polyimide (nm) |
|---|---|---|---|---|---|
| wafer 1 | 577.54 | 578.86 | 579.3 | 1.763 | 95 |
| wafer 2 | 580.63 | 581.14 | 581.01 | 0.387 | 921 |
| wafer 3 | 578.76 | 579.36 | 579.49 | 0.725 | 400 |
| wafer 4 | 602.31 | 602.47 | 602.59 | 0.279 | 2850 |
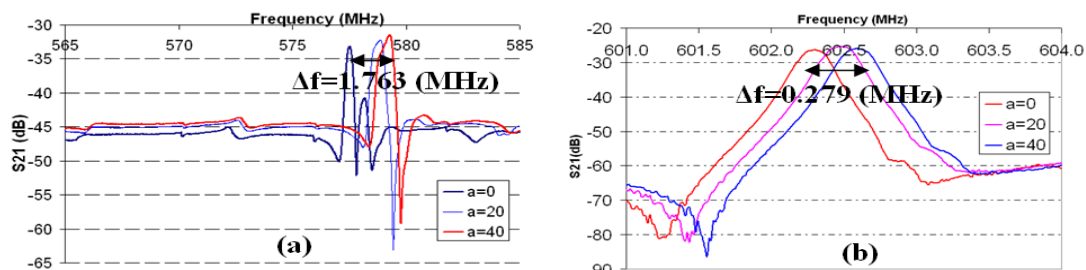


Figure 5.33   Effect of polyimide on the center frequency, thickness of polyimide is 95nm in (a), and is 2850nm in (b)
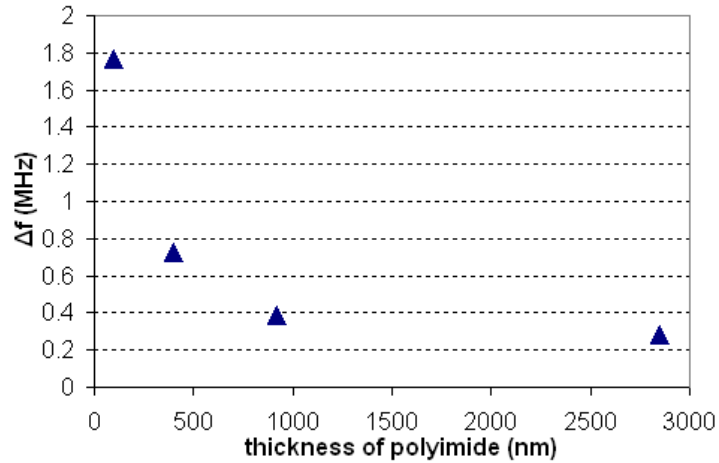
Figure 5.34   The effect of different thickness of polyimide on the center frequency

These effects of polyimide on center frequency can be explained by that the attenuation rate of absorber is proportional to the volume of the absorber film. The attenuation rate of 3.0-3.5 μm thick and 14 μm, 20 μm thick polyimide films were measured by other groups [139] and [140], respectively. And in our work, the polyimide dependence of center frequency is found.

This dependence could be explained by using circuit model in Chapter 2, section 2.3.3 or section 2.4.4. In this model, an ideal absorber is used, there is no reflected wave. By applying the circuit theory for matching condition, we need to have two terminal admittances of values G0. In this characterization, thin polyimide film doesn't absorb completely the wave, that is equivalent to using other values of two terminal admittances in the circuit model. The effect of thin polyimide film on the center frequency of SAW devices are modeled as in Figure 5.35.
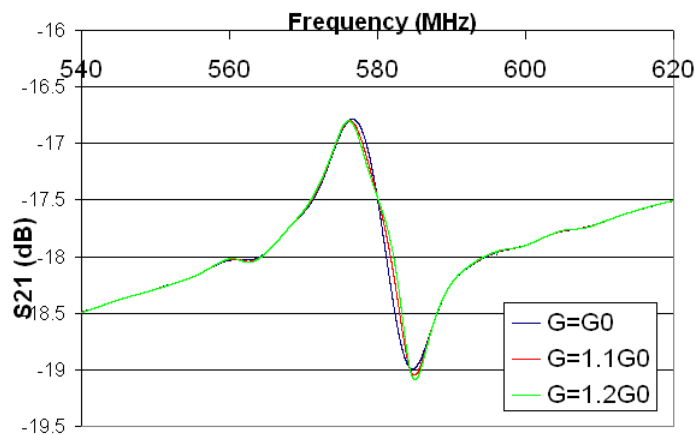


Figure 5.35   Simulation of $S_{21}$(dB), effects of polyimide films on the $f_0$

It would be too difficult to find out the relation between the volume of polyimide and value of terminal admittance G in the model. However, the approach stated above that uses the different values of G in the equivalent circuit could explain the effect of polyimide.

Another important conclusion from this section is that to reduce the effect of polyimide on center frequency, the attenuation rate of polyimide should be high. Because of the limitation of the device size, the thickness of the absorber film should be increased.

### 5.3.6      Device under pressure

The SAW delay line is fabricated with the buried $SiO_2$ layer thickness of 2µm, the thickness of AlN is 2µm, $SiO_2$ is 200nm, wavelength is 8µm. At the end of fabrication, the membrane of device is bent (as stated in Chapter 4). The membrane deformation is measured by WYKO system (see Appendix  C, section C. 3), and result is shown in Figure 5.36.
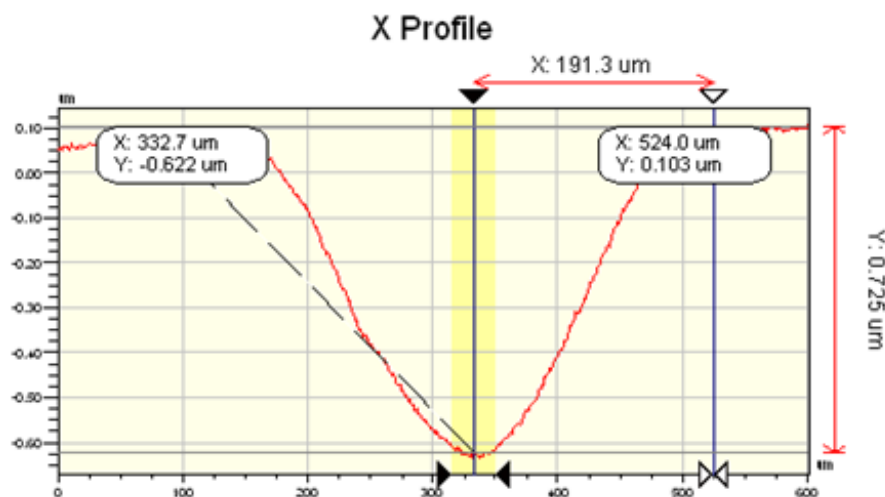


Figure 5.36   Measured membrane deformation

Because of this membrane bend, the maximum applied pressure is 1.3 bar.

#### 5.3.6.1  Phase shift

Figure 5.37 shows the measured phase shift by applied pressure. Measured phase shift is $3^0$. The calculated value (in Chapter 3, section 3.3.4) is $4^0$. The difference between these values would be due to the measurement error. In conclusion, there is a good agreement between measured and calculated values of phase shift by pressure.
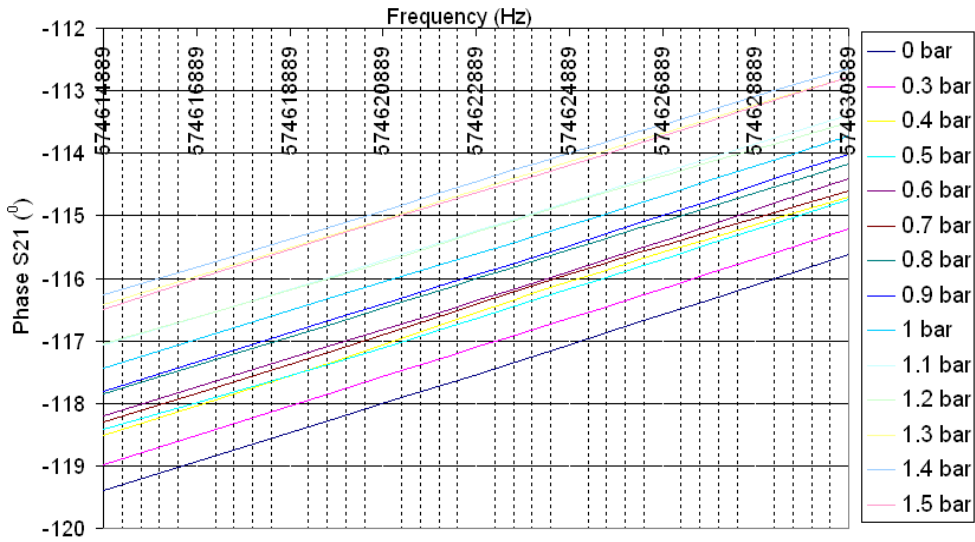
Figure 5.37   Measured phase shift by pressure

### 5.3.6.2  Frequency shift

Figure 5.38 shows the measured frequency variation of SAW delay line under pressure.
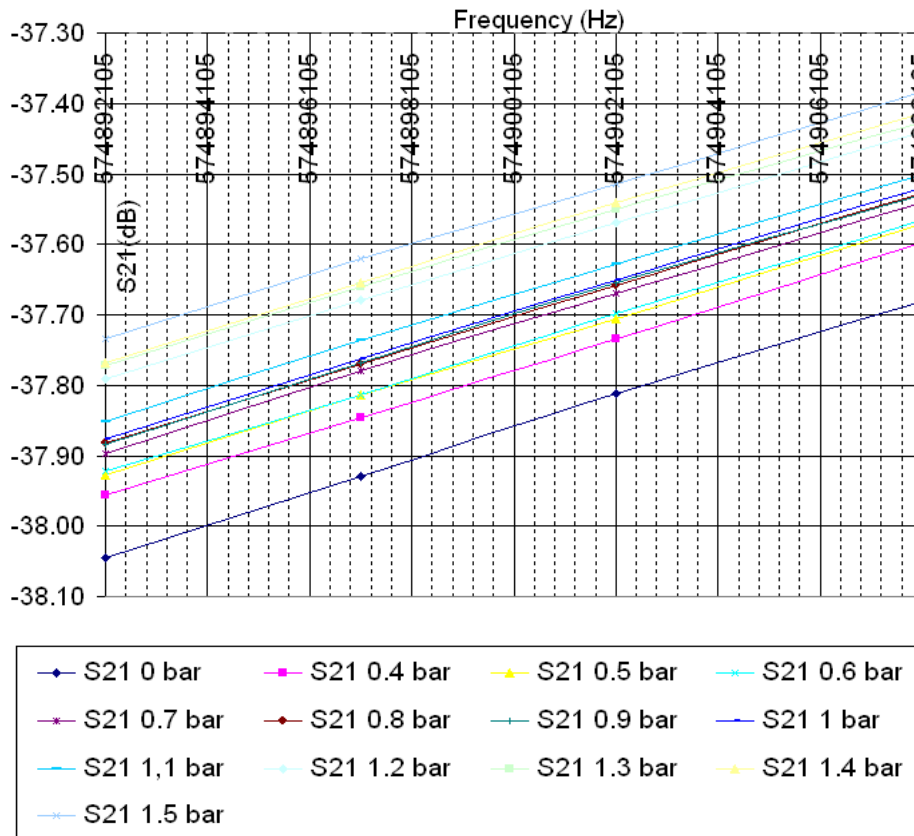


Figure 5.38   $S_{21}$ variation under pressure
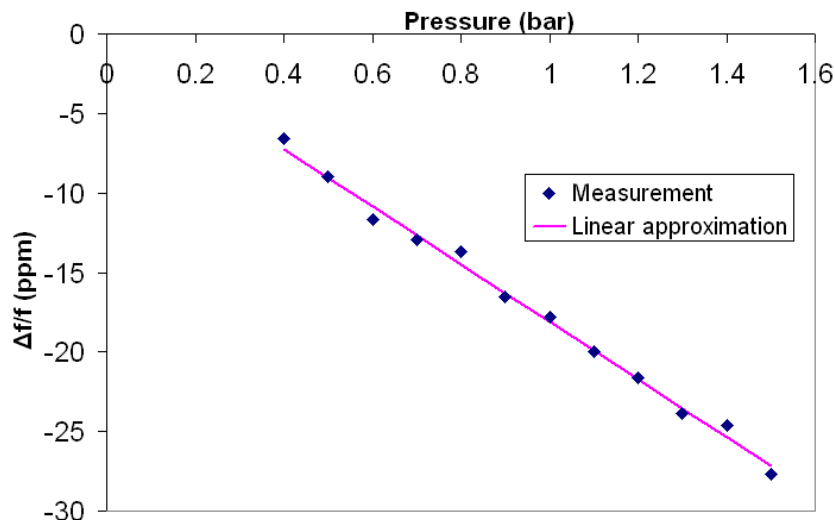
Figure 5.39   Frequency variation under pressure

The SAW device under test with applied pressure has the center frequency $f_0$ is 574.145 MHz. The measured frequency variation by pressure is $\Delta f/P$=-10.4 kHz/bar.

And, the pressure sensitivity for this device (from measurement in Figure 5.39) is $\frac{\Delta f}{f_0}(ppm) = -18.11(ppm/bar)$.

The calculated pressure sensitivity for device under test with pressure as shown in Chapter 3, section 3.3 (khAlN=1.57, khSiO$_2$=0.1571) is -12.34 (ppm/bar). The difference between measured and calculated values could come from the error in measurement equipment and the pressure display.

Compared with the SAW pressure sensor ZnO/Si (khZnO=1.18) done by the group in [13] with pressure sensitivity is -5(ppm/bar), the result obtained in our work would be interesting and promising.

## 5.4    CONCLUSION

This chapter presents the parametric tests, the experimental setup, major experimental results and also the explanations and analyses of obtained results.

The parametric tests are used to make a fast process control of the deposited/etched layers. These are electrical tests and come as an added value to the well known optical tests. They allow controlling process stability over time. After the parametric tests, the non working devices were removed from the map test in order to decrease the testing time that was long for a large number of devices.

Our devices were characterised and obtain major results. The first important parameter is acoustic propagation losses. We obtained a good agreement with the literature in which the propagation losses increase approximately as the frequency squared. Another important parameter is coupling factor which was extracted by using measured data of $S_{11}$ parameter. From this extraction technique, we saw that the change of measured coupling factor values versus AlN thickness is similar with that of calculated values. Besides, the measured coupling factor is higher than the theoretical one. This difference was explained.

Another new result is good effects of Mo layer on performance of device was analysed. We saw that using bottom Mo layer could increase the crystal quality of AlN, and save the die area on the wafer. These good effects would be interesting.

Besides, a new result was done in which the effect of thin polyimide film on the center frequency was analysed. We obtained a important conclusion from this analysis is that to reduce the effect of polyimide on center frequency, the thickness of the absorber film should be increased due to the limitation of the device size.

As the goal of this work is pressure sensor, the pressure sensitivity of frequency shift is important. The result obtained in the pressure sensitivity of our device is $\dfrac{\Delta f}{f_0}(ppm) = -18.11(ppm/bar)$. Compared with the SAW pressure sensor ZnO/Si in literature which had pressure sensitivity of -5(ppm/bar), the result obtained in our work would be interesting and promising.

# CONCLUSION and PERSPECTIVE

Surface acoustic wave (SAW) devices are widely used today in a variety of applications both in consumer electronics as well as in research measurements: industrial, commercial, medical applications and military equipments. Among these applications, the pressure sensor plays a key role in many industrial, automotive applications. In SAW pressure sensor, the pressure induced stress and strain. Consequently the propagation path of acoustic waves will be modified and therefore the frequency response of the device. The pressure can be obtained by measuring frequency or phase response change. The goal of this thesis is design, simulation, fabrication and characterization of SAW pressure sensor using AlN and technological facilities available in CEA-LETI. The AlN is chosen thank to its good properties in high temperature until $1000^0$C, its high acoustic velocity and its compatibility with microelectronic process.

To follow this goal, firstly, we calculated and analysed the SAW parameters in different structures of AlN/SiO$_2$/Si, AlN/Si, and AlN/Mo/Si. An important conclusion is that the wave velocity and coupling factor could depend on the wave propagation medium. In each kind of SAW structure using AlN, we found the range of thickness of AlN layer in which there is a weak dependence of the wave velocity, coupling factor on the AlN layer thickness. The SAW devices should be fabricated to facilitate manufacturing.

- For AlN/Si structure, this range is $khAlN \geq 3$.

- For AlN/Mo/Si, if this kind of SAW device is fabricated in the range from $khAlN \geq 2.7$ to facilitate manufacturing, the using of Mo layer is useless. Consequently, to take full advantage of using Mo layer in term of wave velocity and coupling factor, it should be required to control the fabrication process carefully to obtain the required AlN thickness from khAlN=1.02 to khAlN=2.7. The further advantage of using Mo is also presented in term of AlN property.

- For AlN/SiO$_2$/Si, this range is $khAlN \geq 5$ for khSiO$_2$=0.7854. Besides, using SiO$_2$ layer would reduce temperature dependence of frequency. To choose the thickness of SiO$_2$ layer, it would consider the effect of temperature dependence and analyses of wave velocity, coupling factor.

After the SAW parameters are known, the models of SAW device based on equivalent circuits of Mason model and COM theory were used. For usefulness and reduction of time in

design process, the equivalent circuit based on COM model, in which $K_{11}$, $K_{12}=0$ ($K_{ij}$ are coupling coefficient between two finger of an IDT) is proposed to be used.

Following these models, we gave the development of model used for SAW pressure sensor. Besides, we also performed the mechanical analysis of membrane under pressure and the pressure sensitivity calculations. Besides, in this work, we analysed the effect of frequency variation due to temperature change in SAW device using AlN. For pressure application, this sensitivity must be reduced.

We also used Finite Element Method (FEM) to get a visual view and to verify the results obtained from the analytic method. However, the computational cost to simulate a whole SAW device is extremely high, or the amount of elements can not be handled by our computer resources. Besides, it takes a long time and it requires a trial and error to find the results of center frequency, wave velocity and coupling factor. Consequently, to reduce time, in our work, the analytical method and equivalent circuit are used to extract the parameters of SAW devices; FEM was used to get a 3D view and explain some results that can not be explained by the analytic method.

From these calculations, we saw that in all kinds of SAW structure, there would be the tradeoffs between temperature reduction, coupling factor, wave velocity and pressure sensitivity and facility in manufacturing. Consequently, these SAW parameters, as well as the environment in which device is used should be concerned.

After finishing the calculation, simulation and analysis of SAW device, we proposed surface micromachining to fabricate the devices. This kind of fabrication process could create exactly the dimensions of membrane used in pressure sensor, and it also allows having a well defined membrane with any geometry due to the silicon etch stop wall. Following decision of choosing surface micromachining, we designed the mask for fabrication process. Fabrication process using surface micromachining was done successfully. However, the fabrication process needs to be controlled very carefully, especially in PSG deposition and etching process to remove the buried $SiO_2$ layer.

As AlN was used as piezoelectric layer in SAW device, we paid attention to piezoelectric response of AlN as well as characterization of AlN film. We found that to increase the piezoelectric response of AlN, there are three ways that can be done:

    d.  Using the bottom Mo layer.

    e.  Decrease the roughness of the layer below AlN layer until be smaller than 0.2nm. This requirement can be obtained by using CMP.

      f.   Increase the thickness of AlN.

Retaining good properties of AlN film in high temperature was characterised and confirmed.

After finishing the fabrication process, we used the parametric tests to make a fast process control of the deposited/etched layers and Vector Network Analyzer to measure the S parameters of the SAW devices. Our devices were characterised and obtain major results. The first important parameter is acoustic propagation losses. We obtained a good agreement with the literature in which the propagation losses increase approximately as the frequency squared. Another important parameter is coupling factor which was extracted by using measured data of $S_{11}$ parameter. From this extraction technique, we saw that the change of measured coupling factor values versus AlN thickness is similar with that of calculated values. Besides, the measured coupling factor is higher than the theoretical one. This difference was explained.

Another new result is good effects of Mo layer on performance of device. We saw that using bottom Mo layer could increase the crystal quality of AlN, and save the die area on the wafer. To insure acoustic waves attenuation at the ends of propagation path, the use of polyimide was studied. The effect of thin polyimide film on the center frequency was analysed. An important conclusion from this analysis is that to reduce the effect of polyimide on center frequency, the thickness of the absorber film should be increased to reduce the device size.

As the goal of this work is pressure sensor, the pressure sensitivity of frequency shift is important. The result obtained in the pressure sensitivity of our device is $\dfrac{\Delta f}{f_0}(ppm) = -18.11(ppm/bar)$. Compared with the SAW pressure sensor ZnO/Si in literature which had pressure sensitivity of -5(ppm/bar), the result obtained in our work would be interesting and promising.

Fabrication process in this work using surface micromachining was done successfully. However, this process could be developed to reduce the time of fabrication, and to obtain the better SAW device. In our work, SOI substrate with 2µm in thickness buried $SiO_2$ layer is used. There were some wafers that have the sticking problem of membrane due to stress and due to small thickness of $SiO_2$. To avoid this problem, the SOI substrate with larger thickness buried $SiO_2$ is proposed. Also, using larger thickness of buried $SiO_2$ layer, the pressure operation range of SAW pressure sensor could be increased.

Besides, a big challenge would be the fabrication of the whole system including electronic circuit and SAW pressure sensor on the same wafer.

The proposed SAW device using AlN could also be developed to use in other applications, for instance, humidity, temperature sensor, …

# List of publications

**Conference:**

1. **Hoang Trang,** BENECH Philippe, REY Patrice, VAUDAINE Marie-Helene, LEMAITRE-AUGER Pierre, DANEL Jean-Sébastien, ROBERT Philippe, "Temperature-Compensated Structure For Saw Pressure Sensor In Very High Temperature", IEEE International Frequency Control Symposium IEEE-FCS, Geneva, Switzerland, 2007.
2. **Hoang Trang,** BENECH Philippe, REY Patrice, VAUDAINE Marie-Helene, LEMAITRE-AUGER Pierre, DANEL Jean-Sébastien, ROBERT Philippe, "Trade-Off between Issues in AlN/SiO2/Si Pressure Sensor", IEEE International Conference on PERSPECTIVE TECHNOLOGIES AND METHODS IN MEMS DESIGN, Memstech 2007, Ukraine, 2007.
3. **Hoang Trang,** Patrice REY, Marie-Helene VAUDAINE, Philippe BENECH**,** "The crystal orientation of the Aluminum Nitride (AlN) films for SAW pressure sensor application in very high temperature", International Workshop On Nanotechnology And Application IWNA 2007, VietNam, 2007.
4. **Hoang Trang**, BENECH Philippe, REY Patrice, VAUDAINE Marie-Helene, ROBERT Philippe, "A novel structure of AlN/SiO2/Si, AlN/Si SAW filter", IEEE FCS, 2008.
5. **Hoang Trang**, BENECH Philippe, REY Patrice, VAUDAINE Marie-Helene, ROBERT Philippe, "Effect of Mo layer on performance of AlN/Si SAW filter", IEEE FCS, 2008.
6. **Hoang Trang**, REY Patrice, VAUDAINE Marie-Helene, BENECH Philippe, "Effect of thin Polyimide film on Performance of AlN/SiO2/Si SAW Device", IEEE PRIME, 2008.

**Journal:**

1. **Hoang Trang**, BENECH Philippe, REY Patrice, VAUDAINE Marie-Helene, ROBERT Philippe, "Effect of Mo layer on performance of AlN/Si SAW filter", is now under reviewed in IEEE Transactions on Ultrasonics, Ferroelectrics, and Frequency Control, submitted in May, 2008.

# Appendix A
# Properties of Si, SiO$_2$, AlN and Mo

Table A. 1   ELASTIC CONSTANT OF Si, SiO$_2$

| Material | Young's Modulus E (GPa) | Poisson's Ratio $\upsilon$ |
|---|---|---|
| Si | 106.85 | 0.342 |
| SiO$_2$ | 42.93 | 0.376 |

Table A. 2   ELASTIC CONSTANT OF AlN and Mo

| Elastic constant (x $10^9$ N/m$^2$) | $c_{11}$ | $c_{12}$ | $c_{13}$ | $c_{33}$ | $c_{44}$ |
|---|---|---|---|---|---|
| AlN | 410 | 149 | 99 | 389 | 125 |
| Mo | 440.7 | 246.862 | 246.862 | 438.867 | 96.002 |

Table A. 3   PIEZOELECTRIC CONSTANT OF AlN

| Piezoelectric constant (C/m$^2$) | $e_{15}$ | $e_{31}$ | $e_{33}$ |
|---|---|---|---|
| AlN | -0.48 | -0.58 | 1.55 |

Table A. 4   DIELECTRIC CONSTANTS OF Si, SiO$_2$

| Dielectric constants | $\varepsilon_{11}/\varepsilon_0$ | $\varepsilon_{33}/\varepsilon_0$ |
|---|---|---|
| Si | 10.62 | 10.62 |
| SiO$_2$ | 3.32 | 3.32 |

Table A. 5   DIELECTRIC CONSTANTS OF AlN

| Dielectric constants ($\varepsilon/\varepsilon_0$) | Static | High frequency |
|---|---|---|
| AlN | 8.5 | 4.6 |

Table A. 6   MASS DENSITY OF Si, SiO$_2$, AlN AND Mo

| Mass density (x $10^3$ kg/m$^3$) | p |
|---|---|
| Si | 2.33 |
| SiO$_2$ | 2.2 |
| AlN | 3.23 |
| Mo | 10.075 |

# Appendix B
# Development of calculation for equivalent circuit of SAW device

## B. 1 EQUIVALENT CIRCUIT FOR NORMAL IDT INCLUDING N PERIODIC SECTIONS
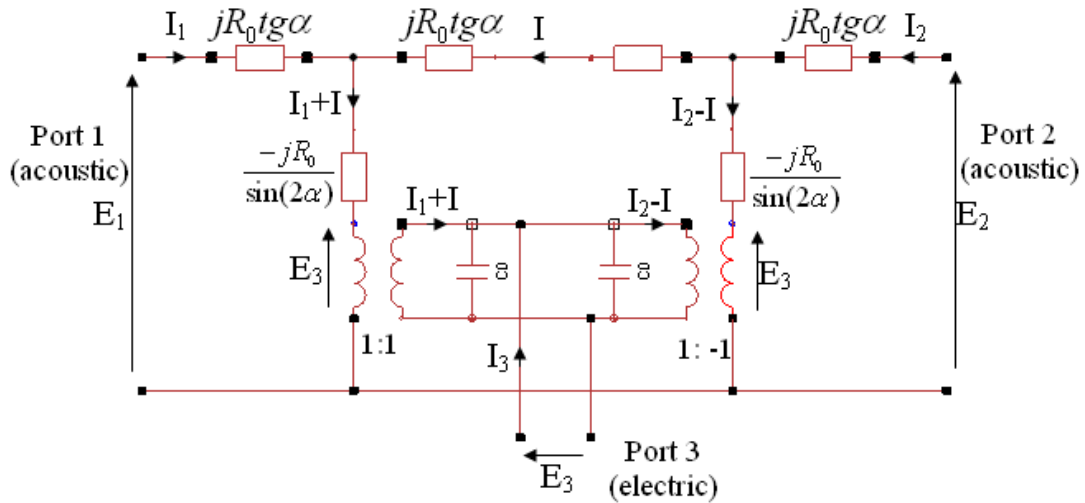
Figure B. 1   Mason equivalent circuit for one periodic section in "crossed-field" model
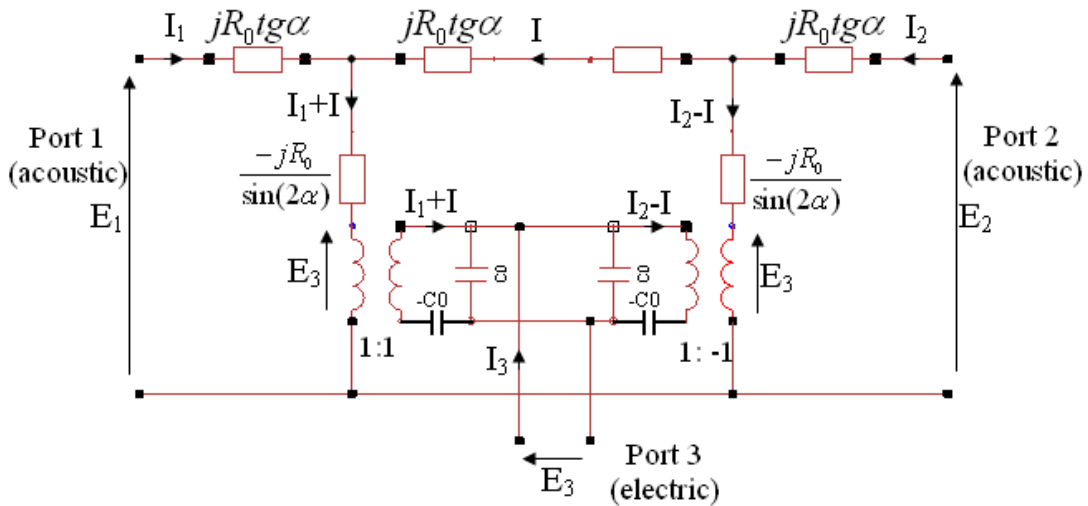
Figure B. 2   Mason equivalent circuit for one periodic section in "in-line field" model

One periodic section can be expressed by the 3-port network as follows:
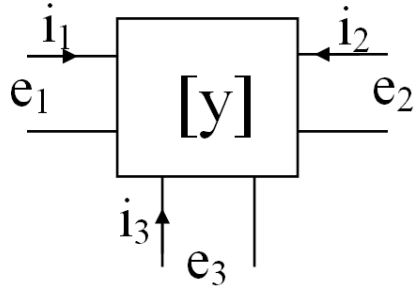
Figure B. 3   One periodic section represented by 3-port network, admittance matrix [y]

$$\begin{bmatrix} i_1 \\ i_2 \\ i_3 \end{bmatrix} = \begin{bmatrix} y_{11} & y_{12} & y_{13} \\ y_{21} & y_{22} & y_{23} \\ y_{31} & y_{32} & y_{33} \end{bmatrix} \begin{bmatrix} e_1 \\ e_2 \\ e_3 \end{bmatrix}$$    eq.(B. 1)

By the symmetrical properties of one periodic section (the voltage applied at port 3 will result in stress of the same value at port 1 and 2), the [y] matrix in eq.(B. 1) becomes eq.(B. 2) for Figure B. 4 and becomes eq.(B. 3) for Figure B. 5.



$$\begin{bmatrix} i_1 \\ i_2 \\ i_3 \end{bmatrix} = \begin{bmatrix} y_{11} & y_{12} & y_{13} \\ y_{12} & y_{11} & -y_{13} \\ y_{13} & -y_{13} & y_{33} \end{bmatrix} \begin{bmatrix} e_1 \\ e_2 \\ e_3 \end{bmatrix}$$    eq.(B. 2)
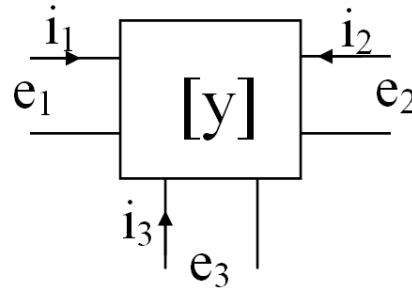
Figure B. 4   3-port network representation of one periodic section, with the change of sign between $Y_{13}$ and $Y_{23}$ to ensure that acoustic power flows symmetrically away from transducer



$$\begin{bmatrix} i_1 \\ i_2 \\ i_3 \end{bmatrix} = \begin{bmatrix} y_{11} & y_{12} & y_{13} \\ -y_{12} & -y_{11} & y_{13} \\ y_{13} & -y_{13} & y_{33} \end{bmatrix} \begin{bmatrix} e_1 \\ e_2 \\ e_3 \end{bmatrix}$$    eq.(B. 3)
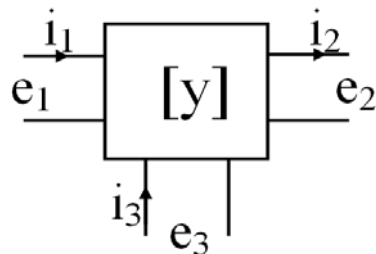
Figure B. 5   3-port network representation of one periodic section, with the no change of sign between $Y_{13}$ and $Y_{23}$

Applying circuit theory, definitions of [y] matrix elements are presented:

$$y_{11} = \left.\frac{i_1}{e_1}\right|_{\substack{e_2=0 \\ e_3=0}} \qquad ; \qquad y_{12} = \left.\frac{i_1}{e_2}\right|_{\substack{e_1=0 \\ e_3=0}}$$

$$y_{13} = \left.\frac{i_1}{e_3}\right|_{\substack{e_1=0 \\ e_2=0}} \qquad ; \qquad y_{33} = \left.\frac{i_3}{e_3}\right|_{\substack{e_1=0 \\ e_2=0}} \qquad\qquad \text{eq.(B. 4)}$$

And using trigonometric functions as follows:

$$tg\,\alpha - \frac{2}{\sin(2\alpha)} = -\cot g\,\alpha$$

$$tg\,\alpha - \frac{1}{\sin(2\alpha)} = \frac{1}{2}\left(tg\,\alpha - \cot g\,\alpha\right) \qquad\qquad \text{eq.(B. 5)}$$

$$tg\,\alpha \frac{3\cos(2\alpha)+1-tg\,\alpha\sin(4\alpha)-tg\,\alpha\sin(2\alpha)}{tg\,\alpha\sin(4\alpha)+tg\,\alpha\sin(2\alpha)-\cos(2\alpha)} = -tg(4\alpha)$$

The [y] matrix can be obtained for 2 models as follows:

+ for the "crossed-field" model:

$$y_{11} = -jG_0 \cot g(4\alpha)$$

$$y_{12} = \frac{jG_0}{\sin(4\alpha)}$$

$$y_{13} = -jG_0 tg\,\alpha \qquad\qquad \text{eq.(B. 6)}$$

$$y_{33} = j(2\omega C_0 + 4G_0 tg\,\alpha)$$

+ for the "in-line field" model:

$$y_{11} = -jG_0 \cot g\alpha \left( \frac{G_0}{\omega C_0} - \cot g(2\alpha) \right) \left[ 2 - \frac{\left( \frac{G_0}{\omega C_0} - \frac{1}{\sin(2\alpha)} \right)^2}{\left( \frac{G_0}{\omega C_0} - \cot g(2\alpha) \right)^2} \right]$$

$$y_{12} = jG_0 \frac{\cot g\alpha \left( \frac{G_0}{\omega C_0} - \frac{1}{\sin(2\alpha)} \right)^2}{2 \left( \frac{2G_0}{\omega C_0} - \cot g\alpha \right) \left( \frac{G_0}{\omega C_0} - \cot g(2\alpha) \right)}$$

$$y_{13} = -jG_0 \frac{tg\alpha}{1 - \frac{2G_0}{\omega C_0} tg\alpha}$$

$$y_{33} = \frac{j2\omega C_0}{1 - \frac{2G_0}{\omega C_0} tg\alpha}$$

eq.(B. 7)

In IDT including N periodic sections, the N periodic sections are connected acoustically in cascade and electrically in parallel as Figure B. 6.
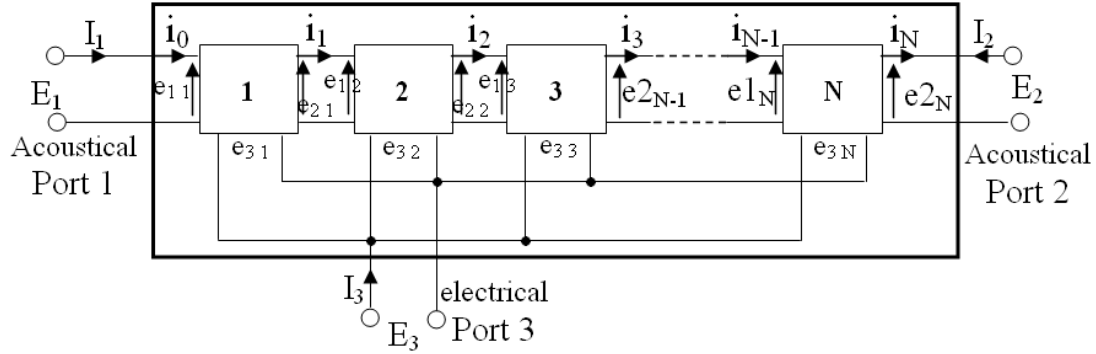


Figure B. 6  IDT including the N periodic sections connected acoustically in cascade and electrically in parallel

Because the symmetric properties of the IDT including N section like these of one periodic section, and from eq.(B. 2), eq.(B. 3), Figure B. 4 and Figure B. 5, the [Y] matrices of N-section IDT are represented as follows:

$$[Y] = \begin{bmatrix} Y_{11} & Y_{12} & Y_{13} \\ -Y_{12} & -Y_{11} & Y_{13} \\ Y_{13} & -Y_{13} & Y_{33} \end{bmatrix} \text{ corresponds to model}$$

(a)

$$[Y] = \begin{bmatrix} Y_{11} & Y_{12} & Y_{13} \\ Y_{12} & Y_{11} & -Y_{13} \\ Y_{13} & -Y_{13} & Y_{33} \end{bmatrix} \text{ corresponds to model}$$

(b)
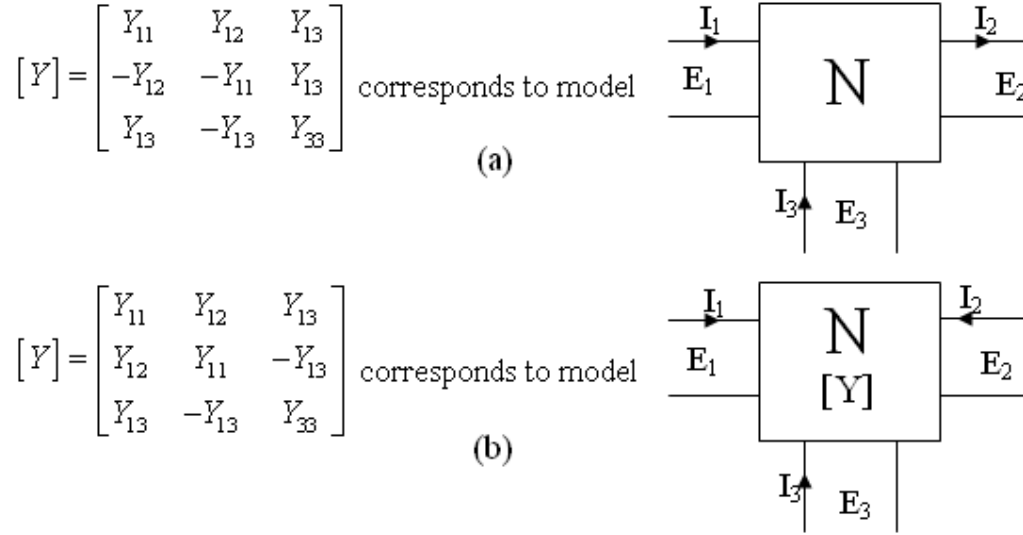
Figure B. 7   The [Y] matrices and the model corresponsive models

Since the periodic sections are identical, the recursion relation as follows can be obtained:

$$e_{1\,m} = e_{2\,m-1} \qquad \text{eq.(B. 8)}$$

$$e_{3\,N} = e_{3\,N-1} = e_{3\,N-2} = \ldots = e_{3\,2} = e_{3\,1} = E_3 \qquad \text{eq.(B. 9)}$$

$$i_{1\,m} = i_{2\,m-1} \qquad \text{eq.(B. 10)}$$

With m is integer number, m=1,2, …, N-1, N

The total transducer current is the sum of currents flowing into the N sections.

$$I_3 = i_{3\,1} + i_{3\,2} + \ldots + i_{3\,N-1} + i_{3\,N}$$

$$= (y_{13}e_{1\,1} - y_{13}e_{2\,1} + y_{33}\,e_{3\,1}) + (y_{13}e_{1\,2} - y_{13}e_{2\,2} + y_{33}\,e_{3\,2}) + \ldots \qquad \text{eq.(B. 11)}$$

$$+ (y_{13}e_{1\,N-1} - y_{13}e_{2\,N-1} + y_{33}\,e_{3\,N-1}) + (y_{13}e_{1\,N} - y_{13}e_{2\,N} + y_{33}\,e_{3\,N})$$

By applying eq.(B. 8), eq.(B. 9) and boundary conditions ($e_{11} = E_1$, $e_{2N}=E_2$), eq.(B. 11) becomes:

$$I_3 = y_{13}e_{1\,1} - y_{13}e_{2\,N} + Ny_{33}E_3$$

$$= y_{13}E_1 - y_{13}E_2 + Ny_{33}\,E_3 \qquad \text{eq.(B. 12)}$$

From Figure B. 7, the $Y_{13}$ and $Y_{33}$ can be expressed as:

$$Y_{13} = y_{13} \qquad \text{eq.(B. 13)}$$

$$Y_{33} = Ny_{33} \qquad \text{eq.(B. 14)}$$

Because the N periodic sections are connected acoustically in cascade and electrically in parallel, the model as in Figure B. 5 should be used to obtain the [Y] matrix of N-section IDT.

From eq.(B. 3) for one section, the $i_1$ and $i_2$ can be expressed

$$i_1 = y_{11}e_1 + y_{12}e_2 + y_{13}\,e_3$$

eq.(B. 15)

$$i_2 = -y_{12}e_1 - y_{12}e_2 + y_{13}\,e_3$$

Equations eq.(B. 15) can be represented in matrix form like [ABCD] form in electrical theory as follows:

$$\begin{bmatrix} e_2 \\ i_2 \end{bmatrix} = [K]\begin{bmatrix} e_1 \\ i_1 \end{bmatrix} + [L]e_3$$

eq.(B. 16)

Where

$$[K] = \begin{bmatrix} -\dfrac{y_{11}}{y_{12}} & \dfrac{1}{y_{12}} \\ \dfrac{y_{11}^2 - y_{12}^2}{y_{12}} & -\dfrac{y_{11}}{y_{12}} \end{bmatrix}$$

eq.(B. 17)

$$[L] = \begin{bmatrix} -\dfrac{y_{13}}{y_{12}} \\ \dfrac{y_{11}y_{13} + y_{12}y_{13}}{y_{12}} \end{bmatrix}$$

eq.(B. 18)

By applying eq.(B. 16) into N-section IDT as in Figure B. 6 and using eq.(B. 9), the second recursion relation is obtained as follows:

$$\begin{bmatrix} e_m \\ i_m \end{bmatrix} = [K]\begin{bmatrix} e_{m-1} \\ i_{m-1} \end{bmatrix} + [L]E_3$$

eq.(B. 19)

Where m is integer number, m=1,2, …, N-1, N

Starting eq.(B. 19) by using with m=N, and reducing m until m=1 gives the expression:

$$\begin{bmatrix} e_N \\ i_N \end{bmatrix} = [Q]\begin{bmatrix} e_0 \\ i_0 \end{bmatrix} + [X]E_3$$

eq.(B. 20)

Where

$$[Q] = [K]^N$$

eq.(B. 21)

$$[X] = \begin{bmatrix} X_1 \\ X_2 \end{bmatrix} = \sum_{n=0}^{N-1} [K]^n [L] \qquad \text{eq.(B. 22)}$$

Solving eq.(B. 20) and using the boundary conditions ($e_0 = E_1$, $i_0 = I_1$) gives:

$$I_1 = -\frac{Q_{11}}{Q_{12}} E_1 + \frac{1}{Q_{12}} E_2 - \frac{X_1}{Q_{12}} E_3 \qquad \text{eq.(B. 23)}$$

Consequently,

$$Y_{11} = -\frac{Q_{11}}{Q_{12}} \qquad \text{eq.(B. 24)}$$

$$Y_{12} = \frac{1}{Q_{12}} \qquad \text{eq.(B. 25)}$$

$$Y_{13} = -\frac{X_1}{Q_{12}} \qquad \text{eq.(B. 26)}$$

The $Y_{13}$ is known by eq.(B. 13), so eq.(B. 26) and matrix $[X]$ don't need to be solved.

To solve eq.(B. 24) and eq.(B. 25), matrix $[Q]$ should be solved.

In "crossed-field" model, matrix $[Q]$ can be represented in a simple form as follows:

$$[K] = \begin{bmatrix} \cos(4\alpha) & -jR_0 \sin(4\alpha) \\ -jG_0 \sin(4\alpha) & \cos(4\alpha) \end{bmatrix} \qquad \text{eq.(B. 27)}$$

$$[K]^2 = \begin{bmatrix} \cos(8\alpha) & -jR_0 \sin(8\alpha) \\ -jG_0 \sin(8\alpha) & \cos(8\alpha) \end{bmatrix} \qquad \text{eq.(B. 28)}$$

$$[K]^3 = \begin{bmatrix} \cos(12\alpha) & -jR_0 \sin(12\alpha) \\ -jG_0 \sin(12\alpha) & \cos(12\alpha) \end{bmatrix} \qquad \text{eq.(B. 29)}$$

. . . . . . etc. Consequently, matrix $[Q]$ will be given:

$$[Q] = [K]^N = \begin{bmatrix} \cos(N4\alpha) & -jR_0 \sin(N4\alpha) \\ -jG_0 \sin(N4\alpha) & \cos(N4\alpha) \end{bmatrix} \qquad \text{eq.(B. 30)}$$

From eq.(B. 24) and eq.(B. 25), $Y_{11}$ and $Y_{12}$ in "cross-field" model can be expressed:

$$Y_{11} = -jG_0 \cot g(N4\alpha) \qquad \text{eq.(B. 31)}$$

$$Y_{12} = \frac{jG_0}{\sin(N4\alpha)}$$

<div align="right">eq.(B. 32)</div>

In conclusion, matrix [Y] representation of N-section IDT is:

+ In "crossed-field" model, from eq.(B. 6), eq.(B. 13), eq.(B. 14), eq.(B. 31) and eq.(B. 32):

$$Y_{11} = -jG_0 \cot g(4N\alpha)$$

$$Y_{12} = \frac{jG_0}{\sin(4N\alpha)}$$

$$Y_{13} = -jG_0 tg\alpha$$

$$Y_{33} = jN(2\omega C_0 + 4G_0 tg\alpha)$$

<div align="right">eq.(B. 33)</div>

+ In "in-line field" model, from eq.(B. 7), eq.(B. 13), eq.(B. 14), eq.(B. 24) and eq.(B. 25):

$$Y_{11} = -\frac{Q_{11}}{Q_{12}}$$

$$Y_{12} = \frac{1}{Q_{12}}$$

$$Y_{13} = -jG_0 \frac{tg\alpha}{1 - \frac{2G_0}{\omega C_0} tg\alpha}$$

$$Y_{33} = \frac{j2\omega NC_0}{1 - \frac{2G_0}{\omega C_0} tg\alpha}$$

<div align="right">eq.(B. 34)</div>

Where [Q] can be calculated from eq.(B. 17) and eq.(B. 21).

## B. 2 EQUIVALENT CIRCUIT FOR "N+1/2" MODEL IDT

In case IDT includes N periodic sections (like in section 2.3.1 plus one finger (in color red) as shown in Figure B. 8 that we call "N+1/2" model IDT.
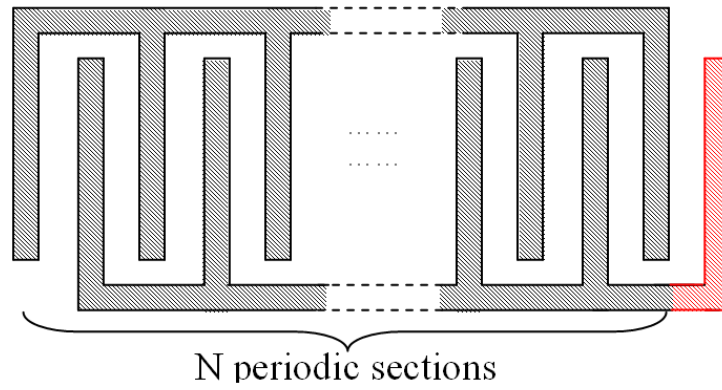
Figure B. 8   "N+1/2" model IDT

The equivalent circuit for this model is shown in Figure B. 9 and the matrix [Yd] representation is shown as in Figure B. 10 (letter "d"  stands for **d**ifferent from model [Y] in section 2.3.1
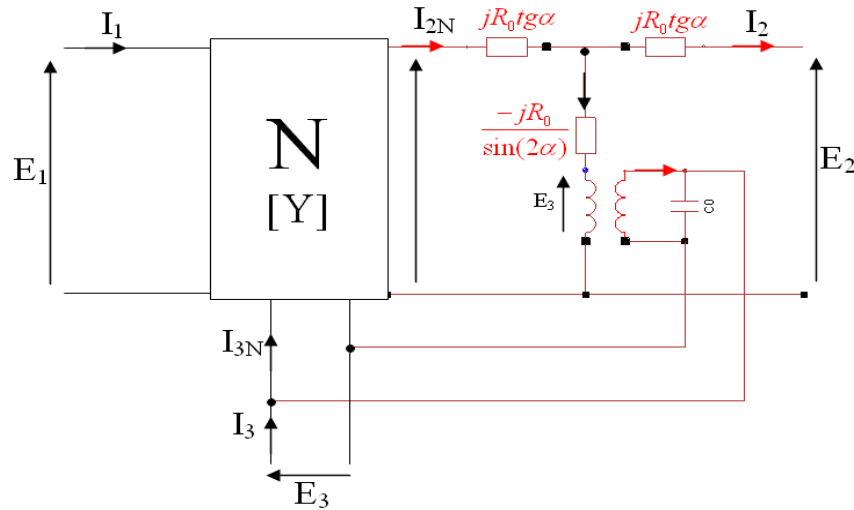


Figure B. 9   Equivalent circuit of "N+1/2" model IDT
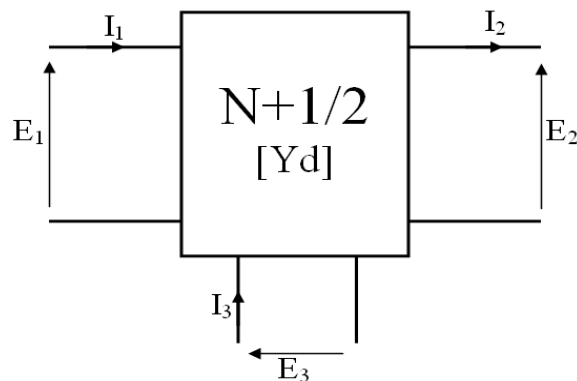


Figure B. 10   [Yd] matrix representation of "N+1/2" model IDT

The form of matrix [Yd] is:

$$[Yd] = \begin{bmatrix} Yd_{11} & Yd_{12} & Yd_{13} \\ Yd_{21} & Yd_{22} & Yd_{23} \\ Yd_{31} & Yd_{32} & Yd_{33} \end{bmatrix} \qquad \text{eq.(B. 35)}$$

The elements of [Yd] matrix for "crossed-field" model are given as follows:

$$Yd_{11} = jG_0 \left\{ \frac{1}{\sin^2(4N\alpha)(\cot g(2\alpha) + \cot g(4N\alpha))} - \cot g(4N\alpha) \right\} \qquad \text{eq.(B. 36)}$$

$$Yd_{12} = \frac{jG_0}{\sin(4N\alpha)} \left\{ \cos(2\alpha) - \frac{\sin(2\alpha)[\cot g(4N\alpha)\cos(2\alpha) - \sin(2\alpha)]}{\cos(2\alpha) + \cot g(4N\alpha)\sin(2\alpha)} \right\} \qquad \text{eq.(B. 37)}$$

$$Yd_{13} = jG_0 \left\{ \frac{(-tg\alpha + 2\cot g(4N\alpha)\sin^2\alpha + \sin(2\alpha))\sin(2\alpha)}{\sin(4N\alpha)(\cos(2\alpha) + \cot g(4N\alpha)\sin(2\alpha))} + \frac{2\sin^2\alpha}{\sin(4N\alpha)} - tg\alpha \right\}$$

eq.(B. 38)

$$Yd_{21} = -jG_0 \frac{1}{\sin(4N\alpha)(\cos(2\alpha) + \cot g(4N\alpha)\sin(2\alpha))} \qquad \text{eq.(B. 39)}$$

$$Yd_{22} = jG_0 \frac{\cot g(4N\alpha)\cos(2\alpha) - \sin(2\alpha)}{\cos(2\alpha) + \cot g(4N\alpha)\sin(2\alpha)} \qquad \text{eq.(B. 40)}$$

$$Yd_{23} = jG_0 \frac{-tg\alpha + 2\cot g(4N\alpha)\sin^2(2\alpha) + \sin(2\alpha)}{\cos(2\alpha) + \cot g(4N\alpha)\sin(2\alpha)} \qquad \text{eq.(B. 41)}$$

$$Yd_{31} = -jG_0 tg\alpha \qquad \text{eq.(B. 42)}$$

$$Yd_{32} = -jG_0 \sin(2\alpha) \qquad \text{eq.(B. 43)}$$

$$Yd_{33} = j\omega C_0(2N-1) + jG_0 \left\{ \sin(2\alpha) + (4N+1)tg\alpha \right\} \qquad \text{eq.(B. 44)}$$

## B. 3   SCATTERING MATRIX [S] FOR IDT

The scattering matrix [S] of a three-port network characterized by its admittance matrix [Y] is given by [40]:

$$S = \Pi_3 - 2Y(\Pi_3 + Y)^{-1} \qquad \text{eq.(B. 45)}$$

Where $\Pi_3$ is the 3x3 identity matrix.

After expanding this equation, the scattering matrix elements for a general three-port network are given by the following expressions:

$$S_{11} = \frac{1}{M}\left\{(1+Y_{33})(1-Y_{11}+Y_{22}-Y_{11}Y_{22}+Y_{12}Y_{21})+Y_{13}[Y_{31}(1+Y_{22})-Y_{21}Y_{32}]+Y_{23}[Y_{32}(Y_{11}-1)-Y_{12}Y_{31}]\right\}$$

eq.(B. 46)

$$S_{12} = -\frac{2}{M}\left[Y_{12}(1+Y_{33})-Y_{13}Y_{32}\right]$$

eq.(B. 47)

$$S_{13} = -\frac{2}{M}\left[Y_{13}(1+Y_{22})-Y_{12}Y_{23}\right]$$

eq.(B. 48)

$$S_{21} = -\frac{2}{M}\left[Y_{21}(1+Y_{33})-Y_{23}Y_{31}\right]$$

eq.(B. 49)

$$S_{22} = \frac{1}{M}\left\{(1+Y_{33})(1+Y_{11}-Y_{22}-Y_{11}Y_{22}+Y_{12}Y_{21})+Y_{13}[Y_{31}(Y_{22}-1)-Y_{21}Y_{32}]+Y_{23}[Y_{32}(Y_{11}+1)-Y_{12}Y_{31}]\right\}$$

eq.(B. 50)

$$S_{23} = -\frac{2}{M}\left[Y_{23}(1+Y_{11})-Y_{13}Y_{21}\right]$$

eq.(B. 51)

$$S_{31} = -\frac{2}{M}\left[Y_{31}(1+Y_{22})-Y_{21}Y_{32}\right]$$

eq.(B. 52)

$$S_{32} = -\frac{2}{M}\left[Y_{32}(1+Y_{11})-Y_{12}Y_{31}\right]$$

eq.(B. 53)

$$S_{33} = \frac{1}{M}\left\{(1-Y_{33})(1+Y_{11}+Y_{22}+Y_{11}Y_{22}-Y_{12}Y_{21})+Y_{13}[Y_{31}(Y_{22}+1)-Y_{21}Y_{32}]+Y_{23}[Y_{32}(Y_{11}+1)-Y_{12}Y_{31}]\right\}$$

eq.(B. 54)

where

$$M = \det(\Pi_3+Y)$$
$$= (1+Y_{33})[(1+Y_{11})(1+Y_{22})-Y_{12}Y_{21}]-Y_{23}[Y_{32}(1+Y_{11})-Y_{12}Y_{31}]-Y_{13}[Y_{31}(1-Y_{22})-Y_{21}Y_{32}]$$

eq.(B. 55)

For model IDT including N identical sections, these equations can be further simplified. In case of Figure B. 7(b):

$$Y_{11} = Y_{22}$$
$$Y_{21} = Y_{12}$$
$$Y_{31} = Y_{13}$$
$$Y_{23} = Y_{32} = -Y_{13}$$

eq.(B. 56)

Therefore, $S_{ij}$'s take the following form

$$S_{11} = S_{22} = \frac{1}{M}\left\{(1+Y_{33})(1-Y_{11}^2+Y_{12}^2)+2Y_{13}^2(Y_{11}+Y_{12})\right\}$$

eq.(B. 57)

$$S_{12} = S_{21} = -\frac{2}{M}\left[Y_{12}(1+Y_{33})+Y_{13}^2\right]$$

eq.(B. 58)

$$S_{13} = S_{31} = -\frac{2}{M}Y_{13}(1+Y_{11}+Y_{12})$$

eq.(B. 59)

$$S_{23} = S_{32} = -S_{13}$$

eq.(B. 60)

$$S_{33} = \frac{1}{M}\left\{(1-Y_{33})[(1+Y_{11})^2-Y_{12}^2]+2Y_{13}^2(1+Y_{11}+Y_{12})\right\}$$

eq.(B. 61)

Where

$$M = (1+Y_{33})[(1+Y_{11})^2-Y_{12}^2]-2Y_{13}^2(1+Y_{12})$$

eq.(B. 62)

## B. 4   EQUIVALENT CIRCUIT FOR SAW DEVICE BASE ON MASON MODEL, [ABCD] MATRIX REPRESENTATION

### B.4. 1   [ABCD] MATRIX REPRESENTATION OF IDT

In SAW device, each input and output IDTs have one terminal connected to admittance $G_0$. Therefore, one IDT can be represented as two-port network. [ABCD] matrix (as in Figure B. 11) is used to represent each IDT, because [ABCD] matrix representation has one interesting property that in cascaded network, the [ABCD] matrix of total network can be obtained easily by multiplying the matrices of elemental networks.
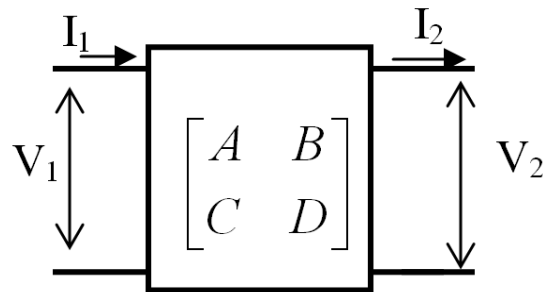


Figure B. 11   [ABCD] representation of two-port network for one IDT

To find the [ABCD] matrix for one IDT in SAW device, the condition that no reflected wave at one terminal of IDT, and the current-voltage relations by [Y] matrix in section are used as follows:
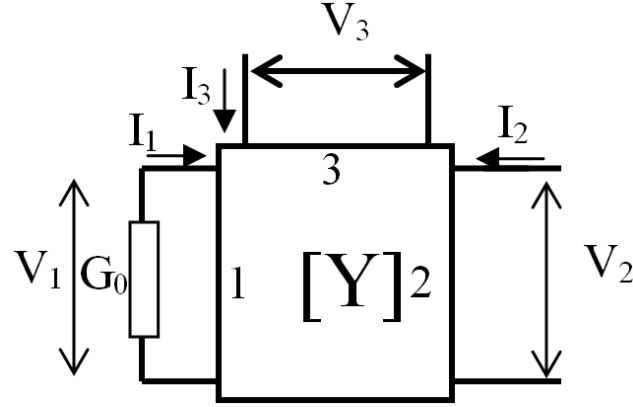


Figure B. 12   Two-port network for one IDT

$$\begin{bmatrix} I_1 \\ I_2 \\ I_3 \end{bmatrix} = \begin{bmatrix} Y_{11} & Y_{12} & Y_{13} \\ Y_{12} & Y_{11} & -Y_{13} \\ Y_{13} & -Y_{13} & Y_{33} \end{bmatrix} \begin{bmatrix} V_1 \\ V_2 \\ V_3 \end{bmatrix}$$

eq.(B. 63)

And $I_1 = -G_0 V_1$

eq.(B. 64)

From these current-voltage relations, the $V_3$ and $I_3$ are given:

$$V_3 = \frac{Y_{11}^2 - Y_{12}^2 + Y_{11}G_0}{Y_{12}Y_{13} + Y_{11}Y_{13} + Y_{13}G_0} V_2 - \frac{G_0 + Y_{11}}{Y_{12}Y_{13} + Y_{11}Y_{13} + Y_{13}G_0} I_2$$

eq.(B. 65)

$$I_3 = \frac{-(Y_{13}Y_{12} + Y_{13}Y_{11} + Y_{13}G_0)^2 + (Y_{11}Y_{33} - Y_{13}^2 + Y_{33}G_0)(Y_{11}^2 - Y_{12}^2 + Y_{11}G_0)}{(G_0 + Y_{11})(Y_{12}Y_{13} + Y_{11}Y_{13} + Y_{13}G_0)} V_2 - \frac{Y_{11}Y_{33} - Y_{13}^2 + Y_{33}G_0}{Y_{12}Y_{13} + Y_{11}Y_{13} + Y_{13}G_0} I_2$$

eq.(B. 66)

From eq.(B. 65) and eq.(B. 66), equivalence between port 3 in Figure B. 12 equals to port 1 in Figure B. 11, and consideration of direction of current $I_2$ in Figure B. 11 and Figure B. 12, [ABCD] matrix representation for two-port network of IDT in obtained:

$$A = \frac{Y_{11}^2 - Y_{12}^2 + Y_{11}G_0}{Y_{12}Y_{13} + Y_{11}Y_{13} + Y_{13}G_0}$$

eq.(B. 67)

$$B = \frac{G_0 + Y_{11}}{Y_{12}Y_{13} + Y_{11}Y_{13} + Y_{13}G_0}$$

eq.(B. 68)

$$C = \frac{-(Y_{13}Y_{12} + Y_{13}Y_{11} + Y_{13}G_0)^2 + (Y_{11}Y_{33} - Y_{13}{}^2 + Y_{33}G_0)(Y_{11}{}^2 - Y_{12}{}^2 + Y_{11}G_0)}{(G_0 + Y_{11})(Y_{12}Y_{13} + Y_{11}Y_{13} + Y_{13}G_0)}$$

eq.(B. 69)

$$D = \frac{Y_{11}Y_{33} - Y_{13}{}^2 + Y_{33}G_0}{Y_{12}Y_{13} + Y_{11}Y_{13} + Y_{13}G_0}$$

eq.(B. 70)

In case of "crossed-field" model, the [ABCD] can be further simplified:

$$A = \frac{\sin(4N\alpha) - j\cos(4N\alpha)}{tg\alpha\left[1 - \cos(4N\alpha) - j\sin(4N\alpha)\right]}$$

eq.(B. 71)

$$B = \frac{A}{G_0}$$

eq.(B. 72)

$$D = \frac{\sin(4N\alpha)}{1 - \cos(4N\alpha) - j\sin(4N\alpha)}\left[N(2\omega C_0 Z_0 \cot\alpha + 4)(\cot(4N\alpha) + j) + tg\alpha\right]$$

eq.(B. 73)

$$C = -\frac{1}{B} + G_0 D$$

eq.(B. 74)

One interesting property of [ABCD] of "crossed-field" mode is:

$$AD-BC=1$$

eq.(B. 75)

This means [ABCD] matrix is reciprocal.

In SAW device, the ouput IDT is inverse of input IDT. By the reciprocal property of [ABCD], the [ABCD] matrix of output IDT can be easily obtained:

$$A_{output} = D_{input}$$

eq.(B. 76)

$$B_{output} = B_{input}$$

eq.(B. 77)

$$C_{output} = C_{input}$$

eq.(B. 78)

$$D_{output} = A_{input}$$

eq.(B. 79)

in which N is replaced by M (number of periodic sections in output IDT)

Consequently, the [ABCD] matrix of output IDT is:

$$A_{out} = \frac{\sin(4M\alpha)}{1 - \cos(4M\alpha) - j\sin(4M\alpha)}\left[M(2\omega C_0 Z_0 \cot\alpha + 4)(\cot(4M\alpha) + j) + tg\alpha\right]$$

eq.(B. 80)

$$B_{out} = \frac{1}{G_0}\frac{\sin(4M\alpha) - j\cos(4M\alpha)}{tg\alpha\left[1 - \cos(4M\alpha) - j\sin(4M\alpha)\right]}$$

eq.(B. 81)

$$D_{out} = \frac{\sin(4M\alpha) - j\cos(4M\alpha)}{tg\alpha\left[1 - \cos(4M\alpha) - j\sin(4M\alpha)\right]}$$

eq.(B. 82)

$$C_{out} = -\frac{1}{B_{out}} + G_0 A_{out}$$

eq.(B. 83)

At the center frequency $f_0$, the [ABCD] matrix becomes infinite since $\alpha=0.5\pi(f/f_0)= 0.5\pi$. However, [ABCD] elements may be calculated by expanding for frequency very near frequency $f_0$.

By setting:

$$\alpha = \frac{\pi}{2}\frac{f - f_0}{f_0} + \frac{\pi}{2} = \frac{x}{2N} + \frac{\pi}{2}$$

eq.(B. 84)

Where $x = N\pi\frac{f - f_0}{f_0}$

eq.(B. 85)

By using the limit of some functions as follows:

$$\lim_{x\to0}[\sin(4N\alpha)] = \lim_{x\to0}[\sin(2x)] \approx 2x$$

eq.(B. 86)

$$\lim_{x\to0}[\cos(4N\alpha)] = \lim_{x\to0}[\cos(2x)] \approx 1$$

eq.(B. 87)

$$\lim_{x\to0}[tg\alpha] = \lim_{x\to0}[-\cot(\frac{x}{2N})] \approx -\frac{2N}{x}$$

eq.(B. 88)

The [ABCD] matrix of input IDT is obtained:

$$A \approx \frac{2x - j}{j4N}$$

eq.(B. 89)

$$B \approx \frac{1}{G_0}\frac{2x - j}{j4N}$$

eq.(B. 90)

$$C \approx 2\pi f C_0 x - 4NG_0 - j\left(\pi f C_0 + \frac{4NG_0}{2x - j}\right)$$

eq.(B. 91)

$$D \approx 2\pi f C_0 Z_0 x - 4N - j\pi f C_0 Z_0$$

eq.(B. 92)

### B.4. 2 [ABCD] MATRIX REPRESENTATION OF PROPAGATION PATH

Based on equivalent circuit star model of propagation path in Chapter 2, section 2.3.2, [ABCD] matrix representation of propagation way can be obtained clearly:

$$A_{path} = D_{path} = \cos 2\theta$$
<div align="right">eq.(B. 93)</div>

$$B_{path} = C_{path} = j \sin 2\theta$$
<div align="right">eq.(B. 94)</div>

$$\text{With } \theta = \frac{\pi fl}{v}$$
<div align="right">eq.(B. 95)</div>

Where l is the length of propagation path between two IDTs.

So, [ABCD] matrix representations of input IDT, propagation way and output IDT are obtained. They are cascaded as Figure B. 13:
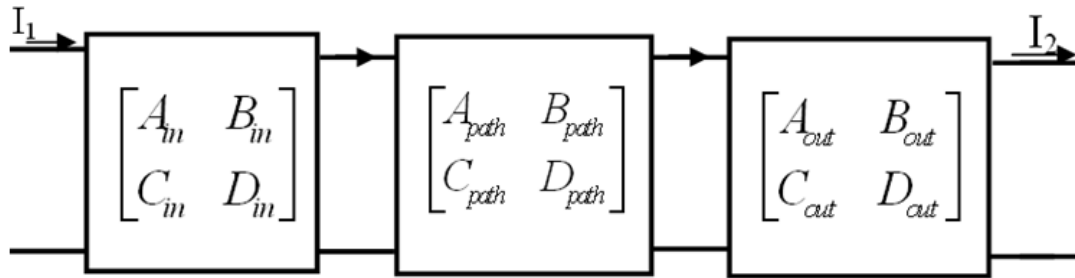


Figure B. 13   Cascaded [ABCD] matrices of input IDT, propagation way and output IDT

And the [ABCD] equivalent matrix of SAW device is shown in Figure B. 14
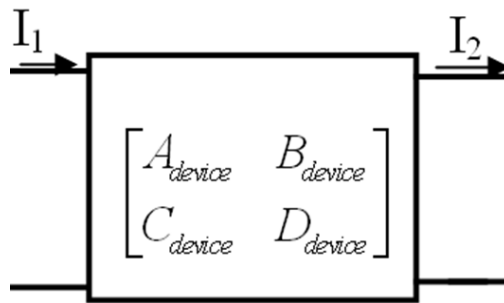


Figure B. 14   [ABCD] matrix of SAW device

[ABCD] matrix of delay line SAW is

$$\begin{bmatrix} A_{device} & B_{device} \\ C_{device} & D_{device} \end{bmatrix} = \begin{bmatrix} A_{in} & B_{in} \\ C_{in} & D_{in} \end{bmatrix} \begin{bmatrix} A_{path} & B_{path} \\ C_{path} & D_{path} \end{bmatrix} \begin{bmatrix} A_{out} & B_{out} \\ C_{out} & D_{out} \end{bmatrix}$$
<div align="right">eq.(B. 96)</div>

$$A_{device} = A_{in}A_{path}A_{out} + B_{in}C_{path}A_{out} + A_{in}B_{path}C_{out} + B_{in}D_{path}C_{out} \qquad \text{eq.(B. 97)}$$

$$B_{device} = A_{in}A_{path}B_{out} + B_{in}C_{path}B_{out} + A_{in}B_{path}D_{out} + B_{in}D_{path}D_{out} \qquad \text{eq.(B. 98)}$$

$$C_{device} = C_{in}A_{path}A_{out} + D_{in}C_{path}A_{out} + C_{in}B_{path}C_{out} + D_{in}D_{path}C_{out} \qquad \text{eq.(B. 99)}$$

$$D_{device} = C_{in}A_{path}B_{out} + D_{in}C_{path}B_{out} + C_{in}B_{path}D_{out} + D_{in}D_{path}D_{out} \qquad \text{eq.(B. 100)}$$

Where [ABCD]$_{in}$ is calculated from eq.(B. 71), eq.(B. 72), eq.(B. 73) and eq.(B. 74).

[ABCD]$_{out}$ is calculated from eq.(B. 80), eq.(B. 81), eq.(B. 82) and eq.(B. 83).

[ABCD]$_{path}$ is calculated from eq.(B. 93) and eq.(B. 94).

# Appendix  C
# Equipments used to control each fabrication step and to characterise device

After each step of fabrication, the devices are characterized to verify some requirements of each step, and consider whether the process can be continued or not. The devices were characterized morphologically by using optical, infrared microscopes, scanning electron microscope (SEM), optical interferometer and atomic force micrograph (AFM) equipments.

## C. 1   OPTICAL MICROSCOPES

The first method utilises Optical MicroScopes Olympus BH2-UMA, BH3-FO4A with Color View Soft Imaging System.

One image taken by Optical MicroScopes is shown as Figure C. 1.
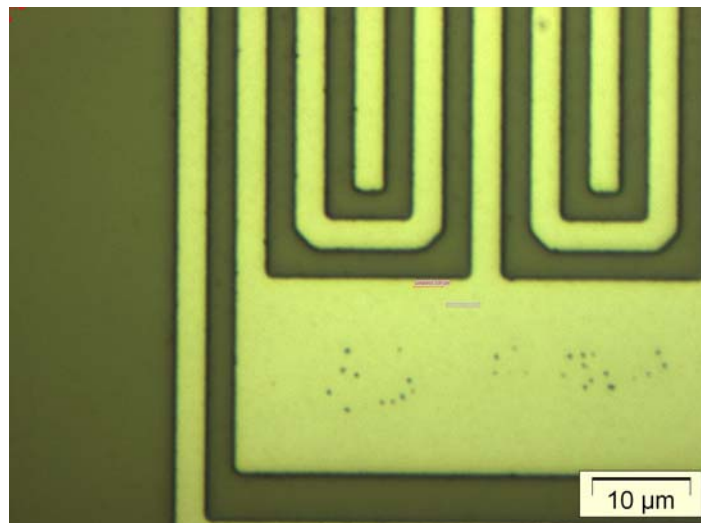


Figure C. 1   Optical Microscope image

## C. 2   SCANNING ELECTRON MICROSCOPE (SEM)

The second method used to record images was a Scanning Electron Microscope (SEM). All scanning electron micrographs for this research were taken with a Hitachi S-4160 SEM. This equipment is useful to verify the device after each step of fabrication. One example is shown in Figure C. 2 and Figure C. 3. Figure C. 2 shows the result after etching polyimide during 170s; it still remains polyimide near the edge of the metal. Consequently, the time of

etching polyimide is increased to 10s, and the step of etching was done again with the etching time of 10s. Result is shown as Figure C. 3 in which the remaining polyimide is removed.
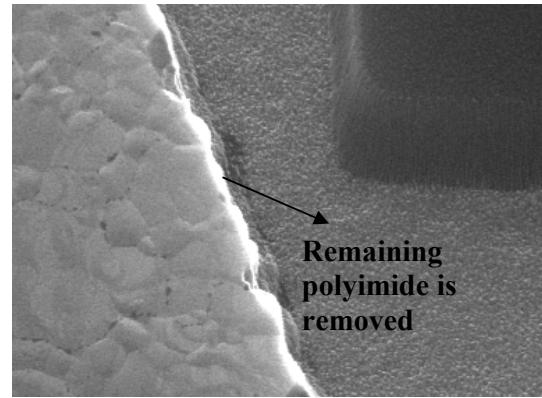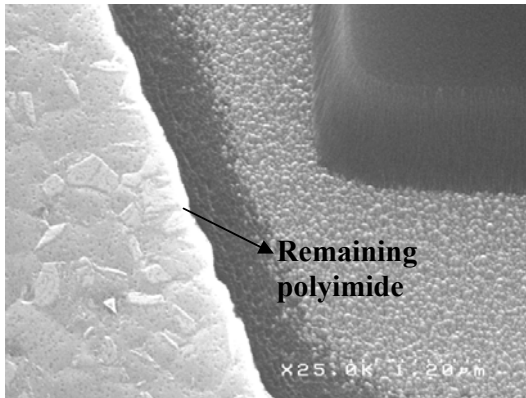


Figure C. 2   Etching polyimide during 170s          Figure C. 3   Etching polyimide during 180s

## C. 3   VEECO PROFILING SYSTEM

The third method is The Veeco WYKO NT3300 Profiling system. This is an optical profiler providing three-dimensional surface profile measurement without contact. WYKO surface profiler systems use two technologies to measure a wide range of surface heights: Phase Shifting Interferometry (PSI) mode (allows to measure smooth surfaces, small step), and Vertical Scanning Interferometry (VSI) mode (allows to measure rough surfaces, steps up to one millimetre high). One example taken by WYKO after creating membrane by HF etching is shown in Figure C. 4 and Figure C. 5 that allows us to measure the deformation of the membrane and the surface roughness.
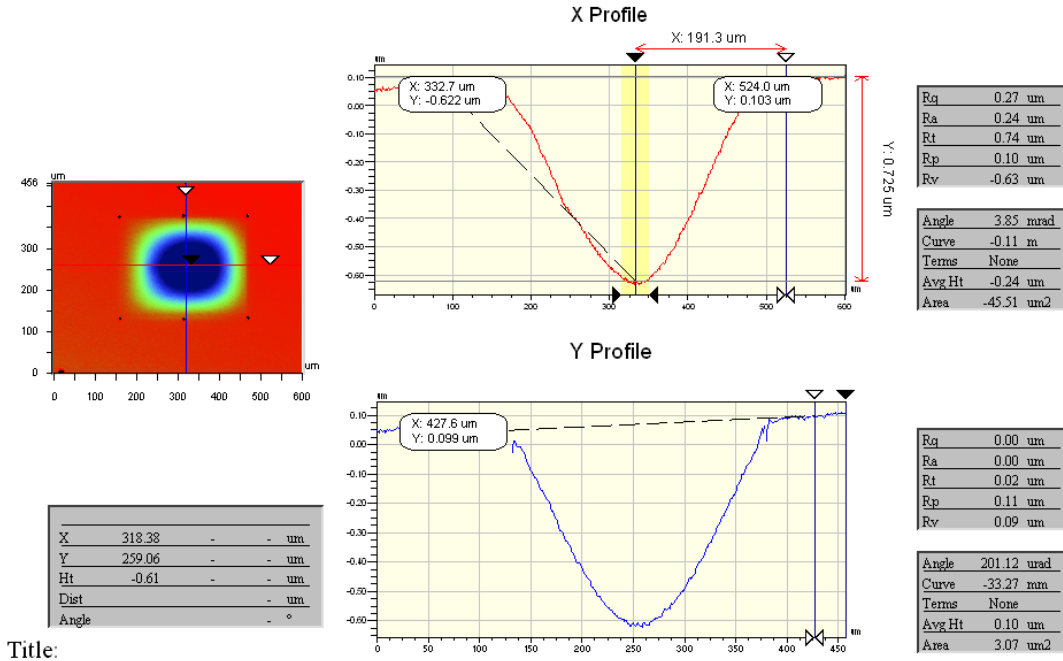
Figure C. 4   WYKO used to measure membrane deformation in 2-D
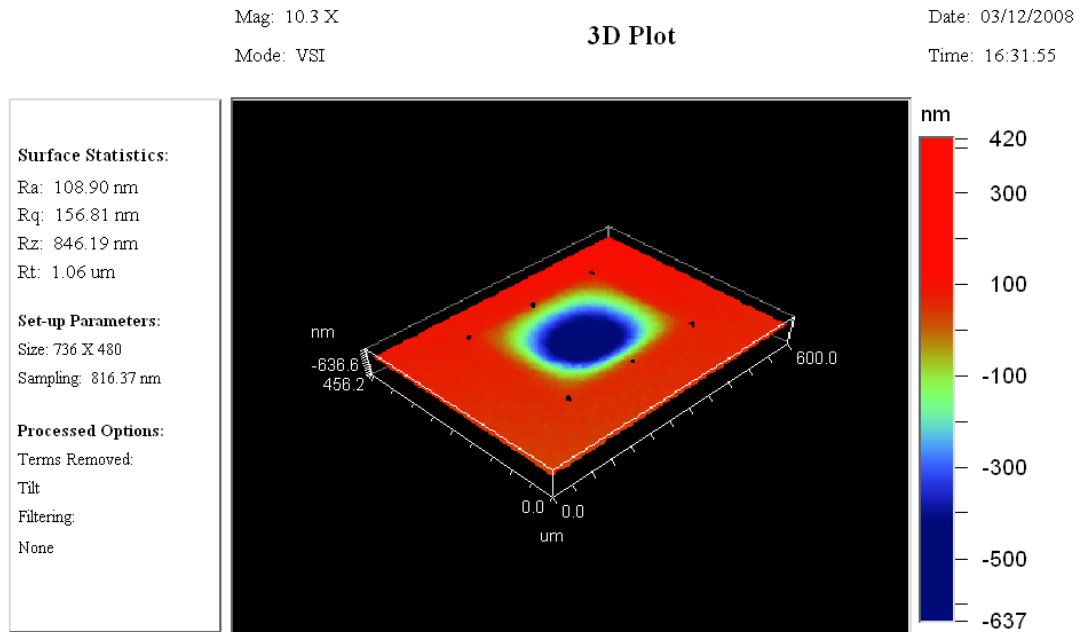


Figure C. 5   WYKO used for 3-dimensional surface profile measurement

Figure C. 6 shows the 3-D profile of device at the end of fabrication process.
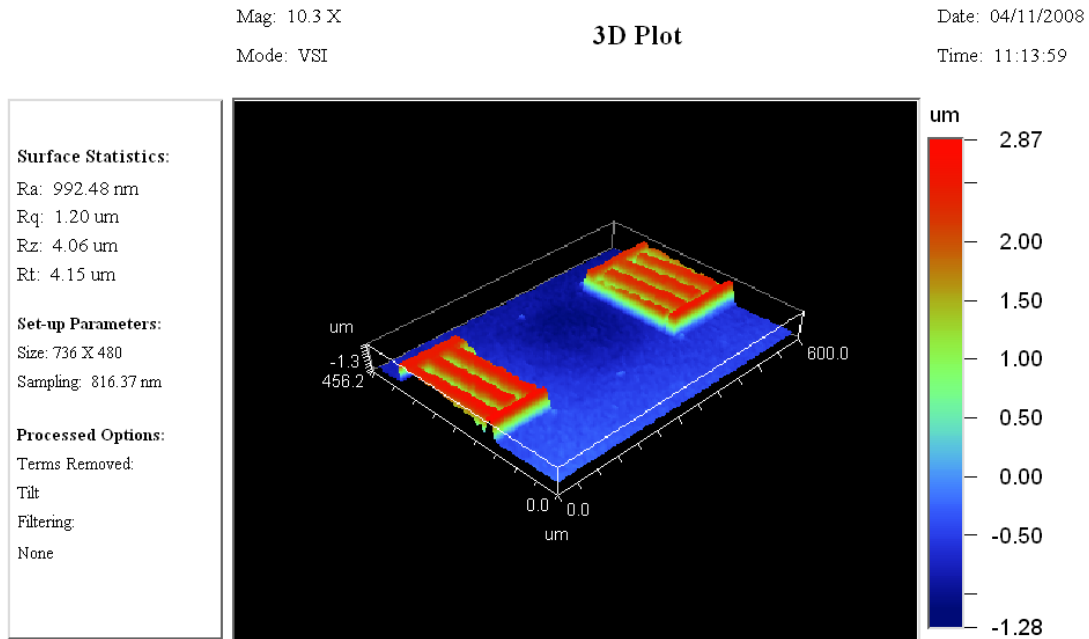
Figure C. 6   3-D profile of device fabricated completely

## C. 4   ATOMIC FORCE MICROGRAPH (AFM)

The morphological analysis of devices is also done by using the atomic force micrograph (AFM). The AFM examinations were performed by using a Nanoscope III (Digital Instrusment) operating in non-contact mode using TESP-ESP probes with silicon cantilever of length 125 µm, force constant of 42 N/m, high resonance frequency of 320kHz. The AFM is used to measure the roughness of a deposited layer. The roughness measurement is also done and verified by WYKO.

Figure C. 7 shows the AFM image of Si layer after that indicates the roughness Rms of 0.31nm. While the result from WYKO measurement (see Figure C. 8 and Figure C. 9) shows that Rms is 0.32nm. Consequently, to measure the roughness of a layer, AFM or WYKO could be used.
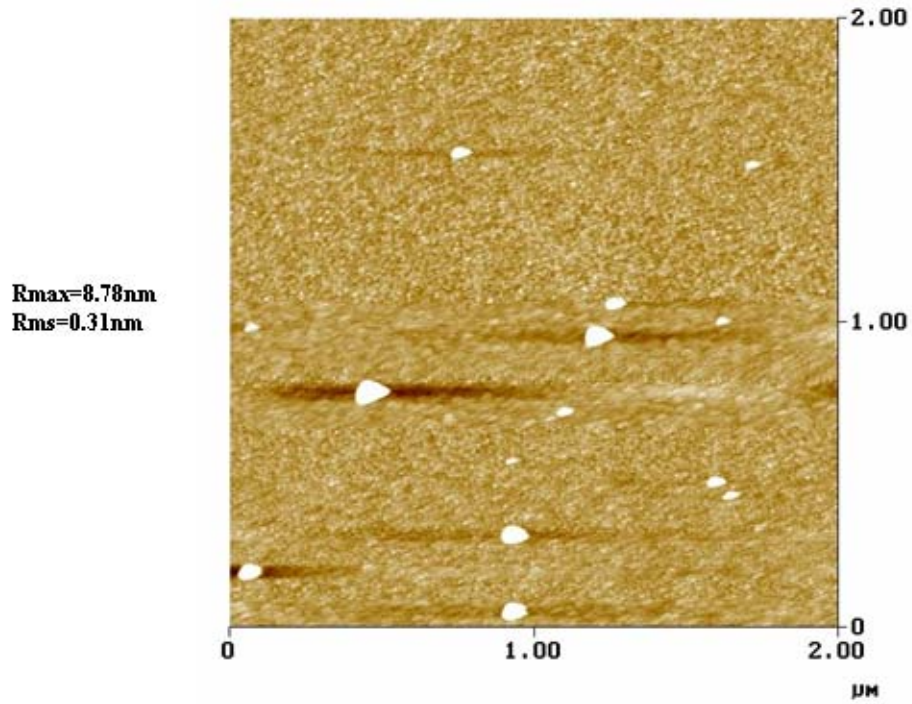
Figure C. 7   AFM image of Si layer
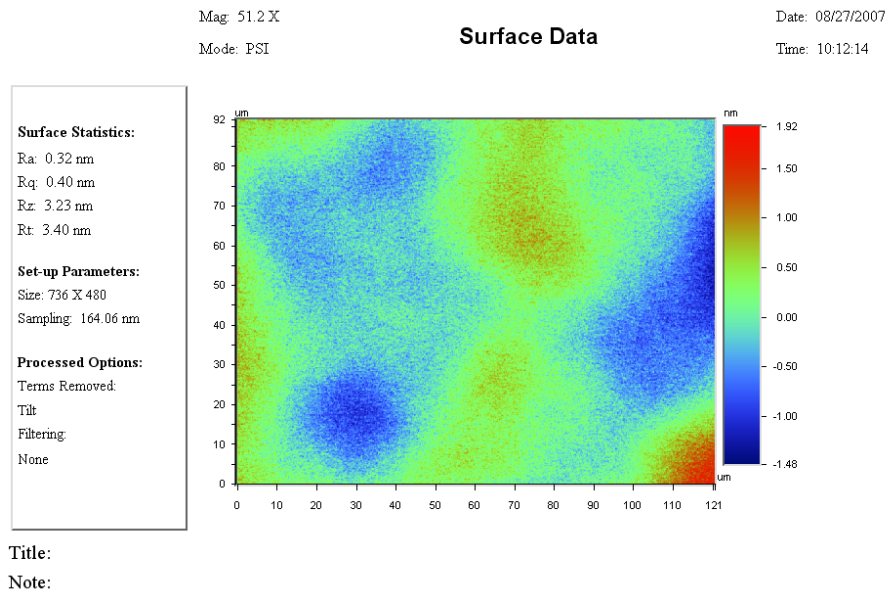


Figure C. 8   WYKO 2-D used to measure the roughness of Si layer
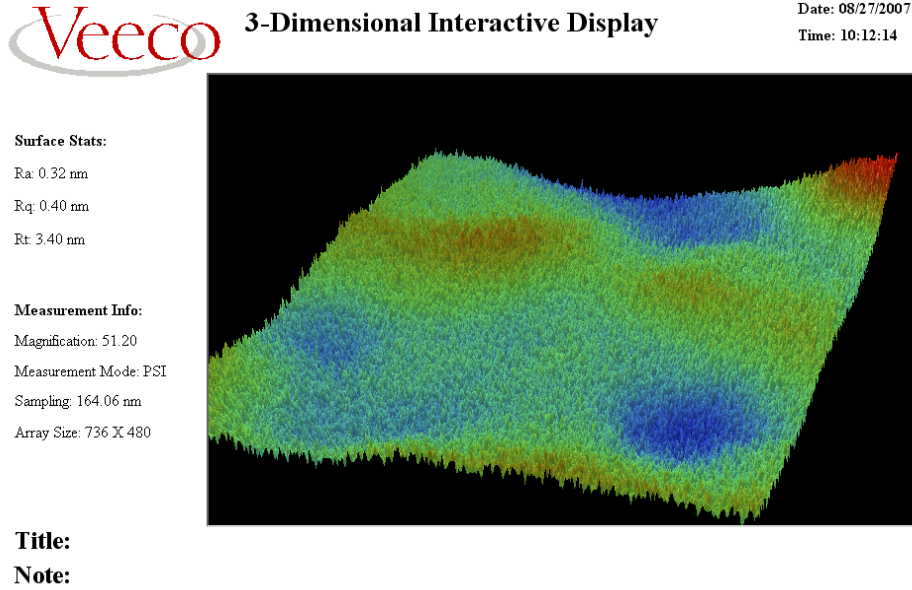
Figure C. 9   WYKO 3-D used to measure the roughness of Si layer after etching by HF 49% during 110 minutes

## C. 5   X-RAY DIFFRACTION (XRD) SYSTEM

In this study, Aluminium nitride (AlN) material is used as a piezoelectric active layer. It is important to characterise the crystal orientation of AlN films. It was determined by x-ray diffraction (XRD) system and evaluated by the full-width at half-maximum (FWHM) of x-ray rocking curves.

These crystalline orientation measurements are done with the conditions in Table C. 1.

Table C. 1   FWHM MEASUREMENT CONDITIONS

| Measurement condition | |
|---|---|
| Anode material | Cu |
| K-Alpha1 wavelength | 1.540598 |
| K-Alpha2 wavelength | 1.544426 |
| Ratio K-Alpha2/K-Alpha1 | 0.5 |
| Generator voltage | 40 |
| Tube current | 15 |
| Scan range | 11.025 – 25.005 |
| Scan step size | 0.02 |
| Number of points | 669 |
| Scan type | Continuous |
| Time per step | 0.2 |

## C. 6  SURFACE PROFILER TENCOR P-11

Surface Profiler TENCOR P-11 is other equipment used in this research. TENCOR P-11 is computerised, highly sensitive Surface Profiler that measures roughness, step height, and other surface characteristics in variety of applications. In this research, it is used to measure the thickness of layers.

## C. 7  FLEXUS F2320 DUAL WAVELENGTH STRESS MEASUREMENT SYSTEM

Stress in MEMS or microelectronics is a processing and reliability concern, especially for structures with thin films and small dimensions [162]. The metallic, dielectric, piezoelectric materials used have coefficients of thermal expansion (CTE) that differ substantially from those of MEMS, microelectronic substrates, such as silicon. Consequently, temperature changes, both during processing and in service, result in stresses in the films. In addition, many deposition processes, sputtering, evaporation, electroplating, and chemical vapor deposition, particularly low-temperature plating, sputtering processes and electroplating, result also in films with very different residual stress [162], [163].

The stresses that arise from these various causes are often quite large and may exceed the strength of the film, resulting in cracking or interfacial failure. The stress problems may become evident during fabrication process and make an otherwise attractive process nonviable; it may appear while in production and cause a yield loss; or, most serious of all, it may result in delayed failure and thus be a reliability problem.

The stress of a layer on a substrate has been determined by observing the curvature of the film and substrate after film deposition [162]-[165].

In this study, a commercial wafer curvature measurement system, a Flexus F2320 Dual Wavelength stress measurement system (KLA-Tencor Corporation [166]), was used to measure the wafer curvature and calculate the stress in the film. The principle of this measurement is the comparison of the curvature of the substrate before and after film deposition.

The quantitative analysis of the radius of curvature of a multilayer structure to extract the stress in the layers of the structure was first developed by G.G.Stoney [167], in which an expression for the curvature of a bimetallic strip was developed:

$$\sigma = \frac{Eh^2}{6Rt}$$

eq.(C. 1)

Where $\sigma$ is the stress, E is Young's modulus of the basic metal (or substrate), h is the thickness of the basic metal (substrate), t is the thickness of the coating (or film), and R is the radius of curvature of the bend strip. This expression is used when the thickness of the coating (film) is considered to be infinitesimal compared to the thickness of the basic metal (substrate).

The Stoney equation, with modification to account for biaxial stresses is shown as follows [168]-[171]:

$$\sigma = \frac{1}{(1-\upsilon)} \frac{Eh^2}{6Rt}$$

eq.(C. 2)

Where $\upsilon$ is the Poisson'ratio of the basic metal (substrate).

The Flexus F2320 Dual Wavelength stress measurement system uses a dual laser system to measure the radius of curvature, and calculate the stress by eq.(C. 2). The radius that is used in eq.(C. 2) must be corrected for initial curvature of the bare wafer. The uncoated wafer is scanned for the initial radius $R_1$, before deposition, and then scanned again for the radius $R_2$, after the film deposition. Then, the radius in eq.(C. 2) is as follows:

$$\frac{1}{R} = \frac{1}{R_2} - \frac{1}{R_1}$$

eq.(C. 3)

Consequently, the expression eq.(C. 2) become eq.(C. 4), and the stress was measured as follows:

$$\sigma = \frac{1}{(1-\upsilon)} \left( \frac{1}{R_2} - \frac{1}{R_1} \right) \frac{Eh^2}{6t}$$

eq.(C. 4)

# REFERENCE

[1]. Igor Aleksandrovich Viktorov, "Rayleigh and Lamb Waves, Physical Theory and Applications", Plenum Press, translated from Russian, with a Foreword by Warren P.Mason, 1967.

[2]. E.Benes, M.Groschl, F.Seifert, A.Pohl, "Comparison Between BAW and SAW Sensor Principle", IEEE Transactions on Ultrasonics, Ferroelectrics and Frequency Control, Vol.45, No.5, September 1998, pp.1314-1330.

[3]. D.S.Ballantine, R.M.White, S.J.Martin, A.J.Ricco, E.T.Zellers, G.C.Frye, H.Wohtien, "Acoustic Wave Sensor Theory, Design, and Physico-Chemical Applications", Academic Press, 1997, ISBN 0-12-0774607.

[4]. G.Schimetta, F.Dollinger, G.Scholl, R.Weigel, "A wireless pressure and temperature measurement using a SAW hybrid sensor", IEEE MTT-S Digest, 2000.

[5]. G.Schimetta, F.Dollinger, G.Scholl, R.Weigel, "Wireless pressure and temperature measurement using a SAW hybrid sensor", IEEE Ultrasonics Symposium, 2000.

[6]. G.Schimetta, F.Dollinger, G.Scholl, R.Weigel, "Optimized design and fabrication of a wireless pressure and temperature sensor unit based on SAW transponder technology", IEEE Microwave Symposium Digest, 2001, pp.335-358.

[7]. H.Scherr, G.Scholl, F.Seifert, R.Weigel, "Quartz pressure sensor based on SAW reflective delay line", IEEE Ultrasonics Symposium, 1996, pp.347-350.

[8]. A.Pohl, F.Seifert, "New applications of Wirelessly interrogable passive SAW sensors", IEEE Transactions On Microwave Theory and Techniques, Vol.46, No.12, December 1998.

[9]. Affred Pohl, Franz Seifert, "Wirelessly interrogable surface acoustic wave sensors for vehicular applications", IEEE Transactions On Instrumentation and Measurement, Vol.46, No.4, August 1997.

[10]. A.Talbi, Ph.D thesis, "Sensibilité des dispositifs à ondes élastiques de surface réalisés sur des structures monocouches de quartz et structure bicouche de ZnO/Si aux déformations mécaniques: application au capteur de pression", in French, December, 2003.

[11]. A.Talbi, M.Elhakiki, F.Sarry, O.Elmazria, L.Le Brizoual, P.Alnot, "A study of surface acoustic wave pressure sensor in ZnO/quartz structure", Sensors, Proceedings of IEEE, 2004, pp.550-553.

[12]. A.Talbi, F.Sarry, L.Le Brizoual, O.Elmazria, P.Alnot, "Development of SAW pressure sensor using ZnO/Si Structure", 2004 IEEE International Ultrasonics, Ferroelectrics, and Frequency Control Joint 50th Anniversary Conference, 2004, pp.566-570.

[13]. A.Talbi, F.Sarry, L.Le Brizoual, O.Elmazria, and P.Alnot, "Sezawa Mode SAW Pressure Sensors Based on ZnO/Si Structure", IEEE Transactions On Ultrasonics, Ferroelectrics, and Frequency Control, Vol. 51, No. 11, November 2004, pp.1421- 1426.

[14]. S.W.Wenzel, Richard M.White, "A multisensor employing an ultrasonic Lamb-wave oscillator", IEEE Transactions on Electron Devices, Vol.35, No.6, June 1988.

[15]. W.Mueller, Agilent Technologies, "A brief overview of FBAR technology", white paper, July 20, 2001, www.semiconductor.agilent.com.

[16]. R.Jakkaraju, et al., "Integrated approach to electrode and AlN depositions for bulk acoustic wave (BAW) devices" Microelectronic Engineering, Vol. 70, 2003, pp.566-570.

[17]. T.Nishihara, T.Yokoyama, T.Miyashita, Y.Satoh, "High performance and miniature thin film bulk acoustic wave filters for 5 GHz", Proc. IEEE Ultrasonic Symposium, Vol. 1, 2002, pp.969-972.

[18]. C.Zinck, A.de Grave, R.Jakkaraju, E.Defay, M.Harris, "A piezoelectric actuated SiN clamp-clamp beam for micro switch applications", Proc. Thinfilms 2004.

[19]. C.Zinck, Ph.D thesis, "Technologie et Caractérisations de Films Minces Piézoélectriques pour la Réalisation de Micro-systèmes", in French, 2004.

[20]. J. A. Ruffner, P.G. Clem, B.A. Tuttle, D. Dimos, D.M. Gonzales, "Effect of substrate composition on the piezoelectric response of reactively sputtered AlN thin Films", Thin Solid Films, Vol. 354, 1999, pp.256-261.

[21]. J. H.Harris, R.A.Youngman, R.G.Teller, "On the nature of the oxygenrelated defect in aluminum nitride", Journal of Material Resource, Vol. 5, 1990, pp.1763-1773.

[22]. M.A.Dubois, P.Muralt, "Stress and piezoelectric properties of aluminum nitride thin films deposited onto metal electrodes by pulsed direct current reactive sputtering" J. Appl. Phys. Vol. 89, 2001, pp.6389-6395.

[23]. M.Clement, E.Iborra, J.Sangrador, A.Sanz-Hervás, L.Vergara, and M.Aguilar, "Influence of sputtering mechanisms on the preferred orientation of aluminum nitride thin films", Journal of Applied Physics., Vol. 94, 2003, pp.1495-1500.

[24]. H.Nakahata, A.Hachigo, K.Higaki, S.Fujii, S.Shikata, and N.Fujimori, "Theoretical study on SAW characteristics of layered structures including a diamond layer", IEEE Transactions on Ultrasonics, Ferroelectrics and Frequency Control, vol. 42, 1995, pp. 362-375.

[25]. H.Nakahata, H. Kitabayashi, T.Uemura, A.Hachigo, K.Higaki, S.Fhjii, Y.Seki, K.Yoshida, and S.Shikata, "Study on surface acoustic wave characteristics of SiOz/ interdigitaltransducer/ ZnO/ diamond structure and fabrication of 2.5 GHz narrow band filter," Journal of Applied Physics., vol. 37, 1998, pp.2918-2922.

[26]. G.A.Slack, T.F.McNelly, "Growth of high purity AlN crystals", Journal of Crystal Growth 34, 1976, pp.263-279.

[27]. T.Uemura, S.Fujii, K.Itakura, H.Kitabayashi, A.Hachigo, H.Nakahata, S.Shikata, K.Ishibashi, T.Imai, "Development of Low Loss and High Q Value Diamond Surface Acoustic Wave (SAW) Devices Consisting of Fine-Grained Diamond", SEI Technical Review No.54, June 2002, pp.41-46.

[28]. B.M.Epelbaum, M.Bickerman, A.Winnacker, "Growth of bulk AlN crystals for SAW devices", University of Erlangen-Nurnberg, Dept of Materials Science 6, Martensstr.7, D-91058 Erlangen, Germany.

[29]. J.Bjurstrom, D.Rosen, I.Katardjiev, V.M.Yanchev, I.Petrov, "Dependence of the Electromechanical Coupling on the Degree of Orientation of c-Textured Thin AlN Films", IEEE Transactions On Ultrasonics, Ferroelectrics, And Frequency Control, Vol. 51, No. 10, October 2004.

[30]. H.M.Liaw, and F.*S*. Hickernell, "The characterization of sputtered polycrystalline aluminum nitride on silicon by surface acoustic wave measurements", IEEE Transactions On Ultrasonics, Ferroelectrics, And Frequency Control, Vol. 42, No. 3, May 1995.

[31]. O.Elmazria, V.Mortet, M.E.Hakiki, M.Nesladek, P.Alnot, "High velocity SAW using aluminum nitride film on unpolished nucleation side of free-standing CVD diamond", IEEE Transactions On Ultrasonics, Ferroelectrics, And Frequency Control, Vol. 50, No. 6, June 2003.

[32]. O.Elmazria, M.E.Hakiki, V.Mortet, B.M.Assouar, M.Nesladek, M.Vanecek, P.Bergonzo, P.Alnot, "Effect of diamond nucleation process on propagation losses of AlN/diamond SAW filter", IEEE Transactions On Ultrasonics, Ferroelectrics, And Frequency Control, Vol. 51, No. 12, December 2004.

[33]. E.Iborra, M.Clement, J.Sangrador, A.Sanz-Hervas, L.Vergara, M.Aguilar, "Effect of particle bombardment on the orientation and the residual stress of sputtered AlN films for SAW devices", IEEE Transactions On Ultrasonics, Ferroelectrics, And Frequency Control, Vol. 51, No. 3, March 2004, pp.352-358.

[34]. K.S.Kao, C.C.Cheng, and Y.C.Chen, "Synthesis and surface acoustic wave properties of AlN films deposited on $LiNbO_3$ substrates", IEEE Transactions On Ultrasonics, Ferroelectrics, And Frequency Control, Vol. 49, No. 3, March 2002.

[35]. M.Akiyama, K.Nagao, N.Uneo, H.Tateyama, T.Yamada, "Influence of metal electrodes on crystal orientation of aluminum nitride thin films", Science Direct, Vacuum 74, 2004, pp.699-703.

[36]. Y.Takagaki, T.Hesjedal, O.Brandt, K.H.Ploog, "Surface-acoustic-wave transducers for the extremely-high-frequency range using AlN∕SiC(0001)", Institute Of Physics Publishing, Semicond. Sci. Technol. 19 (2004) 256–259.

[37]. M.Benetti, D.Cannata, A.DAmico, F.Di Pietrantonio, A.Macagnano, E.Verona, "SAW Sensors on Aln/Diamond/Si Structures", IEEE, 0-7803-8692-2/04/2004.

[38]. C.C.W.Ruppel, W.Ruile, G.Scholl, K.Ch.Wagner, and O.Manner, "Review of models for low-loss filter design and applications", IEEE Ultransonics Symposium, pp.313-324, 1994.

[39]. L.A.Coldren, and R.L.Rosenberg, "Scattering matrix approach to SAW resonators" , IEEE Ultrasonics Symposium, 1976, pp.266-271.

[40]. R.W.Newcomb, "Linear Multiport Synthesis", McGraw Hill, 1966.

[41]. C.Elachi, "Waves in Active and Passive Periodic Structures: A Review", Proceedings of the IEEE, vol.64, No.12, December 1976, pp.1666-1698

[42]. M.Hikita, A.Isobe, A.Sumioka, N.Matsuura, and K.Okazaki, "Rigorous Treatment of Leaky SAW's and New Equivalent Circuit Representation for Interdigital Transducers", IEEE Transactions on Ultrasonics, Ferroelectrics, and Frequency Control, Vol.43, No.3, May 1996.

[43]. L.F.Brown, and D.L.Carlson, "Ultrasound Transducer Models for Piezoelectric Polymer Films", IEEE Transactions on Ultrasonics, Ferroelectrics, and Frequency Control, Vol.36, No.3, May 1989.

[44]. K.Hashimoto, and M.Yamaguchi, "Precise simulation of surface transverse wave devices by discrete Green function theory", IEEE Ultrasonics Symposium, 1994, pp.253-258.

[45]. K.Hashimoto, G.Endoh, and M.Yamaguchi, "Coupling-of-modes modelling for fast and precise simulation of leaky surface acoustic wave devices", IEEE Ultrasonics Symposium, 1995, pp.251-256.

[46]. K.Hashimoto, and M.Yamaguchi, "General-purpose simulator for leaky surface acoustic wave devices based on Coupling-Of-Modes theory", IEEE Ultrasonics Symposium, 1996, pp.117-122.

[47]. K.Hashimoto, "Surface Acoustic Wave Devices in Telecommunications, Modelling and Simulation", Springer, 2000, ISBN: 9783540672326.

[48]. P.M.Smith, and C.K.Campbell, "A Theoretical and Experimental Study of Low-Loss SAW Filters with Interdigitated Interdigital Transducers", IEEE Transactions on Ultrasonics, Ferroelectrics, and Frequency Control, Vol.36, No.1, January 1989, pp.10-15.

[49]. C.K.Campbell, "Modelling the Transverse-Mode Response of a Two-Port SAW Resonator", IEEE Transactions on Ultrasonics, Ferroelectrics, and Frequency Control, Vol.38, No.3, May 1991, pp.237-242.

[50]. C.K.Campbell, P.M.Smith, and P.J.Edmonson, "Aspects of Modeling the Frequency Response of a Two-Port Waveguide-Coupled SAW Resonator-Filter", IEEE Transactions on Ultrasonics, Ferroelectrics, and Frequency Control, Vol.39, No.6, November 1992, pp.768-773.

[51]. C.K.Campbell, "Longitudinal-Mode Leaky SAW Resonator Filters on $64^0$ Y-X Lithium Niobate", IEEE Transactions on Ultrasonics, Ferroelectrics, and Frequency Control, Vol.42, No.5, September 1995, pp.883-888.

[52]. C.K.Campbell, and P.J.Edmonson, "Conductance Measurements on a Leaky SAW Harmonic One-Port Resonator", IEEE Transactions on Ultrasonics, Ferroelectrics, and Frequency Control, Vol.47, No.1, January 2000, pp.111-116.

[53]. C.K.Campbell, and P.J.Edmonson, "Modeling a Longitudinally Coupled Leaky-SAW Resonator Filter with Dual-Mode Enhanced Upper-Sideband Suppression", IEEE Transactions on Ultrasonics, Ferroelectrics, and Frequency Control, Vol.48, No.5, September 2001, pp.1298-1301.

[54]. J.Munshi, and S.Tuli, "A Circuit Simulation Compatible Surface Acoustic Wave Interdigital Transducer Macro-Model", IEEE Transactions on Ultrasonics, Ferroelectrics, and Frequency Control, Vol.51, No.7, July 2004, pp.782-784.

[55]. M.P.Cunha, and E.L.Adler, "A Network Model For Arbitrarily Oriented IDT Structures", IEEE Transactions on Ultrasonics, Ferroelectrics, and Frequency Control, Vol.40, No.6, November 1993, pp.622-629.

[56]. D.R.Mahapatra, A.Singhal, and S.Gopalakrishnan, "Numerical Analysis of Lamb Wave Generation in Piezoelectric Composite IDT", IEEE Transactions on Ultrasonics, Ferroelectrics, and Frequency Control, Vol.52, No.10, October 2005, pp.1851-1860.

[57]. A. B. Bhattacharyya, Suneet Tuli, and S.Majumdar, "SPICE Simulation of Surface Acoustic Wave Interdigital Transducers", IEEE Transactions on Ultrasonics, Ferroelectrics, and Frequency Control, Vol.42, No.4, July 1995, pp.784-786.

[58]. C.M.Panasik, and B.J.Hunsinger, "Scattering Matrix Analysis Of Surface Acoustic Wave Reflectors And Transducers", IEEE Transactions On Sonics And Ultrasonics, Vol.SU-28, No.2, March 1981, pp.79-91.

[59]. W.Soluch, "Admittance Matrix Of A Surface Acoustic Wave Interdigital Transducer", IEEE Transactions on Ultrasonics, Ferroelectrics, and Frequency Control, Vol.40, No.6, November 1993, pp.828-831.

[60]. W.Soluch, "Scattering Matrix Approach To One Port SAW Resonators", IEEE Frequency Control Symposium, 1999, pp.859-862.

[61]. W.Soluch, "Design of SAW Synchronous Resonators on ST Cut Quartz", IEEE Transactions on Ultrasonics, Ferroelectrics, and Frequency Control, Vol.46, No.5, September 1999, pp.1324-1326.

[62]. W.Soluch, "Scattering Matrix Approach To One-Port SAW Resonators", IEEE Transactions on Ultrasonics, Ferroelectrics, and Frequency Control, Vol.47, No.6, November 2000, pp.1615-1618.

[63]. W.Soluch, "Scattering Matrix Approach To STW Resonators", IEEE Transactions on Ultrasonics, Ferroelectrics, and Frequency Control, Vol.49, No.3, March 2002, pp.327-330.

[64]. W.Soluch, "Scattering Analysis Of Two-Port SAW Resonators", IEEE Transactions on Ultrasonics, Ferroelectrics, and Frequency Control, Vol.48, No.3, May 2001, pp.769-772.

[65]. W.Soluch, "Scattering Matrix Approach To STW Multimode Resonators", Electronics Letters, 6th January 2005, Vol.41, No.1.

[66]. K.Nakamura, "A Simple Equivalent Circuit For Interdigital Transducers Based On The Couple-Mode Approach", IEEE Transactions on Ultrasonics, Ferroelectrics, and Frequency Control, Vol.40, No.6, November 1993, pp.763-767.

[67]. K. Nakamura, and K.Hirota, "Equivalent circuit for Unidirectional SAW-IDT's based on the Coupling-Of-modes theory", IEEE Trans on Ultrasonics, Ferroelectrics, and Frequency Control, Vol.43, No.3, May 1996, pp.467-472.

[68]. A.H.Fahmy, and E.L.Adler, "Propagation of acoustic surface waves in multilayers: A matrix description." Applied Physics Letter, vol. 22, No.10, 1973, pp. 495-497.

[69]. E.L.Adler, "Matrix methods applied to acoustic waves in multilayers", IEEE Transactions on Ultrasonics, Ferroelectrics, and Frequency Control, Vol.37, No.6, November 1990, pp.485-490.

[70]. E.L.Adler, "SAW and Pseudo-SAW properties using matrix methods", IEEE Transactions on Ultrasonics, Ferroelectrics, and Frequency Control, Vol.41, No.5, September 1994, pp.699-705.

[71]. G.F.Iriarte, F.Engelmark, I.V.Katardjiev, V.Plessky, V.Yantchev, "SAW COM-parameter extraction in AlN/diamond layered structures", IEEE Transactions On Ultrasonics, Ferroelectrics, And Frequency Control, Vol. 50, No. 11, November 2003.

[72]. M.Mayer, G.Kovacs, A.Bergmann, and K.Wagner, "A Powerful Novel Method for the Simulation of Waveguiding in SAW Devices", IEEE Ultrasonics Symposium, 2003, pp.720-723.

[73]. W.P.Mason, "Electromechanical Transducer and Wave Filters", second edition, D.Van Nostrand Company Inc, 1948.

[74]. W.P.Mason, "Physical Acoustics", Vol 1A, Academic Press, New York 1964.

[75]. S.D.Senturia, "Microsystem Design", Kluwer Academic Publishers, 2001, ISBN 0-7923-7246-8.

[76]. W.Marshall Leach, "Controlled-Source Analogous Circuits and SPICE models for Piezoelectric transducers", IEEE Transactions on Ultrasonics, Ferroelectrics, and Frequency Control, Vol.41, No.1, January 1994.

[77]. D.A.Berlincourt, D.R.Curran and H.Jaffe, Chapter 3, "Piezoelectric and Piezomagnetic Materials and Their Function in Tranducers".

[78]. W.R.Smith, H.M.Gerard, J.H.Collins, T.M.Reeder, and H.J.Shaw, "Analysis of Interdigital Surface Wave Transducers by Use of an Equivalent Circuit Model", IEEE Transaction on MicroWave Theory and Techniques, No.11, November 1969, pp.856-864.

[79]. C. K. Campbell, "Surface acoustic wave devices," in Mobile and Wireless Communications, New York: Academic, 1998.

[80]. O.Tigli, and M.E.Zaghloul, "A Novel Saw Device in CMOS: Design, Modeling, and Fabrication", IEEE Sensors journal, vol. 7, No. 2, February 2007, pp.219-227.

[81]. K.Nakamura, "A Simple Equivalent Circuit For Interdigital Transducers Based On The Couple-Mode Approach", IEEE Transactions on Ultrasonics, Ferroelectrics, and Frequency Control, Vol.40, No.6, November 1993, pp.763-767.

[82]. M.Hofer, N.Finger, G.Kovacs, J.Schoberl, S.Zaglmayr, U.Langer, and R.Lerch, "Finite-Element Simulation of Wave Propagation in Periodic Piezoelectric SAW Structures", IEEE Transactions on Ultrasonics, Ferroelectrics, and Frequency Control, Vol.53, No.6, June 2006, pp.1192-1201.

[83]. M. Hofer, N. Finger, G. Kovacs, J. Schoberl, U. Langer, and R. Lerch, "Finite-element simulation of bulk and surface acoustic wave (SAW) interaction in SAW devices" , IEEE Ultrasonics Symposium, 2002.

[84]. Online: http://www.comsol.com/

[85]. Online: http://www.coventor.com/

[86]. Online: http://www.ansys.com/

[87]. M.E.Hakiki, O.Elmazria, M.B.Assouar, V.Mortet, L.Le Brizoual, M.Vanecek, P.Alnot, "ZnO/AlN/diamond layered structure for SAW devices combining high velocity and high electromechanical coupling coefficient", Science Direct, Diamond & Related Materials 14, 2005, pp.1175–1178.

[88]. B.Diem, P.Rey, S.Renard, S.V.Bosson, H.Bono, F.Michel, M.T.Delaye, G.Delapierre, "SOI 'SIMOX'; from bulk to surface micromachining, a new age for silicon sensors and actuators", Sensors and Actuators A, vol. 46, 1995, pp.8-16.

[89]. C. Campbell, "Surface acoustic wave devices and their signal processing applications", Academic Press, 1989.

[90]. D. P. Morgan, "Surface-Wave Devices for Signal Processing", Elsevier, 1991.

[91]. M.Hikita, N.Shibagaki, K.Sakiyama, K.Hasegawa, "Design Methodology and Experimental Results for New Ladder-Type SAW Resonator Coupled Filters", IEEE Transactions on Ultrasonics, Ferroelectrics, and Frequency Control, Vol.42, No.4, July 1995.

[92]. V. I. Anisimkin, I. M. Kotelyanskii, V. I. Fedosov, C. Caliendo, P.Verardi, and E. Verona, "Analysis of the different contributions to the response of SAW gas sensors", IEEE Ultrasonics Symposium,1995.

[93]. V. I. Anisimkin, I. M. Kotelyanskii, P. Verardi, and E. Verona, "Elastic properties of thin-film palladium for surface acoustic wave (SAW) sensors", Sensors and Actuators, B: Chemical, vol. B23, 1995, pp.203-208.

[94]. R.M.White, "Acoustic sensors for physical, chemical and biochemical applications", IEEE International Frequency Control Symposium, 1998, pp.587-594.

[95]. M. Penza, V. I. Anisimkin, "Surface acoustic wave humidity sensor using polyvinyl-alcohol film", Sensors and Actuators A: Physical, Volume 76, Issues 1-3, 30 August 1999, pp. 162-166.

[96]. A.Pohl, "A Review of Wireless SAW Sensors", IEEE Transactions on Ultrasonics, Ferroelectrics, and Frequency Control, Vol.47, No.2, March 2000.

[97]. D. D. Stubbs, S.-H. Lee, and W. D. Hunt, "Molecular recognition for electronic noses using surface acoustic wave immunoassay sensors," IEEE Sensors Journal, vol. 2, 2002, pp. 294-300.

[98]. M. Z. Atashbar, B. J. Bazuin, M. Simpeh, and S. Krishnamurthy, "3-D Finite element simulation model of SAW Palladium Thin Film Hydrogen Sensor",IEEE International Ultrasonics, Ferroelectrics and Frequency control Joint 50th Anniversary Conference, 2004.

[99]. L.M.Reindl, I.M.Shrena, "Wireless Measurement of Temperature Using Surface Acoustic Waves Sensors", IEEE Transactions on Ultrasonics, Ferroelectrics, and Frequency Control, Vol.51, No.11, November 2004.

[100]. M.N.Hamidon, V.Skarda, N.M.White, F.Krispel, P.Krempl, M.Binhack, W.Buff, "Fabrication of high temperature surface acoustic wave devices for sensor applications", Sensors and Actuators A, 123-124, 2005, pp.403-407.

[101]. M. Z. Atashbar, B. J. Bazuin, M. Simpeh, and S. Krishnamurthy, " 3D FE simulation of H2 SAW gas sensor.," Sensors and Actuators, B: Chemical, vol. B111-B112, 2005, pp. 213-218.

[102]. D.S Ballantine, R.M.White, S.J.Martin, A.J.Ricco, E.T.Zellers, G.C.Frye, H.Wohtien, "Acoustic Wave Sensor Theory, Design and Physico-Chemical Applications", Academic Press, 1997, ISBN 0-12-077460-7.

[103].   A. J. Ricco, S. J. Martin, and Z. T.E., "Surface acoustic wave gas sensors based on film conductivity changes" Sensors and Actuators, vol. 8, 1985.

[104].   P.R.van der Meer, Gerard C.M. Meijer, Michiel J. Vellekoop, Harry M.M.Kerkvliet, Ton J.J. van den Boom, "A temperature-controlled smart surface-acoustic-wave gas sensor", Sensors and Actuators A: Physical, Volume 71, Issues 1-2, November, 1998, pp.27-34.

[105].   Z. Li, Y. Jones, J. Hossenlopp, R. Cernosek, and F. Josse, "Analysis of liquid-phase chemical detection using guided shear horizontal-surface acoustic wave sensors", Analytical Chemistry, vol. 77, 2005, pp. 4595-4603.

[106].   S.Cular, V.R. Bhethanabotla, D.W. Branch, "Hexagonal Surface Acoustic Wave Devices for Enhanced Sensing and Materials Characterizaton", IEEE Ultrasonics Symposium, 2005, pp.2309-2312.

[107].   S.K.R.S. Sankaranarayanan, V.R. Bhethanabotla, B.Joseph, "Finite Element Modeling of Hexagonal Surface Acoustic Wave Device in LiNbO3", IEEE Sensors Conference, 2007, pp. 353-356.

[108].   S.Cular, V.R. Bhethanabotla, D.W. Branch, "Vapor Discrimination Using a Hexagonal Surface Acoustic Wave Device", IEEE Ultrasonics Symposium, 2006, pp.1794-1796.

[109].   L. Qin, H. Cheng, J. M. Li, and Q.-M. Wang, "Characterization of polymer nanocomposite films using quartz thickness shear mode (TSM) acoustic wave sensor", Sensors and Actuators, A: Physical, vol. A136, 2007, pp.111-117.

[110].   C.C.W.Ruppel, W.Ruile, G.Scholl, K.Ch.Wagner, and O.Manner, "Review of models for low-loss filter design and applications", IEEE Ultransonics Symposium, 1994, pp.313-324.

[111].   L.A.Coldren, and R.L.Rosenberg, "Scattering matrix approach to SAW resonators", IEEE Ultrasonics Symposium, 1976, pp.266-271.

[112].   J.J. Campbell, W.R. Jones, "A method for estimating optimal crystal cuts and propagation directions for excitation of piezoelectric surface waves", IEEE Transaction on Sonics Ultrasonics. SU-15 (4), 1968, pp.209–217.

[113].   E.Akcakaya, E.L.Adler, and G.W.Farnell, "Apodization of Multilayer Bulk-Wave Transducers", IEEE Transactions on Ultrasonics Ferroelectrics and Frequency Control, Vol.36, No.6, November 1989, pp 628-637.

[114].   E.L.Adler, J.K.Slaboszewicz, G.W.FARNELL, and C.K.JEN, "PC Software for SAW Propagation in Anisotropic Multilayers", IEEE Transactions on Ultrasonics Ferroelectrics and Frequency Control, Vol.37, No.2, May 1990, pp.215-223.

[115].   E.L.Adler, "SAW and Pseudo-SAW Properties Using Matrix Methods", IEEE Transactions on Ultrasonics Ferroelectrics and Frequency Control, Vol.41, No.6, pp.876-882, September 1994.

[116].   K. A. Ingebrigtsen, "Surface waves in piezoelectrics", Journal of Applied Physics, Vol.40, No.7, 1969, pp.2681-2686.

[117].   Y.Suzuki, H.Shimizu, M.Takeuchi, K.Nakamura, and A.Yamada, "Some studies on SAW resonators and multiple-mode filters", IEEE Ultrasonics Symposium Proceedings, 1976, pp.297-302.

[118].   N.Tirole, A.Choujaa, D.Hauden, G.Martin, "Lamb waves pressure sensor using an AlN/Si structure", IEEE Ultrasonics Symposium, 1993, pp. 371-374.

[119].   R.Hull, "Properties of Crystalline Silicon", INSPEC publication, ISBN: 0-85296-933-3, 1999.

[120].   P.Wu, N.W.Emanetoglu, X.Tong, Y.Lu, "Temperature Compensation of SAW in ZnO/SiO2/Si structure", IEEE Ultrasonics Symposium 2001.

[121].   R.R.Reeber, K.Wang, "High Temperature Elastic Constant Prediction of Some Group III-Nitrides", The Materials Research Society, 2001.

[122].   Yu.Goldberg, "Properties of Advanced Semiconductor Materials. GaN, AlN, InN, BN, SiC, SiGe", chapter 2, John Wiley & Son Inc.

[123].   G.Bu, D.Ciplys, M.Shur, L.J.Schowalter, S.Schujman, R.Gaska, "Temperature coefficient of SAW frequency in single crystal bulk AlN", Electronics Letters, Vol.39, No.9, May, 2003.

[124].   B.Auld, "Acoustic Fields and Waves in Solids", 2nd edition, Melbourne, FL: Krieger, 1990.

[125].    F.Moreita, M.E.Hakiki, F.Sarry, L.L.Brizoual, O.Elmazria, and P.Alnot, "Numerical Development of ZnO/Quartz Love Wave Structure for Gas Contamination Dectection", IEEE Sensors Journal, Vol.7, No.3, March, 2007, pp.336-341.

[126].    S.P.Timoshenko, "Theory of Plates and Shells", second edition, McGraw-Hill, 1959.

[127].    S.K.Clark, and K.D.Wise, "Pressure Sensitivity in Anisotropically Etched Thin-Diaphragm Pressure Sensor", IEEE Transactions on Electron Devices, Vol.ED-26, No.12, December, 1979, pp.1887-1896.

[128].    W.C.Young, "Roark's Formulas for Stress and Strain", sixth Edition, McGraw-Hill, 1989.

[129].    E.Ventsel, T.Krauthammer, "Thin Plates and Shells, Theory, Analysis, and Applications", Marcel Dekker, 2001.

[130].    R.J.Hohlfelder, "Bulge And Blister Testing Of Thin Films And Their Interfaces", PhD thesis, Stanford University, 1998.

[131].    M.Saadaoui, "Optimisation des Circuits passifs micro-ondes suspendus sur membrane dielectrique", in French, PhD thesis, l'Universite Paul Sabatier de Toulouse.

[132].    M.B.Kanoun, A.E.Merad, G.Merad, J. Cibert, and H.Aourag, "Prediction study of elastic properties under pressure effect for zincblende BN, AlN, GaN and InN", Solid-State Electronics, vol.48, pp.1601–1606, 2004.

[133].    A. J. Ricco, S. J. Martin, and Z. T.E., "Surface acoustic wave gas sensors based on film conductivity changes" Sensors and Actuators, vol. 8, 1985.

[134].    Z. Li, Y. Jones, J. Hossenlopp, R. Cernosek, and F. Josse, "Analysis of liquid-phase chemical detection using guided shear horizontal-surface acoustic wave sensors", Analytical Chemistry, vol. 77, 2005, pp. 4595-4603.

[135].    Oliver A. Williams, Vincent Mortet, Michael Daenen, and K. Haenen, "Nanocrystalline diamond enhanced thickness shear mode resonator", Applied Physics Letters., vol. 90, 2007.

[136].    A.Choujaa, N.Tirole, C.Bonjour, G.Martin, D.Hauden, P.Blind, A.Cachard, C.Pommier, "AlN/silicon Lamb-wave microsensors for pressure and gravimetric measurements", Sensors and Actuators A, vol. 46, 1995, pp.179-182.

[137].    H.P.Lobl, M.Klee, O.Wunnicke, R.Kiewitt, R.Dekker, E.V.Pelt, "Piezo-electric AlN and PZT films for micro-electronic applications", IEEE Ultrasonics Symposium, 1999, pp.1031-1036.

[138].    M.Akiyama, CN.Xu, M.Kodama, I.Usui, K.Nonaka, T.Watanabe, "Preparation of highly oriented Aluminum Nitride thin films on Polycrystalline Substrates by Helicon Plasma Sputtering and Annealing", Journal of American Ceramic Society, vol. 84, 2001, pp.1917-1920.

[139].    C.A.Johnsen, T.L.Bagwell, J.L.Henderson, P.C.Bray, "Polyimide as An Acoustic Absorber For High Frequency SAW Application", IEEE Ultrasonics Symposium, 1988, pp. 279-284.

[140].    W.C.Qian, A.Venema, "An Acoustic Absorption Film for SAW Devices", Sensors and Actuators A, 1991, pp.535-539.

[141].    B. A. Auld, Acoustic Fields and Waves in Solids, Vol I, Wiley, 1973, pp. 86-97.

[142].    M.Suthers, G.Este, R.Streater, B.MacLaurin, "Suppression of Spurious SAW signals", IEEE Ultrasonics Symposium, 1986, pp. 37-42.

[143].    A.C.Anderson, V.S.Dohat, W.T.Brogan, "Attenuating thin films for SAW devices", Ultrasonics Symposium Proceedings, IEEE Cat.#80CH1602-2, pp. 442-445.

[144].    Online: www.hdmicrosystems.com.

[145].    Michel Heitzmann, Christian Vizioz, "Metal Etching", ST-GRESSI report, February, 1996.

[146].    Shimada et al, "Surface acoustic wave device and method for manufacturing same", US Patent, No. US 7,154,206 B2; 26 December, 2006, pp.1-32.

[147].    Haluzak et al, "MEMS packaging structure and methods", US Patent, No. US 7,288,464 B2; 30 October, 2007, pp.1-13.

[148].    Patel et al, "Methods for depositing, releasing and packaging micro-electomechanical devices on wafer substrates", US Patent, No. US 7,198,982 B2; 03 April, 2007, pp.1-25.

[149]. Diem et al, "Process for producing a pressure transducer using silicon-on-insulator technology", US Patent, No. US 5,510,276; 23 April, 1996, pp.1-15.

[150]. L.J.Van der Pauw, "A method of measuring specific resistivity and Hall effect of discs of arbitrary shape", Philips Research Reports, Vol .13, No.1, February, 1958, pp.1–9.

[151]. L.J.Van der Pauw, "A method of measuring the resistivity and Hall coefficient on Lamellae of arbitrary shape", Philips Technical Review, Vol .20 , 1958, pp.220–224.

[152]. G.Tartavel, "Bibliotheque de motifs", Compte Rendu Technique, Groupe de travail 'Realisation de masques au batiment 41', 2004, pp.1-20.

[153]. C.H.Yu, W.Y.Chiu, H.L.Kao, "Textured and smooth AlN films prepared by helicon sputtering system [for SAW device applications]", Electronics Letters, vol.37, 2001, pp.253-255.

[154]. H.P.Lobl, M.Klee, O.Wunnicke, R.Kiewitt, R.Dekker, E.V.Pelt, "Piezo-electric AlN and PZT films for micro-electronic applications", IEEE Ultrasonics Symposium, 1999, pp.1031-1036.

[155]. F.Martin, P.Muralt, "Thickness dependence of the properties of highly c-axis textured AlN thin films", Journal of Vacuum Science Technology, 2004, pp.361-365.

[156]. K.Tsubouchi, N.Mikoshiba, "Zero temperature-coefficient SAW devices on AlN epitaxial films", IEEE Transaction on Sonics and Ultrasonics, Vol. SU-21, No.5, 1985, pp.634-644.

[157]. J.H.Hines, D.C.Malocha, "A simple transducer equivalent circuit parameter extraction technique", IEEE Ultrasonics Symposium, 1993, pp.173-177.

[158]. F.S.Hickernell, "The characterization of SAW coupling factor from paired IDT insertion loss measurements", IEEE Ultrasonics Symposium, 2002, pp.231-234.

[159]. S. Cular, S. K.R.S. Sankaranarayanan, and V. R. Bhethanabotla, "Enhancing effects of microcavities on shear-horizontal surface acoustic wave sensors: A finite element simulation study", Applied Physics Letters, 92, 2008.

[160]. E.Iborra, L.Vergara, J.Sangrador, M.Clement, A.Sanz-Hervas, and J.Olivares, "Circuital Model for the Analysis of the Piezoelectric Response of AlN Films using SAW filters", IEEE Transactions on Ultrasonics, Ferroelectrics, and Frequency Control, Vol.54, No.11, November, 2007, pp.2367-2375.

[161]. R.W.Newcomb, "Linear Multiport Synthesis", McGraw Hill, 1966.

[162]. P. A. Flinn, D. S. Gardner, and W. D. Nix, "Measurement and interpretation of stress in aluminum-based metallization as a function of thermal history" , IEEE transaction on Electron Devices, Vol. ED-34, No.3, 1987, pp.689–698.

[163]. P. A. Flinn, "Measurement and interpretation of stress in copper films as a function of thermal history," Journal of Materials Research, Vol. 6, No. 7, 1991, pp.1498–1501.

[164]. R. W. Hoffman, "The mechanical properties of thin condensed films", Physical Thin Films, vol. 3, 1966, pp. 211–273.

[165]. P. H. Townsend, and D. M. Barnett, "Elastic relationships in layered composite media with approximation for the case of thin films on a thick substrate", Journal of Applied Physics, vol. 62, no. 11, 1987, pp. 4438–4444.

[166]. Online: www.kla-tencor.com.

[167]. G.G.Stoney, "The tension of metallic films deposited by electrolysis", Proceding Royal Society, 1909, pp.172-175.

[168]. R.J.Jaccodine, and W. A. Schlegel, "Measurement of strains at Si-SiO2 interface", Journal of Applied Physics, vol. 37, 1966, pp. 2429.

[169]. G.H.Olsen, and M.Ettenberg, "Calculated stresses in multilayerd heroepitaxial structures", Journal of Applied Physics,. vol. 48, 1977, pp. 2543.

[170]. A.K.Sinha, H.J.Levinstein, and T.E.Smith, "Thermal stresses and cracking resistance of dielectric films (SiN, Si3N4; and SiO2) on Si substrates", Journal of Applied Physics, vol. 49, no. 4, 1978, pp. 2423.

[171]. J.T.Pan, and I.Blech, "In situ stress measurement of refractory metal silicides during sintering,", Journal of Applied Physics, vol. 55, no. 8, 1984, pp. 2874–2880.

## Résumé

L'objectif de cette thèse est la conception d'un capteur de pression à ondes de surface utilisant le nitrure d'aluminium (AlN). Les études théoriques, la réalisation et la caractérisation du capteur de pression sur différentes structures à ondes de surface sont présentées.

La modélisation du capteur est effectuée en utilisant un circuit équivalent basé sur le modèle de Mason et la méthode des modes couplés. Les paramètres des ondes de surfaces sont obtenus par calcul et analysés pour différentes structures telles que AlN/SiO2/Si, AlN/Si et AlN/Mo/Si. A partir de ces analyses, nous avons montré que la vitesse des ondes ainsi que le facteur de couplage peuvent dépendre du milieu de propagation. Pour chaque type de structure utilisant l'AlN, nous déterminons la plage d'épaisseur de la couche d'AlN pour laquelle la vitesse des ondes et le facteur de couplage présentent une faible dépendance au regard de l'épaisseur d'AlN. Les dispositifs à ondes de surface doivent être conçus, en particulier pour le choix des épaisseurs de différentes couches, en tenant compte de la précision du procédé de fabrication, afin de réduire les dispersions de caractéristiques des capteurs. En outre, nous avons analysé le comportement mécanique de la membrane en présence d'une pression et nous en avons déduit la sensibilité du capteur. Les effets des variations de température sur une structure à ondes de surface (SAW) sont étudiés. Pour des applications dans le domaine de la mesure de pressions, nous proposons une méthode de réduction des effets des variations de température.

Pour le précédé de fabrication, nous proposons d'utiliser le micro-usinage de surface. Ce type de procédé de fabrication permet d'obtenir exactement les dimensions des membranes utilisées dans les capteurs de pression et il permet aussi de réaliser tout type de géométrie grâce au procédé d'arrêt de gravure du silicium. Les films de nitrure d'aluminium sont caractérisés au cours de la fabrication. Nous avons trouvé que pour améliorer le comportement piézoélectrique de l'AlN, trois voies sont possibles : utiliser une couche de molybdène sous l'AlN, réduire la rugosité de la couche se trouvant sous l'AlN jusqu'à 0,2 nm et augmenter l'épaisseur de l'AlN.

Les pertes acoustiques de propagation, le facteur de couplage, l'effet d'une couche de Mo et l'effet du film mince de polyimide sur la fréquence centrale sont analysés expérimentalement. En conclusion, la sensibilité de pression mesurée de notre dispositif est présentée. Ce dernier résultat est très prometteur.

**Mots clés** : ondes acoustique de surface, Nitrure d'Aluminium (AlN), micro-usinage de surface, capteur de pression

## Abstract

The goal of this thesis is the design of a surface acoustic wave (SAW) pressure sensor using Aluminium Nitride (AlN). Theoretical studies, realization, and characterization of the pressure sensor on different SAW structures are presented.

The modeling of the sensor was performed using an equivalent circuit based on Mason model and Coupling-Of-Mode. The theoretical study, SAW parameters in different structures of $AlN/SiO_2/Si$, AlN/Si, and AlN/Mo/Si are calculated and analyzed. From these analysis, the wave velocity as well as coupling factor could depend on the wave propagation medium. For each structure using AlN, we establish the range of thickness of AlN layer, in which there is a weak dependence of the wave velocity and coupling factor on the AlN layer thickness. The SAW devices should be designed, in particular for the choice of the thicknesses of the different layers, by taking into account the accuracy of the manufacturing process, to reduce dispersion effects on the sensors characteristics. Besides, we also performed the mechanical analysis of the membrane under pressure and we have deduced the pressure sensitivity. The effect of frequency variation due to temperature change in SAW device using AlN is given. For pressure measurement applications, we propose a method to reduce temperature change effects.

Concerning the fabrication process, we propose to use surface micro-machining. This kind of fabrication process allows to obtain exactly the dimensions of membranes used in pressure sensors and it also allows to have any kind of geometry due to the silicon etch stop wall. Characterizations of AlN film are done during fabrication process. We found that to increase the piezoelectric behavior of AlN, there are three possible ways: using a bottom Mo layer, decreasing the roughness of the layer below the AlN layer up to 0.2nm and increasing the thickness of AlN.

Acoustic propagation losses, coupling factor, effect of Mo layer and the effect of thin polyimide film on the center frequency are experimentally analyzed. Finally, the measured pressure sensitivity of our device is presented. This last result is promising.

**Key words**: surface acoustic wave (SAW), Aluminium Nitride (AlN), surface micro-machining; pressure sensor